

New Physics and New Technologies in Next-Generation Neutrino Experiments.

Tommaso Boschi

1st April 2020

Submitted in partial fulfilment of the requirements
of the Degree of Doctor of Philosophy

QUEEN MARY UNIVERSITY OF LONDON
Particle Physics Research Centre, School of Physics and Astronomy

and

UNIVERSITY OF DURHAM
Institute for Particle Physics Phenomenology

I, Tommaso Boschi, confirm that the research included within this thesis is my own work or that where it has been carried out in collaboration with, or supported by others, that this is duly acknowledged below and my contribution indicated. Previously published material is also acknowledged below.

I attest that I have exercised reasonable care to ensure that the work is original, and does not to the best of my knowledge break any UK law, infringe any third party's copyright or other Intellectual Property Right, or contain any confidential material.

I accept that the College has the right to use plagiarism detection software to check the electronic version of the thesis.

I confirm that this thesis has not been previously submitted for the award of a degree by this or any other university.

The copyright of this thesis rests with the author and no quotation from it or information derived from it may be published without the prior written consent of the author.

Signature: Tommaso Boschi

Date: 1st April 2020

Details of collaboration and publications:

Chapter 1 and partially Chapters 2 and 3 provide an overview of background work, which does not constitute original research of this thesis. The remainders of Chapter 2 and Chapter 3 are completed as part of respectively the Super-Kamiokande and Hyper-Kamiokande collaborations. In Chapter 2, the simulation of the californium-252 source and the development of a gadolinium concentration monitoring device were carried out by the author in collaboration with B. Richards. The neutron calibration procedure was developed by members of the Super-Kamiokande collaboration. The extensive testing of the gadolinium-loaded water Cherenkov technique was carried by the Super-Kamiokande and EGADS collaborations. In Chapter 3, the oscillation analysis was developed by members of the Super-Kamiokande and Hyper-Kamiokande collaborations, in particular R. Wendell and M. Jiang. The improvements to the fitting framework was developed by the author, thanks to the support of members of the Hyper-Kamiokande collaborations, especially M. Friend, M. Scott, and T. Dealtry. Inputs to the analysis are provided by T. Dealtry. The work of Chapters 4 and 5 was performed in collaboration with S. Pascoli and P. Ballett as published in Ref. [1]. The discussion on neutrino mass models of Chapter 4 was led by S. Pascoli with fundamental inputs by P. Ballett. The derivation of the formulae of Sections 4.2 and 4.3 was done by the author and P. Ballett. The prediction of the ν_τ flux contribution in Chapter 5 was done by the author, thanks to the useful discussions with R. Ruiz, whereas the other contributions to the flux were provided by the DUNE collaboration. The simulation of the Near Detector of DUNE in Chapter 5 was developed by the author, as well as the framework to carry out sensitivity studies. The mass matrix scan in Section 5.4 was carried out by the author, thanks to the useful discussions with C. Weiland and M. Lucente. Except where stated, all the graphs and plots in the thesis were made by the author.

Abstract

We are living a pivotal moment for neutrino physics. A new generation of experiments is about to begin and will extend our understanding of neutrinos. Very large scale experiments, like Hyper-Kamiokande, will collect unprecedented statistics and will constrain oscillation parameters to high precision: the CP violation phase, the octant of θ_{23} , and the mass hierarchy are likely to be determined. Many are the experimental difficulties behind a successful megaton water Cherenkov detector, but improvements in photodetection technologies luckily allow such an ambitious project. One of the most important challenges is to keep systematical uncertainties under control, so as they do not dominate over statistical errors. Assessing the impact of the systematics on the overall sensitivity of the experiment is a fundamental requirement to the final success of Hyper-Kamiokande.

Thanks to powerful accelerator facilities, future long baseline experiments, such as DUNE, will also explore the intensity frontier of neutrino physics and study rare phenomena. Numerous extension to the Standard Model (SM) and alternative theories have been introduced to explain neutrino masses and mixings. These new scenarios often predict new physics, the signature of which is accessible to next-generation experiments. An interesting example comes from low-scale see-saw models, which consider GeV-scale neutral leptons coupled to SM particles with suppressed mixing angles. The near detector system of DUNE is an ideal place for searches of these particles, thanks to high exposure that compensate small event rates.

Current neutrino experiments have also joined this new venture; Super-Kamiokande has been extensively refurbished in view of a new phase, starting in early 2020, in which the detector will turn into a supernova observatory. This is achieved by doping the water of Super-Kamiokande with gadolinium, in order to increase the efficiency of neutron tagging up to 90 %. The use of gadolinium is a novel technique which will be adopted by many existing and planned experiments. The benefits of improved neutron tagging are not limited just to supernova neutrinos, but to a plethora of other studies, such as reactor and atmospheric neutrinos or proton decay.

In this thesis, all of the topics above are addressed. After a review of SM neutrino physics in Chapter 1, the gadolinium-loaded water Cherenkov technique is discussed in Chapter 2 with particular focus on Super-Kamiokande. A new technique to monitor gadolinium concentration in water using UV spectroscopy and an improved method for neutron calibration using a californium source are presented. Chapter 3 deals with CP violation in neutrino oscillation and the potential of Hyper-Kamiokande to constraining oscillation parameters. The methodology used to asses the experimental sensitivity is described in detail. First estimations are shown with the full systematic model and some of its variations are also taken into account. In Chapter 4 a possible Standard Model extension to explain neutrino masses is considered, and the phenomenology of such models is extensively studied in the context of a beam dump experiment. The prospect of the DUNE's near detector to searches of heavy neutral lepton decays is then evaluated in Chapter 5. It is found that the DUNE ND is capable of extending current limits on these searches, reaching regions of the parameter space extremely interesting from a theoretical point of view.

Contents

List of Figures	7
List of Tables	9
1 Neutrinos in the Standard Model	11
1.1 Electroweak sector	12
1.1.1 Electroweak interactions	13
1.1.2 Higgs mechanism	14
1.1.3 Fermion mixing	16
1.2 Neutrino oscillations	16
1.2.1 Neutrino mixing	17
1.2.2 Propagation of neutrinos in vacuum	18
1.2.3 Propagation of neutrinos in matter	21
1.3 Neutrino production	25
1.3.1 Solar and supernova neutrinos	26
1.3.2 Atmospheric neutrinos	29
1.3.3 Accelerator neutrinos	31
1.4 Neutrino interactions	33
1.4.1 Coherent elastic neutrino–nucleus scattering	34
1.4.2 Neutrino–electron scattering	36
1.4.3 Neutrino scattering with nucleons	37
2 The future of Super-Kamiokande	41
2.1 Cherenkov detectors	42
2.2 Neutron thermalisation and neutron capture	43
2.3 The Super-Kamiokande experiment	45
2.3.1 Background control	46
2.3.2 The gadolinium phase of Super-Kamiokande	48
2.4 Neutron calibration in Super-Kamiokande	50
2.5 Monitoring gadolinium concentration	53
3 CP violation with HK	61
3.1 CP violation in neutrino oscillations	62
3.2 Hyper-Kamiokande experiment	65
3.3 Sensitivity studies	66
3.3.1 Event samples	66
3.3.2 Oscillation space	67
3.3.3 Test statistic	68
3.3.4 Far detector prediction	71

3.3.5	Validation of the fitter	72
3.4	Systematic studies	75
3.4.1	Systematic model	75
3.4.2	Sensitivity with the nominal systematic model	77
3.4.3	Variations of the nominal model	80
4	Phenomenology of heavy neutral leptons	85
4.1	Heavy neutrinos in seesaw models	86
4.2	Heavy neutrino decay	89
4.2.1	Majorana neutrinos	91
4.2.2	Pseudo-Dirac neutrinos	96
4.3	Heavy neutrino production	98
4.3.1	Two-body decays	100
4.3.2	Three-body decays	102
5	HNL discovery with the DUNE experiment	105
5.1	The near detector of DUNE	106
5.1.1	Exposure	108
5.1.2	Flux prediction	109
5.2	Simulation of events at the DUNE ND	111
5.2.1	Background evaluation	112
5.2.2	HNL decay events and signal efficiency	114
5.2.3	Selection example	114
5.3	Sensitivities of the DUNE ND	117
5.3.1	Single dominant mixing	118
5.3.2	Two dominant mixings	121
5.4	Mass model constraints from the DUNE ND	124
5.4.1	Mass model scan	124
5.4.2	Overall sensitivity	125
5.5	Determining the nature of HNLs	128
6	Conclusions	133
A	List of systematics	139
A.1	BANFF systematics	139
A.2	SK & FSI systematics	140
A.3	Atmospheric systematics	140
B	Open charm production	141

List of Figures

1.1	Oscillation probability for an initial ν_e and ν_μ	19
1.2	Solar standard model prediction of the solar neutrino flux	28
1.3	Survival probability of ν_e measured by BOREXINO	28
1.4	Neutrino flux from a core-collapse supernova	29
1.5	Energy spectrum of cosmic rays	30
1.6	Prediction of atmospheric neutrinos	31
1.7	Prediction of ν_μ and $\bar{\nu}_\mu$ at the Booster Neutrino Beam	32
1.8	Prediction of ν_μ at T2K	32
1.9	Generic CC and NC tree-level weak interactions	33
1.10	Neutrino–nucleus cross-sections at low neutrino energies	34
1.11	Neutrino–nucleus cross-sections at high neutrino energies	38
2.1	View of the Super-Kamiokande detector	46
2.2	Reconstructed fully-contained events in Super-Kamiokande	47
2.3	Dependency of neutron capture efficiency with respect to gadolinium concentration	48
2.4	Schematic of the band-pass filtration system and the fast recirculation loop in EGADS	48
2.5	Neutron cross-sections on hydrogen and gadolinium-157	50
2.6	Normalised energy distribution of Am-Be and ^{252}Cf sources	51
2.7	Setup used to test a californium source	52
2.8	Distribution of PMT peaks measured with a californium source	53
2.9	Distribution of optical photons from the simulation of a neutron calibration device	53
2.10	Performance of different scintillators from the simulation of a neutron calibration device	54
2.11	Gadolinium absorption spectra	55
2.12	Ocean HDX spectra with a 10 cm water sample	56
2.13	Linear fit between Gd concentration and absorption with a 10 cm water sample	57
2.14	Schematic of the device used for testing the 100 cm water sample	58
2.15	Gadolinium absorption spectrum of the 100 cm water sample	59
2.16	Linear fit between Gd concentration and absorption with a 100 cm water sample	60
3.1	Effect of δ_{CP} on the oscillation probability	64
3.2	Views of the Hyper-Kamiokande experiment	65
3.3	Predicted distribution of one ring e -like events	70
3.4	Predicted distribution of one ring μ -like events	71
3.5	Prediction of events with a simplified systematic model	72
3.6	χ^2 profiles for Δm_{32}^2 , $\sin^2 2\theta_{13}$, and $\sin \theta_{23}$ with a simplified systematic model	73
3.7	Contour lines of Δm_{32}^2 versus $\sin^2 2\theta_{13}$, χ^2 profiles for δ_{CP} , and sensitivity to $\delta_{\text{CP}} \sin \theta_{23}$ with a simplified systematic model	74

3.8	Correlation matrix of the beam systematic model	76
3.9	χ^2 profiles for Δm_{32}^2 , $\sin^2 2\theta_{13}$, and $\sin \theta_{23}$ with the nominal systematic model . .	78
3.10	Sensitivity to δ_{CP} with the nominal systematic model	79
3.11	Sensitivity to δ_{CP} with the nominal model and unknown hierarchy	79
3.12	χ^2 profiles for δ_{CP} , Δm_{32}^2 , $\sin^2 2\theta_{13}$, and $\sin \theta_{23}$ and contours for Δm_{32}^2 versus $\sin \theta_{23}$ and δ_{CP} versus $\sin^2 2\theta_{13}$ with variations on the nominal systematic model	81
3.13	Sensitivity to $\delta_{\text{CP}} = 0$ with variations on the nominal systematic model	82
4.1	Schematic for LNV dependency of mass spectrum in an inverse seesaw model . .	88
4.2	Branching ratios for HNL decays integrated over the angular variables	91
4.3	Feynman diagrams for HNL two-body decays into pseudoscalar mesons.	92
4.4	Feynman diagrams for HNL three-body leptonic decays.	94
4.5	Helicity factors for production of HNL	100
4.6	Scale factors for production of HNL	101
5.1	View of the near detector complex of DUNE	107
5.2	Prediction of neutrino fluxes at the near detector of DUNE	109
5.3	Fluxes of heavy neutrinos from the decay channel $D_s^+ \rightarrow \tau^+ N$	110
5.4	Sensitivity regions to individual channels for dominant mixings with background analysis	119
5.5	Sensitivity regions to individual channels for dominant mixings without background analysis	120
5.6	Sensitivity regions to individual channels for two dominant mixings	123
5.7	Combined sensitivity for dominant mixings for channels with good discovery prospects	127
5.8	Comparison of ISS(2,3) with short baseline anomalies	128
5.9	Sensitivity to distinction between Majorana and Dirac HNL	130
B.1	Diagrams contributing to open charm production at the partonic level	142

List of Tables

1.1	Best fit values for neutrino oscillation parameters	21
1.2	Processes emitting ν_e in the pp chain and the CNO cycle	27
3.1	Sample events for atmospheric data	67
3.2	Parameter space used in the oscillation analysis	68
3.3	Variations of the nominal systematic model	80
4.1	Available channels for HNL decay with a mass below D_s^\pm	90
4.2	Production channels at beam dump facilities yielding neutrinos	99
5.1	Exposures of major beam dump experiments	108
5.2	Expected rates for CC and NC interaction in the near detector of DUNE	111
5.3	Detection thresholds and energy/momentum and angular resolutions used in the near detector simulation	112
5.4	Decay channels with good discovery prospect and their signals and backgrounds .	113
5.6	Efficiencies of selection cuts of two-body decays	115
5.7	Efficiencies of selection cuts of three-body decays	116
5.8	Efficiencies of selection cuts of EM-detected decay	117
5.9	Results for sensitivity with dominant mixing to channels with background analysis	118
5.10	Results for sensitivity with dominant mixing to channels without background analysis	121
5.11	Results for sensitivity with two dominant mixing	122

Chapter 1

Neutrinos in the Standard Model

The Standard Model (SM) is a renormalisable Yang-Mills theory [2] that describes the strong, electromagnetic, and weak interactions of elementary particles in the framework of quantum field theory [3–5]. It is based on the local gauge symmetry group

$$\mathrm{SU}(3)_C \otimes \mathrm{SU}(2)_L \otimes \mathrm{U}(1)_Y \quad (1.1)$$

where C , L and Y denote respectively colour, left-handed chirality and weak hyper-charge. The gauge group uniquely determines the interactions and the number of vector gauge bosons that correspond to the generators of the group. The electroweak subgroup $\mathrm{SU}(2)_L \otimes \mathrm{U}(1)_Y$ undergoes a spontaneous symmetry breaking process out of which three of the four vector bosons acquire mass (W^\pm and Z bosons) and the last one, the photon, remains massless. This process requires at least one scalar boson with a nonzero vacuum expectation value [6, 7]. The colour symmetry does not break and does not mix with the electroweak sector. The generators of its algebra correspond to eight massless gluons. The gauge and scalar bosons are coupled to fermion fields, which are irreducible representations of the Poincaré group. The known elementary fermions are divided in two categories: quarks and leptons. They are distinguished by the fact that quarks participate in all the interactions whereas leptons participate only in the electroweak interactions. Since the number and properties of the gauge bosons are determined by the SM group, the only independent parameters left are the coupling constants of the interactions, which can be constrained from experiments. The number and the masses of scalar bosons and fermions are also to be determined experimentally, keeping in mind that they must transform according to the representations of the symmetry group and the fermion representations must lead to the cancellation of quantum anomalies.

Despite being the most successful theory of particle physics to date, the SM is actually limited in its description of reality in that some evidence is not explained nor addressed. The most outstanding breakthrough is the discovery of neutrino oscillation which was awarded the Nobel Prize in Physics in 2015 and has proven that the neutrinos are not all massless as imposed by the SM. Mass terms for the neutrinos can be actually included in the SM, although with the implication of theoretical and naturalness problems. Likewise, the SM is unable to provide an explanation of the observed asymmetry between matter and antimatter. It was noted by Sakharov that a solution to this puzzle would require some form of C and CP violation in the early Universe, along with Baryon number violation and out-of-equilibrium interactions [8]. There is also plenty of evidence suggesting the presence of dark matter in the Universe [9–11], and there are a variety of theoretical and experimental endeavours trying to unearth its nature. These facts suggest that the Standard Model is not a complete theory and additional physics Beyond the Standard Model (BSM) is required.

The study of neutrinos is for sure one of the most promising probes to BSM physics and is of vital importance to the future development of particle physics, in particular through precision measurement of their interactions. A deep understanding of neutrino interactions, and neutrino–nucleon interactions in particular, could lead to a great impact on long-baseline experiments, proton decay searches, and supernova detection. Since the SM is a renormalisable theory, even its quantum corrections are insensitive to the physics beyond the SM. For this reason, the SM is phenomenologically very successful and so far has been able to describe all the known phenomena, except for the indications in favour of neutrino oscillations as it will be discussed in the following chapters.

1.1 Electroweak sector

The electroweak (EW) sector of the SM is formed by the direct product of the weak isospin group $SU(2)_L$ and the hyper-charge group $U(1)_Y$. The two groups are connected by the Gell-Mann–Nishijima [12, 13] relation which connects the I_3 component of the weak isospin operator and the hyper-charge operator Y with the charge operator Q as

$$Q = I_3 + \frac{Y}{2} . \quad (1.2)$$

Left-handed chiral components of the fermion fields form doublets under $SU(2)_L$

$$\mathbf{L}_L = \begin{pmatrix} \nu_L \\ \ell_L \end{pmatrix} , \quad \mathbf{Q}_L = \begin{pmatrix} \mathbf{q}_L^U \\ \mathbf{q}_L^D \end{pmatrix} , \quad (1.3)$$

where the left-handed fields (in boldface) represent the fermion families

$$\nu_L = \begin{pmatrix} \nu_{eL} \\ \nu_{\mu L} \\ \nu_{\tau L} \end{pmatrix} , \quad \ell_L = \begin{pmatrix} e_L \\ \mu_L \\ \tau_L \end{pmatrix} , \quad \mathbf{q}_L^D = \begin{pmatrix} d_L \\ s_L \\ b_L \end{pmatrix} , \quad \text{and} \quad \mathbf{q}_L^U = \begin{pmatrix} u_L \\ c_L \\ t_L \end{pmatrix} . \quad (1.4)$$

The right-handed fields, instead, transform simply as singlets and they are

$$\ell_R = \begin{pmatrix} e_R \\ \mu_R \\ \tau_R \end{pmatrix} , \quad \mathbf{q}_R^D = \begin{pmatrix} d_R \\ s_R \\ b_R \end{pmatrix} , \quad \text{and} \quad \mathbf{q}_R^U = \begin{pmatrix} u_R \\ c_R \\ t_R \end{pmatrix} . \quad (1.5)$$

The right-handed components of the neutrino fields, $\nu_{\alpha R}$, are not historically considered in the SM because neutrinos are assumed to be massless and the ν_R components are *sterile* under any charge of the SM. Furthermore, the helicity of neutrinos was measured to be consistent with left chirality [14]. The EW Lagrangian is therefore the most general renormalisable Lagrangian invariant under the local symmetry $SU(2)_L \otimes U(1)_Y$:

$$\begin{aligned} \mathcal{L}_{\text{EW}} = & i \bar{\mathbf{L}}_L \not{D} \mathbf{L}_L + i \bar{\mathbf{Q}}_L \not{D} \mathbf{Q}_L + i \bar{\ell}_R \not{D} \ell_R + i \bar{\mathbf{q}}_R^D \not{D} \mathbf{q}_R^D + i \bar{\mathbf{q}}_R^U \not{D} \mathbf{q}_R^U \\ & - \frac{1}{4} B_{\mu\nu} B^{\mu\nu} - \frac{1}{4} \mathbf{A}_{\mu\nu} \mathbf{A}^{\mu\nu} + (D_\mu H)^\dagger (D^\mu H) - \mu^2 H^\dagger H - \lambda (H^\dagger H)^2 \\ & - \left(\bar{\mathbf{L}}_L Y^\ell H \ell_R + \bar{\mathbf{Q}}_L Y^D H \mathbf{q}_R^D + \bar{\mathbf{Q}}_L Y^U \tilde{H} \mathbf{q}_R^U + \text{h.c.} \right) , \end{aligned} \quad (1.6)$$

where the covariant derivative satisfies gauge invariance and is defined as

$$D_\mu = \partial_\mu + ig \mathbf{A}_\mu \cdot \mathbf{I} + ig' B_\mu \frac{Y}{2} , \quad (1.7)$$

and $\tilde{H} = i\sigma_2 H^*$ is the conjugate Higgs field. It is important to note that Dirac mass terms for fermion fields other than neutrinos are anyway forbidden by the gauge symmetry. These terms will become manifest once the symmetry is broken through the Higgs mechanism (see Section 1.1.2). The vector boson fields $\mathbf{A}^\mu = (A_1^\mu, A_2^\mu, A_3^\mu)$ and B^μ correspond respectively to the three generators $\mathbf{I} = (I_1, I_2, I_3)$ of the $SU(2)_L$ group and the generator Y of the $U(1)_Y$ group. The $SU(2)_L$ generators are $I_a = \sigma_a/2$, with σ_a the Pauli matrices, and thus satisfy the commutation relation

$$[I_a, I_b] = i\varepsilon_{abc} I_c , \quad (1.8)$$

where ε_{abc} is the Levi-Civita tensor.

1.1.1 Electroweak interactions

Expanding the covariant derivative and ignoring kinetic terms, the interaction terms for the lepton sector are retrieved

$$\mathcal{L}_{\text{int,L}} = -\frac{1}{2} \sum_{\alpha} (\bar{\nu}_{\alpha L} \quad \bar{\ell}_{\alpha L}) \begin{pmatrix} gA_3 - g'\not{B} & g(A_1 - iA_2) \\ g(A_1 + iA_2) & -gA_3 - g'\not{B} \end{pmatrix} \begin{pmatrix} \nu_{\alpha L} \\ \ell_{\alpha L} \end{pmatrix} - g' \bar{\ell}_{\alpha R} \not{B} \ell_{\alpha R} , \quad (1.9)$$

where α is the family generation index. Defining the combinations

$$W^\mu = (A_1^\mu - iA_2^\mu) / \sqrt{2} \quad (1.10)$$

$$Z^\mu = \cos \vartheta_W A_3^\mu - \sin \vartheta_W B^\mu \quad (1.11)$$

$$A^\mu = \sin \vartheta_W A_3^\mu + \cos \vartheta_W B^\mu , \quad (1.12)$$

the electromagnetic field A^μ is expressed as a rotation of A_3^μ and B^μ , thus recovering QED; the new field Z^μ also mediates neutral current processes. The Lagrangian in Eq. (1.9) can therefore be divided into two parts, $\mathcal{L}_{\text{int,L}} = \mathcal{L}_{\text{CC,L}} + \mathcal{L}_{\text{NC,L}}$, describing charged-current (CC) and neutral-current (NC) interactions. These are

$$\mathcal{L}_{\text{CC,L}} = -\frac{g}{2\sqrt{2}} j_{\text{CC,L}}^\mu W_\mu + \text{h.c.} , \quad (1.13)$$

$$\mathcal{L}_{\text{NC,L}} = -\frac{g}{2\cos \vartheta_W} j_{\text{NC,L}}^\mu Z_\mu + g \sin \vartheta_W \bar{\ell} \not{A} \ell , \quad (1.14)$$

where the W and Z vector bosons have been factorised out, leaving the fermionic currents

$$j_{\text{CC,L}}^\mu = \bar{\nu} \gamma^\mu (1 - \gamma^5) \ell , \quad (1.15)$$

$$j_{\text{NC,L}}^\mu = \bar{\nu} \gamma^\mu (g_V^\nu - g_A^\nu \gamma^5) \nu + \bar{\ell} \gamma^\mu (g_V^\ell - g_A^\ell \gamma^5) \ell . \quad (1.16)$$

The constant g' has been rewritten in terms of g and ϑ_W by setting to zero the coupling of neutrinos to the electromagnetic field which implies

$$g \sin \vartheta_W = g' \cos \vartheta_W . \quad (1.17)$$

The weak mixing angle ϑ_W is also known as *Weinberg angle* and it is estimated to be approximately $\sin^2 \vartheta_W \simeq 0.231$ from either studies of neutrino neutral-current processes at low energies or studies of the Z mixing with the photon in Drell-Yan processes at higher energies [15]. Another important relation comes from the charged lepton couplings with the electromagnetic field which must coincide with the QED Lagrangian. It follows that $g \sin \vartheta_W = q_e$ and so $g^2 + g'^2 = q_e^2$. The constants g_V and g_A , introduced in Eq. (1.16), can be defined for any fermion f as

$$g_V^f = I_3^f - 2q^f \sin^2 \vartheta_W \quad \text{and} \quad g_A^f = I_3^f . \quad (1.18)$$

Thanks to this notation, the interaction Lagrangians for the quark sector can be written in the same form of Eqs. (1.13) and (1.13), where the fermionic currents of Eqs. (1.15) and (1.16) now become

$$j_{\text{CC},Q}^\mu = \bar{\mathbf{q}}^U \gamma^\mu (1 - \gamma^5) \mathbf{q}^D, \quad (1.19)$$

$$j_{\text{NC},Q}^\mu = \bar{\mathbf{q}}^U \gamma^\mu (g_V^U - g_A^U \gamma^5) \mathbf{q}^U + \bar{\mathbf{q}}^D \gamma^\mu (g_V^D - g_A^D \gamma^5) \mathbf{q}^D. \quad (1.20)$$

1.1.2 Higgs mechanism

In the EW Lagrangian of Eq. (1.6), the Higgs H is a complex scalar field and an $\text{SU}(2)_L$ doublet

$$H(x) = \begin{pmatrix} H^+(x) \\ H^0(x) \end{pmatrix}, \quad (1.21)$$

the potential of which, $V(H)$, can spontaneously break if $\lambda > 0$ and $\mu^2 < 0$, where

$$V(H) = \mu^2 H^\dagger H + \lambda (H^\dagger H)^2. \quad (1.22)$$

Defining

$$v \equiv \sqrt{-\frac{\mu^2}{\lambda}}, \quad (1.23)$$

the potential $V(H)$ finds its minimum for $H^\dagger H = v^2/2$ which corresponds to the lowest energy state, or vacuum. In general, fermion and nonzero spin boson fields must have a vanishing vacuum expectation value (vev), so as to preserve the Lorentz symmetries of space and time. The same applies to charged scalar fields, since the vacuum is electrically chargeless. On the other hand, neutral scalar fields can have a nonzero value in vacuum and so the vev of the Higgs field could be given by

$$\langle H \rangle = \frac{1}{\sqrt{2}} \begin{pmatrix} 0 \\ v \end{pmatrix}. \quad (1.24)$$

This value spontaneously breaks the EW group $\text{SU}(2)_L \otimes \text{U}(1)_Y$, but it remains invariant under the gauge transformations from the $\text{U}(1)_Q$ group, with Q from Eq. (1.2), which guarantees the existence of a massless gauge boson associated with the photon. To study what happens around the vacuum state, the scalar field can be expanded around its vev and by choosing the unitary gauge three of the four real scalar fields are rotated away since they are unphysical, simplifying to

$$H(x) = \frac{1}{\sqrt{2}} \begin{pmatrix} 0 \\ v + h(x) \end{pmatrix}. \quad (1.25)$$

Using the definition of the EW fields in Eq. (1.10), the covariant derivative of Eq. (1.7) applied to the Higgs field reads

$$D_\mu H(x) = \frac{1}{\sqrt{2}} \begin{pmatrix} i \frac{g}{\sqrt{2}} W_\mu(x) [v + h(x)] \\ \partial_\mu h(x) - i \frac{g}{2 \cos \vartheta_W} Z_\mu(x) [v + h(x)] \end{pmatrix}. \quad (1.26)$$

The Lagrangian terms with the Higgs field therefore become

$$\begin{aligned} \mathcal{L}_{\text{Higgs}} = & \frac{1}{2} (\partial h)^2 - v^2 \lambda h^2 - \lambda h^3 - \frac{\lambda}{4} h^4 + \frac{g^2 v^2}{4} W_\mu^\dagger W^\mu + \frac{g^2 v^2}{8 \cos^2 \vartheta_W} Z_\mu Z^\mu \\ & + \frac{g^2 v}{2} W_\mu^\dagger W^\mu h + \frac{g^2 v}{4 \cos^2 \vartheta_W} Z_\mu Z^\mu h \\ & + \frac{g^2}{4} W_\mu^\dagger W^\mu h^2 + \frac{g^2}{8 \cos^2 \vartheta_W} Z_\mu Z^\mu h^2. \end{aligned} \quad (1.27)$$

The second term of the first line is a mass term for the scalar field, from which the mass of the Higgs boson is determined to be $m_H = v\sqrt{2\lambda} = \sqrt{-2\mu^2}$. The fifth and sixth terms represent the mass terms for the W and Z bosons, namely

$$m_W = \frac{gv}{2} \quad , \quad m_Z = \frac{gv}{2\cos\vartheta_W} \quad , \quad (1.28)$$

and the following parameter

$$\rho = \frac{m_W^2}{m_Z^2 \cos^2\vartheta_W} \quad (1.29)$$

is predicted to be $\rho = 1$ in the SM. The other terms of 1.27 describe self-interactions of the Higgs and interactions with the W and Z vector bosons.

Applying the same expansion of Eq. (1.25) to the Yukawa terms of the SM Lagrangian, couplings between left and right chiral fields and trilinear couplings of the fermions with the Higgs are obtained. The lepton section becomes

$$\mathcal{L}_{H,L} = -\frac{v}{\sqrt{2}} \bar{\ell}_L Y^\ell \ell_R - \frac{1}{\sqrt{2}} \bar{\ell}_L Y^\ell \ell_R h + \text{h.c.} \quad , \quad (1.30)$$

and the same is found in the quark sector:

$$\begin{aligned} \mathcal{L}_{H,Q} = & -\left(\frac{v}{\sqrt{2}} \bar{q}_L^D Y^D q_R^D + \frac{v}{\sqrt{2}} \bar{q}_L^U Y^U q_R^U \right) \\ & -\left(\frac{1}{\sqrt{2}} \bar{q}_L^D Y^D q_R^D h + \frac{1}{\sqrt{2}} \bar{q}_L^U Y^U q_R^U h \right) + \text{h.c.} \end{aligned} \quad (1.31)$$

The terms in the Lagrangians of Eqs. (1.30) and (1.31) proportional to $\bar{f}_L f_R = \bar{f} f$ are Dirac mass terms for the fermion f . There is no principle by which the Yukawa coupling matrices Y^f should be *a priori* diagonal, however without a diagonal matrix the fermion masses are not properly defined. Being a generic complex matrix, the diagonalisation can be performed via a biunitary transformation

$$V_L^{\dagger} \left(\frac{v}{\sqrt{2}} Y^f \right) V_R = \frac{v}{\sqrt{2}} \hat{Y}_\alpha^f \equiv \text{diag} \left(\frac{y_\alpha^f v}{\sqrt{2}} \right) \quad , \quad (1.32)$$

where V_L and V_R are both unitary matrices. The fermion masses are defined by the Yukawa couplings

$$m_\alpha^f \equiv \frac{y_\alpha^f v}{\sqrt{2}} \quad , \quad (1.33)$$

with α the family generation index. The biunitary transformation acts on the lepton fields as

$$\hat{\ell}_L = V_L^{\ell\dagger} \ell_L \quad , \quad \hat{\ell}_R = V_R^{\ell\dagger} \ell_R \quad (1.34)$$

and on the quark fields as

$$\begin{aligned} \hat{q}_L^D &= V_L^{D\dagger} q_L^D \quad , \quad \hat{q}_R^D = V_R^{D\dagger} q_R^D \\ \hat{q}_L^U &= V_L^{U\dagger} q_L^U \quad , \quad \hat{q}_R^U = V_R^{U\dagger} q_R^U . \end{aligned} \quad (1.35)$$

Dropping the “hat notation” to denote mass eigenfields, the lepton sector becomes

$$\mathcal{L}_{\text{mass}} = - \sum_{\alpha=e,\mu,\tau} \frac{y_\alpha^\ell v}{\sqrt{2}} \bar{\ell}_\alpha \ell_\alpha = - \sum_{\alpha=e,\mu,\tau} m_\alpha \bar{\ell}_\alpha \ell_\alpha \quad , \quad (1.36)$$

and similarly for quarks

$$\begin{aligned}\mathcal{L}_{\text{mass}} &= - \sum_{\alpha=d,s,b} \left(\frac{y_\alpha^D v}{\sqrt{2}} \bar{q}_\alpha^D q_\alpha^D \right) - \sum_{\beta=u,c,t} \left(\frac{y_\beta^U v}{\sqrt{2}} \bar{q}_\beta^U q_\beta^U \right) \\ &= - \sum_{\alpha=d,s,b} (m_\alpha \bar{q}_\alpha^D q_\alpha^D) - \sum_{\beta=u,c,t} (m_\beta \bar{q}_\beta^U q_\beta^U) .\end{aligned}\quad (1.37)$$

As stressed previously, in the SM there are no right-handed neutrino fields, necessary to obtain Dirac mass terms: the neutrinos are simply massless by definition.

1.1.3 Fermion mixing

The same transformations of Eqs. (1.34) and (1.35) should be equally applied to all the parts of the EW Lagrangian. Let us start from the quark charged current expressed in Eq. (1.19)

$$j_{\text{CC},Q}^\mu = 2 \bar{q}_L^U \gamma^\mu q_L^D = 2 \bar{q}_L^U V_L^{U\dagger} \gamma^\mu V_L^D \hat{q}_L^D = 2 \bar{q}_L^U \gamma^\mu V \hat{q}_L^D , \quad (1.38)$$

where the unitary matrix $V = V_L^{U\dagger} V_L^D$, called Cabibbo-Kobayashi-Maskawa (CKM) matrix, describes the mixing between quark fields in weak interaction processes when initial and final states represent particles with definite masses. The same mixing matrix however does not appear in the NC current of Eq. (1.20). Defining the couplings $2g_L^f = g_V^f + g_A^f$ and $2g_R^f = g_V^f - g_A^f$, the current with explicit mass eigenstates becomes

$$\begin{aligned}j_{\text{NC},Q}^\mu &= 2g_L^U \bar{q}_L^U \gamma^\mu q_L^U + 2g_R^U \bar{q}_R^U \gamma^\mu q_R^U + 2g_L^D \bar{q}_L^D \gamma^\mu q_L^D + 2g_R^D \bar{q}_R^D \gamma^\mu q_R^D \\ &= 2g_L^U \bar{q}_L^U V_L^{U\dagger} \gamma^\mu V_L^U \hat{q}_L^U + 2g_R^U \bar{q}_R^U V_R^{U\dagger} \gamma^\mu V_R^U \hat{q}_R^U \\ &\quad + 2g_L^D \bar{q}_L^D V_L^{D\dagger} \gamma^\mu V_L^D \hat{q}_L^D + 2g_R^D \bar{q}_R^D V_R^{D\dagger} \gamma^\mu V_R^D \hat{q}_R^D \\ &= 2g_L^U \bar{q}_L^U \gamma^\mu \hat{q}_L^U + 2g_R^U \bar{q}_R^U \gamma^\mu \hat{q}_R^U + 2g_L^D \bar{q}_L^D \gamma^\mu \hat{q}_L^D + 2g_R^D \bar{q}_R^D \gamma^\mu \hat{q}_R^D .\end{aligned}\quad (1.39)$$

The neutral current with massive fields has the same form of the neutral current with unrotated fields. This is also true for the electromagnetic current of the EW Lagrangian. The phenomenon is called Glashow-Iliopoulos-Maiani (GIM) mechanism [16], by which flavour-changing neutral currents (FCNCs) are forbidden at tree level thanks to the unitarity of the electroweak interaction, but allowed in suppressed loop diagrams.

Looking at the lepton sector, the transformations of Eq. (1.34) are not analogously defined for the neutrino fields. Therefore, neutrino states can be arbitrarily chosen such that $\hat{\nu}_L = V_L^{\ell\dagger} \nu_L$, where V_L^ℓ is the same of Eq. (1.34). The lepton charged current therefore remains unchanged

$$j_{\text{CC},L}^\mu = 2 \bar{\nu}_L \gamma^\mu \ell_L = 2 \bar{\nu}_L V_L^{\ell\dagger} \gamma^\mu V_L^\ell \hat{\ell}_L = 2 \bar{\nu}_L \gamma^\mu \hat{\ell}_L . \quad (1.40)$$

The fields $\hat{\nu} = (\hat{\nu}_e, \hat{\nu}_\mu, \hat{\nu}_\tau)$ are called *flavour neutrino fields*, because they only couple to the corresponding charged lepton fields in the equation above. As in the case of the quark fields, the GIM mechanism applies even for the leptonic neutral current thanks to the unitarity of the matrices V_L^ℓ and V_R^ℓ .

1.2 Neutrino oscillations

As seen in Section 1.1, the SM does not consider right-handed neutrino fields. For this reason, a Yukawa term coupling the lepton $\text{SU}(2)_L$ doublet with the conjugate Higgs field does

not appear in the EW Lagrangian. It follows that after the spontaneous symmetry breaking caused by the nonzero Higgs vev the neutrinos do not gain Dirac mass terms, as the other fermions do. This “asymmetry” between fermion fields can be easily resolved by extending the SM and introducing the right-handed neutrino fields

$$\boldsymbol{\nu}_R = \begin{pmatrix} \nu_{eR} \\ \nu_{\mu R} \\ \nu_{\tau R} \end{pmatrix}. \quad (1.41)$$

These fields are chargeless under all the SM gauge groups and therefore are not directly coupled to any vector boson and as such their existence is not easily testable. Having now both chiralities, Dirac mass terms can be constructed for neutrinos, leading to neutrino mixing and so the neutrino oscillation phenomenon, observed in various neutrino experiments.

1.2.1 Neutrino mixing

Thanks to this extension, the following Yukawa term is now allowed

$$\mathcal{L}_{\text{EW}} \supset - \left(\bar{\mathbf{L}}_L Y^\ell H \boldsymbol{\ell}_R + \bar{\mathbf{L}}_L Y^\nu \tilde{H} \boldsymbol{\nu}_R + \text{h.c.} \right), \quad (1.42)$$

and using the expansion of Eq. (1.25) the Yukawa matrix can be diagonalised by a biunitary transformation to define masses for the neutrino fields. This leads to new mass eigenfields

$$\hat{\boldsymbol{\nu}}_L = V_L^{\nu\dagger} \boldsymbol{\nu}_L = \begin{pmatrix} \nu_{1L} \\ \nu_{2L} \\ \nu_{3L} \end{pmatrix}, \quad \hat{\boldsymbol{\nu}}_R = V_R^{\nu\dagger} \boldsymbol{\nu}_R = \begin{pmatrix} \nu_{1R} \\ \nu_{2R} \\ \nu_{3R} \end{pmatrix}, \quad (1.43)$$

where the fields $\nu_i = \nu_{iL} + \nu_{iR}$ describe Dirac neutrinos with definite masses. Having now neutrino mass eigenstates, the lepton charged current of Eq. (1.15) becomes

$$j_{\text{CC,L}}^\mu = 2 \bar{\boldsymbol{\nu}}_L \gamma^\mu \boldsymbol{\ell}_L = 2 \bar{\hat{\boldsymbol{\nu}}}_L V_L^{\nu\dagger} \gamma^\mu V_L^\ell \hat{\boldsymbol{\ell}}_L = 2 \bar{\hat{\boldsymbol{\nu}}}_L \gamma^\mu U \hat{\boldsymbol{\ell}}_L, \quad (1.44)$$

where the unitary matrix $U = V_L^{\nu\dagger} V_L^\ell$ is completely analogous to the CKM matrix of the quark weak charged current. This matrix is called Pontecorvo-Maki-Nakagawa-Sakata (PMNS) matrix. Since the flavour of charged lepton is uniquely defined by their masses, it is customary to redefine the left-handed flavour neutrino fields as

$$\boldsymbol{\nu}_L = U \hat{\boldsymbol{\nu}}_L, \quad (1.45)$$

which allows to write the charged current Lagrangian in terms of flavour neutrinos being careful that if neutrino masses are taken into account mixing of the fields occurs:

$$\begin{aligned} \mathcal{L}_{\text{CC,L}} &= -\frac{g}{\sqrt{2}} \sum_{\alpha=e,\mu,\tau} \bar{\nu}_\alpha \not{W} (1 - \gamma^5) \ell_\alpha + \text{h.c.} \\ &= -\frac{g}{\sqrt{2}} \sum_{\alpha=e,\mu,\tau} \sum_{i=1}^3 U_{\alpha i}^* \bar{\nu}_i \not{W} (1 - \gamma^5) \ell_\alpha + \text{h.c.} \end{aligned} \quad (1.46)$$

The GIM mechanism is still valid and no mixing takes place in neutral current interactions.

1.2.2 Propagation of neutrinos in vacuum

The effect of neutrino mixing is mostly visible in the propagation of neutrinos in space-time. Neutrinos with flavour α are produced and detected in charged current interactions in association with a charged lepton, according to Eq. (1.46). Approximating the neutrino fields to plane-waves, the flavour states are described by the following combination of mass states

$$|\nu_\alpha\rangle = \sum_i U_{\alpha i}^* |\nu_i\rangle, \quad (1.47)$$

where the mass eigenstates are orthonormal, $\langle \nu_i | \nu_j \rangle = \delta_{ij}$, and thanks to the unitarity of the PMNS matrix the relation $\langle \nu_\alpha | \nu_\beta \rangle = \delta_{\alpha\beta}$ holds. The probability of producing and detecting a neutrino of the same flavour in the same point of space-time is trivially one. However, in a typical neutrino experiment, production and detection of neutrinos happen in two different locations and times. The massive neutrino states $|\nu_i\rangle$ are eigenstates of the Hamiltonian, with the particle energies as eigenvalues:

$$\mathcal{H} |\nu_i\rangle = E_i |\nu_i\rangle = \sqrt{\mathbf{p}^2 + m_i^2} |\nu_i\rangle, \quad (1.48)$$

and \mathbf{p} is the momentum of the produced flavour neutrino. The Hamiltonian dictates the time evolution of the states through the Schrödinger's equation, and so assuming neutrinos evolve as plane waves a solution to the equation is given by

$$|\nu_i(t)\rangle = e^{-iE_i t} |\nu_i\rangle \quad \text{and} \quad |\nu_\alpha(t)\rangle = \sum_i U_{\alpha i}^* e^{-iE_i t} |\nu_i\rangle. \quad (1.49)$$

Using the relation of Eq. (1.47), the pure neutrino flavour state $|\nu_\alpha(t)\rangle$ at $t = 0$ can be expressed as a superposition of flavour states at time $t > 0$

$$|\nu_\alpha(t)\rangle = \sum_{\beta=e,\mu,\tau} \left(\sum_i U_{\alpha i}^* e^{-iE_i t} U_{\beta i} \right) |\nu_\beta\rangle. \quad (1.50)$$

Hence, the transition probability from a state ν_α to a state ν_β over a certain amount of time t is calculated to be

$$P(\nu_\alpha \rightarrow \nu_\beta) \equiv |\langle \nu_\alpha | \nu_\beta(t) \rangle|^2 = \sum_{ij} U_{i\alpha}^* U_{\beta i} U_{\alpha j} U_{j\beta}^* e^{-i(E_j - E_i)t}. \quad (1.51)$$

The energies of ultrarelativistic neutrinos can be approximated by

$$E_i \simeq E + \frac{m_i^2}{2E}, \quad (1.52)$$

and the propagation time is naturally replaced by the propagation length, i.e. $t \simeq L$, since it is easier to determine experimentally. Adopting these approximations, the probability of Eq. (1.51) reads

$$P(\nu_\alpha \rightarrow \nu_\beta) \equiv |\langle \nu_\alpha | \nu_\beta(t) \rangle|^2 = \sum_{ij} U_{i\alpha}^* U_{\beta i} U_{\alpha j} U_{j\beta}^* \exp\left(-i \frac{\Delta m_{ij}^2 L}{2E}\right), \quad (1.53)$$

where $\Delta m_{ij}^2 = m_i^2 - m_j^2$ are the squared mass differences of the neutrinos. The probability of Eq. (1.53) is called *oscillation probability* because it shows an oscillatory behaviour with respect

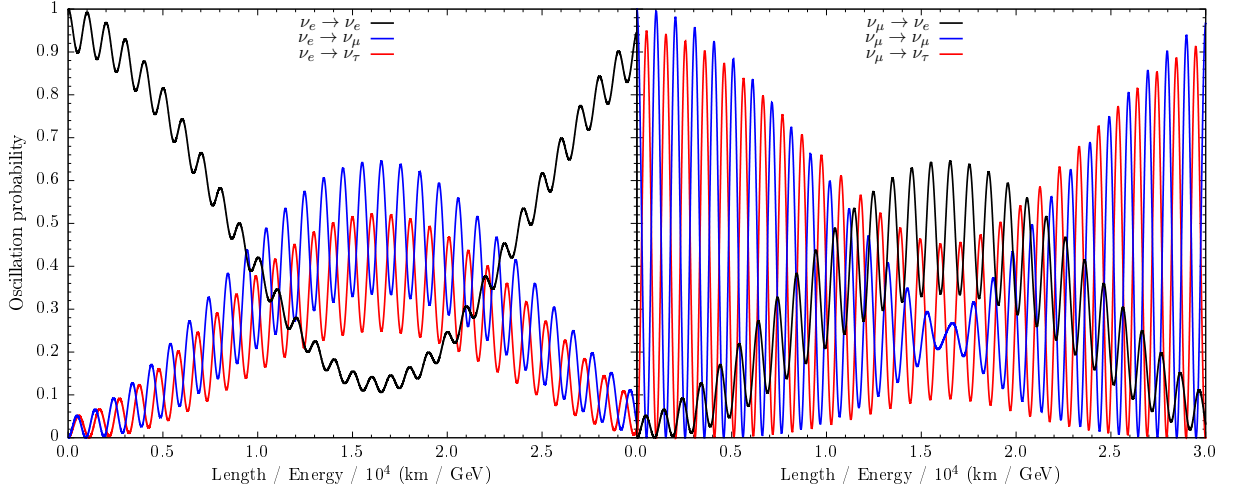


Figure 1.1: Oscillation probability for an initial ν_e (left) and ν_μ (right), clearly manifesting an oscillatory behaviour with respect to L/E . The oscillation parameters used here are $\Delta m_{21}^2 = 7.6 \times 10^{-5} \text{ eV}^2$, $\Delta m_{32}^2 = 2.4 \times 10^{-3} \text{ eV}^2$, $\sin^2 \theta_{12} = 0.32$, $\sin^2 2\theta_{13} = 0.1$, $\sin^2 \theta_{23} = 0.5$, and $\delta_{\text{CP}} = 0$.

to the ratio L/E , while the other parameters—the PMNS matrix elements and the neutrino masses—are constants of nature. The probabilities for initial ν_e and ν_μ to be detected as ν_e , ν_μ , or ν_τ is shown on Fig. 1.1 as function of L/E . The transition probability for $\alpha = \beta$ is usually called *disappearance probability*, and for $\alpha \neq \beta$ is called *appearance probability*, because experiments typically measure the amount of neutrinos of a certain flavour at the production site and at the detection site.

The oscillating term is the result of the interference between different massive neutrinos which propagate at different velocities while coherency between states is preserved. It could happen that neutrinos are produced or detected incoherently, for which interference terms do not appear, or that the detector resolution on propagation length or neutrino energy is limited and so the probability is averaged. In both cases, the oscillation probability simplifies to

$$\langle P(\nu_\alpha \rightarrow \nu_\beta) \rangle = \sum_i |U_{\alpha i}|^2 |U_{\beta i}|^2, \quad (1.54)$$

and for $\alpha \neq \beta$ it can be shown that the maximum value this averaged probability can take is

$$\langle P(\nu_\alpha \rightarrow \nu_\beta) \rangle_{\text{max}} = \frac{1}{N}, \quad (1.55)$$

with N the number of massive neutrinos. Under these circumstances, the mixing matrix behaves as if its entries have all the same absolute value, in an eventuality called *N-maximal mixing*. This corresponds to minimal average disappearance probability and maximal average appearance probability, equal to $1/N$ in each possible channel.

Apart from this limit scenario, the PMNS matrix and analogously the CKM matrix are generic unitary $N \times N$ matrices, where N is the number of fermion generations. A matrix with this characteristics depends on N^2 independent real parameters, divided among

$$\frac{N(N-1)}{2} \text{ mixing angles and } \frac{N(N+1)}{2} \text{ phases}, \quad (1.56)$$

even though not all the phases are observables or give physical effects. Due to the unitarity of the neutral currents, only the weak charged current manifests these phases, although $2N - 1$

phases can be reabsorbed by a redefinition of the fermion fields. Excluding the CC term, the SM Lagrangian is invariant under a global phase transformation of the lepton and quark fields, such as

$$\mathbf{f}_\alpha \mapsto e^{i\phi_\alpha^\mathbf{f}} \mathbf{f}_\alpha . \quad (1.57)$$

Let us apply this to the CC current of Eq. (1.46). A common phase can be factorised outside

$$j_{\text{CC,L}}^\mu = 2 \sum_{i=1}^3 \sum_{\alpha=e,\mu,\tau} \bar{\nu}_{Li} \gamma^\mu e^{-i\varphi_i^\nu} V_{\alpha i}^* e^{i\varphi_\alpha^\ell} \ell_{L\alpha} \quad (1.58)$$

$$= 2e^{-i(\varphi_3^\nu - \varphi_\tau^\ell)} \sum_{i=1}^3 \sum_{\alpha=e,\mu,\tau} \bar{\nu}_{Li} \gamma^\mu e^{-i(\varphi_i^\nu - \pi_3^\nu)} V_{\alpha i}^* e^{i(\varphi_\alpha^\ell - \varphi_\tau^\ell)} \ell_{L\alpha} , \quad (1.59)$$

showing that there are only $2N - 1$ phases that can be reabsorbed in a redefinition of the fields. A common rephasing would leave the charged current unchanged. It follows that the number of physical phases is

$$\frac{N(N+1)}{2} - 2N + 1 = \frac{(N-1)(N-2)}{2} \quad (1.60)$$

and so the total physical parameters are

$$\frac{N(N-1)}{2} + \frac{(N-1)(N-2)}{2} = (N-1)^2 . \quad (1.61)$$

In the case of three generations, the PMNS matrix can be described by three mixing angles and just one physical phase. It is typically parameterised as

$$U = \begin{pmatrix} 1 & 0 & 0 \\ 0 & c_{23} & s_{23} \\ 0 & -s_{23} & c_{23} \end{pmatrix} \begin{pmatrix} c_{13} & 0 & s_{13}e^{-i\delta_{\text{CP}}} \\ 0 & 1 & 0 \\ -s_{13}e^{i\delta_{\text{CP}}} & 0 & c_{13} \end{pmatrix} \begin{pmatrix} c_{12} & s_{12} & 0 \\ -s_{12} & c_{12} & 0 \\ 0 & 0 & 1 \end{pmatrix} , \quad (1.62)$$

where $c_{ij} \equiv \cos \theta_{ij}$ and $s_{ij} \equiv \sin \theta_{ij}$. The angle δ_{CP} is the physical phase responsible for CP violation (see Section 3.1). From a model building point of view, the complex phase may arise from complex Yukawa couplings and/or from a relative phase in the vacuum expectation values of Higgs fields. It is important to note that if neutrinos were Majorana fermions, there would be two additional physical phases and the mixing matrix would contain an extra contribution:

$$U' = U \begin{pmatrix} 1 & 0 & 0 \\ 0 & e^{-i\gamma_1} & 0 \\ 0 & 0 & e^{-i\gamma_2} \end{pmatrix} , \quad (1.63)$$

where U is the same matrix of Eq. (1.62). However, due to the structure of the oscillation probability (see Eq. (1.53)) the Majorana phases do not contribute to neutrino oscillation. The CKM matrix can be parameterised in an analogous way.

The best known value of the mixing angles and mass-squared differences are reported in Table 1.1. The δ_{CP} phase has not been determined as well as the other oscillation angles, and synergies between current experiments are used to get the best estimates before next-generation experiments start operation (see Section 3). Only one of the two independent squared mass differences is known with its relative sign and it is the so-called *solar mass difference* Δm_{21}^2 . The absolute value of the other mass difference $|\Delta m_{32}^2|$, known as *atmospheric mass difference*, has a best value fit which depends on the assumed sign [17]. If the atmospheric mass difference is positive, then the order between neutrino masses is $m_1 < m_2 \ll m_3$, otherwise the order is $m_3 \ll m_1 < m_2$. The first scenario is referred to as *normal hierarchy*, whereas the second one

Table 1.1: Best fit values for neutrino oscillation parameters [17]. This result includes Super-Kamiokande data and assumes a normal mass ordering.

Parameter	Value	Error
$\sin^2 \theta_{12}$	0.310	$^{+0.013}_{-0.012}$
$\sin^2 2\theta_{13}$	0.0875	$^{+0.0025}_{-0.0025}$
$\sin^2 \theta_{23}$	0.563	$^{+0.018}_{-0.024}$
δ_{CP}/π	-0.772	$^{+0.217}_{-0.156}$
$\Delta m_{21}^2/10^{-5} \text{ eV}^2$	7.39	$^{0.21}_{-0.20}$
$ \Delta m_{32}^2 /10^{-3} \text{ eV}^2$	2.528	$^{+0.029}_{-0.031}$

as *inverted hierarchy*. At first order, it is not possible to extract the hierarchy information from a measurement of neutrino oscillation in vacuum, using simply Eq. (1.53). The sign of Δm_{21}^2 is accessible thanks to the matter effects on the propagation of solar neutrinos. For the Sun–Earth baseline, the oscillation probability is more sensitive to the solar mass difference, since

$$\frac{|\Delta m_{21}^2|}{2} \frac{L}{E} \sim \pi, \quad (1.64)$$

and solar neutrino experiments have constrained $\Delta m_{21}^2 \cos 2\theta_{12} > 0$ (see Section 1.2.3); by convention the octant of θ_{12} is fixed to have $\Delta m_{21}^2 > 0$. The existing data is not sufficient to determine the sign of the atmospheric mass difference, the knowledge of which would define the neutrino mass hierarchy.

1.2.3 Propagation of neutrinos in matter

Neutrinos propagating in a dense medium can interact with its particles, although the probability of an incoherent inelastic scattering is very small (see Section 1.4). For example the characteristic cross-section for neutrino–neutron elastic scattering is of the order

$$\sigma \simeq \frac{G_F^2 E_\nu^2}{\pi} \sim 10^{-43} \text{ cm}^2 \left(\frac{E_\nu}{\text{MeV}} \right)^2 \quad (1.65)$$

where E_ν is the neutrino energy and G_F is the Fermi constant introduced later in Eq. (1.121). The mean free path of a neutrino passing through a material with number density n can be approximated as

$$\ell \sim \frac{1}{n \sigma}, \quad (1.66)$$

assuming the target particles are at rest. In matter, the main targets are nucleons with mass $m \simeq 1 \text{ GeV}$. If the number density is $n \simeq \mathcal{N}_A \text{ cm}^{-3}$, the mean free path is

$$\ell \sim \frac{10^{14} \text{ cm}^3}{(E/\text{GeV})}. \quad (1.67)$$

The Earth, with an approximate diameter of 10^9 cm is opaque only to neutrinos with energies above 100 TeV. On the other hand, solar neutrinos with energies of the order of 0.1 MeV have a mean free path through matter of 0.1 light years. The interaction rate changes significantly

in materials with a very high number density, such as in neutron stars or supernovae. It was first noted in Ref. [18] that neutrinos propagating in dense regions are subject to an effective potential due to the coherent forward elastic scattering with the particles in the medium. In coherent interactions it still is possible to have interference between the scattered and the unscattered neutrino waves which enhances the effect of matter in the neutrino propagation. Differently from vacuum interference, in this case the effect of the medium is not on the intensity of the propagating neutrino beam, which remains unchanged, but on the phase velocity of the wave packets. The phenomenon can be seen as a refractive index that modifies the mixing of neutrinos.

The forward scattering possible for neutrinos in matter are CC interactions of ν_e on electrons and NC interactions of any neutrino on electron, protons, and neutrons. The effective four-point Hamiltonians for these interactions (see Eqs. (1.119) and (1.120)) are, up to Fierz reordering,

$$\mathcal{H}_{\text{CC}} = \frac{G_F}{\sqrt{2}} [\bar{\nu}_e \gamma^\mu (1 - \gamma^5) \nu_e] [\bar{e} \gamma_\mu (1 - \gamma^5) e] , \quad (1.68)$$

$$\mathcal{H}_{\text{NC}} = \frac{G_F}{\sqrt{2}} \sum_{\alpha=e,\mu,\tau} [\bar{\nu}_\alpha \gamma^\mu (1 - \gamma^5) \nu_\alpha] \sum_{\mathfrak{f}=e,p,n} [\bar{\mathfrak{f}} \gamma_\mu (g_V^F - g_A^F \gamma^5) \mathfrak{f}] . \quad (1.69)$$

The fermions, either electrons, neutrons, or protons, must have identical four-momenta and helicities in their initial and final states, thanks to the coherent nature of the scattering. The effective Hamiltonian can therefore be averaged on the fermion background, using a statistical distribution ρ of the fermion energy at a given temperature of the medium which normalises to the total number of particles

$$N_{\mathfrak{f}} = \int d^3p \rho(E_{\mathfrak{f}}, T) . \quad (1.70)$$

After averaging over the helicities of the fermions, terms proportional to the neutrino currents are obtained

$$\langle \mathcal{H}_{\text{CC}} \rangle = V_{\text{CC}} \bar{\nu}_{eL} \gamma^0 \nu_{eL} , \quad (1.71)$$

$$\langle \mathcal{H}_{\text{NC}} \rangle = \sum_{\mathfrak{f}=e,p,n} V_{\text{NC}}^{\mathfrak{f}} \sum_{\alpha=e,\mu,\tau} \bar{\nu}_{\alpha L} \gamma^0 \nu_{\alpha L} , \quad (1.72)$$

where the effective potentials are

$$V_{\text{CC}} = \sqrt{2} G_F n_e , \quad (1.73)$$

$$V_{\text{NC}}^{\mathfrak{f}} = \sqrt{2} G_F n_{\mathfrak{f}} g_V^{\mathfrak{f}} . \quad (1.74)$$

The vector coupling constants for electrons and protons are equal and opposite

$$g_V^e = -g_V^p = -\frac{1}{2} + 2 \sin^2 \vartheta_W , \quad (1.75)$$

but due to the neutrality of matter the densities have the same value, i.e. $n_e = n_p$, and so their NC contributions cancel out. Neutrons are the only particles providing an overall potential to neutrino neutral-current interactions and since they are chargeless the corresponding potential is

$$V_{\text{NC}} = -\frac{\sqrt{2}}{2} G_F n_{\mathfrak{f}} . \quad (1.76)$$

The total Hamiltonian is $\mathcal{H} = \mathcal{H}_0 + \mathcal{H}_{\text{m}}$, where \mathcal{H}_0 is the Hamiltonian in vacuum (see Eq. (1.48)). The operator \mathcal{H}_{m} acts on neutrino flavour state as

$$\mathcal{H}_{\text{m}} |\nu_\alpha\rangle = V_\alpha |\nu_\alpha\rangle , \quad (1.77)$$

and the total potential is defined as

$$V_\alpha = V_{\text{CC}}\delta_{\alpha e} + V_{\text{NC}} = \sqrt{2} G_F \left(n_e \delta_{\alpha e} - \frac{1}{2} n_n \right). \quad (1.78)$$

The massive neutrino states are eigenstates of the free Hamiltonian, but for \mathcal{H}_m the description in the flavour basis is simpler. It is convenient to define the transition amplitude

$$\phi_{\alpha\beta}(t) = \langle \nu_\beta | \nu_\alpha(t) \rangle, \quad (1.79)$$

from which the transition probability is simply

$$P(\nu_\alpha \rightarrow \nu_\beta) = |\phi_{\alpha\beta}(t)|^2. \quad (1.80)$$

From Eqs. (1.48) and (1.77), it follows that

$$\mathcal{H} \phi_{\alpha\beta}(t) = \sum_\rho \left(\sum_i U_{\beta i} E_i U_{\rho i}^* + \delta_{\beta\rho} V_\beta \right) \phi_{\alpha\rho}(t). \quad (1.81)$$

With this relation, the propagation of neutrinos in matter can be derived in complete analogy to the vacuum oscillation. The evolution of neutrino states in time comes from solving the Schrödinger's equation and the probability of flavour transition is then accordingly derived. Using the same approximations introduced for vacuum oscillations, the evolution equation becomes

$$i \frac{d}{dx} \phi_{\alpha\beta}(x) = \sum_\rho \left(\sum_i \frac{\Delta m_{i1}^2}{2E} U_{\beta i} U_{\rho i}^* + \delta_{\beta\rho} \delta_{\rho e} V_{\text{CC}} \right) \phi_{\alpha\rho}(x). \quad (1.82)$$

The term

$$p + \frac{m_1^2}{2E} + V_{\text{NC}} \phi_{\alpha\beta}(x) \quad (1.83)$$

has been removed, since it generates a common phase to all flavours and so it is irrelevant to flavour transitions.

The treatment of oscillations in matter for three-neutrino mixing can be quite intricate, because of the combinations between the different mass-squared differences. Let us consider a simpler scenario of only two neutrino generations, ν_e and ν_μ . Assuming the initial flavour being $\alpha = e$, the evolution equation is now

$$\begin{aligned} i \frac{d}{dx} \begin{pmatrix} \phi_{ee} \\ \phi_{e\mu} \end{pmatrix} &= \mathcal{H}_F \begin{pmatrix} \phi_{ee} \\ \phi_{e\mu} \end{pmatrix} \\ &= \frac{1}{4E} \begin{pmatrix} -\Delta m^2 \cos 2\theta + A_{\text{CC}} & \Delta m^2 \sin 2\theta \\ \Delta m^2 \sin 2\theta & \Delta m^2 \cos 2\theta - A_{\text{CC}} \end{pmatrix} \begin{pmatrix} \phi_{ee} \\ \phi_{e\mu} \end{pmatrix}, \end{aligned} \quad (1.84)$$

where $\Delta m^2 = m_2^2 - m_1^2$ and θ is the mixing angle, as in

$$\begin{pmatrix} \nu_e \\ \nu_\mu \end{pmatrix} = \begin{pmatrix} \cos \theta & \sin \theta \\ -\sin \theta & \cos \theta \end{pmatrix} \begin{pmatrix} \nu_1 \\ \nu_2 \end{pmatrix}, \quad (1.85)$$

and

$$A_{\text{CC}} \equiv 2\sqrt{2} E G_F n_e. \quad (1.86)$$

The effective Hamiltonian \mathcal{H}_F of Eq. (1.84) can be diagonalised by means of an orthogonal transformation

$$O_M = \begin{pmatrix} \cos \theta_M & \sin \theta_M \\ -\sin \theta_M & \cos \theta_M \end{pmatrix}, \quad (1.87)$$

to obtain

$$\mathcal{H}_M = O_M^T \mathcal{H}_F O_M = \frac{1}{4E} \text{diag}(-\Delta m_M^2, \Delta m_M^2) . \quad (1.88)$$

The effective mixing angle θ_M is defined by

$$\tan 2\theta_M = \frac{\tan 2\theta}{1 - \frac{A_{CC}}{\Delta m^2 \cos 2\theta}} \quad (1.89)$$

and the effective mass-squared difference Δm_M^2 reads

$$(\Delta m_M^2)^2 = (\Delta m^2 \cos 2\theta - A_{CC})^2 + (\Delta m^2 \sin \theta)^2 . \quad (1.90)$$

It was found in Refs. [19, 20] that it is possible to have a resonant flavor transitions when neutrinos propagate in a medium with varying density, with the effective mixing angle passing through the maximal mixing value of $\pi/4$. This resonance condition is achieved when

$$A_{CC} = \Delta m^2 \cos 2\theta , \quad (1.91)$$

or equivalently when the electron density reads

$$n_e = \frac{\Delta m^2 \cos 2\theta}{2\sqrt{2}E G_F} . \quad (1.92)$$

By transforming the transition probability to the mass basis by means of O_M , the evolution equation becomes

$$i \frac{d}{dx} \begin{pmatrix} \phi'_{e1} \\ \phi'_{e2} \end{pmatrix} = \begin{pmatrix} -\frac{\Delta m_M^2}{4E} & -i \frac{d\theta_M}{dx} \\ i \frac{d\theta_M}{dx} & \frac{\Delta m_M^2}{4E} \end{pmatrix} \begin{pmatrix} \phi'_{e1} \\ \phi'_{e2} \end{pmatrix} . \quad (1.93)$$

It is interesting to note that if the matter profile is constant, then $d\theta_M/dx = 0$ and the structure of the oscillation probability simplifies to a two-flavour oscillation in vacuum, with effective mixing angle θ_M and mass-squared difference Δm_M^2 . On the other hand, if the matter density is not constant, the variation of θ_M must be taken into account. From Eq. (1.89), it reads

$$\frac{d\theta_M}{dx} = \frac{\sin 2\theta_M}{2\Delta m^2} \frac{dA_{CC}}{dx} . \quad (1.94)$$

If the variation of the effective matter angle is small compared to the diagonal terms of the Hamiltonian of Eq. (1.93), then the transition between neutrino mass states in matter is negligible. With the condition

$$\frac{\Delta m_M^2}{4E} \left| \frac{d\theta_M}{dx} \right|^{-1} = \frac{(\Delta m_M^2)^2}{2E \sin 2\theta_M} \left| \frac{dA_{CC}}{dx} \right|^{-1} \gg 1 \quad (1.95)$$

satisfied along the neutrino path, the transition is said to be *adiabatic* and flavour conversion occurs without oscillation between states.

The condition of adiabaticity is typically met for solar and supernova neutrinos, for which the medium profile smoothly changes from the high density of the core to the vacuum or the detector density, which is practically negligible. Neutrinos are produced in astrophysical sources mostly in the electron flavour (see Section 1.3). Regarding terrestrial experiments, the distance between the source and the detector is much larger than the detector itself, which means that only the averaged probability can be measured. If at production the matter potential is well

below the resonance value, i.e. $A_{CC} \ll \Delta m^2 \cos \theta$, the matter effects are negligible and the propagation occurs almost in vacuum with an average survival probability

$$\langle P(\nu_e \rightarrow \nu_e) \rangle = 1 - \frac{1}{2} \sin^2 2\theta . \quad (1.96)$$

If the matter potential at production is closer to the resonant potential, i.e. $A_{CC} \lesssim \Delta m^2 \cos \theta$, the resonance is not crossed, but the propagation can still be described by an adiabatic propagation. The survival probability is now

$$\langle P(\nu_e \rightarrow \nu_e) \rangle = \frac{1}{2} + \frac{1}{2} \cos 2\theta_M \cos 2\theta , \quad (1.97)$$

where θ_M is the effective mixing angle in matter at the production point. Since the resonance condition is not met, $\cos \theta_M$ has the same sign of $\cos \theta$ and so $\langle P(\nu_e \rightarrow \nu_e) \rangle > 1/2$. When the potential is such that $A_{CC} \gtrsim \Delta m^2 \cos \theta$, the resonance can be crossed and this occurs if $\cos 2\theta > 0$, assuming $\Delta m^2 > 0$. It follows that the produced neutrino ν_e has a larger component of ν_2 in matter, but when in vacuum the main component becomes ν_1 . Finally, if the density is much higher than the resonance one, i.e. $A_{CC} \gg \Delta m^2 \cos \theta$, the effective mixing angle in matter is maximal, $\theta_M \simeq \pi/2$, and so the ν_e is produced mostly as ν_2 . As the neutrino travels to regions of lower density crossing the resonance adiabatically, the final mixing angle in matter tends to the mixing angle in vacuum and so $\nu_2 = \sin \theta \nu_e + \cos \theta \nu_\mu$. If the vacuum angle θ is small, the overall effect is a smooth conversion from ν_e to ν_μ . The survival probability becomes the same of Eq. (1.97) and this mechanism is known as Mikheyev-Smirnov-Wolfenstein (MSW) effect. When the condition of adiabaticity is violated, there might be transition between the two neutrino mass states in matter. The expression in Eq. (1.95) gets its minimum value with

$$\frac{d^2 \cos 2\theta}{dx^2} = 0 , \quad (1.98)$$

and the survival probability is modified into [21]

$$\langle P(\nu_e \rightarrow \nu_e) \rangle = \frac{1}{2} + \left(\frac{1}{2} - P_{12} \right) \cos 2\theta_M \cos 2\theta , \quad (1.99)$$

where P_{12} is the crossing transition probability between the two states ν_1 and ν_2 at the resonance. The adiabatic case is recovered when $P_{12} = 0$.

1.3 Neutrino production

Neutrinos are the most abundant fermions in the Universe. With the expansion and cooling of the Universe, the interaction rate of primordial neutrinos decreased below the expansion rate, resulting in a decoupling of the neutrinos from the other particles. These *relic neutrinos* form what is called the Cosmic Neutrino Background (CνB), a radiation analogous to the Cosmic Microwave Background (CMB) which also decoupled at the early stages of the Universe. The CνB formed well before the CMB, due to the weak nature of neutrino interactions, and it has a temperature given by the relation

$$T_\nu = \left(\frac{4}{11} \right)^{1/3} T_\gamma = (1.945 \pm 0.001) \text{ K} . \quad (1.100)$$

This relation makes an exact prediction of the temperature of the neutrinos T_ν , connecting it with the photon temperature T_γ , which is accurately measured by CMB surveys. The temperature is equivalent to $T_\nu = (1.676 \pm 0.001) \times 10^{-4} \text{ eV}$. By comparing this energy to the measured

mass differences from oscillation experiments (see Table 1.1) one can infer that at least two mass states of relic neutrinos are nonrelativistic. However, neutrinos at these energies are almost impossible to detect with the current technologies and it will be a challenge for next-generation experiments.

The density of relativistic neutrinos can be related to the density of photons, thanks to Eq. (1.100) by which

$$\frac{\rho_\nu}{\rho_\gamma} = \frac{7}{8} \left(\frac{4}{11} \right)^{1/3} N_{\text{eff}} , \quad (1.101)$$

and so the energy density with respect to the critical density is

$$\Omega_{\nu_R} h^2 = \left(\frac{4}{11} \right)^{1/3} \Omega_\gamma h^2 , \quad (1.102)$$

with h the Hubble constant. When the neutrinos are nonrelativistic, their energy density is given by $\rho_\nu \simeq \sum_i m_i n_i$, where n_i are the number density of each species which are equal to each other up to negligible corrections from flavour effect. Using the expression of Eq. (1.101) and knowing the number density of photons n_γ , the total energy density of nonrelativistic neutrinos today is

$$\Omega_{\nu_{NR}} h^2 = \frac{\sum_i m_i}{94.14 \text{ eV}} , \quad (1.103)$$

and the contribution of relativistic neutrinos to the total mass is also negligible. Due to the fact that the density of Eq. (1.103) can never be greater than the energy density of all matter in the Universe, a naive bound on the neutrino masses can be derived:

$$\sum_i m_i \lesssim 13 \text{ eV} . \quad (1.104)$$

The limit can be improved with more precise theoretical considerations under Λ CDM assumption which combined with the latest cosmological surveys decreases down to $\sum_i m_i \lesssim 0.12$ [22].

Other than cosmological neutrinos, these elusive fermions are produced and involved in a large variety of processes. They are emitted in astrophysical processes, such as supernova explosions, blazars, and in the nuclear reactions of the cores of stars. Cosmic ray interactions with the Earth's atmosphere also produce neutrinos from decays of secondary mesons. Human-made sources include accelerator facilities in which neutrino beams are produced in a controlled environment, as well as those emitted by nuclear reactors. Neutrinos are also the products of natural-occurring β -decays, from the study of which neutrinos were first hypothesised. The study of the rare double- β decay is of utter importance, because the proposed neutrinoless manifestation of this decay is a true lepton number violating process, the detection of which has deep and considerable connotations for neutrino mass theories [23].

In the following sections the most relevant sources for the neutrino experiment mentioned in this thesis are discussed.

1.3.1 Solar and supernova neutrinos

Neutrinos emitted by the Sun were the first astrophysical source of neutrinos detected. They are produced by thermonuclear reactions occurring in the solar core. Being a G-type star in the main sequence, the Sun is powered mostly from proton–proton chain (pp) and partly by the carbon–nitrogen–oxygen cycle (CNO). In both these processes, the net result is the conversion of four protons and two electrons into an α -particle and two electron neutrinos

$$4p + 2e^- \longrightarrow {}^4\text{He} + 2\nu_e , \quad (1.105)$$

Table 1.2: Processes occurring in the pp chain (left) and the CNO cycle (right) that emit ν_e . The first column of the pp chain table lists the typical label with which the processes are referred to; the neutrinos of the CNO cycle are labelled with the name of the decaying nuclide. In both tables, the maximum neutrino energy is also reported.

Label	Process	E_{\max} (MeV)	Process	E_{\max} (MeV)
pp	$p + p \longrightarrow {}^2\text{H} + e^+ + \nu_e$	0.423	${}^{13}\text{N} \longrightarrow {}^{13}\text{C} + e^+ + \nu_e$	1.198 MeV
pep	$p + e^- + p \longrightarrow {}^2\text{H} + \nu_e$	1.445	${}^{15}\text{O} \longrightarrow {}^{15}\text{N} + e^+ + \nu_e$	1.732 MeV
hep	${}^3\text{He} + p \longrightarrow {}^4\text{He} + e^+ + \nu_e$	18.778	${}^{17}\text{F} \longrightarrow {}^{17}\text{F} + e^+ + \nu_e$	1.736 MeV
${}^7\text{Be}$	${}^7\text{Be} + e^- \longrightarrow {}^7\text{Li} + \nu_e$	0.386		
${}^8\text{Be}$	${}^8\text{Be} \longrightarrow {}^8\text{Be}^* + e^+ + \nu_e$	0.862		
	$\longrightarrow 2 {}^4\text{He} + e^+ + \nu_e$	~ 15		

along with the release of 26.731 MeV in the form of photons or kinetic energy of the neutrinos. The processes of the pp chain and CNO cycle releasing neutrinos are listed in Table 1.2. Due to their evasive nature and low energy, solar neutrinos are difficult to study in detail and therefore a reliable theoretical model describing the solar nuclear reactions is needed. The standard solar model (SSM), developed by Bahcall and collaborators [24], perfectly agrees with data from helioseismology [25], such as the speed of sound and the density profile of the Sun. For this reason, the SSM is considered to provide a credible estimate of the flux of neutrinos produced in the Sun, the distribution of which is reported in Fig. 1.2. The first neutrino experiments, such as Homestake [26], GALLEX/GNO [27], and SAGE [28, 29], were in strong disagreement with the predictions of the SSM. The so-called *solar neutrino problem* was later solved by the SNO experiment [30] which demonstrated the presence of flavour transition, explained theoretically by the MSW effect (see Section 1.2.3). The low-background and low-threshold BOREXINO experiment [31] was able to measure different solar neutrinos across the energy spectrum reaching good agreement with the theoretical prediction of flavour transition in matter [32], as demonstrated in Fig. 1.3.

The second astrophysical source of neutrinos ever identified was the supernova (SN) explosion SN1987A which occurred on the 23rd of February, 1987, in the Large Magellanic Cloud. It was the only SN explosion which was detected also through its neutrino emission. In spite of this fact, supernova explosions are the most intense sources of neutrinos in the Universe. Historically, SNe are classified by their spectral characteristics near maximal luminosity. This is dictated by the composition of the progenitor star. The main subdivision is between spectra with or without hydrogen lines, respectively called type II and type I. Further classification of type I SNe comes from the presence of silicon and helium. Type Ia SN, the spectrum of which shows strong Si lines, is the only SN type that is not accompanied by a substantial neutrino emission. This is because the mechanism of explosion comes from the accretion of a white dwarf to the point where the pressure of the degenerate electron gas can no longer sustain the gravitational pull. The limit is known as *Chandrasekhar limit* and it is around $1.4 M_\odot$ [34]. When the white dwarf collapses, the fusion of carbon and oxygen heavy nuclei is activated and an enormous quantity of energy is freed in thermonuclear processes.

On the other hand, the supernovae of type Ib and Ic (with He lines) and II explode via a core-collapse, liberating an intense flux of neutrinos. Old stars with a mass between $8 M_\odot \lesssim M \lesssim 40 M_\odot$ tend to stratify in layers of elements undergoing fusion, with the lightest (H) in the outer shell burning progressively into heavier nuclei (He, C, Ne, Mg, Si, ...) up to iron at the core. After carbon ignition, the neutrino luminosity of the star comes mainly from a long silicon burning phase. The *pre-supernova* neutrinos from Si fusion, in fact, make up

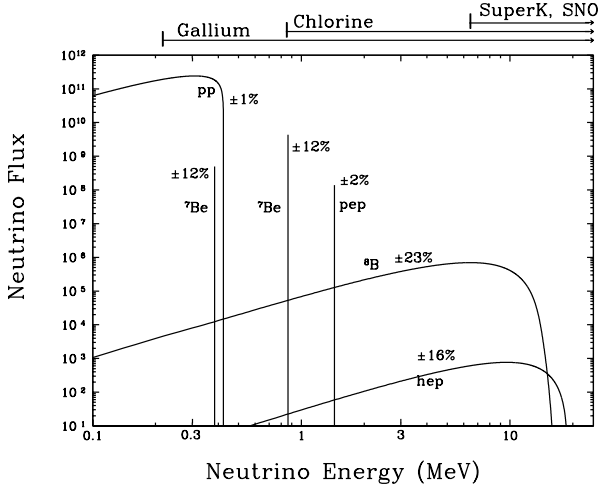


Figure 1.2: The neutrino flux from the pp chain, predicted with the solar standard model. Neutrinos from two-body processes are monoenergetic, whereas three-body ones present a continuous spectrum. The threshold energies of major solar neutrino experiments are shown for comparison. Taken from [33].

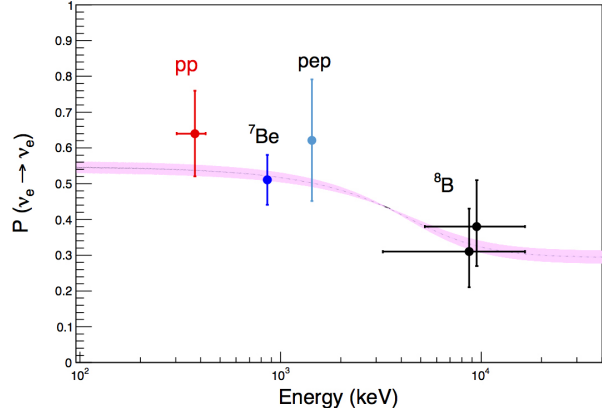


Figure 1.3: Survival probability of ν_e produced by the different nuclear reactions in the pp chain, as measured by BOREXINO. The violet band corresponds to the $\pm 1\sigma$ prediction of the flavour transition in the Sun. Taken from [32].

roughly 1 % of the total energy that is emitted during the star's core-collapse. At this stage, the gravitational pressure is balanced overall by the thermonuclear energy released in each shell, but in the Fe core for which exothermic reactions are not allowed. The mass of the core is sustained by the pressure of degenerate relativistic electrons which is reduced by photodissociation of iron



a reaction which absorbs 124.4 MeV, and electron capture with neutrinos escaping the supernova



Once the Fermi pressure is no longer sufficient to contrast the core, this collapses and the increase in temperature accelerates photodissociation and electron capture in a positive feedback reaction. The density of the core however increases until when neutrinos from electron capture are trapped inside and so the collapse becomes an adiabatic process. The free-falling core is finally stopped by the pressure of degenerate nonrelativistic nucleons. The abrupt halt causes a shock wave that propagates to the outer parts of the core and slows down the imploding mantle. As the wave propagates through the in-falling dense matter of the outer core, its energy is dissipated by the photodissociation of nuclei into nucleons, leading to an intensification of the electron capture rate thanks to the copious number of free protons. The electron neutrinos pile up behind the opaque wave until the shock reaches a layer of lower density and the ν_e are released in a few milliseconds in what is called *neutronisation burst*, carrying away around 10^{50} erg. In most scenarios, the shock wave stalls and the bounce mechanism from the core alone is not enough to cause an explosion. The remnant of the core, which is forming a proto-neutron star, can revive the shock if its mass is large enough. In the hot core, numerous neutrinos are produced in all flavours by electron–positron annihilation, electron–nucleon and nucleon–nucleon bremsstrahlung, and electron neutrinos from electron or positron capture. These neutrinos remain trapped between the core and the mantle regions with a density high

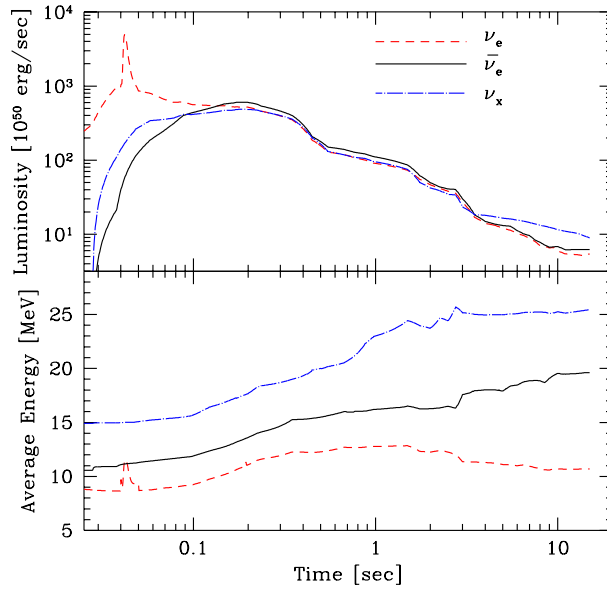


Figure 1.4: Time and energy profile of the predicted neutrino flux from a supernova core-collapse of mass $M \simeq 20 M_{\odot}$. Other neutrino flavours than ν_e and $\bar{\nu}_e$ are collectively represented by $\nu_X = (\nu_{\mu} + \bar{\nu}_{\mu} + \nu_{\tau} + \bar{\nu}_{\tau})/4$. From the prediction, the neutronisation burst of ν_e is visible at early stages of the explosion, whereas neutrinos of all flavours are emitted at later times. Taken from [35].

enough such that their mean free path is smaller than the supernova radius. The size of this region, known as *neutrinosphere*, depends on the ν energies and flavours and emits a thermal flux of neutrinos the energy of which is believed to revive the shock up to explosion. The luminosity of neutrinos in this phase does not peak as for the neutronisation burst, but presents a long hump on a time scale of a few seconds, as seen in Fig. 1.4. The average energies are typically higher for muon and tau neutrinos, since they are produced in deeper region of the SN, and their values strongly depend on the model (see for example Refs. [35–37]). The energies for both neutrinos and antineutrinos usually range between 10 MeV and 30 MeV.

The estimated rate of supernova explosions in our Galaxy is relatively low, around two to three explosions per century [38]. Considering the whole Universe however this rate should be much higher. All core-collapse SNe in the causally-connected Universe are isotropically distributed and therefore an isotropic and time-independent neutrino flux should exist. This stochastic flux is known as *Diffuse Supernova Neutrino Background* (DSNB) and the detectable neutrinos are called *Supernova Relic Neutrinos* (SRN). The energy density of SRN is around 0.01 eV cm^{-3} which is roughly ten times less than that of the CMB, but it is comparable to the density number of all photons from stars. The energy spectrum should peak at a few MeV, where the inverse beta decay (IBD) interaction for $\bar{\nu}_e$ dominates (see Section 1.4.3). This process is the best discovery prospect for SRN in water Cherenkov experiments like Super-Kamiokande, thanks to low background and a high cross-section in this energy region [39]. Despite being a challenging task, the detection of the DSNB is fundamental for astrophysics and stellar formation, because the study of SNe cannot rely just on very rare galactic core-collapse explosions.

1.3.2 Atmospheric neutrinos

Atmospheric neutrinos are generated by the interactions of cosmic rays with the Earth’s atmosphere. Primary cosmic rays are mainly composed by energetic protons or heavier nuclei,

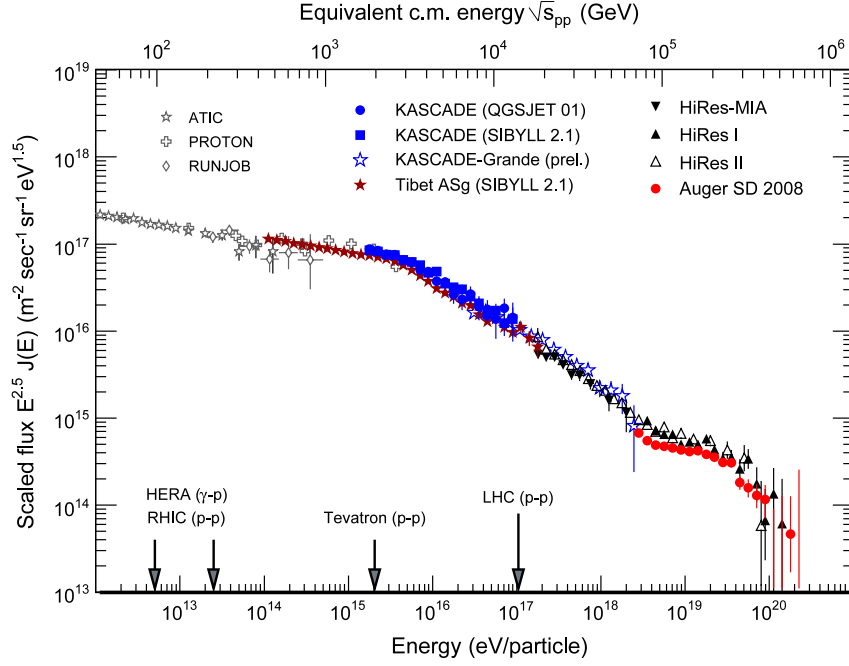


Figure 1.5: Measurement of cosmic rays over the entire energy spectrum, where the change of energy dependence (*knee*) is visible at around 10^{15} eV. The flux is multiplied by the power law $E^{2.5}$. Taken from Ref. [40].

originated from the Sun or outside the solar system. Their interactions with nuclei in the atmosphere produce pseudoscalar mesons such as pions and kaons, which rapidly decay into charged leptons and neutrinos. Due to helicity suppression, two-body decays of π^\pm and K^\pm favour the muon channel

$$\pi^\pm \rightarrow \mu^\pm + \bar{\nu}_\mu^{(-)}, \quad (1.108)$$

$$K^\pm \rightarrow \mu^\pm + \bar{\nu}_\mu^{(-)}. \quad (1.109)$$

The muon itself decays with a relatively longer lifetime releasing two neutrinos per decay:

$$\mu^+ \rightarrow e^+ + \nu_e + \bar{\nu}_\mu, \quad (1.110)$$

$$\mu^- \rightarrow e^- + \bar{\nu}_e + \nu_\mu. \quad (1.111)$$

At sufficient low energies around $E \lesssim 1$ GeV, all of the muons decay before reaching the ground and so the neutrino fluxes follow the proportions of neutrino flavours

$$\phi_{\nu_e} : \phi_{\nu_\mu} = 1 : 2, \quad (1.112)$$

$$\phi_{\nu_\mu} : \phi_{\bar{\nu}_\mu} = 1 : 1, \quad (1.113)$$

$$\phi_{\nu_e} : \phi_{\bar{\nu}_e} = \phi_{\mu^+} : \phi_{\mu^-}. \quad (1.114)$$

At higher energies, the amount of muons hitting the ground before decaying increases, changing the ratio between flavours. The energy range of primary cosmic rays goes from a few hundreds of MeV up to about 10^{20} eV, as it is shown in Fig. 1.5. The isotropy in the angular distribution of cosmic rays and their energies suggest that they are produced mostly outside the solar system. Above a few GeV, the cosmic ray spectrum approximately follows $E^{-2.7}$, apart in the region between $10^{15.5}$ eV and $10^{17.7}$ eV where the behaviour is $E^{-3.0 \sim -3.3}$ (*knee*). The maximum

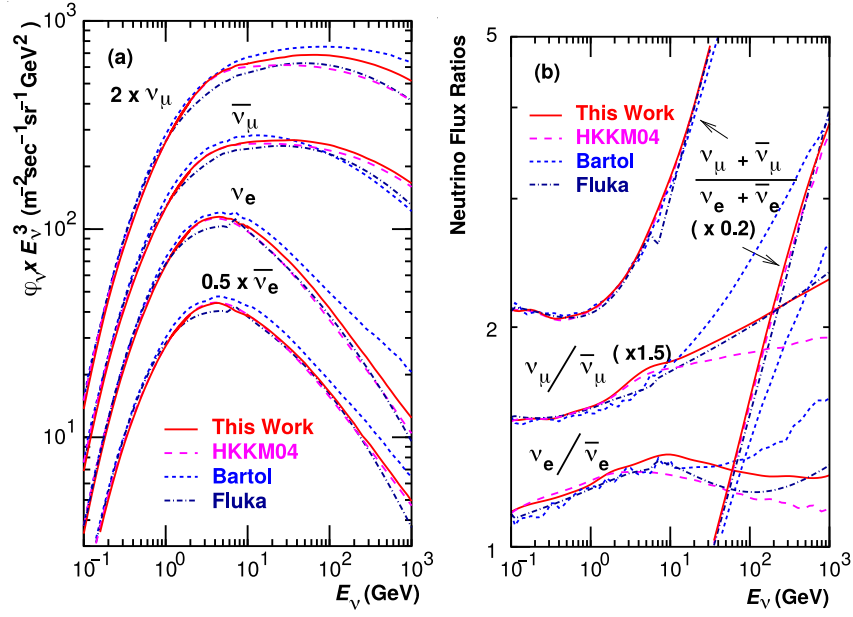


Figure 1.6: Prediction of atmospheric neutrinos created with a 3D simulation of Earth’s atmosphere and including geomagnetic effects. The flux prediction (left) shows that the most probable energy for electron neutrinos is around a few GeV, but for muon neutrinos goes up to hundred GeV. The ratio of flavours is shown as a function of energy on the right. Taken from [44].

theoretical limit is near 10^{20} eV [41], after which the spectrum is suppressed because of the interactions between cosmic rays and photons of the cosmic microwave background, known as Greisen-Zatsepin-Kuzmin (GZK) cutoff [42, 43].

The neutrinos are produced isotropically around the atmosphere with energies up to a few hundreds of TeV, peaking at tens of GeV, even though the energy distribution is flavour dependent. Although the production point of neutrinos varies in altitude, with a most probable value around 15 km, for an experiment on the Earth’s surface neutrinos are coming from all directions with the flight path depending on the zenith angle to the origin. This means that the distance travelled by atmospheric neutrinos varies from a minimum of a few kilometres to a maximum equal to the Earth’s diameter, 1.2×10^4 km. It was observed by the Super-Kamiokande experiment that the flavour ratio of atmospheric neutrinos from positive and negative zenith angle were different, implying the presence of neutrino oscillation [45]. A correct prediction of the atmospheric flux becomes instrumental when studying oscillation physics; computational-intensive 3D simulations have reached state-of-the-art precision with negligible statistical errors thanks to the implementation of geomagnetic models [44, 46]. The predictions of the model used by the Super-Kamiokande experiment is shown in Fig. 1.6, thanks to which the evidence of neutrino oscillation was confirmed.

1.3.3 Accelerator neutrinos

Atmospheric neutrinos provide an invaluable source for studying the properties of neutrinos, such as the squared mass differences and the mixing angles. However, the uncertainty on the path lengths of neutrinos from production to detection can downgrade the precision of the measurement. Accelerator facilities try to overcome this limitation. Neutrino beams are derived from a similar mechanism that generates atmospheric neutrinos. A proton beam directed on a fixed target typically yields a large number of pions and kaons, but also heavier mesons the

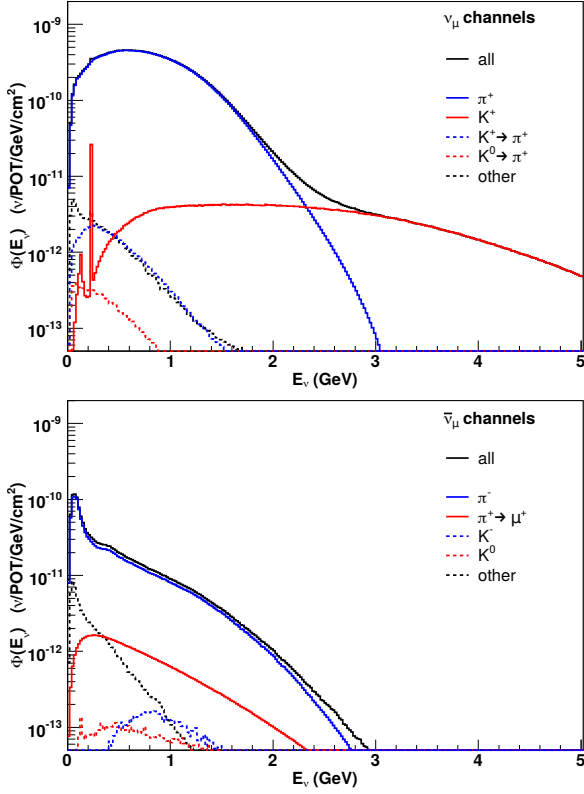


Figure 1.7: Prediction of the ν_μ (top) and $\bar{\nu}_\mu$ (bottom) fluxes at the Booster Neutrino Beam. The contributions from different parent particles are highlighted. Taken from Ref. [47].

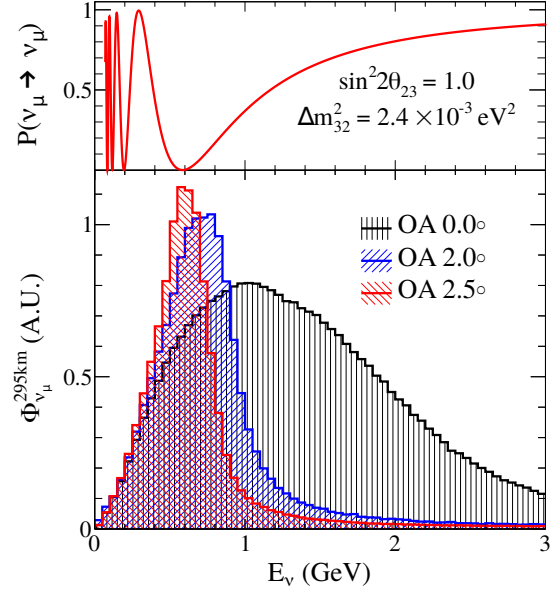


Figure 1.8: Prediction of the ν_μ flux at T2K (bottom), showing the profile at different off-axis angles (OA). At 2.5° from the axis, the energy distributions peaks in correspondence of a minimum for the ν_μ disappearance probability (top). Taken from Ref. [48].

amount of which depends on the energy of the protons and the choice of the target. All these secondary particles decay leptonically or semileptonically via CC weak interactions thus creating the neutrino beam. Pions and kaons principally decay into ν_μ because two-body electronic modes are disfavoured by helicity suppression. Muons decay in turn into equal numbers of ν_e and $\bar{\nu}_\mu$. Other production sources of ν_e and ν_μ are the three-body decays of K^0 and K^+ . As an example, the parentage composition of the Booster Neutrino Beam flux [47] is shown in Fig. 1.7, highlighting that pions are the main source of low energy neutrinos and kaons of energetic ones. Above the neutral kaon mass, the first significant source of neutrino is given by the D_s^+ meson, for which helicity suppression again favours the production of heavy charged-leptons, and so τ leptons and ν_τ are more likely to be emitted than the other flavours. Each of the subsequent τ^+ decays produces a $\bar{\nu}_\tau$. The production of charm mesons however requires a very high energy proton beam and therefore for practical reasons this contribution is disregarded in most experiments.

The energy and angular distributions of the neutrinos reflect the kinematic properties of the parent particles, which are in turn produced with a variety of angles and energies. Given its wide angular distribution, the neutrino beam may not give rise to the high statistics required by typical long baseline oscillation experiments. To improve the quality of the beam, a focusing system is typically put into place by partially surrounding the target with one or more pulsed toroidal electromagnets, called *horns*. The horns are activated with pulsed currents of hundreds

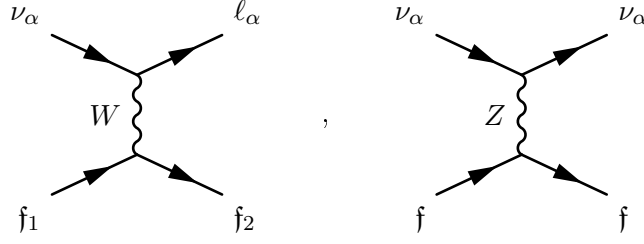


Figure 1.9: Generic CC (right) and NC (left) tree-level interactions with neutrinos involved. Note that these diagrams have illustration purpose only, and time flow convention is not respected.

of kiloampere for a few microseconds in coincidence with the proton beam arriving at the target. Within the horn cavity, the pulse creates a magnetic field that decreases radially with respect to the axis of the horn, meaning that the peak intensity of the magnetic field is reached at the inner regions of the toroid. By changing the direction of the pulsed current it is possible to select and focus particles of the desired charge. The configuration for which positively charged pions are focused and negatively ones are rejected is referred to as Forward Horn Current (FHC) and the resulting beam is mainly composed of neutrinos. With a Reverse Horn Current (RHC) configuration, negative pions are selected and the beam is principally made of antineutrinos. The two operation modes are also known as ν -mode and $\bar{\nu}$ -mode. Despite the optimal design of the horn, kaons and other short-lived mesons cannot be deflected as efficiently as pions and muons, and therefore the neutrino beam always presents an intrinsic spread. In certain cases, the neutrino experiment is located off the axis of the beam, as for the T2K [48] and NO ν A [49] experiments. The energy distribution of neutrinos emitted away from the beam axis loses some dependency from the parent meson and the profile becomes approximately monochromatic [50]. This characteristic is favourable in oscillation experiment, in which the ratio between baseline and neutrino energy should be fixed and known. In Fig. 1.8, the T2K flux prediction is shown at different angles; with an off-axis angle of 2.5° the energy distribution is strongly peaked at the minimum of the disappearance channel $\nu_\mu \rightarrow \nu_\mu$.

1.4 Neutrino interactions

Neutrino interactions in their flavour states are described by Eqs. (1.15) and (1.16). Replacing the values of g_V^ν and g_A^ν for a neutrino, the relevant Lagrangian terms are

$$\mathcal{L}_{CC,\nu} = -\frac{g}{2\sqrt{2}} \sum_{\alpha=e,\mu,\tau} \bar{\nu}_\alpha W (1 - \gamma^5) \ell_\alpha + \text{h.c.} , \quad (1.115)$$

$$\mathcal{L}_{NC,\nu} = -\frac{g}{4 \cos \vartheta_W} \sum_{\alpha=e,\mu,\tau} \bar{\nu}_\alpha Z (1 - \gamma^5) \nu_\alpha . \quad (1.116)$$

For energies below the W and Z mass, the allowed tree-level interactions involving at least one neutrino are any allowed variation of the processes represented in Fig. 1.9. The vector bosons cannot be produced on shell and so their field operator must contract with some other external field. The amplitudes of the processes shown in Fig. 1.9 are

$$i\mathcal{M}_{CC} = i \frac{g^2}{8} \bar{u}_{\ell_\alpha} \gamma^\mu (1 - \gamma^5) u_{\nu_\alpha} \frac{\eta_{\mu\nu}}{q^2 - m_W^2 + i\varepsilon} \bar{u}_{f_2} \gamma^\nu (1 - \gamma^5) V_{12} u_{f_1} , \quad (1.117)$$

$$i\mathcal{M}_{NC} = i \frac{g^2}{8 \cos \vartheta} \bar{u}_{\nu_\alpha} \gamma^\mu (1 - \gamma^5) u_{\nu_\alpha} \frac{\eta_{\mu\nu}}{q^2 - m_Z^2 + i\varepsilon} \bar{u}_f \gamma^\nu (g_V^f - g_A^f \gamma^5) u_f , \quad (1.118)$$

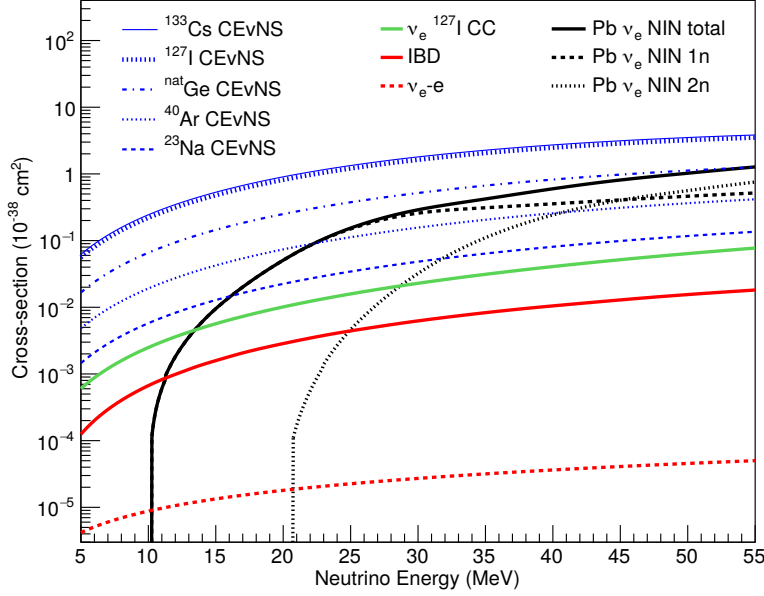


Figure 1.10: Behaviour of the neutrino–nucleus cross-sections for various targets, as a function of the neutrino energy. The cross-sections for neutrino-induced neutrons (NIN), inverse beta decay (IBD), and elastic scattering of ν_e on electrons are also shown for comparison. Taken from Ref. [51].

where k is the momentum of the propagator and V_{12} is a possible mixing between generic fermions f_1 and f_2 . Due to the typical energies involved, the momentum propagating between the particles is small compared to the masses of the intermediate bosons and therefore their mass can be factorised out, resulting in the four-point interactions

$$i\mathcal{M}_{\text{CC}} \simeq i \frac{G_F^2}{\sqrt{2}} \bar{u}_{\ell_\alpha} \gamma^\mu (1 - \gamma^5) u_{\nu_\alpha} \bar{u}_{f_2} \gamma^\mu (1 - \gamma^5) V_{12} u_{f_1} , \quad (1.119)$$

$$i\mathcal{M}_{\text{NC}} \simeq i \frac{G_F^2}{\sqrt{2}} \bar{u}_{\nu_\alpha} \gamma^\mu (1 - \gamma^5) u_{\nu_\alpha} \bar{u}_f \gamma^\mu (g_V^f - g_A^f \gamma^5) u_f , \quad (1.120)$$

where the relation in Eq. (1.29) was used and a new constant was introduced

$$\frac{G_F}{\sqrt{2}} = \frac{g^2}{8m_W^2} . \quad (1.121)$$

The constant $G_F = 1.166\,378\,7 \times 10^{-5} \text{ GeV}^{-2}$ in Eq. (1.121) is called Fermi’s constant and it is obtained from measuring the muon lifetime [15].

In the following sections the most important neutrino interactions with matter are reviewed, from low to high energies.

1.4.1 Coherent elastic neutrino–nucleus scattering

The neutrino coupling to the Z boson opens the possibility of a coherent interaction with all the nucleons in an atomic nucleus, if the momentum exchange q^2 is significantly small [52]. This interaction is called coherent elastic neutrino–nucleus scattering, or “CE ν NS”. The coherence

condition corresponds to target nucleons in phase with each other when $q^2 \lesssim 1/R^2$, where R is the size of the nucleus. This restricts the process to energies below a few tens of MeV. However, the probability of interaction scales with the square nuclear mass, enhancing at low energies the cross-section with respect to the interaction with individual nucleons. This is depicted in Fig. 1.10 where the CE ν NS cross-section for a few different nuclear species is shown as a function of neutrino energy.

The signature of this reaction is a recoil of the target nucleus, since low-energy neutrinos are not easily detected. The differential cross-section with respect to the recoil energy T reads [52, 53]

$$\frac{d\sigma}{dT} = \frac{G_F^2}{2\pi} M \left[(G_V + G_A)^2 + (G_V - G_A)^2 \left(1 - \frac{T}{E}\right)^2 - (G_V^2 - G_A^2) \frac{MT}{E^2} \right], \quad (1.122)$$

where M is the mass of the target, E the energy of the incoming neutrino and

$$G_V = [g_V^p Z + g_V^n N] F_V(q^2) \quad (1.123)$$

$$G_A = [g_A^p (Z_+ - Z_-) + g_A^n (N_+ - N_-)] F_A(q^2). \quad (1.124)$$

The vector and axial coupling constants for protons and neutrons are

$$\begin{aligned} g_V^p &= \frac{1}{2} - 2 \sin^2 \vartheta_W, & g_A^p &= \frac{1}{2}, \\ g_V^n &= -\frac{1}{2}, & g_A^n &= -\frac{1}{2}. \end{aligned} \quad (1.125)$$

Z_{\pm} and N_{\pm} are respectively the number of protons and neutrons with spin up or spin down, and $F_V(q^2)$ and $F_A(q^2)$ are the vector and axial nuclear form factors. The vector contribution dominates strongly for most nuclei, whereas the axial term shows an effect only on unpaired nucleons, which are typically just a few compared to the total number of nucleons or none for spin-zero nuclei. Neglecting the axial form factor, the cross-section for a small recoil $T \lesssim E$ simplifies to

$$\frac{d\sigma}{dT} \simeq \frac{G_F^2}{8\pi} M F^2(q^2) [N + (4 \sin^2 \vartheta_W - 1)Z]^2 \left(2 - \frac{MT}{E^2}\right). \quad (1.126)$$

The angular dependence of the scattering is then

$$\frac{d\sigma}{d\cos\theta} \simeq \frac{G_F^2}{8\pi} [N + (4 \sin^2 \vartheta_W - 1)Z]^2 E (1 + \cos\theta). \quad (1.127)$$

Since $\sin^2 \vartheta_W = 0.231$, the CE ν NS cross-section is strongly dependent on the squared number of neutrons N , with just a little contribution from the squared atomic number Z .

For heavy nuclei and sufficiently intense neutrino sources, the measurement of CE ν NS can be achieved using relatively small active volumes. This was first demonstrated by the COHERENT collaboration [54] which successfully observed the coherent scattering for the first time using a 14.57 kg CsI[Na] scintillating crystal and collecting 1.76×10^{23} protons on target [51]. The measurement of CE ν NS is of utter importance for direct dark matter experiments, since the so-called *neutrino floor* is due to CE ν NS interactions of solar and atmospheric neutrinos. This scattering also presents a chance for significant tests of the SM or searches of new physics, like nonstandard neutrino interactions and the dark sector [55] (see also Ref. [56]).

1.4.2 Neutrino–electron scattering

The easiest interaction to study between neutrinos and matter components at low energies is the neutrino–electron elastic scattering

$$\bar{\nu}_{\alpha}^{(-)} + e^{-} \rightarrow \bar{\nu}_{\alpha}^{(-)} + e^{-} . \quad (1.128)$$

Using the effective four-point amplitudes of Eq. (1.120), one can calculate the differential cross-sections in the laboratory frame with an initial electron at rest:

$$\frac{d\sigma}{dq^2} = \frac{G_F^2}{\pi} \left[\kappa_1^2 + \kappa_2^2 \left(1 - \frac{q^2}{2(p_{\nu} \cdot p_e)} \right)^2 - \kappa_1 \kappa_2 m_e^2 \frac{q^2}{2(p_{\nu} \cdot p_e)^2} \right] . \quad (1.129)$$

The quantities κ_1 and κ_2 depend on the neutrino flavour and embeds CC and NC contributions; they are expressed in terms of the vector and axial coupling of Eq. (1.18) and they read

$$\kappa_1^{\nu_e} = \kappa_2^{\bar{\nu}_e} = 1 + \frac{g_V^{\ell} + g_A^{\ell}}{2} = \frac{1}{2} + \sin^2 \vartheta_W , \quad (1.130)$$

$$\kappa_2^{\nu_e} = \kappa_1^{\bar{\nu}_e} = \frac{g_V^{\ell} - g_A^{\ell}}{2} = \sin^2 \vartheta_W , \quad (1.131)$$

$$\kappa_1^{\nu_{\mu,\tau}} = \kappa_2^{\bar{\nu}_{\mu,\tau}} = \frac{g_V^{\ell} + g_A^{\ell}}{2} = -\frac{1}{2} + \sin^2 \vartheta_W , \quad (1.132)$$

$$\kappa_2^{\nu_{\mu,\tau}} = \kappa_1^{\bar{\nu}_{\mu,\tau}} = \frac{g_V^{\ell} - g_A^{\ell}}{2} = \sin^2 \vartheta_W . \quad (1.133)$$

The quantity q^2 is the transfer momentum between the initial and final electrons. Denoting $T_e = E_e - m_e$ as the kinetic energy of the outgoing electron, it follows that

$$q^2 = 2 m_e T_e . \quad (1.134)$$

With some kinematics, the kinetic energy is found to be

$$T_e = \frac{2 m_e E_{\nu}^2 \cos^2 \theta}{(m_e + E_{\nu})^2 - E_{\nu}^2 \cos^2 \theta} , \quad (1.135)$$

which has a maximum value when the neutrino is not deviated in the scattering, i.e. $\cos \theta = 1$, and it equates

$$T_e^{\max} = \frac{2 E_{\nu}^2}{m_e + 2 E_{\nu}} . \quad (1.136)$$

The differential cross-section in Eq. (1.129) can be given as a function of the electron scattering angle θ with respect to the incoming neutrino with energy E_{ν}

$$\begin{aligned} \frac{d\sigma}{d \cos \theta} = & \frac{2 G_F^2 m_e}{\pi} \frac{4 E_{\nu}^2 (m_e + E_{\nu})^2 \cos^2 \theta}{[(m_e + E_{\nu})^2 - E_{\nu}^2 \cos^2 \theta]^2} \times \\ & \left[g_1^2 + g_2^2 \left(1 - \frac{2 m_e E_{\nu} \cos^2 \theta}{(m_e + E_{\nu})^2 - E_{\nu}^2 \cos^2 \theta} \right)^2 - \frac{2 m_e^2 \cos^2 \theta g_1 g_2}{(m_e + E_{\nu})^2 - E_{\nu}^2 \cos^2 \theta} \right] . \end{aligned} \quad (1.137)$$

For the electron neutrino ν_e , both CC and NC interactions are allowed and for the electron antineutrino $\bar{\nu}_e$ the s -channel and t -channel diagrams are swapped, whereas for $\alpha = \mu, \tau$ only neutral-current interactions exist. It results that the total cross-section for $\bar{\nu}_e$, $\nu_{\mu,\tau}$, and $\bar{\nu}_{\mu,\tau}$

are approximately and respectively 42 %, 16 %, and 14 % of the total cross-section of electron neutrinos, which goes for $\sqrt{s} \gg m_e$ as

$$\sigma_{\nu_e} \simeq 93 \times 10^{-46} \text{ cm}^2 \frac{s}{\text{MeV}^2} . \quad (1.138)$$

The proportions between these interaction probabilities have been an important discriminant for the SNO and SK experiments [57] in solving the solar neutrino problem (see Section 1.3.1), since the rate of neutrino–electron scattering is related to the neutrino flavour.

1.4.3 Neutrino scattering with nucleons

At higher energies, the dominant neutrino interaction mode is with nucleons in matter, thanks to the W and Z couplings of the quark components and the currents of Eqs. (1.38) and (1.39). In general, these processes can be categorised according to the momentum transfer. For $q^2 \lesssim m_N$, elastic interactions dominate and are brought about by neutral currents. When this occurs via neutral currents, all flavour of neutrinos and antineutrinos can scatter off both neutrons and protons in what is referred to as “NC elastic” (NCE) scattering. The process is the same for neutrinos and antineutrinos

$$\nu_\alpha + N \rightarrow \nu_\alpha + N \quad \text{or} \quad \bar{\nu}_\alpha + N \rightarrow \bar{\nu}_\alpha + N . \quad (1.139)$$

Once neutrinos acquire sufficient energy they can also undergo the analogous charged current counterpart, called “quasi-elastic” (CCQE) interaction, due to the fact that the recoiling nucleon changes its charge and mass transfer occurs. The allowed processes are

$$\nu_\alpha + n \rightarrow p + \ell_\alpha^- \quad \text{and} \quad \bar{\nu}_\alpha + p \rightarrow n + \ell_\alpha^+ , \quad (1.140)$$

with $\alpha = e, \mu, \tau$. The process for $\bar{\nu}_e$ is historically referred to as *inverse beta decay* (IBD) and it is the principal mode of detection of electron antineutrinos [58]. The differential cross-sections for the CCQE scattering in the laboratory frame are given by

$$\frac{d\sigma_{CC}}{dq^2} = \frac{G_F^2 |V_{ud}|^2 m_N^4}{8\pi (p_\nu \cdot p_N)^2} \left[A(q^2) \pm B(q^2) \frac{s-u}{m_N^2} + C(q^2) \frac{(s-u)^2}{m_N^4} \right] , \quad (1.141)$$

$$\frac{d\sigma_{CC}}{d\cos\theta} = -\frac{G_F^2 |V_{ud}|^2 m_N^2}{4\pi} \frac{p_l}{E_\nu} \left[A(q^2) \pm B(q^2) \frac{s-u}{m_N^2} + C(q^2) \frac{(s-u)^2}{m_N^4} \right] , \quad (1.142)$$

where N denotes the nucleon and the plus sign refers to $N = n$ and the minus sign to $N = p$. The functions $A(q^2)$, $B(q^2)$, and $C(q^2)$ for the charged-current process are:

$$A(q^2) = \frac{m_l^2 + q^2}{m_N^2} \left\{ \left(1 + \frac{q^2}{4m_N^2} \right) G_A^2 - \left(1 - \frac{q^2}{4m_N^2} \right) \left(F_1^2 - \frac{q^2}{4m_N^2} F_2^2 \right) + \frac{q^2}{m_N^2} F_1 F_2 \right. \\ \left. - \frac{m_l^2}{4m_N^2} \left[(F_1 + F_2)^2 + (G_A + 2G_P)^2 - \frac{1}{4} \left(1 + \frac{q^2}{4m_N^2} \right) G_P^2 \right] \right\} , \quad (1.143)$$

$$B(q^2) = \frac{q^2}{m_N^2} G_A (F_1 + F_2) , \quad (1.144)$$

$$C(q^2) = \frac{1}{4} \left(G_A^2 + F_1^2 + \frac{q^2}{4m_N^2} F_2^2 \right) . \quad (1.145)$$

The terms F_1 , F_2 , G_A , and G_P are form factors and are functions of q^2 . The nucleon form factors $F_1 = F_1^p - F_1^n$, $F_2 = F_2^p - F_2^n$ are known respectively as *Dirac* and *Pauli* form factors.

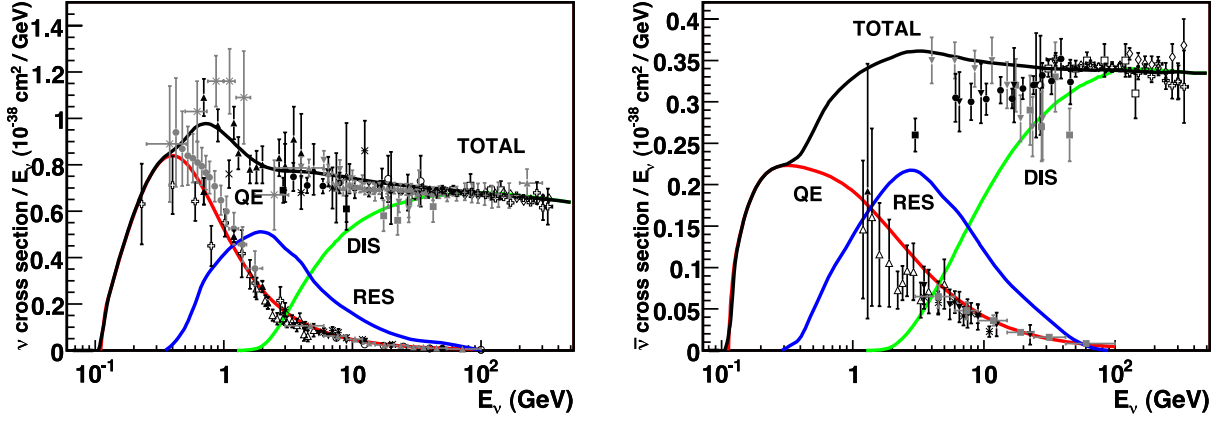


Figure 1.11: Total neutrino (left) and antineutrino (right) cross-section measurements and predictions for an isoscalar target as a function of energy. The contributions from quasi-elastic (QE, red), resonance (RES, blue), and deep-inelastic scattering (DIS, green) are highlighted. Resonant modes only give a substantial contribution in a small energy region between 1 GeV and 10 GeV, explaining the difficulty in constraining theoretical models. Taken from Ref. [60].

For $q^2 = 0$, they simplify to

$$\begin{aligned} F_1^p(0) &= 1, & F_1^n(0) &= 0, \\ F_2^p(0) &= \frac{2m_p\mu_p}{e\hbar} - 1, & F_2^n &= \frac{2m_p\mu_n}{e\hbar}, \end{aligned} \quad (1.146)$$

where μ_p and μ_n are the proton and neutron magnetic momenta. For $q^2 \neq 0$ they are more conveniently described by the Sachs electric and magnetic momenta [59]. The *pseudoscalar* form factor G_P is usually ignored in cross-section calculations, whereas the *axial* form factor is parameterised as

$$G_A(q^2) = \frac{g_A}{\left(1 + \frac{q^2}{m_A^2}\right)^2}. \quad (1.147)$$

All the form factors are usually fitted from data of neutrino experiments since they give non-negligible contributions to the systematic uncertainties, particularly the *axial mass* m_A which is arbitrarily assumed to be $m_A = 1.0$ GeV in many neutrino event generators. The NCE cross-section has the same structure as in Eqs. (1.141) and (1.142), apart from the mixing term $|V_{ud}|^2$ and the corresponding neutral-current form factors

$$F_{1,2}^N = \pm \frac{1}{2}(F_{1,2}^p - F_{1,2}^n) - 2\sin^2\vartheta_W F_{1,2}^N - \frac{1}{2}F_{1,2}^N, \quad (1.148)$$

where the plus sign is for $N = p$ and the minus sign for $N = n$.

CCQE interactions are of vital importance for neutrino physics, because the measurement of its differential cross-section give precious information on the nucleon form-factors which are difficult to measure with a different probe. Also, the two-body nature of the interactions is such that the kinematic properties of the incoming neutrino can be determined with good precision. This is relevant especially for oscillation experiments, in which the energy of the neutrino can be estimated from the momentum of the outgoing charge lepton p_ℓ and its angle with the direction of the incoming neutrino θ_ℓ , if known. If the target nucleon is at rest compared to the neutrino energy, then this can be calculated as:

$$E_\nu = \frac{m_n E_\ell + \frac{1}{2}(m_p^2 - m_n^2 - m_\ell^2)}{m_n - E_\ell + p_\ell \cos \theta_\ell}. \quad (1.149)$$

The neutrino–hadron cross-sections as a function of energy are shown in Fig. 1.11. The QE cross-section drops for neutrino energies above 1 GeV as the available q^2 increases. At energies between $1 \text{ GeV} \lesssim E_\nu \lesssim 10 \text{ GeV}$, processes such as multinucleon emission or baryon resonance become relevant. Correlated pairs of nucleons inside the nucleus can be simultaneously ejected, in the so-called 2p-2h interactions, or the nucleon itself can excite into a baryonic resonance before decaying and emitting a charged or a neutral pion. There are many theoretical models explaining these multibody interactions [61–63], and neutrino interaction generators, like GENIE [64] or NEUT [65], often implement more than one. The determination of the correct paradigm is a hard task, due to the difficulty of the measurement of resonant modes. In fact, at $q^2 \gg m_n$ or for $E_\nu \gtrsim 50 \text{ GeV}$, deep inelastic scattering (DIS) is the dominant mode since the neutrino has enough energy to scatter directly off a constituent quark and to fragment the original nucleon.

Chapter 2

The future of Super-Kamiokande

The typical total cross-section for an accelerator neutrino ($E_\nu \sim 1 \text{ GeV}$) is of the order of 10^{-38} cm^2 and for a solar neutrino ($E_\nu \lesssim 10 \text{ MeV}$) it is roughly one order of magnitude lower, as it can be evinced from Figs. 1.10 and 1.11. These small values make the detection of neutrinos a challenging task. Neutrino experiments usually compensate the small cross-section by instrumenting large active volumes, so that a statistically significant amount of neutrino interactions with matter can be recorded. By studying final-state particles some knowledge on the incoming neutrino may be retrieved. Large volumes however are prone to intense background too, either from cosmic rays or natural radioactivity. Passive or active techniques to reduce such undesired events must be therefore put into place. Neutrino physics has greatly progressed in recent times thanks to both massive detectors and improvements in detection technologies. The most emblematic examples of neutrino experiments are Sudbury Neutrino Observatory (SNO) and Super-Kamiokande (SK) which respectively demonstrated solar [30] and atmospheric [45] neutrino oscillations. The picture of three-flavour neutrino oscillations has since been studied in depth by numerous experiments with not only atmospheric and solar neutrinos, but also with neutrinos from reactor and accelerator facilities. Current and future neutrino experiments rely on the experimental techniques that were pioneered and perfected by these two successful experiments.

SK and SNO are both Cherenkov detectors, in which a large body of water — heavy water in the case of SNO — is surrounded by photodetectors to capture Cherenkov radiation emitted by the charged leptons produced in neutrino CC and NC interactions. The volumes of SNO and SK are located in mines so as to take advantage of the thick rock overburden, which acts as a passive shield to cosmic muons. An outer detector system provides a passive and active veto to the fiducial region of both experiments. These simple measures are responsible for the suppression of the majority of backgrounds. However, backgrounds from atmospheric neutrino interactions with or without neutron emission together with β -decay from spallation events induced by cosmic rays are more difficult to control. These events can generate electrons or positrons that pass the selection criteria and so contaminate candidate samples of CC quasi-elastic events (CCQE, see Section 1.4.3) much needed for oscillation studies [66, 67]. The neutrons emitted in antineutrino CCQE interactions could be used to discriminate such events. As we are entering a precision era for neutrino experiments, the capability of detecting neutrons in signal and background events is in fact becoming a crucial requisite especially for detectors studying solar, supernova, or reactor neutrinos. One of the most promising approaches is the addition of gadolinium to the active medium of the detector. Certain isotopes of Gd have a very high cross-section for neutron capture accompanied with the emission of high energy photons which makes neutron detection more efficient. Many existing neutrino experiments are already

using Gd-loaded water or Gd-loaded scintillator for neutron tagging, such as EGADS [68], ANNIE [69], and RENO [70], and future experiments are planning to adopt the same approach.

In the next phase of SK, hundred tons of gadolinium sulphate will be dissolved in water, making Super-Kamiokande the largest Gd-doped water Cherenkov detector. The benefits and challenges of this technique are extensively covered in this chapter, after a review of the working principle of a generic Cherenkov detector in Section 2.1 and the theory of neutron thermalisation and neutron capture in Section 2.2. The Super-Kamiokande experiment is briefly introduced in Section 2.3, with an emphasis on the techniques currently in place to control backgrounds, searches limited by irreducible background, and the improvements provisioned by the gadolinium phase of SK. The neutron calibration procedure of the detector is explained in Section 2.4 and a promising substitute for the neutron calibration device is there introduced. Finally, a novel technique to monitor gadolinium concentration in water using UV spectroscopy is presented in Section 2.5 and the first laboratory results are reported.

2.1 Cherenkov detectors

Light travelling through a transparent material undergoes a reduction of its phase velocity due to a superposition with the electromagnetic fields of the electrons in the medium. The change in velocity will therefore depend on the frequency of the incoming photons. The ratio of the new phase velocity and the speed of light in vacuum defines the *refractive index* of the material

$$n(\lambda) = \frac{c}{v_P(\lambda)} , \quad (2.1)$$

which is greater than one by definition.

A charged particle moving at a velocity faster than the speed of light in a medium emits a coherent electromagnetic radiation, called *Cherenkov radiation*. Provided that the distance covered by the particle in the medium is large compared to the emitted wavelength, the radiation is produced when [71]

$$\beta \equiv \frac{v}{c} > \frac{1}{n} , \quad (2.2)$$

where v is the velocity of the particle. The minimum energy of the particle to reach this condition is therefore

$$E_{\text{thr}} = m \sqrt{1 + \frac{1}{n^2 - 1}} , \quad (2.3)$$

with m the mass of the charged particle. As the particle is moving faster than c/n , the wave front of the EM radiation forms a cone which follows the charged particle. The angular aperture θ of such cone is given by

$$\cos \theta = \frac{1}{n\beta} . \quad (2.4)$$

The maximum angle is reached by ultrarelativistic particles for which $\beta \simeq 1$. The charged particle, however, will progressively lose kinetic energy in the medium due to ionisation, slowing down until its energy falls below the threshold E_{thr} . As soon as the condition of Eq. (2.2) does not hold anymore, the particle stops emitting radiation and the cone of light reduces to a truncated cone which forms a ring when projected onto a surface.

Many particle physics experiments take advantage of this effect, in order to convert the passage of charged particles into detectable light. A volume of transparent material, such as water, ice, or aerogel, can be instrumented with photodetectors to capture Cherenkov radiation. Liquid scintillators are also employed in such detectors despite not being transparent to

the radiation: most scintillators absorb the Cherenkov light and re-emit it isotropically at a different wavelength, therefore losing the information on directionality. The number of photons emitted by a charged particle of charge z per unit path length and per unit energy interval, or equivalently to the wavelength λ , has a distribution that follows the Frank-Tamm formula [72]

$$\frac{\partial^2 N}{\partial x \partial \lambda} = \frac{2 \pi \alpha z^2}{\lambda^2} \left(1 - \frac{1}{\beta^2 n^2(\lambda)} \right) = \frac{2 \pi \alpha z^2}{\lambda^2} \sin^2 \theta, \quad (2.5)$$

where α is the fine structure constant and z is the charge of the particle. Due to the inverse dependence on λ^2 , most of the Cherenkov photons are emitted at shorter wavelengths. However, a real medium is always dispersive and allowed frequencies are restricted to the region for which $n(\lambda) > 1/\beta$. The radiation is hence typically emitted in the near visible and ultraviolet regions of the EM spectrum. At higher frequencies, for example in the x-ray region, the refractive index drops below one and Cherenkov photons cannot be produced at these shorter wavelengths. Experiments exploiting the Cherenkov effect try to match the sensitivity band of photodetectors to the radiation region. Photomultipliers (PMT) are the detectors of choice, thanks to their low noise and capability of single photodetection, but microchannel plates (MCP) and silicon photomultipliers (SiPM) are used too (see e.g. [73]). This technique is largely used in neutrino detection, since it easily allows to transform large volumes of some transparent or scintillating medium into a detector sensitive to charged particles. Amongst the most notable examples, the IceCube experiment is the largest Cherenkov detector [74], in which more than five thousands PMTs are deployed into the Antarctic ice, covering a volume of one cubic kilometre.

Charged-current interactions of neutrinos on a nucleon produce charged leptons that are likely to acquire most of the incoming neutrino momentum thanks to the heavy mass of the nucleon. If the energy of the outgoing lepton is above the threshold of Eq. (2.3), the emitted radiation can be collected and used to reconstruct the interacting neutrino's properties, with some limited resolution (see Eq. (1.149)). The photons collected on the light sensors are correlated to the particle's energy, whereas the location and timing of the hit photodetectors is used to reconstruct the vertex and the direction of the interaction. The directionality information is lost in scintillator Cherenkov detectors, because scintillating materials typically emit light isotropically. The topology and pattern of the radiation collected are often used for event classification; a precise particle identification is possible in some cases, such as in SK which is discussed in Section 2.3.

2.2 Neutron thermalisation and neutron capture

Neutrons have a very long lifetime and since they cannot directly emit Cherenkov radiation they can travel quite some distance from their production point without being detected. Neutrons interact with nuclei in various ways, depending on their energy and the target nucleus. The interactions are divided in three typologies: scatterings, which can be elastic or inelastic, absorptions, such as radiative capture or fission, and nucleon transfer reactions. The kinetic energy of the neutron T , sometimes referred to as the *detection temperature*, is the main factor in determining the dominant interaction mode. For fast neutrons, with $T > 1$ MeV, elastic scattering is the prevailing process and for some target nuclei the only mode possible. The cross-section for these energetic neutrons present some resonance peaks the structure of which depends on the target nuclei. The elastic scattering cross-section at energies below 1 MeV is almost independent of the neutron energy. This is true for most light isotopes, but some intermediate and heavy elements present specific behaviours at higher energy. Neutrons with a kinetic energy $T \simeq 0.025$ eV are called *thermal neutrons* because a Maxwell-Boltzmann distribution at the temperature of 290 K peaks at that energy; such neutrons are in thermal equilibrium

with the surrounding medium. At thermal energies and below, the most important interaction is neutron absorption, the cross-section of which follows the “ $1/v$ law”, with v being the velocity of the neutron. In this region, the absorption cross-section increases as the velocity of the neutron, i.e. its temperature, decreases:

$$\sigma \sim \frac{1}{v} \sim \frac{1}{T} . \quad (2.6)$$

Being in thermal equilibrium and having a lower kinetic energy allows the neutron to form a compound nucleus with the target, which might undergo spontaneous fission or radiation emission if it is a nonfissile nuclide. For energies between a few eV and hundreds of keV there are resonances in the capture cross-section which are strongly dependent on the target isotope, but also on the temperature of the material. In fact, the thermal motions of the target relative to the incident neutron broadens the resonance peaks, even though the integrated cross-section over the energy range remains constant. This effect is called *Doppler broadening* and results in a decreased likelihood of capture or fission when the target material has a wide energy distribution.

Fast neutrons slow down to thermal energies via subsequent elastic collisions until the free neutron is captured by some nucleus: this process is called *thermalisation*. Considering a scattering between a neutron and a nucleus,

$$n + A \rightarrow n + A , \quad (2.7)$$

the final state energy of the neutron depends on the outgoing angle $\hat{\theta}$ in the centre of mass frame [75]

$$E_f = E_i \frac{(1 + \zeta) + (1 - \zeta) \cos \hat{\theta}}{2} , \quad (2.8)$$

where $E_{i,f}$ are the initial and final energies of the free neutron. The kinematic factor ζ is defined as

$$\zeta = \frac{(m_n - M_A)^2}{(m_n + M_A)^2} \simeq \frac{(1 - A)^2}{(1 + A)^2} , \quad (2.9)$$

where m_n is the neutron mass, $M_A \approx A m_n$ is the mass of the nucleon and A the mass number. Using classic mechanics, the scattering angle θ in the laboratory frame is given by

$$\cos \theta = \frac{A \cos \hat{\theta} + 1}{\sqrt{1 + 2 A \cos \hat{\theta} + A^2}} , \quad (2.10)$$

and the average scattering angle can be therefore estimated as

$$\langle \cos \theta \rangle = \frac{\int d\Omega \cos \theta}{\int d\Omega} = \frac{2}{3A} . \quad (2.11)$$

On average, heavy targets will modify the neutron’s path more significantly than light ones. For hydrogen ($A = 1$), the average angle is $\langle \theta \rangle \simeq 48^\circ$, but for heavier elements with large atomic mass the average angle $\langle \theta \rangle \rightarrow 90^\circ$. Assuming uniform isotropic scattering, the average outgoing energy for the neutron is

$$\langle E_f \rangle = \frac{\int d\Omega E_f}{\int d\Omega} = E_i \frac{1 + \zeta}{2} . \quad (2.12)$$

This means that if each collision decreases the neutron energy by the same factor as in Eq. (2.12), after n interactions the neutron energy is

$$E_n = E_0 \left(\frac{1 + \zeta}{2} \right)^n = E_0 e^{-n\xi} . \quad (2.13)$$

The thermalisation process follows an exponential law and ξ represents the typical energy decrease in log-scale which on average equals to [75]

$$\langle \xi \rangle = \frac{\int d\Omega \log \left(\frac{E_i}{E_f} \right)}{\int d\Omega} = \frac{\zeta - \zeta \log \zeta - 1}{\zeta - 1} = 1 + \frac{(A-1)^2}{2A} \log \frac{A-1}{A+1} . \quad (2.14)$$

The average number of collisions a neutron undergoes when propagating in a medium can be then computed with the above expression. Lighter nuclides turn out to be more effective at slowing down neutrons than heavier ones due to the A -dependency of ξ . For example, the number of interactions necessary for a fast neutron to decelerate to thermal energies in lead ($A = 208$) is about hundred times the number of interactions that would occur in hydrogen. In most cases, the media in which neutrons propagate are compounds with more than one type of target. The energy decrease for these materials is an average of the individual components weighted by their respective elastic cross-sections [75]

$$\xi_{\text{tot}}(E) = \frac{\sum_k \sigma_k(E) \xi_k(E)}{\sum_k \sigma_k(E)} . \quad (2.15)$$

In this simplified scenario, the impact of resonance capture has been overlooked which is only manifest at around the keV energy range. While fast neutrons with energies above 1 MeV are being slowed down to thermal energies, the mean free path decreases with the neutron's velocity and the likelihood of resonance capture increases. These captures affect the relative neutron flux around the energy of the resonance peaks, which might be widened by the Doppler broadening effect.

2.3 The Super-Kamiokande experiment

The Super-Kamiokande experiment (SK) [76] is a water Cherenkov detector, located in the Kamioka mine, under Mt. Ikeno in the Gifu prefecture, Japan. A schematic of the cavern is shown in Fig. 2.1. The rock overburden of roughly 1000 m (2700 m.w.e.), shields very efficiently the experiment and only cosmic rays with energies above 1.3 TeV can reach the detector: the muon flux at SK is about $6 \times 10^{-8} \text{ cm}^{-2} \text{ s}^{-1} \text{ sr}^{-1}$, which translates to a rate of 2 Hz in the fiducial volume. The detector consists of a cylindrical stainless steel tank, with a height of 41.4 m and a diameter of 39.3 m, and it is filled with 50 kt of ultra pure water. The water region is separated in two concentric cylindrical regions, called the inner detector (ID, 33.8 m in diameter) and the outer detector (OD), the latter working as a passive and active veto. The two regions are separated by a 55 cm insensitive region containing the support structure for the PMTs and their cables. The ID is instrumented with 11 129 20" Hamamatsu R3600 PMTs, facing towards the inside of the tank. Since the 2001 implosion accident, the photocathode of each PMT is protected by UV-transparent acrylic domes and the side of the tube with fibre-reinforced plastic. The photocoverage of the inner surface is around 40 %; the remaining surface not occupied by a PMT is lined with black sheet to reduce light reflection. The main goal of the OD is to tag events originating or finishing outside the ID. The only signal events that can originate inside

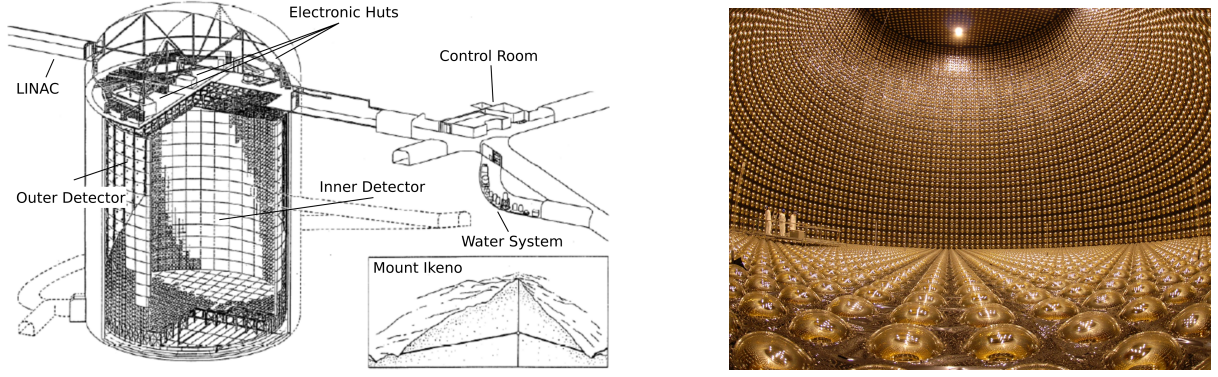


Figure 2.1: Cut-open view (left) of the Super-Kamiokande detector in Kamioka mine, located at the centre of Mt. Ikeno. On the right, a wide-angle picture of the inside of the tank; each golden bulb is a 20" PMT.

the ID without triggering the OD are neutrino or proton decay events. The OD is instrumented with 1885 8" Hamamatsu R1408 PMTs which are optically coupled to wavelength shifting plates to increase light collection. Sheets of white tyvek maximise the propagation of photons inside the OD and help the reconstruction of events occurring at the edges of the cylinder tank, also known as *corner-clipping events*.

The refractive index of water in the visible and ultraviolet region is $n \geq 1.33$, and so a charged particle can emit Cherenkov radiation if it is travelling with speed $\beta \gtrsim 0.75$. This translates to an energy threshold of 0.78 MeV for electrons, 160.26 MeV for muons, 211.69 MeV for pions, and 1423.13 MeV for protons, which are the particles usually detected in SK. The Cherenkov photons, thanks to the high-purity water, reach the walls of the tank forming ring patterns which are recorded by the PMTs. From the charge deposited on the photodetectors and the time information, the event reconstruction algorithm estimates the interaction vertex, the direction and the energy of the incoming particle. The same algorithm performs particle identification by looking at the topology and the multiplicity of the ring patterns. For example, an electron travelling in the water is more likely to be scattered compared to a muon which, on the other hand, will follow a straighter path: the electron-induced ring is therefore less defined and fuzzier than the muon-induced one. This can be appreciated from the reconstructed events of Fig. 2.2 showing an electron-like and a muon-like ring originated from neutrino interactions. Pions usually interact hadronically with oxygen nuclei and the high cross-section does not allow long tracks; their Cherenkov rings are also less defined than the muon ones. Muon and pion events can be accompanied by secondary rings from the electrons produced in their decays. Energetic gamma rays can also be detected, as for instance the ones from π^0 decays, thanks to the rings produced by Compton-scattered or pair-produced electrons.

2.3.1 Background control

As part of the strategies to tackle backgrounds, only events originating at the centre of the ID are considered to be valid neutrino interactions. The materials of the walls of the tank, and particularly the glass of the PMTs, contain radioactive material, such as isotopes of thorium, uranium and potassium. These impurities can mimic a signal event in the MeV energy region, crucial for solar neutrino studies. The selection algorithm in most of the SK analyses simply discards any reconstructed event with the interaction vertex less than 200 cm away from the ID walls. This criterion defines a fiducial volume (FV) which is around 22.5 kt in water mass. The water used to fill the tank may also contain impurities that cause background events, among

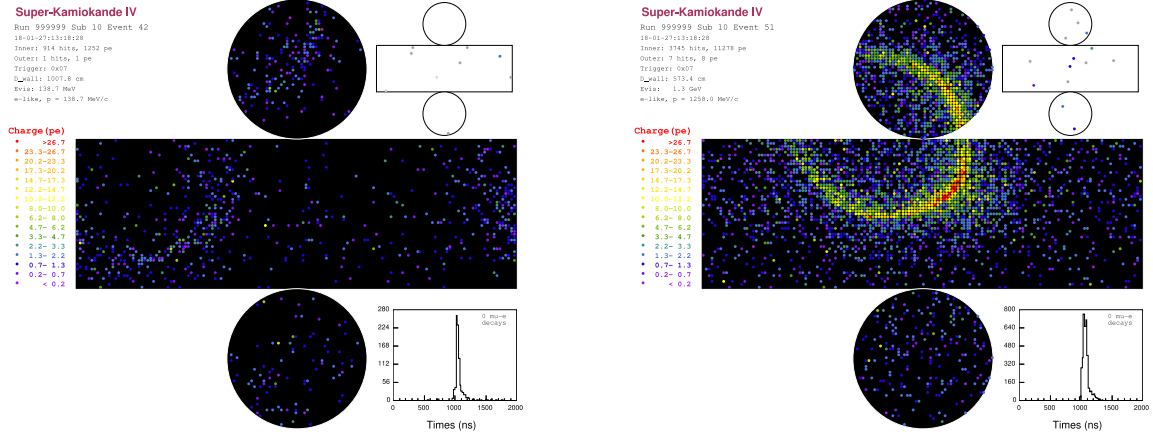


Figure 2.2: Reconstructed fully-contained events in the fiducial volume of Super-Kamiokande. Electron rings (left) are less defined than muon ones (right) because they are scattered more along their path. The developed cylinders on the top right of each figure show the outer detector hits. The histograms on the bottom right corners are the time distributions of the events.

which radon. Thus, the water in the tank is continuously filtered at a flow rate of 60 t/hour by a water purification system (see Section 2.3.2). An air purification system pumps radon-free air into the SK area inside the mine so that the amount of radon that dissolves into the water system is reduced. The level of contamination reached is usually less than 3 mBq/m³. As a comparison, unpurified air can peak at about 1200 Bq/m³. Thanks to these precautions and state-of-the-art electronics [77], the current energy threshold for SK is 3.5 MeV.

Super-Kamiokande has provided much evidence in the experimental understanding of neutrinos, be it originated in solar, atmospheric, or accelerator facilities. Despite the large exposure of the experiment and excellent background control, some studies are still curbed by statistical uncertainty and would benefit from simply collecting more data. Other searches, instead, suffer from irreducible background events, as for example the detection of Supernova Relic Neutrinos (SRNs), an incoherent background spectrum produced from all previous core-collapse supernova explosions in the Universe (see Section 1.3.1). The observation of SRNs would be of great importance for improving our knowledge on the population of core-collapse SNe and the rate of star formation. The average energies of these neutrinos are around a few tens of MeV, at which the largest cross-section corresponds to inverse beta decay (IBD, see Fig. 1.4.3). For energies between $14 \text{ MeV} < E_\nu < 30 \text{ MeV}$, this measurement is afflicted by nonrelativistic muons produced by atmospheric neutrinos which are below Cherenkov threshold and decay into electrons, known as *invisible muon decays* [78]. At lower energies, the dominant backgrounds between 10 MeV and 18 MeV are decays of muon-induced spallation products [79], and below 10 MeV interactions from reactor neutrinos. No SRN has been detected yet [66, 80], but theoretical predictions place the diffuse supernova neutrino background flux (DSNB, see Section 1.3.1) within a factor of four below the upper limit obtained by SK in 2003 [81, 82]. Even though a more recent and detailed analysis with increased efficiency, lower energy threshold, and expanded statistics revealed less stringent limits [80], neutron tagging capabilities could reduce the invisible muon background by a factor of five and remove the spallation background; this could lead to the detection of the DSNB for the first time [83].

Searches of galactic supernova bursts could also avail of an improved background suppression. SK will be exposed to a huge number of neutrino events if a core-collapse supernova occurs inside our galaxy. Such an event would provide not only an early warning system for other observatories, but also information about the neutrino spectrum, time profile, and information

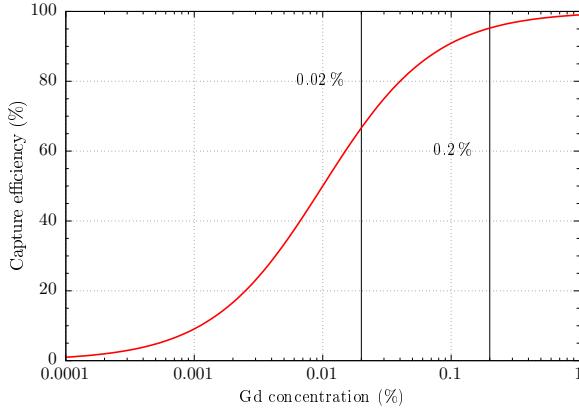


Figure 2.3: Estimated dependency of neutron capture efficiency on gadolinium with respect to the gadolinium concentration in water. Super-Kamiokande will start with a 0.02 % Gd-load, increasing up to 0.2 % to reach an expected ~ 90 % capture efficiency.

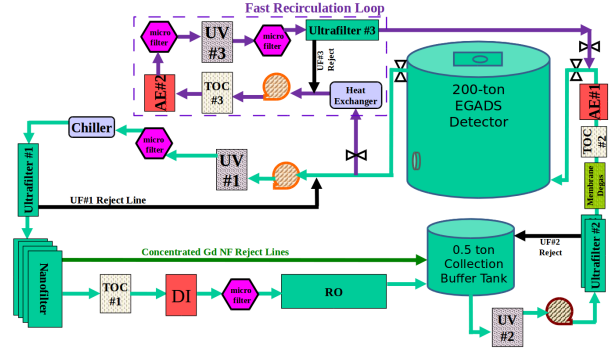


Figure 2.4: Schematic of the band-pass filtration system and the fast recirculation loop in EGADS, where the main components of the system are highlighted: anion-exchange resins (AE), ultraviolet lamp (UV), total organic compound lamp (TOC), deionising system (DI), reverse osmosis stage (RO). See text and Ref. [68] for details.

about early stages of the core-collapse process, like pre-supernova neutrinos from the silicon burning phase [84]. A sizeable amount of the neutrinos emitted are actually antineutrinos in the energies where the IBD cross-section dominates. Detecting the neutron in the final state is fundamental for distinguishing whether the incoming particle is a neutrino or an antineutrino. Improved neutron tagging also helps to understand atmospheric and accelerator neutrino interactions and final states. The possibility of separating neutrinos and antineutrinos can at least raise the data of antineutrino events. At energies $E_\nu > 1$ GeV, the number of CCQE interactions decreases and often additional neutrons from 2p-2h interactions or pions from baryon resonance are also released in the scattering process. The possibility of detecting such multiple nucleon emission can improve the purity of CCQE samples. Finally, neutron-induced background in proton decay searches can be reduced, since most channels do not require neutrons to appear in the final state.

2.3.2 The gadolinium phase of Super-Kamiokande

Gadolinium-157 has the highest thermal neutron capture cross-section amongst any stable nuclides. It is estimated to be 2.537×10^5 b and its natural abundance is around 15.65 %. Another isotope of gadolinium with similar abundance is ^{155}Gd , at 14.80 %, which also presents a very high neutron capture cross-section 6.074×10^4 b. Dissolving gadolinium compounds in water could therefore considerably increase the neutron capture probability, as proposed for the first time in Ref. [85]. Gd-doped water enhances the capture cross-section, with an effective cross-section of 49×10^3 b for a 0.2 % concentration, compared to pure water with ~ 0.3 b on a free proton. Upon capturing a neutron, the Gd nucleus emits three to four gamma rays having a total energy of about 8 MeV. Such energetic photons can produce Cherenkov light via Compton-scattering and therefore they can be reliably detected in a large detector volume. The neutron in gadolinium-loaded water thermalises more quickly than in just pure water, with a characteristic time of $\sim 30 \mu\text{s}$, and it can be captured by a Gd nucleus with an estimated efficiency of 90 % [85] for a 0.2 % Gd solution. The efficiency dependency on the concentration is shown in Fig. 2.3.

In the next phase of the Super-Kamiokande experiment, called SK-Gd, a gadolinium salt compound will be dissolved in the detector to improve the ability to identify neutrons. The gadolinium phase is supposed to start in late 2020. This will be possible thanks to extensive R&D performed by the EGADS experiment [68]. In Ref. [85], gadolinium trichloride GdCl_3 was proposed, but the current full-scale plan for SK and EGADS has settled on using gadolinium sulphate $\text{Gd}_2(\text{SO}_4)_3$. This choice was determined by a few requirements by which a Gd compound candidate must comply. In addition to the aforementioned salts, a third option could have been gadolinium nitrate $\text{Gd}(\text{NO}_3)_3$. The candidate compound must be water soluble, also in large amounts, but all of the three gadolinium salts easily dissolve in water. If used in very large quantities, as it will be for SK-Gd, the compound must be safe for the detectors components and it should be nontoxic. None of the above salts are toxic, but GdCl_3 is corrosive and not suitable for a full scale test. Soak tests in a Gd solution at 25°C showed that the rubber friction pads used to hold the inner detector PMTs are susceptible to the sulphate, even though they seem to be affected also by pure water. In over twenty years of operation of SK, the effect has never been noticed, meaning the filtration system removes the impurities from this material with great success. Taking into account the different scales between the detector and the test and that the typical temperature of the water in SK is around 13°C , the case was deemed not to be a potential problem. It is also necessary that the gadolinium solution maintains a high level of optical transparency, so that optical photons of Cherenkov radiation can propagate inside the tank without attenuation. The $\text{Gd}(\text{NO}_3)_3$ is opaque in the UV region of the electromagnetic spectrum, for wavelengths less than 350 nm, and this unfortunately is where a large fraction of Cherenkov light is detected by SK PMTs. This left $\text{Gd}_2(\text{SO}_4)_3$ as the only choice possible, having good transparency in the UV and optical regions.

The most challenging aspect of a gadolinium-loaded water Cherenkov detector is the filtration system. The SK water purification system produces ultra pure water, close to the theoretical maximum, with a resistivity around $18\text{ M}\Omega\cdot\text{cm}$. This high purity is achieved thanks to several filtration stages, including microfilters, ultrafilters discarding particles with a size less than $0.1\text{ }\mu\text{m}$, UV lamps for bacterial growth, reverse osmosis, vacuum and membrane degasifier, and anion-exchange resins. The current process, without modifications, would completely remove the dissolved gadolinium. Therefore, in order to keep good water quality and high transparency, it is necessary to adapt the purification system such that it can remove all impurities, ions included, except Gd^{3+} and its anionic partner $(\text{SO}_4)^{2-}$. A new filtration system, called “band-pass filtration system”, has been devised for EGADS and runs in parallel to the fast-recirculation loop [68]. The schematic is illustrated in Fig. 2.4. The water from the Cherenkov tank is first cleaned by microfilters and UV light. The Gd solution is then cooled down, as the sulphate dissolves better at lower temperatures before passing through an ultrafilter. At this stage, a series of nanofilters splits up the water line into Gd-enriched water and water with less than one part-per-million of gadolinium. The concentrated line goes directly back to a buffer collection tank, whereas the gadolinium-free line is first cleaned by deionisation and reverse osmosis. In the collection tank, dissolved air is removed by a membrane degasifier and resins are used for the final purification. After full loading up to a concentration of 0.2 % of Gd, the water transparency in EGADS is found to be within typical SK values thanks to the water filtration system which can maintain good water quality and minimise gadolinium losses.

The water system for the gadolinium phase of SK will be essentially a scaled version of the EGADS filtration system. During the first stage, a solution of 0.02 % in $\text{Gd}_2(\text{SO}_4)_3$ mass will be loaded in SK; it will be progressively increased up to 0.2 % after the first commissioning. When the experiment will be decommissioned in the future, the gadolinium will be extracted from the water system to avoid dispersing it in the environment. This process was also tested successfully by the EGADS experiment.

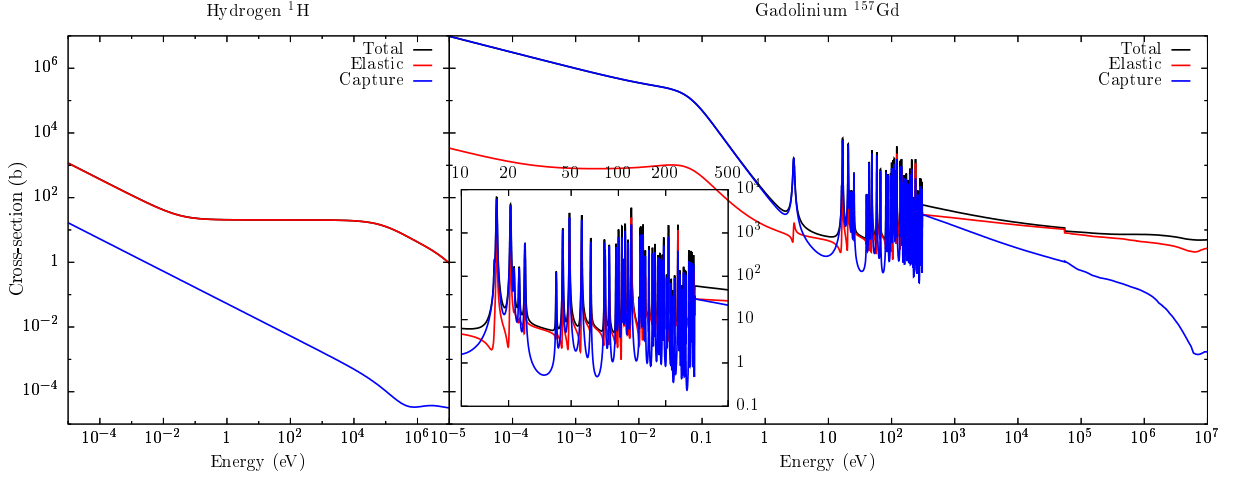


Figure 2.5: Neutron cross-sections on hydrogen (left) and gadolinium (right) as a function of energy from Ref. [86]. The dominant component for ^1H is elastic scattering, despite neutron capture reaches relative high cross-section values for subthermal neutrons ($T < 2.5\text{ meV}$). Fast neutrons interact on ^{157}Gd via elastic scattering, but for lower energies the main contribution comes from neutron capture cross-section. The $1/v$ dependency can be appreciated in both cases. The inset on the right plot shows a detail of the resonance region of the cross-section, between 10 eV and 500 eV.

2.4 Neutron calibration in Super-Kamiokande

From the considerations of Section 2.2, water is a good moderator for thermalising fast neutrons. Its energy decrease is $\xi_{\text{H}_2\text{O}} \simeq 0.93$, when the kinetic energy of the neutron is in the range $2.5\text{ meV} \lesssim T \lesssim 0.1\text{ MeV}$. Neutrons that reach subthermal energies enter the $1/v$ regions in which the capture probabilities increases as T^{-1} . Hydrogen presents a relative high cross-section for neutron capture, as it can be seen from Fig. 2.5: the cross-section for a thermal neutron on hydrogen is measured to be 332.6 mb [87]. The capture cross-section on oxygen ^{16}O is around 0.19 mb , four orders of magnitude smaller than the capture on hydrogen and therefore typically neglected. The hydrogen capture is followed by the emission of a single 2.2 MeV photon from the de-excitation of the newly-formed deuterium. The characteristic time for Maxwellian neutrons with energy below 10 MeV to thermalise and being captured by hydrogen in water has been measured to be $(204.8 \pm 0.4)\text{ }\mu\text{s}$ [88]. The typical time and energy of this event require special triggers and dedicated analysis in SK to correctly identify the neutron capture on hydrogen. Since the SK-IV phase, after any primary event above the standard higher energy threshold is detected, a time window of $535\text{ }\mu\text{s}$ is saved with no threshold requirement, so that approximately the 92 % of neutron capture signals are collected. The 2.2 MeV photon produces on average $7\sim 8$ PMT hits, which are difficult to reconstruct accurately. The PMT hits are expected to happen in a narrow timing distribution and to be anisotropic. A 10 ns sliding window is used to look for γ candidates with more than 7 hits and less than 50 to avoid high energy backgrounds. With these simple selection criteria, an efficiency of 33.2 % is obtained from a simulation of neutron capture events, with 4.5 background events expected per neutrino event. The background rejection is improved by feeding the simulated data of the selected candidates to a neural network, which retains an overall efficiency of 20.5 % with 0.018 backgrounds per signal event [89]. The efficiency is found to be highly dependent on the distance travelled by the released neutron due to the fact that knowing the location of the capture significantly reduces the background. A completely analogous search can be used for the gadolinium phase of SK, even though the energy released in the neutron capture process is above the detection threshold, the thermal lifetime is shorter,

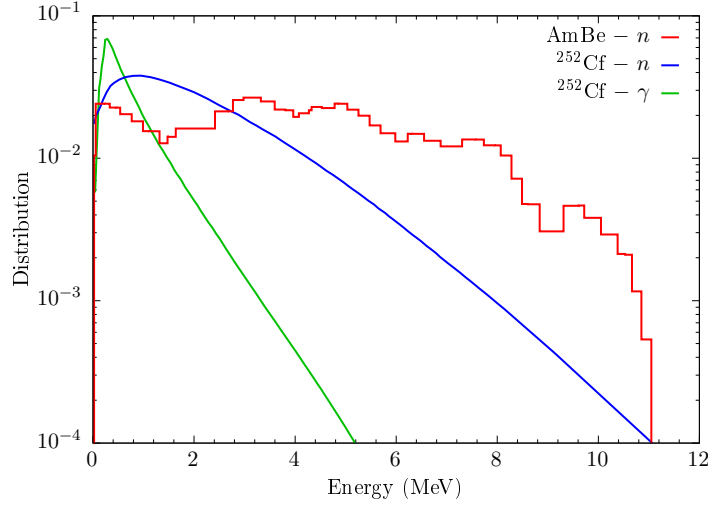


Figure 2.6: Normalised energy distribution of neutrons emitted by an Am-Be source [91] and neutrons and photons from the spontaneous fission of a ^{252}Cf source [92, 93]. The Am-Be emission is more uniform over the energy range, compared to ^{252}Cf which peaks at around 1 MeV.

and the expected efficiency is much higher as explained in Section 2.3.2.

Neutron tagging efficiency in SK is measured with americium-beryllium (Am-Be) [90]. In an Am-Be source, ^{241}Am decays 100 % of the time into ^{237}Np via α -emission, with a half-life of 432.6 y. The α particle is captured by a ^9Be nucleus to become $^{12}\text{C}^*$ with the emission of a neutron. The carbon de-excites to the ground state with sometimes the emission of a 4.43 MeV photon. This gamma is used to trigger the neutron emission. To maximise this trigger signal, the Am-Be source is placed at the centre of a 5 cm cube of bismuth germanite (BGO) crystal scintillator which is lowered inside the water Cherenkov tank during calibration runs. The gamma ray from the beryllium neutron capture is promptly absorbed by the BGO crystal, with the release of intense scintillation light that triggers the SK detector. Around thousand photoelectrons from the BGO emission are typically observed by the PMTs; this signal triggers the search for neutron capture on hydrogen. The candidates are selected by an analysis similar to the simulation of Ref. [89] and outlined above. Neutrons from beryllium have energies below 10 MeV, as seen in Fig. 2.6, less than the typical neutron energy resulting from atmospheric neutrino interactions. For this reason, in the calibration analysis the neutron capture vertex is assumed to be roughly at the same location of the Am-Be source. The efficiency measured in Ref. [90] ranges from 13.1 % to 24.5 %, the exact value of which is position dependent. These values agree overall with the simulation analysis.

Another possibility as neutron calibration source would be californium-252 which undergoes α -emissions (96.91%) or spontaneous fission (SF, 3.09%). Thanks to a shorter half-life of 2.645 y, a ^{252}Cf source presents a higher activity compared to an Am-Be source with the same number of nucleons. Furthermore, the SF process emits an average of 3.75 neutrons per fission and an average of 10.3 photons summing up to a total energy of 8.2 MeV [92]. As for the case of the Am-Be calibrating device, the photons can be collected by a scintillating material and tag the emission of neutrons. After the trigger signal, multiple neutron captures on hydrogen are expected, separated by short intervals in time of the order of milliseconds. The yield of multiple neutrons is an advantage which the SNO collaboration exploited with a method called *Time Series Analysis*. Multiplicity and time intervals between the detected events can be used to determine the neutron detection efficiency, the neutron mean life inside the detector, and the source activity from nonfission events [94]. Differently from the Am-Be source, the activity

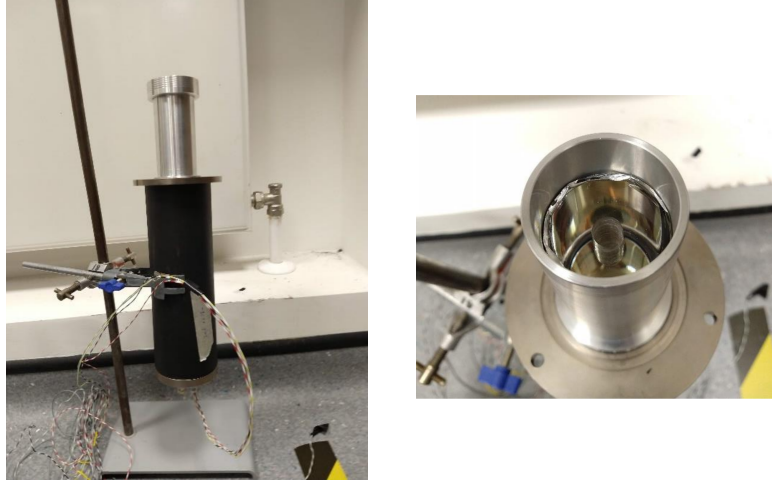


Figure 2.7: Setup used to test the californium source. The plastic scintillator cylinder is encased in an aluminium structure connected to the PMT support (black). The scintillator is optically coupled to the PMT.

of which must be known precisely, the neutron tagging calibration with a californium source can be done in principle regardless of that information. The Time Series Analysis could be implemented also in SK if californium was used as a calibrating source. The fast-neutron and photon energy spectra from ^{252}Cf are shown in Fig. 2.6. The neutrons are emitted with a most-probable energy of 1 MeV and an average energy of 2.1 MeV. Being the average energy of a SF neutron from ^{252}Cf lower than the one from Am-Be, it is reasonable to assume that the capture on hydrogen occurs in the proximity of the source. This would bring about an even more accurate calibration with the californium source, since the location of the capture is an important detail for the measurement of the neutron tagging efficiency.

Some preliminary studies were performed to develop a neutron calibration device with californium for a generic water Cherenkov detector. During laboratory measurements, a ^{252}Cf source with an activity of 4.3 kBq at the time of its production was used. The californium is encapsulated in a double-hull stainless steel cylinder, 9.5 mm in diameter and 37.5 mm high. The source is placed in a simple prototype of the device, shown in Fig. 2.7, consisting of a cylindrical plastic scintillator (EJ-200), coated with mylar to contain optical photons and optically coupled to an ET Enterprise 9902B series PMT. A hole, coaxial to the plastic cylinder, allows to insert the source in the middle of the scintillator which is 3" in length and 1.5" in diameter. The rate of photons emitted by the ^{252}Cf source is measured with this setup; the signal from the PMT is amplified and cleaned by NIM modules and finally recorded with a 14-bit VME digitiser. Without the source inside the scintillator, a dark rate of 1.633 Hz is measured, whereas with the source the rate increases to 41.395 Hz. The distributions of the PMT peaks collected by the digitiser are shown in Fig. 2.8. A predicted activity of 3.1 kBq is expected on the day of the measurement — 446 days after the production of the source — which translates to a SF rate of 96.46 Hz. The SF tagging efficiency with this setup is therefore estimated to be around 41 %.

A GEANT4 [95] simulation of the setup was performed with the aim of optimising the calibration instrument. An ideal device would absorb all the photons converting them into visible light without affecting the neutrons. The plot in Fig. 2.9 shows the correct implementation of the scintillator and PMT efficiencies in the simulation: there is good agreement between the MC distribution and the expected optical photon spectrum. Different volumes and materials are tested for the scintillator in the simulation. As far as materials are concerned, BGO crystal and

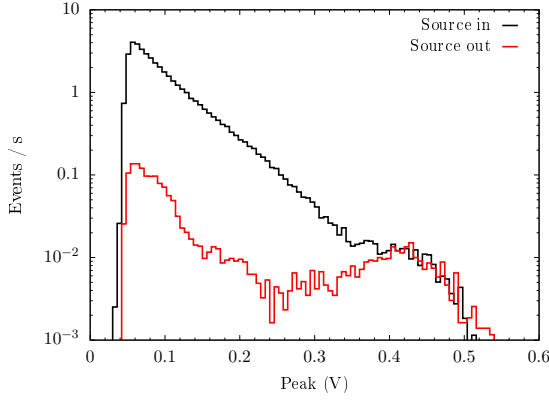


Figure 2.8: Distribution of PMT peaks measured with source inside (black) and source removed from the scintillator (red).

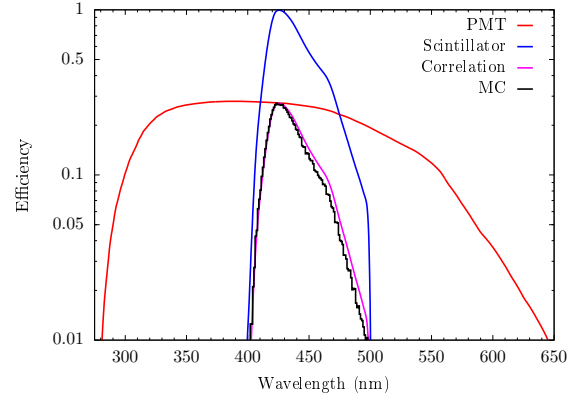


Figure 2.9: Distributions showing PMT quantum efficiency (red), the scintillator yield (blue), their correlation (magenta), and the photons collected by the PMT in the GEANT4 simulation of optical photons (black).

a generic vinyltoluene are chosen. The selected shapes for the volume are a cube and cylinders with a diameter-height-ratio 1:1 and 1:2. The latter shape models the prototype tested in the laboratory. The characteristic size, i.e. the side for the cube and the height for the cylinders, is varied from 1 cm to 40 cm. The simulation tracks the energy deposited in the scintillator by the photons and the number of neutrons escaping the device, from a simulation of 10 000 SF events. The results are shown in Fig. 2.10, where for both photons and neutrons the average value of the fraction of absorbed energy with respect to the initial one is plotted against the size. In terms of materials, the BGO crystal performs better than the plastic scintillator as expected, absorbing almost the entirety of photons and leaving the neutrons mainly unaffected. Apart from not being as efficient as scintillator, the hydrogen in the plastic thermalises the neutrons more than BGO. This would impact the capture time in a water Cherenkov detector. In terms of sizes and shapes, a BGO cube of 4 ~ 6 cm sides seems to maximise photon absorption and minimise the energy loss of neutrons. This is in line with the choice for the calibrating device for SK, which is a 5 cm BGO cube. Both the cylindrical shapes are optimal when the height is 7 ~ 11 cm, but more crystal would be required increasing the cost of the device. As far as the plastic scintillator is concerned, it is more difficult to define an optimal size/shape figure: a cubic scintillator is more efficient in collecting photons, but being the form with the largest volume per given size, it is also more effective in slowing down neutrons. The two cylinder shapes have similar performances, proportional to their volumes.

From the simulation studies, the current design used with the Am-Be source seems to be ideal even for ^{252}Cf . Simply replacing the neutron source in SK and adopting the Time Series Analysis could give a more accurate calibration. It is important to realise that the same calibrating procedure and device can be equally applied to the gadolinium phase of SK and Hyper-Kamiokande in the future. Further R&D is anyway needed to build an optimal device for neutron calibration with a californium source.

2.5 Monitoring gadolinium concentration

The concentration of Gd in water affects the efficiency and timing of neutron captures, which must be known for an accurate measurement of the antineutrino rate. It is therefore fundamental

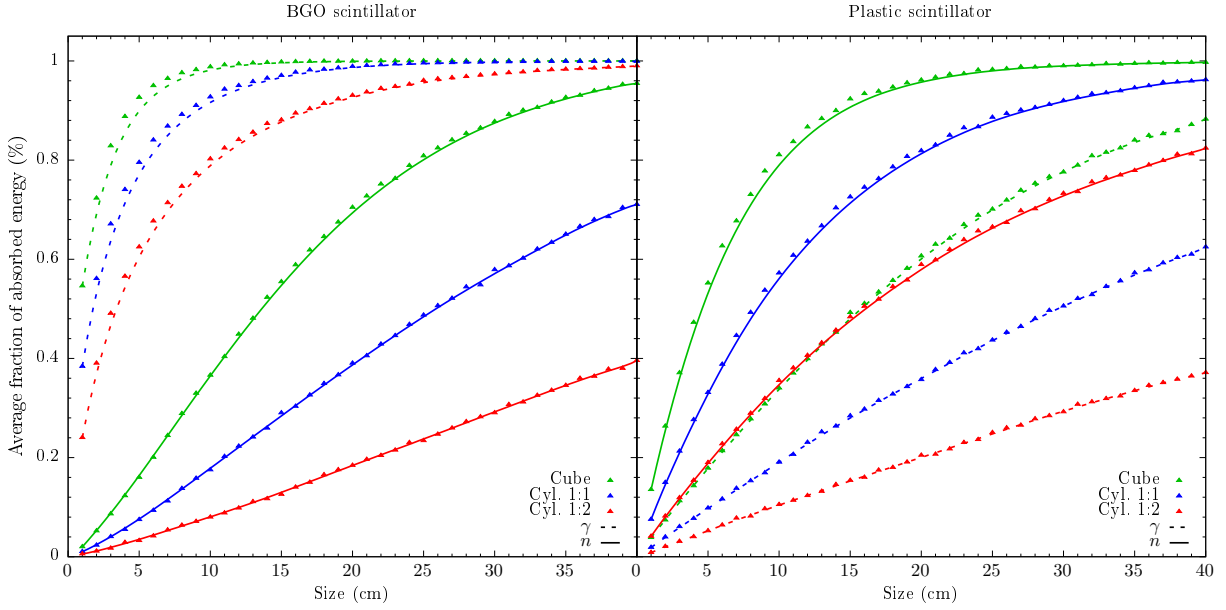


Figure 2.10: Result of the GEANT4 simulation (points), showing the expected performance of different scintillators as a function of the characteristic size. The lines are a smooth interpolation between simulation points. The fraction of absorbed energy per initial energy of neutrons (solid) and photons (dashed) is averaged and plotted against the scintillator size. Three shapes are tested: a cube (green), a cylinder with diameter-height-ratio of 1:1 (blue), and a cylinder with ratio 1:2 (red). On the left, the scintillating material is BGO crystal; on the right, a generic vinyltoluene plastic is used.

to measure the concentration regularly, as this can change in time inside the detector. On large scales, like for SK-Gd, predict the temperature and the flow dependency of the dissolved Gd is not a trivial task. Currently, the EGADS experiment keeps track of the Gd concentration with a Zeeman atomic absorption spectrometer (AAS), located near the site of the experiment. Water samples are collected monthly from the water tank, diluted and atomised inside the AAS machine. The amount of Gd is then compared to known samples of Gd loaded water to determine the concentration. This method reaches currently an accuracy of $\sim 3\%$.

An alternative method for monitoring gadolinium concentration is under study and proposed here. The new concept still uses atomic absorption lines of Gd, but in solution in water, allowing for a more frequent measurement. Gadolinium presents strong emission/absorption lines in the UV region [96]. Using a UV source and a spectrometer it is possible to measure the absorption by gadolinium dissolved in water. The absorbance is directly proportional to the amount of gadolinium and therefore to the concentration, where the absorbance is defined as

$$\mathcal{A}(x) = \log_{10} \frac{I_0(x)}{I_{\text{Gd}}(x)} . \quad (2.16)$$

The quantity I_0 is the intensity of a luminous source at a wavelength x filtering through a reference sample of pure water, whereas I_{Gd} is the intensity of the same source at the same wavelength for a gadolinium loaded water sample. The gadolinium absorption spectrum presents a series of lines in the region between 270 nm and 275 nm and the height of each peak is related to the Gd concentration, thanks to the exponential law

$$I_{\text{Gd}}(x) = I_0(x)e^{-\ell/\lambda} , \quad (2.17)$$

with λ the attenuation length and ℓ the length of the sample. For a fixed cross-section S and a fixed length, the attenuation length will decrease with the absolute quantity of Gd dissolved in

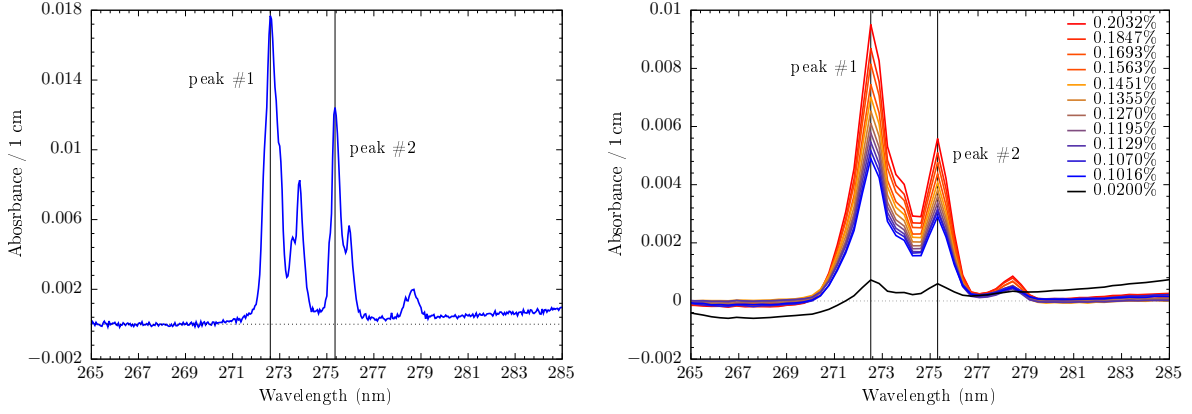


Figure 2.11: Gadolinium absorption spectra between 270 nm and 280 nm. On the left, the spectrum is taken with a high-resolution integrated spectrophotometer Shimadzu UV-2600, revealing numerous peaks in the region of interest for an aqueous solution of 0.2 % gadolinium sulphate. On the right, the spectrum is recorded with a fast spectrometer Ocean HDX, varying the concentration from 0.2 % down to 0.02 %: the height of the peaks scales linearly with the concentration. In both figures, the absorbance is normalised to the length of the sample.

the solution, m_{Gd} , or rather with the concentration ρ_{Gd} , since the volume is constant between the pure water and Gd-loaded water measurements:

$$\rho_{\text{Gd}} = \frac{m_{\text{Gd}}}{S \ell} . \quad (2.18)$$

The Beer-Lambert law relates the optical attenuation of a physical material, containing a single attenuating species of uniform concentration, to the optical path length via a material-specific constant [97]

$$\mathcal{A} = \varepsilon \ell \rho , \quad (2.19)$$

where ε is the molar attenuation coefficient, or *absorptivity* of the attenuating species. By comparing Eq. (2.19) with Eqs. (2.16) and (2.17), the attenuation length λ can be related to concentration and absorptivity as

$$\lambda = \frac{\log_{10}(e)}{\varepsilon \rho} . \quad (2.20)$$

The Beer-Lambert law agrees with the expectation of decreasing attenuation length with increasing concentration.

The concept of tracking gadolinium concentration in water using the absorbance spectrum was proven using a 10 cm cell, the measurements of which are reported in Fig. 2.11. The spectra were taken with a high-resolution spectrophotometer Shimadzu UV2600 and a fast spectrometer Ocean HDX. The Shimadzu spectrophotometer uses two grating systems to select very narrow windows of the electromagnetic spectrum both at the source and at the detection, which is performed by a photomultiplier. A deuterium lamp, integrated in the spectrometer, generates light at UV wavelengths. This machine can reach very high resolutions in wavelengths, however it scans over each wavelengths taking one measurement at the time and resulting in a slow process. The Ocean HDX spectrometer does not have an integrated UV source, but the grating system refracts the light input on a linear CCD, recording the whole electromagnetic spectrum simultaneously. The speed of the measurement with such a spectrometer is only limited by the integration time and reading rate of the CCD. A set of consecutive traces is taken and the error on the measurement is estimated by taking the mean. One of the advantage of the Ocean HDX spectrometer is that it can reach a very high light throughput thanks to a toroidal mirroring

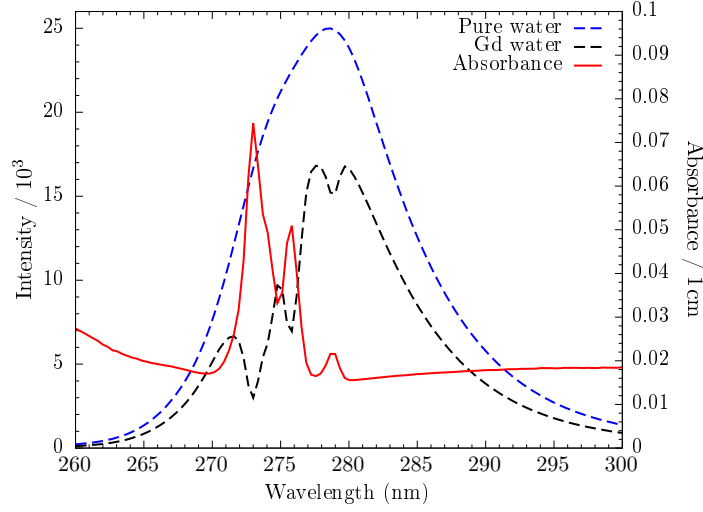


Figure 2.12: Gadolinium absorption measurement taken with the Ocean HDX spectrometer and a 10 cm water sample. The profile of the UV LED is shown when pure water (blue) and Gd-loaded water (black) are used. The absorbance (red) is then extracted from the two intensity measurement.

system which reduces stray light and maximises the dynamic range. These are the deciding factors for monitoring gadolinium concentration with this technique, in addition to the speed of the measurement. Wavelength resolution is not as important, because the relative position of the lines is sufficient to identify them and to compute the correct absorbance. A UV-LED, with emission centred at 275 nm, is used as an illuminating source. The profiles of the LED in pure water and in Gd solution are reported in Fig. 2.12, together with the resulting absorbance.

In an absorbance measurement, however, there could be other sources of absorption, since a light source and a photosensor are needed, in addition to optical interfaces with the sample to measure; the solvent of the sample can also contribute to the overall absorbance. The Beer-Lambert law can be generalised to describe a generic number of attenuating elements, as

$$\mathcal{A} = \sum_{i=0}^N \varepsilon_i \int_0^\ell dz \rho_i(x) = \ell \varepsilon_0 \rho_0 + \sum_{i=1}^N \varepsilon_i \int_0^\ell dz \rho_i(x) = a + b \rho_0, \quad (2.21)$$

where the attenuating species of interest, labelled “0”, has been isolated: if the other elements are constant, there is a linear law with measured absorbance and concentration. The absorbance will also depend on the purity of the solvent — water in this case — and other factors, such as the optical interfaces. It follows that absorption measurements taken with different setup cannot be compared unless the effect of other absorbing elements is well understood. Namely this would require to know the factors a and b of Eq. (2.21), and so calibration of the measurement apparatus is required. The absorption can also be biased by the presence of wavelength-independent factors, or at least independent in the region of the spectrum of interest. Examples of these factors are microbubbles or other impurities in the samples which can block or scatter the light, thus spoiling the measurement. An unbiased estimation of the absorbance can therefore be achieved by using two absorption lines and taking the difference of the peaks:

$$\Delta\mathcal{A} = \mathcal{A}(x_1) - \mathcal{A}(x_2) = \log_{10} \frac{I_0(x_1)}{I(x_1)} - \log_{10} \frac{I_0(x_2)}{I(x_2)}. \quad (2.22)$$

Any wavelength-independent effect is removed doing so. Supposing the true intensity of the reference sample is modified by a factor η and the intensity of the study sample is varied by a

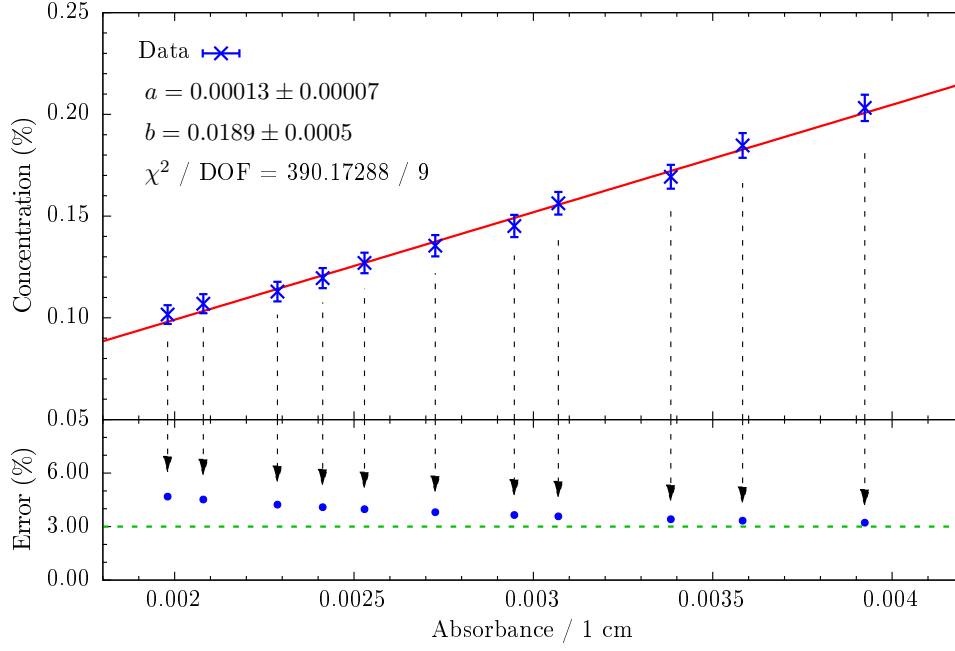


Figure 2.13: The inverse linear fit (red) between concentration and absorption for a 10 cm water sample is shown together with data (blue) on the top panel. The absolute values of the errors are roughly constant with the concentration, as it is mostly dominated by the uncertainties on the linear fit. The relative error (bottom panel) therefore increases with lower concentrations. The rightmost point corresponds to a 0.2 % concentration, the relative error of which is around 3 %.

factor ζ , the absorbance difference is

$$\Delta\mathcal{A} = \log_{10} \frac{\eta I_0(x_1)}{\zeta I(x_1)} - \log_{10} \frac{\eta I_0(x_2)}{\zeta I(x_2)} = \log_{10} \frac{I_0(x_1)}{I(x_1)} - \log_{10} \frac{I_0(x_2)}{I(x_2)}. \quad (2.23)$$

The drawback of this method is that two measurements are needed at the two wavelengths x_1 and x_2 : the error on the measurement will increase by a factor $\sim \sqrt{2}$.

In order to estimate the accuracy of the gadolinium concentration measurement, a prototype based on a 10 cm cell was tested, starting with a 0.2 % gadolinium sulphate concentration which is diluted down to achieve lower concentrations. At each known value of the concentration, the absorption is calculated by averaging one thousands spectra taken with the Gd-loaded water and the pure water samples. In this way, the error on the absorbance is defined as the standard error of the mean. Following Eq. (2.21), a linear interpolation is performed between the absorption peak differences, $\Delta\mathcal{A}$, and the concentrations, ρ_{Gb} ,

$$\Delta\mathcal{A} = a + b \rho_{\text{Gb}}. \quad (2.24)$$

The relation above is then inverted, such that uncertainties from the absorbance measurement can be propagated to the concentration value, as

$$\rho_{\text{Gb}} = \frac{\Delta\mathcal{A} - a}{b}. \quad (2.25)$$

The result of the fit is shown in Fig. 2.13, from which a relative error of $\sim 3\%$ is estimated on the measurement of the 0.2 % concentration. According to Fig. 2.3, this uncertainty translates to a $\sim 1\%$ error on the neutron capture efficiency. The method employing the 10 cm water sample performs similarly to the AAS spectrometry employed in EGADS.

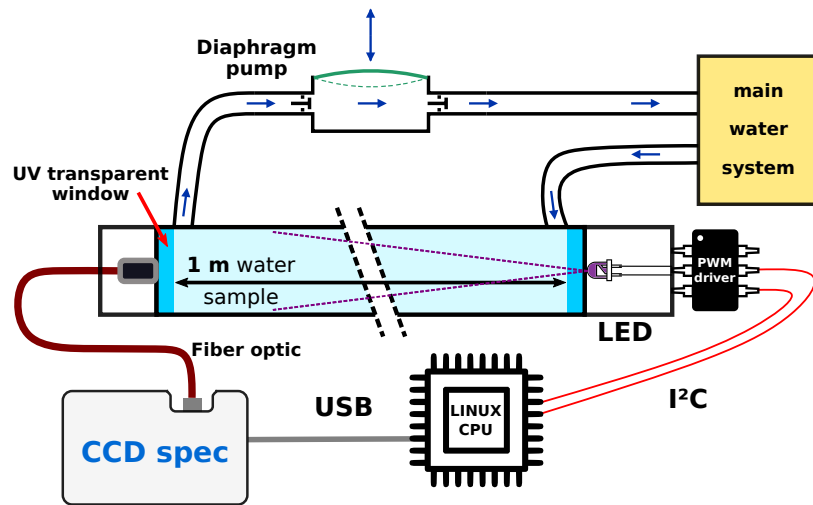


Figure 2.14: Schematic of the device used for testing the 100cm water sample in laboratory. The diaphragm pump circulates the water in the cell and interfaces the device with the main water system. During the test, the pump was leaving a considerable amount of microbubbles in the sample. Waiting 15 minutes between measurement was found to be sufficient to restore the intensity of the light at the spectrometer. The pump, however, might not be needed when the device will be installed in EGADS or SK as the pressure of the water system will be enough to circulate water and fill the 100cm cell. This scenario is favourable since the amount of undesired microbubbles is minimised and the measurement can be taken more frequently.

In the first stage of SK-Gd, a concentration of 0.02% gadolinium sulphate will be loaded and a good sensitivity on this low value is also required. To achieve better sensitivities, a longer water sample can be used to increase absorbance by gadolinium. The resolution should improve with the absolute quantity of Gd, or the sample length in this case, since more light is absorbed and the peaks become more distinct. Thanks to the high light throughput of the Ocean HDX spectrometer, the absorbance of a 100cm water sample was successfully studied. In order to deal with a larger water volume, an automated device was developed to fill the water sample, activate the LED and operate the spectrometer. The diaphragm pump used to circulate the water produced a considerable amount of microbubbles during measurements. It was found that letting the water settle for 15 minutes between measurement was sufficient to remove the majority of microbubbles and so clear the light path. A schematic of the prototype used in laboratory is shown in Fig. 2.14.

At this long scale, effects from optics, LED and spectrometer alignment, and water purity become important. As it can be seen from Fig. 2.15, measurements of the absorption at different concentration levels present a nonflat baseline that can bias the concentration estimation. A five-degree polynomial is employed to fit the baseline which is then removed in order to keep the measurement consistent over time. The same analysis of the 10cm water sample is performed on the 100cm measurement and the dependency of concentration on absorbance is reported in Fig. 2.16. The relative error on the measurement is improved tenfold compared to the 10cm test. For a concentration of 0.2% the error is estimated to be roughly 0.3%, whereas for a 0.02% concentration the error is at most around 1.5%. The calibration procedure, however, needs further investigation since the concentration seems to follow a quadratic law with the absorbance. Nonlinear effects might be originated from the optics, the alignment, or the LED temperature drift. It is expected that this behaviour should be lessened in the final prototype. This device will be eventually installed in EGADS before and SK-Gd later to monitor

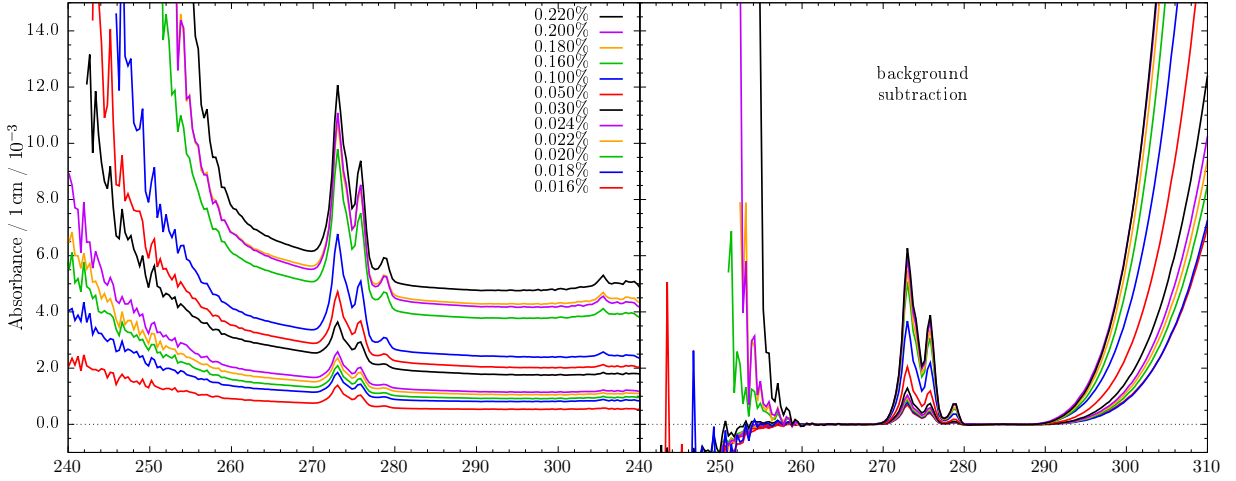


Figure 2.15: Gadolinium absorption lines (right) taken with the automated device on the 100 cm water sample. The baseline of the absorption spectrum appears to be changing with the concentration. This could be due to some contaminant in the Gd-enriched water, which is diluted with pure water at each step. The measurements are also taken at different times and drifts in the electronics or optics might be a concurrent cause. Removing the baseline with a polynomial fit (right) makes the absorption lines comparable.

the gadolinium concentration. Once connected to the water system of these experiments, the pressure of the water flow will be sufficient to fill the 100 cm water cell. This will vastly reduce the amount of microbubbles and allow for an almost continuous measurement. The water will be also more pure than the one used in laboratory testing, being continuously filtered. Overall, the 100 cm demonstrator proved that the absorption UV-spectroscopy technique successfully works with a better accuracy than the current technique AAS technique.

Summary

In this chapter, the upcoming Super-Kamiokande gadolinium phase was outlined, focusing on its advantages and main challenges. All of the current analysis will benefit from the improved neutron tagging efficiency, up to 90 % with a Gd concentration of 0.2 %. This is thanks to the smoking-gun signature of the neutron capture on gadolinium: a handful of photons with a total energy of about 8 MeV and a typical thermalisation time of $\sim 30 \mu\text{s}$. Up until now, the sensitivity of SK to neutron tagging has been assessed with a calibrating device consisting of an Am-Be source encased in a BGO crystal cube. Californium-252 has been investigated as an alternative neutron source, having a higher neutron activity and emitting multiple neutrons per fission events. With the help of a GEANT4 simulation, it was found that the same calibration device used in SK is already of the optimal shape and material to be used with ^{252}Cf instead. The Am-Be neutron source could then be replaced without further modifications of the device, bringing about a more precise neutron calibration. One of the challenges of a Gd-loaded Cherenkov detector is to monitor the gadolinium concentration in water, as this can vary in time or be affected by the water flow and temperature. A new method involving UV absorption spectroscopy is being developed with promising results which takes advantage of the strong Gadolinium absorption lines in the region between 270 nm and 275 nm. The Beer-Lambert law relates absorbance to gadolinium concentration and so the latter can be estimate by measuring the intensity of UV light through a water sample. The precision reached with this method on

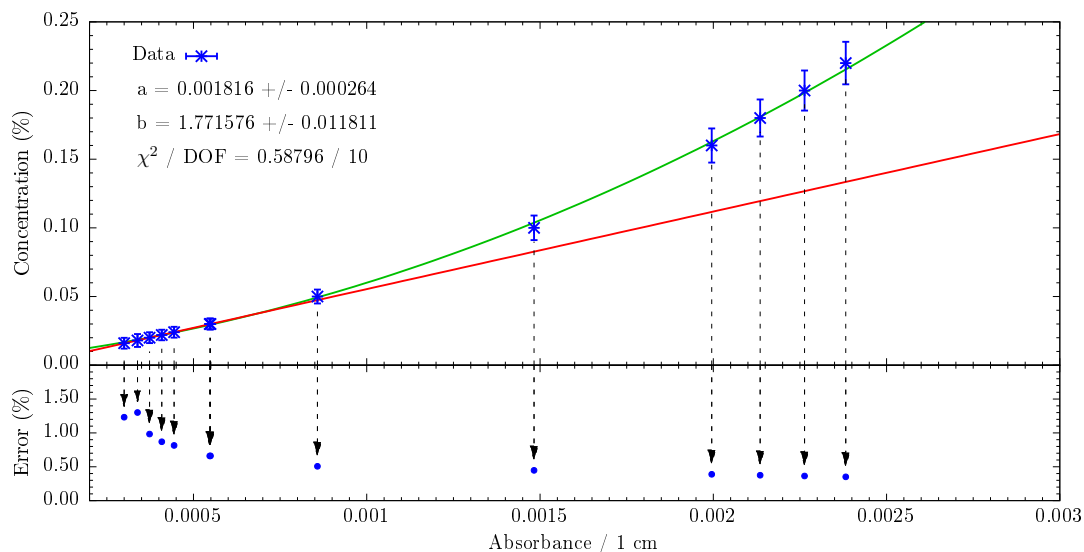


Figure 2.16: The inverse linear fit (red) between concentration and absorption is shown together with data (blue) on the top panel for the 100 cm water sample. The error bars on the top panel are enlarged by a factor of 20. The linear fit is done only with the six leftmost points, since the behaviour appears to be more quadratic (green) than linear. The relative error (bottom panel) is well below the 3 % limit, even for a concentration of 0.02 %.

a 100 cm water sample is around $\sim 0.3\%$ on the full load concentration of 0.2 %. Furthermore, this technique allows for an almost continuous monitoring of the concentration, compared to the current atomic spectroscopy technique in place which is executed with a monthly frequency.

Chapter 3

CP violation with the Hyper-Kamiokande experiment

C and CP violation are some of the conditions required in order to generate an asymmetry between matter and antimatter particles, the others being baryon number violation and interactions out of thermal equilibrium [8]. The amount of CP violation in the quark sector however is not enough to describe the observed baryon asymmetry within the SM [98]. A conceivable CP asymmetry in the lepton sector could be translated into baryogenesis via non-perturbative sphaleronic processes [99]. This mechanism, called *leptogenesis*, would be allowed by the addition of right-handed Majorana neutrinos to the SM which can violate lepton number. Furthermore, the extra fermions can justify light neutrino masses via a *seesaw mechanism* (see Section 4). This elegant solution to explain the baryon asymmetry is a strong motivation for searches of signals of CP violation in the lepton sector. As three generations of leptons exist, a complex phase entirely analogous to the one in the Cabibbo-Kobayashi-Maskawa (CKM) matrix is expected in the mixing matrix of leptons. The CKM matrix arises from mixing of quarks in charged-current interactions (see Eq. (1.38)), when describing the fermion fields in the mass basis. A similar matrix that describes neutrino mass states mixing exists in the lepton sector. It turns out that the best probe to discover CP violation is actually the study of neutrino oscillations, being a purely weak phenomenon in which CP-conjugate processes are well-defined. Current neutrino oscillation experiments are paving the way to the discovery of CP violation and it is foreseen that next-generation experiments such as Hyper-Kamiokande (HK) will determine the value of δ_{CP} , a milestone which requires precise measurements and a thorough understanding of the systematic errors.

In this chapter, a study of the sensitivity of the HK experiment to oscillation parameters is presented, with special emphasis on δ_{CP} . After a review of the theory and phenomenology of CP violation in neutrino oscillation in Section 3.1, the HK experiment is introduced in Section 3.2. A fitting framework which combines atmospheric and beam data samples is employed for the study. The methodology of the sensitivity studies is outlined in Section 3.3, together with the results from a validation test. Finally, the full sensitivity to CP violation with the nominal systematic model is reported in Section 3.4. Despite being very sophisticated, variations of the beam error model are considered since some systematic parameters are still not well understood and some early considerations are drawn at the of this chapter.

3.1 CP violation in neutrino oscillations

The Dirac Lagrangian is invariant under three fundamental transformations of the fermion fields, and these are charge conjugation C, parity P, and time reversal T. The spinor field ψ and $\bar{\psi}$ transform under charge conjugation as

$$\psi(x) \mapsto \psi^C(x) = \xi_C \mathcal{C} \bar{\psi}^T(x) \quad , \quad \bar{\psi}(x) \mapsto \bar{\psi}^C(x) = -\xi_C^* \psi^T(x) \mathcal{C}^\dagger \quad , \quad (3.1)$$

where \mathcal{C} is the charge conjugation operator. The application of the transformation twice returns the same initial field, so ξ_C must be a unitary phase, i.e. $|\xi_C|^2 = 1$. The parity transformation, instead, inverts spatial coordinates and acts on spinor fields as

$$\psi(x) \mapsto \psi^P(x') = \xi_P \gamma^0 \psi(x) \quad , \quad \bar{\psi}(x) \mapsto \bar{\psi}^P(x') = \xi_P^* \bar{\psi}(x) \gamma^0 \quad . \quad (3.2)$$

With two consecutive parity transformations the coordinate system is restored and therefore the unitary phase ξ_P is constrained to be ± 1 or $\pm i$. Vector and axial covariants, respectively $\bar{\psi}_a \gamma^\mu \psi_b$ and $\bar{\psi}_a \gamma^\mu \gamma^5 \psi_b$, transforms oppositely under charge conjugation and spatial inversion, unless $a = b$, and so the $V - A$ structure of weak interactions (see Eqs. (1.15) and (1.16)) violates C and P individually.

The combined transformation of charge conjugation and parity, referred to as CP transformation, is applied to the fields as

$$\psi(x) \mapsto \psi^{CP}(x) = -\xi_{CP} \mathcal{C} \psi^*(x) \quad , \quad \bar{\psi}(x) \mapsto \bar{\psi}^{CP}(x) = -\xi_{CP}^* \psi^T(x) \mathcal{C}^\dagger \gamma^0 \quad , \quad (3.3)$$

where the CP phase ξ_{CP} is also unitary. A CP transformation presents the same coefficient on vector and axial bilinear terms, which means that $V - A$ bilinears are in principle invariant under CP. The weak interactions of the SM are therefore CP-symmetric if the phase of the W boson is chosen accordingly. In the case of generation mixing, the invariance in the quark sector is obtained when

$$j_{CC, Q}^\mu W_\mu \mapsto \left(j_{CC, Q}^\mu W_\mu \right)^\dagger \Leftrightarrow -\xi_W \boldsymbol{\xi}_D V^T \boldsymbol{\xi}_U^\dagger = V^\dagger \quad , \quad (3.4)$$

where the CP phases for the quarks have been promoted into diagonal matrices $\boldsymbol{\xi}_{D,U}$, and V is the CKM matrix. The Lagrangian must be a real scalar, hence by conjugating the conditions in the equation above it follows that $\boldsymbol{\xi}_{D,U}^\dagger = \boldsymbol{\xi}_{D,U}^{-1}$ and that the diagonal matrices are unitary, or

$$\boldsymbol{\xi}_{D,U} = e^{i\xi_{\delta,v}} \quad , \quad (3.5)$$

where the indices δ and v refer respectively to down and up quarks. The condition for CP invariance now becomes

$$e^{i\xi_v} V_{v\delta} e^{-i\xi_\delta} = V_{v\delta}^* \quad . \quad (3.6)$$

This condition cannot be satisfied with an arbitrary choice of the CP phases for the quark fields if the mixing matrix is not real, or $V = V^*$.

It follows from the discussion above that if the mixing matrix presents one or more nonzero complex phases, the quark charged-current weak interactions break the CP symmetry of the SM Lagrangian. The violation of CP is indeed a known process in the quark sector of the standard model. It has been extensively observed [100–104], giving a clear evidence that the CKM matrix is complex. The symmetry is restored when considering the time reversal symmetry: consecutive transformation of C, P, and T leave invariant all possible covariant bilinears, in accordance with the *CPT theorem*.

The Pontecorvo–Maki–Nakagawa–Sakata (PMNS) matrix is usually parameterised as in Eq. (1.62) with the addition of two more phases if the neutrino is Majorana. The PMNS matrix relates flavour states $\alpha = e, \mu, \tau$ with mass eigenstates $i = 1, 2, 3$ as $|\nu_\alpha\rangle = \sum_i U_{\alpha i}^* |\nu_i\rangle$, from which the probability of flavour oscillation in vacuum can be derived (see Eq. (1.53)). The CP-conjugate of a neutrino with negative helicity is an antineutrino with positive helicity which, in terms of neutrino oscillations, means transforming the $\nu_\alpha \rightarrow \nu_\beta$ oscillation channel into the $\bar{\nu}_\alpha \rightarrow \bar{\nu}_\beta$ channel. The violation of CP in neutrino oscillation can be quantified by the asymmetry in oscillation probabilities between neutrinos and antineutrinos which in vacuum reads as

$$A_{\alpha\beta}^{\text{CP}} = P(\nu_\alpha \rightarrow \nu_\beta) - P(\bar{\nu}_\alpha \rightarrow \bar{\nu}_\beta) = 4 \sum_{i>j} \Im[U_{i\alpha}^* U_{\beta i} U_{\alpha j} U_{j\beta}^*] \sin\left(\frac{\Delta m_{ij}^2 L}{2E}\right). \quad (3.7)$$

The quartic product $U_{i\alpha}^* U_{\beta i} U_{\alpha j} U_{j\beta}^*$ is invariant under a reparameterisation of the mixing matrix being a physical observable and it is complex only if $\alpha \neq \beta$ and $i \neq j$. For this reason, CP violation can only be measured in “appearance” channels. The imaginary part of the quartic products is antisymmetric on the indices α, β and i, j . Starting from the unitarity of the mixing matrix, for example $U U^\dagger = 1$, the following relation holds:

$$\sum_{i=1}^3 U_{\alpha i} U_{\beta i}^* = \delta_{\alpha\beta}. \quad (3.8)$$

Multiplying it by $U_{\alpha j}^* U_{\beta j}$, the expression can be written as

$$|U_{\alpha j}|^2 |U_{\beta j}|^2 + \sum_{i \neq j} U_{\alpha i} U_{\beta j} U_{\beta i}^* U_{\alpha j}^* = \delta_{\alpha\beta} |U_{\alpha j}|^2. \quad (3.9)$$

Taking the imaginary part of left-hand and right-hand sides of the equation results into

$$\sum_{\alpha \neq \beta} \Im[U_{\alpha i} U_{\beta j} U_{\beta i}^* U_{\alpha j}^*] = 0. \quad (3.10)$$

The above condition together with the antisymmetry of the indices reveals that the quartic products are all equal up to a sign. This value is called *Jarlskog invariant*. Using the parametrisation of the PMNS matrix in Eq. 1.62, this invariant is usually expressed in terms of the mixing angles as [105]

$$J = \Im[U_{\mu 3} U_{e 2} U_{\mu 2}^* U_{e 3}^*] = \frac{1}{8} \cos \theta_{13} \sin(2\theta_{12}) \sin(2\theta_{13}) \sin(2\theta_{23}) \sin \delta_{\text{CP}}. \quad (3.11)$$

The main channel of interest for long baseline experiments (LBL) is the appearance channel $\nu_\mu \rightarrow \nu_e$. This is for two main reasons: the attainable flux in accelerator experiments is principally composed of muon neutrinos, and the achieved energies are not enough to produce τ leptons at the detection site. Putting together Eqs. (3.7) and (3.11), the asymmetry for this channel looks like

$$\mathcal{A}_{\mu e}^{\text{CP}} = 4 J [\sin \Delta_{12} - \sin \Delta_{13} + \sin \Delta_{23}], \quad (3.12)$$

where $\Delta_{ij} = \Delta m_{ij}^2 L / 4E$, even though the CP asymmetries for each channel are all equal up to a sign,

$$\mathcal{A}_{\mu e} = \mathcal{A}_{\tau \mu} = \mathcal{A}_{e \tau} = -\mathcal{A}_{e \mu} = -\mathcal{A}_{\mu \tau} = -\mathcal{A}_{\tau e}. \quad (3.13)$$

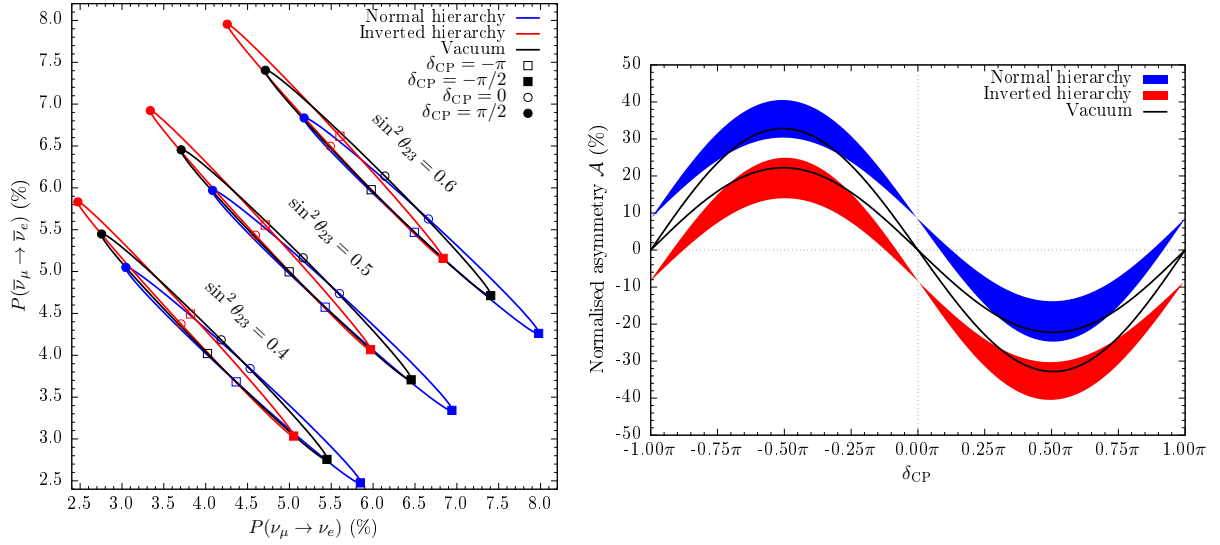


Figure 3.1: Effect of δ_{CP} on the oscillation probability. The oscillation probabilities for neutrinos and antineutrinos are plotted against each other (left), while the CP phase is varied between $-\pi$ and π . The effect of $\sin^2 \theta_{23}$ is also emphasised. The mass hierarchy has a nonnegligible behaviour only if matter oscillation is considered. The normalised asymmetry from Eq. 3.7 is shown on the right. When not specified, both graphs are created with the Design Report oscillation parameters (see Table 3.2). A neutrino energy of 0.6 GeV and a baseline of 295 km was used to calculate the oscillation probability.

Let us recall the hierarchy of the squared mass differences:

$$\Delta m_{\text{sol}}^2 = \Delta m_{21}^2 \ll \Delta m_{\text{atm}}^2 = |\Delta m_{31}^2|. \quad (3.14)$$

The typical energies and baselines of LBL experiments are such that

$$\frac{|\Delta m_{31}^2|}{2} \frac{L}{E} \sim \pi, \quad (3.15)$$

and so in this regime the atmospheric mass difference dominates, meaning that the oscillation probability in vacuum can be well-approximated by an effective two-flavour scenario

$$P(\nu_\alpha \rightarrow \nu_\beta) = \sin^2 2\theta_{\text{eff}} \sin^2 \left(\frac{\Delta m_{31}^2 L}{4E} \right), \quad (3.16)$$

for $\alpha \neq \beta$. As the mixing in the two-flavour limit can be expressed by means of a single angle, it follows that the effective mixing angle θ_{eff} is invariant under CP and so the effective asymmetry vanishes, $\mathcal{A}_{\alpha\beta}^{\text{eff}} = 0$. The data collected by LBL experiments to date does not provide sufficient statistics to be sensitive to the effects of Δm_{21}^2 and the measured neutrino–antineutrino asymmetries cannot be constrained, even though good significance was recently reached by the T2K experiment [106]. Remaining in the limit of Eq. (3.14), the evolution equation including matter effects receives helpful cancellations and it reads

$$i \frac{d}{dx} \begin{pmatrix} \psi_{\alpha 1} \\ \psi_{\alpha 2} \\ \psi_{\alpha 3} \end{pmatrix} = \frac{1}{2E} \begin{pmatrix} s_{13}^2 \Delta m_{31}^2 + A_{CC} & 0 & c_{13} s_{13} \Delta m_{31}^2 \\ 0 & 0 & 0 \\ c_{13} s_{13} \Delta m_{31}^2 & 0 & c_{13}^2 \Delta m_{31}^2 \end{pmatrix} \begin{pmatrix} \psi_{\alpha 1} \\ \psi_{\alpha 2} \\ \psi_{\alpha 3} \end{pmatrix}. \quad (3.17)$$

It is important to observe that the equation depends only on the mixing angle θ_{13} , but it is independent of δ_{CP} . If the experiment is only sensitive to Δm_{31}^2 , an effective two-neutrino mixing

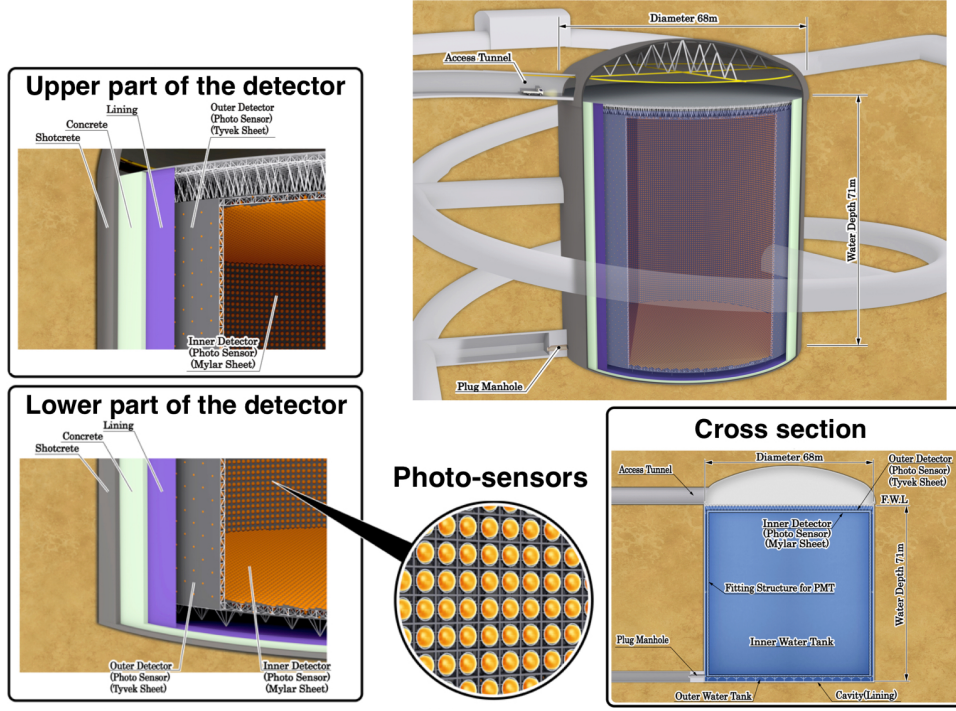


Figure 3.2: Cut-views of the Hyper-Kamiokande experiment.

is in place, even considering matter effects. However, the oscillation probabilities of neutrinos and antineutrinos in matter are not the same because the medium is not CP-invariant and so it induces CP violation in the oscillation probabilities via the matter potential A_{CC} . The effect of δ_{CP} and of matter effects on the asymmetry of Eq. (3.7) are visualised in two different fashions in Fig. 3.1: one graph shows the probabilities of neutrinos and antineutrinos against each other evidencing that these two are different for $\delta_{CP} \neq 0, \pm\pi$; the other figure shows the asymmetry as a function of δ_{CP} .

Given the parametrisation in Eq. 1.62, it is clear that the asymmetry is not measurable if the phase is trivial, *i.e.* $\delta_{CP} = 0$ or $\pm\pi$, or if θ_{13} is vanishing. From a model building point of view, however, a successful leptogenesis requires the parameters to satisfy $|\sin \theta_{13} \sin \delta_{CP}| \gtrsim 0.09$ when the Majorana phases are vanishing [107]. The value of θ_{13} has been measured to be nonzero [108–111] and for this reason it is expected that ongoing and future generation neutrino experiments will constrain the value of δ_{CP} .

3.2 Hyper-Kamiokande experiment

Hyper-Kamiokande (HK) [112] will be the next-generation water Cherenkov detector, studying neutrino interactions and searching for nucleon decays with the ring-imaging technique. The detector will be located in the Tochibora mine, under Mt. Nijugo in the Gifu Prefecture, Japan, just 8 km south from Super-Kamiokande. At this location, the rock overburden is equivalent to 1750 m.w.e. The design of HK is similar to the one of SK (see Section 2.3), with size being the biggest difference. A possible schematic of the detector is shown in Fig. 3.2. The cylindrical tank of HK will be 72 m high and 68 m in diameter, with a fiducial volume of 188.4 kton (total volume 257.8 kton), around 8.4 times the fiducial volume of SK. The photocoverage of the inner detector region will be 40 %, the same of SK, but it translates to roughly forty thousand

photomultipliers (PMTs). New 20" box and line PMTs will be employed, with improved charge and timing resolution, and an increased quantum efficiency which is almost twice as much that of the previous generation of PMTs. The new photosensors must also have a high pressure tolerance to be used at a depth of 60 m and more of water. A study for implementing multi PMT modules, each containing 23 3" PMT, is also being carried out. As SK, the new detector will have an outer detector which is just 1 m wide and instrumented with 3" PMTs. Thanks to incredible statistics and cutting edge resolutions, HK will be capable of a vast variety of physics studies, from accelerator and atmospheric neutrinos to solar and supernova neutrinos. Besides detecting proton decay, the main goal of HK is to measure δ_{CP} and constrain the other oscillation parameters with high precision. This is best achieved by studying accelerator neutrinos which allow a higher control of the experimental variables, and to this end the possibility of installing a second detector in Korea at the secondary oscillation peak is being investigated by the collaboration.

HK will be located 295 km away from the T2K target and at 2.5° off-axis with respect to the beamline. The neutrino beam is generated by a 30 GeV proton beam in the way described in Section 1.3.3. By selecting the direction of the horn's current, an almost pure muon neutrino (or antineutrino) beam is obtained, peaking at 600 MeV. The accelerator facility at J-PARC will undergo a planned upgrade to increase the beam power to 1.3 MW, before HK starts operation. The T2K near detector system, consisting of the detectors ND280 (2.5° off-axis) and INGRID (on-axis) [113], will be refurbished and a new near detector, called *Intermediate Water Cherenkov Detector*, possibly gadolinium-loaded, will be located around 1 km from the target. HK will take data for ten years, collecting a total of 2.7×10^{22} protons on target (POT), divided between ν and $\bar{\nu}$ beam modes. Studies have shown that CP violation discovery is not very sensitive to POT allocation between the two modes [112]. Assuming a POT ratio $\nu : \bar{\nu} = 1 : 3$ and CP conservation, the expected number of fully-contained events in the fiducial volume for the channels $\nu_\mu \rightarrow \nu_e$ and $\bar{\nu}_\mu \rightarrow \bar{\nu}_e$ are respectively 1643 and 15 in ν mode and 206 and 1183 in $\bar{\nu}$ mode. Deviations from these expected numbers could be an indication of CP violation. The project has been recently approved by the Japanese government and data taking is expected to start in 2027.

3.3 Sensitivity studies

At any stage of the experiment it is important to assess the impact of systematic errors on the total sensitivity of HK. Even if real data is not available, it is possible to understand whether the planned volume of data to be collected has enough constraining power to achieve the target precision. The oscillation and systematic parameters are input to a Monte Carlo simulation to build the expected distribution of events. This expected data is then compared to simulated "observed data", which is created by selecting a combination of oscillation parameters in order to mimic the real distributions of events that will be eventually collected. Scanning over the oscillation parameters, the resolution of HK to oscillation parameters and, more importantly, the influence of the systematic uncertainties can be studied. To this end, a fitting framework capable of performing a simultaneous study of beam and atmospheric samples was employed.

3.3.1 Event samples

For the study, SK atmospheric Monte Carlo (MC) data are adapted and scaled to HK fiducial volume in order to form the atmospheric sample. The events are then classified and binned into several two-dimensional histograms of $\log p$ and $\cos \vartheta$, where p and ϑ are respectively the momentum and the azimuthal angle of the reconstructed charged lepton. The histograms are

Table 3.1: The sample events for atmospheric data are used to build 2D distributions in $\log p$ and $\cos \theta$. The number of bins in each direction is listed and they sum up to 2224. The samples are categorised as fully-contained sub-GeV (FC sub-GeV), fully-contained multi-GeV (FC multi-GeV), partially-contained (PC) and upward-going muons (UP- μ).

Event type	Sample	Bins $\log p$	Bins $\cos \theta$
FC sub-GeV	one ring e -like and 0 decay- e	13	20
	one ring e -like and 1 decay- e	13	1
	one ring μ -like and 0 decay- e	13	20
	one ring μ -like and 1 decay- e	13	20
	one ring μ -like and 2 decay- e	13	1
	one ring π^0	13	1
	two rings π^0	5	1
FC multi-GeV	one ring e -like (ν_e)	10	20
	one ring e -like ($\bar{\nu}_e$)	10	20
	one ring μ -like	5	20
	multi ring e -like (ν_e)	8	20
	multi ring e -like ($\bar{\nu}_e$)	8	20
	multi ring μ -like	4	20
	multi ring other	10	20
PC	stopping	4	20
	through-going	5	20
UP-μ	stopping	4	20
	through-going, not showering	1	20
	through-going, showering	1	20

summarised in Table 3.1 where they are categorised as fully-contained (FC), partially-contained (PC), or upward-going muons (UP- μ) events [114]. There are a total of 2224 bins employed for the atmospheric sample.

The beam sample is instead created using a far detector flux prediction which is explained in Section 3.3.4. From the flux prediction, fully-contained candidate events in the fiducial volume are grouped as appearance signals, i.e. $\nu_\mu \rightarrow \nu_e$ and $\bar{\nu}_\mu \rightarrow \bar{\nu}_e$, and background events from disappearance channels. Signal and background distributions in true energy (98 bins) undergo event selection criteria to obtain the distributions in reconstructed energy (87 bins) for the four event samples: one ring e -like in ν -mode; one ring μ -like in ν -mode; one ring e -like in $\bar{\nu}$ -mode; one ring μ -like in $\bar{\nu}$ -mode. A set of 2D smearing matrices, produced by the T2K fitting framework VALOR [115], simulates and replaces the correct event selection process, including tuning of the flux with near detector constraints. These smearing matrices are provided for all samples, acting on signal (CCQE and CCnQE) and background (CCQE, CCnQE, and NC) distributions. The one ring e -like with one electron decay sample, included in T2K analyses, is not considered in this study.

3.3.2 Oscillation space

Both the atmospheric and beam distributions are weighted by the corresponding oscillation probabilities. The oscillation parameters are scanned over the space defined by the four variables

$$\Delta m_{32}^2 \times \sin^2 2\theta_{13} \times \sin^2 \theta_{23} \times \delta_{\text{CP}} \quad (3.18)$$

Table 3.2: The oscillation parameter sets used in this thesis are shown here. The reference set “Design” is taken from the HK design report [112]. The sensitivity studies are carried out in a parameters space built around “Asimov A”, the nominal T2K best fit point [116]. It spans over the four parameters Δm_{23}^2 , $\sin^2 2\theta_{13}$, $\sin^2 \theta_{23}$, and δ_{CP} , whereas Δm_{12} and $\sin^2 2\theta_{12}$ are fixed. The range and number of points scanned are reported in the last two columns.

Parameter	Design	Asimov A	Range	Points
$\Delta m_{12}^2/10^{-5} \text{ eV}^2$	7.60	7.53	–	fixed
$\sin^2 2\theta_{12}$	0.8704	0.8463	–	fixed
$\Delta m_{23}^2/10^{-3} \text{ eV}^2$	2.4	2.509	[2.464:2.554]	13
$\sin^2 2\theta_{13}$	0.1	0.085	[0.070:0.100]	13
$\sin^2 \theta_{23}$	0.5	0.528	[0.426:0.579]	19
δ_{CP}	0	$-\pi/2$	$[-\pi:\pi]$	61

on a grid of respectively $13 \times 13 \times 19 \times 61$ points. The solar squared mass difference and the solar angle θ_{12} are fixed. Apart from δ_{CP} which is scanned over all possible values, the intervals for the other parameters are built around “Asimov A”, the best fit point used by T2K for Asimov and fake data studies [116]. The details of the oscillation space are listed in Table 3.2. For the atmospheric squared mass difference and $\sin^2 2\theta_{13}$, the range is chosen such that it covers a $[-3\sigma, +3\sigma]$ interval, where σ is the error from the Asimov A set; the range for $\sin^2 \theta_{23}$ spans over $[-6\sigma, +3\sigma]$ so that both octants are covered symmetrically. At each point of this space, the event distributions are weighted with the correct oscillation probability for appearance or disappearance channels. The Asimov A point is chosen to be the *true* combination of oscillation parameters to perform sensitivity studies using a χ^2 -test statistic. It is possible to define the exclusion regions for CP conservation by changing the *true* value of the CP phase and by comparing the χ^2 at any value of δ_{CP} with the χ^2 computed at the null hypothesis, i.e. CP conservation or $\delta_{\text{CP}} = 0, \pm\pi$. The exclusion sensitivity as a function of *true* δ_{CP} is quantified by

$$\sigma = \sqrt{\min_{\delta_{\text{CP}}=0, \pm\pi} \chi^2 - \chi_{\text{true}}^2} , \quad (3.19)$$

where χ_{true}^2 is evaluated at the *true* point and matches the best fit value. The normal hierarchy is assumed to be known, except where stated.

3.3.3 Test statistic

Let us define the likelihood

$$\mathfrak{L}(E_n, O_n) = \prod_n \frac{e^{-E_n} E_n^{O_n}}{O_n!} , \quad (3.20)$$

where O_n and E_n are respectively the number of observed and expected events in the n -th bin, which are built using a specific combination of oscillation parameters

$$\Theta \equiv (\Delta m_{32}^2, \sin^2 2\theta_{13}, \sin^2 \theta_{23}, \delta_{\text{CP}}) . \quad (3.21)$$

The expected events are defined by a prediction at the far detector weighted by the oscillation probabilities for parameters Θ , and since there is no real data yet the “observed” events are also given by a prediction weighted with the *true* oscillation point, Θ_{true} . The χ^2 is hence the following log-likelihood ratio

$$\chi^2(\Theta) = -2 \log \left[\frac{\mathfrak{L}(E_n, O_n)}{\mathfrak{L}(O_n, O_n)} \right] = 2 \sum_n \left[E_n - O_n + O_n \log \left(\frac{O_n}{E_n} \right) \right] , \quad (3.22)$$

which is modified according to the “pull approach” χ^2 [117]: the parameters $\boldsymbol{\varepsilon} = \{\varepsilon_j\}$ are introduced to account for systematic uncertainties by replacing

$$E_n \longrightarrow E_n \left(1 + \sum_j f_j^n \varepsilon_j\right), \quad (3.23)$$

where the index j runs over the systematic parameters. A penalty term that includes variances and covariances of such parameters is added to the likelihood, using the inverse of the correlation matrix of the systematic errors, ρ^{-1} . With all these adjustments included, the χ^2 becomes

$$\chi^2(\Theta; \boldsymbol{\varepsilon}) = 2 \sum_n \left[E_n (1 + \sum_j f_j^n \varepsilon_j) - O_n + O_n \log \left(\frac{O_n}{E_n (1 + \sum_j f_j^n \varepsilon_j)} \right) \right] + \sum_{ij} \varepsilon_i \rho_{ij}^{-1} \varepsilon_j. \quad (3.24)$$

The effect of the systematic uncertainties on the event distributions are embedded in the f_j^n parameters, defined as the fractional change induced on the n -th bin by a 1σ variation of the j -th systematic. The amount of change is therefore parameterised by the ε_j variables in units of the uncertainty σ_j . However, being ρ the correlation matrix, the ε_j are promoted to embody the systematic uncertainties. Once the observed sample is defined, the oscillation parameters Θ are scanned over the oscillation space defined in Table 3.2 to estimate the expected events; finally, the χ^2 is profiled with respect to the parameters $\boldsymbol{\varepsilon}$:

$$\chi^2(\Theta) = \min_{\boldsymbol{\varepsilon}} \left[\chi^2(\Theta; \boldsymbol{\varepsilon}) \right]. \quad (3.25)$$

Fixing the combination Θ and dropping it from the notation, the minimisation of the χ^2 leads to the following set of j nonlinear equations

$$\frac{\partial \chi^2}{\partial \varepsilon_j}(\boldsymbol{\varepsilon}) = 0 \quad (3.26)$$

which can be solved iteratively if the condition $\sum_j f_j^n \varepsilon_j < 1$ holds. The system can then be solved with the Gauss-Newton’s method by finding the Hessian of the χ^2 . This gives a linear system, which can be solved iteratively until convergence on ε_j is achieved:

$$\frac{\partial^2 \chi^2(\boldsymbol{\varepsilon}^{(n)})}{\partial \varepsilon_k \partial \varepsilon_j} \cdot \left(\varepsilon_j^{(n+1)} - \varepsilon_j^{(n)} \right) = - \frac{\partial \chi^2(\boldsymbol{\varepsilon}^{(n)})}{\partial \varepsilon_k}, \quad (3.27)$$

with (n) the iteration index. The Gauss-Newton’s algorithm can sometimes be unstable, especially with a large number of parameters, due to its fast convergence. The algorithm is typically improved by adopting the Lavenberg-Marquardt method [118, 119] which modifies the Hessian and the equations become

$$\left[\frac{\partial^2 \chi^2(\boldsymbol{\varepsilon}^{(n)})}{\partial \varepsilon_k \partial \varepsilon_j} + \lambda \max \left(\text{diag} \frac{\partial^2 \chi^2(\boldsymbol{\varepsilon}^{(n)})}{\partial \varepsilon_k \partial \varepsilon_j} \right) \mathbb{1} \right] \cdot \left(\varepsilon_j^{(n+1)} - \varepsilon_j^{(n)} \right) = - \frac{\partial \chi^2(\boldsymbol{\varepsilon}^{(n)})}{\partial \varepsilon_k}. \quad (3.28)$$

The parameter λ is chosen dynamically: if the cost function χ^2 decreases after an iteration step, then λ is reduced; otherwise λ is increased and the step recomputed. In the limit $\lambda \rightarrow 0$, the algorithm approximates the Gauss-Newton’s method and its fast convergence. When λ is large, the linear system resembles a gradient descent with small steps of the order of λ^{-1} , but with a more stable convergence. A “delayed-gratification scheme” is adopted for λ [120], using

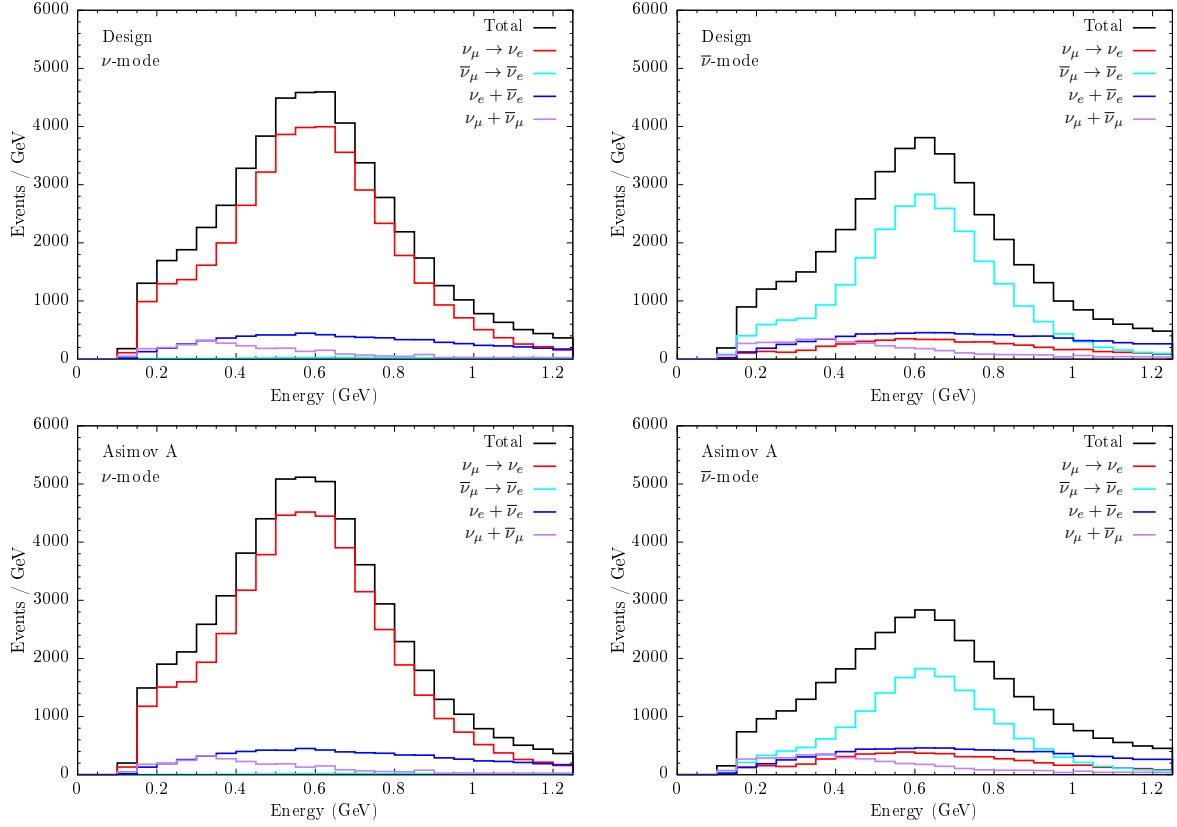


Figure 3.3: The predicted distribution of one ring e -like events with respect to reconstructed energy at HK are shown here for ν -mode (left) and $\bar{\nu}$ -mode. The appearance signals $\nu_\mu \rightarrow \nu_e$ and $\bar{\nu}_\mu \rightarrow \bar{\nu}_e$ are compared to the background events. The spectra on the top and bottom panel are generated using respectively the Design Report and the Asimov A oscillation parameters (see Table 3.2).

an initial value of $\lambda^{(0)} = 1$ and finding an optimal increment and decrement of respectively $\lambda^{(n+1)} = 5 \lambda^{(n)}$ and $\lambda^{(n+1)} = \lambda^{(n)}/10$.

To account for future constraints from other experiments, a Gaussian penalty term is added to the minimised value of χ^2 from Eq. (3.25)

$$\chi_{\text{penalty}}^2 = \frac{(\Theta - \hat{\Theta})^2}{\sigma_{\Theta}^2}. \quad (3.29)$$

In this analysis, only a penalty on the parameter θ_{13} is considered, which is predicted to be constrained to $\sigma(\sin^2 2\theta_{13}) = 0.005$ by future measurements of reactor experiments.

For most of the systematic parameters, a linear response is assumed in the MC. This means that varying the j -th systematic by a known amount, $\beta_j \rightarrow \beta_j + \varepsilon_j \sigma_j$ the number of expected events changes accordingly:

$$\beta_j \xrightarrow{\text{MC}} E_n \quad \implies \quad \beta_j + \varepsilon_j \sigma_j \xrightarrow{\text{MC}} E_n(1 + \varepsilon_j f_n^j). \quad (3.30)$$

Certain systematic uncertainties, such as the CCQE axial-mass scaling factor, the Fermi momentum for ^{16}O , or some of the RPA coefficients, do not present a linear behaviour for small values of ε and they are better described by a four-point linear interpolation of different f_j^n histograms, computed at $\pm 1\sigma$ and $\pm 3\sigma$ variations of the systematic parameter.

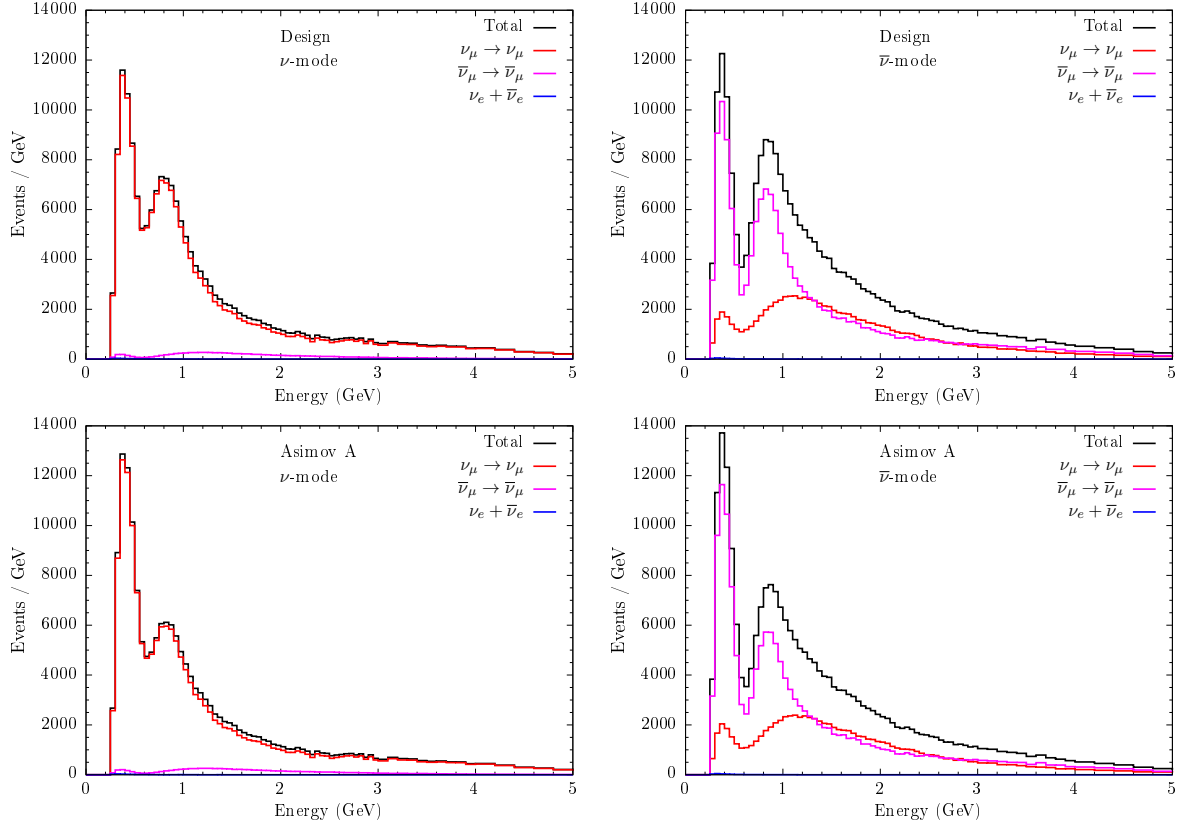


Figure 3.4: The predicted distribution of one ring μ -like events with respect to reconstructed energy at HK are shown here for ν -mode (left) and $\bar{\nu}$ -mode. The disappearance events $\nu_\mu \rightarrow \nu_\mu$ and $\bar{\nu}_\mu \rightarrow \bar{\nu}_\mu$ are compared to the small contributions from electron neutrinos. The spectra on the top and bottom panel are generated using respectively the Design Report and the Asimov A oscillation parameters (see Table 3.2).

3.3.4 Far detector prediction

The simulation of the HK detector heavily relies on the techniques established by the SK and T2K collaborations. Neutrinos interactions are generated using NEUT [65], also employed in SK and T2K. The response of the detector is simulated using the SK-IV full Monte Carlo simulation, which uses the GEANT3 [121]. Events are reconstructed with the SK reconstruction software, which gives a realistic estimate of the HK performance. The criteria to select neutrino candidates in MC simulations follows a similar prescription to the one used in SK. Only fully contained events within the inner detector are considered, provided that the reconstructed vertex is more than 1.5m away from the ID walls (fiducial volume) and that the collected charge from the PMTs, E_{vis} , amounts to an energy greater than 30 MeV. The purity of the data sample is controlled by requiring the detection of a single Cherenkov ring. In this way, the chance of selecting only CCQE events is enhanced. The neutrino energy is reconstructed from the energy of the final-state charged lepton and the angle between the neutrino beam and the charged lepton direction, applying Eq. (1.149). Electron-flavour events are selected by requiring an e -like ring, deposited energy in the range $100 \text{ MeV} < E_{\text{vis}} < 1.25 \text{ GeV}$, and no decay electron associated to the event, typical of a muon decay. The muon sample is built by requiring a μ -like ring, a reconstructed muon momentum greater than 200 MeV and the presence of the electron from the Michel decay of the muon. The simulation is run assuming an

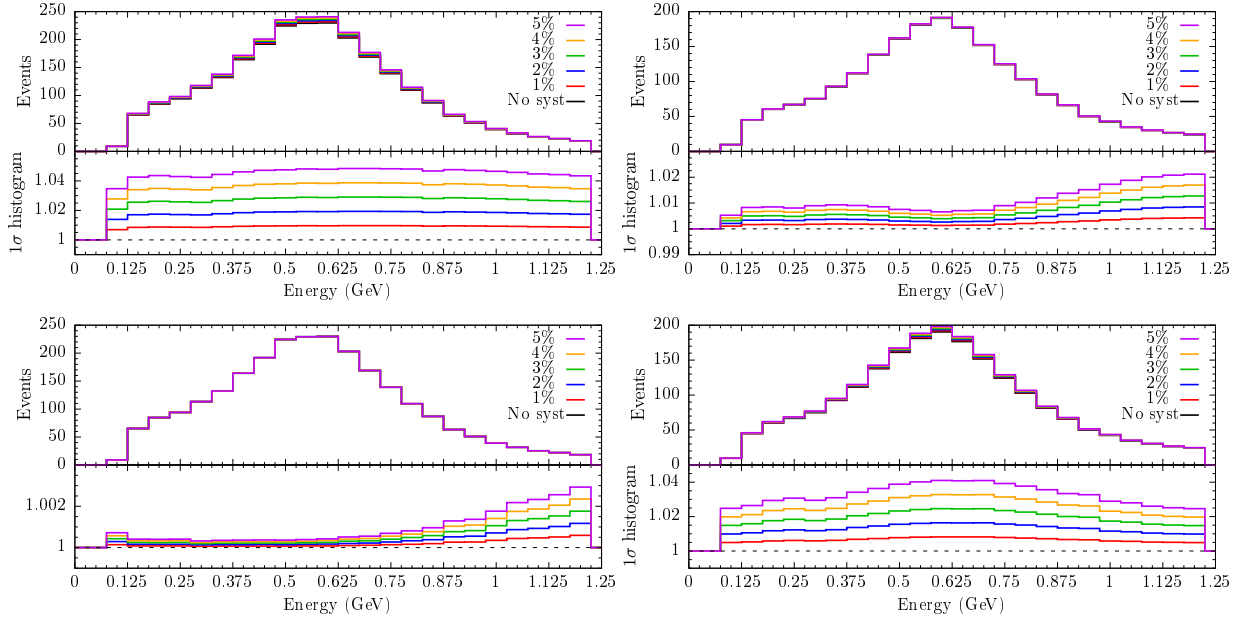


Figure 3.5: Predictions of events at the far detector for the one ring e -like sample in ν -mode (left) and $\bar{\nu}$ -mode (right), where the ν_e (top) and $\bar{\nu}_e$ (bottom) CC cross-section systematics are applied with relative errors between 1 % and 5 % at 1σ . In each figure, the top panel shows how the event distribution is affected, and the bottom panel shows the variations with respect to the prediction without errors applied, which is by definition one plus the 1σ histogram of the error, or $1 + f^n$ (see Eq. (3.23)).

integrated beam power of 13 MW, corresponding to 2.7×10^{22} POT collected over 10 years with a 30 GeV proton beam. The proportion between the amount of data collected in neutrino and antineutrino modes is set to $\nu : \bar{\nu} = 1 : 3$. The ratio is chosen in order to have similar number of events in the ν - and $\bar{\nu}$ -mode samples. The reconstructed spectra from the simulations are shown in Figs. 3.3 and 3.4 where two different oscillation parameter combinations are compared to illustrate the effect of neutrino oscillation; the contributions from different oscillation channels to the overall distributions are also highlighted.

3.3.5 Validation of the fitter

Before employing the full systematic model, the fitting framework is validated with a special systematic set for the beam sample. It is composed of just two systematics: the ν_e and the $\bar{\nu}_e$ CC cross-section uncertainties. These two errors are implemented twice, either as correlated or as anticorrelated, and they are tested at different values (1%, 2%, 3%, 4%, and 5%) for a total of ten combinations. The correlation matrices used are simply

$$\rho = \begin{pmatrix} 1 & 1 \\ 1 & 1 \end{pmatrix} \quad \text{and} \quad \rho = \begin{pmatrix} 1 & -1 \\ -1 & 1 \end{pmatrix}, \quad (3.31)$$

but they are both singular and not invertible. A small offset of 10^{-5} is added to off-diagonal terms to allow the calculation of the χ^2 . Due to the definition of the χ^2 in Eq. (3.24), the difference between fits with the same relative error lies in the correlation matrix, whereas at fixed correlation the effect of the systematics on the likelihood is given by the 1σ histograms.

In Fig. 3.5, the event distributions of the one ring e -like samples (previously presented in Fig. 3.3) are shown with the ν_e and the $\bar{\nu}_e$ CC cross-section uncertainties applied at 1σ for each of the five magnitude levels. It can be seen that the effect of the systematic errors is linear with

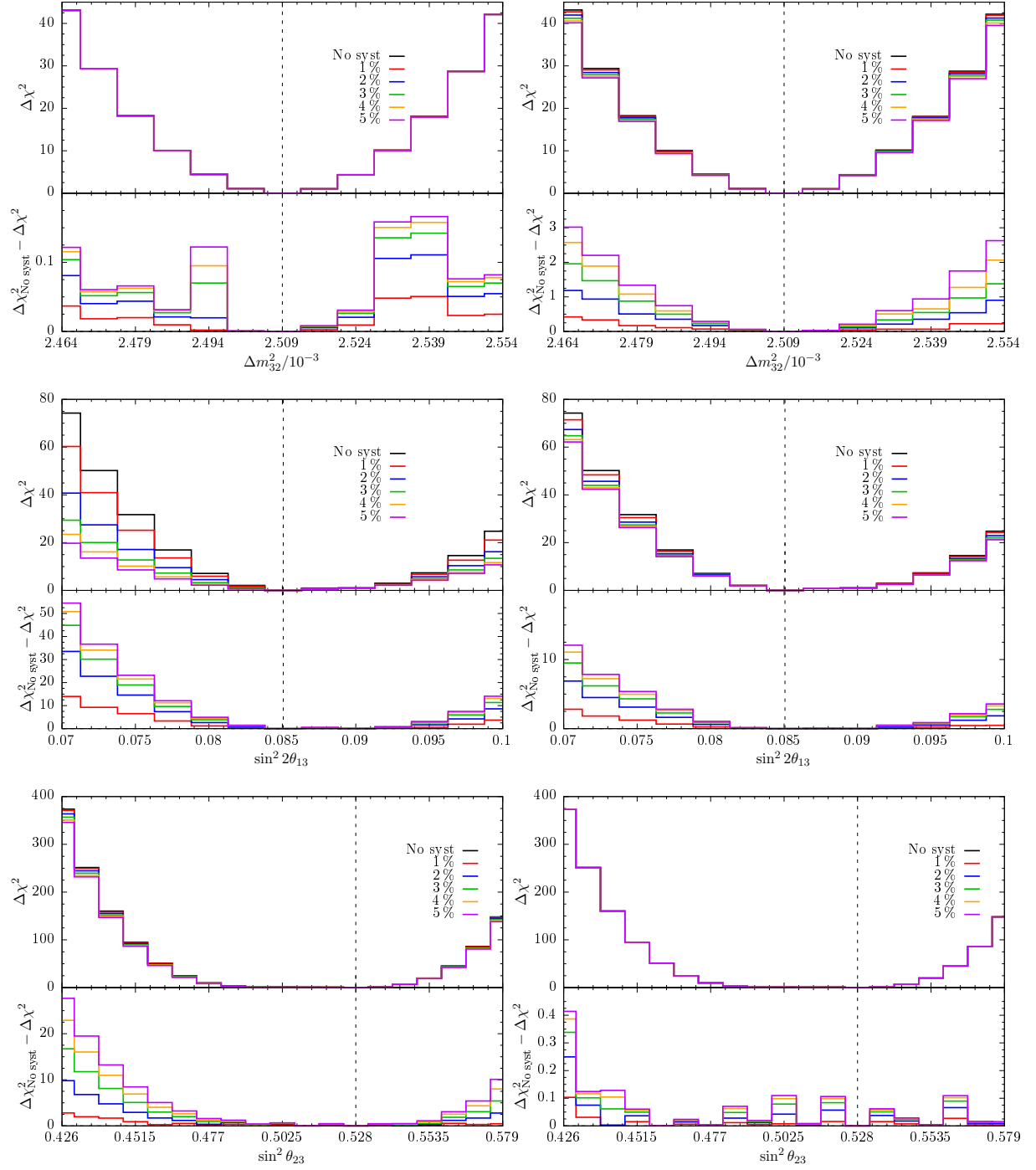


Figure 3.6: The top panels of each figure show the χ^2 profile for Δm_{32}^2 (top), $\sin^2 2\theta_{13}$ (middle), and $\sin^2 \theta_{23}$ for correlated (left) and anticorrelated (right) systematics. The degeneracy in the χ^2 for Δm_{32}^2 is slightly with anticorrelated systematics, whereas the opposite is true for the angles θ_{23} and θ_{13} , even though the latter shows variation not only for correlated, but also for anticorrelated systematics. The bottom panels show instead the difference between the profiles at different error magnitudes and the curve computed without systematic uncertainties (black). The dashed lines show the position of the best fit value, which is always at the nominal Asimov A value.

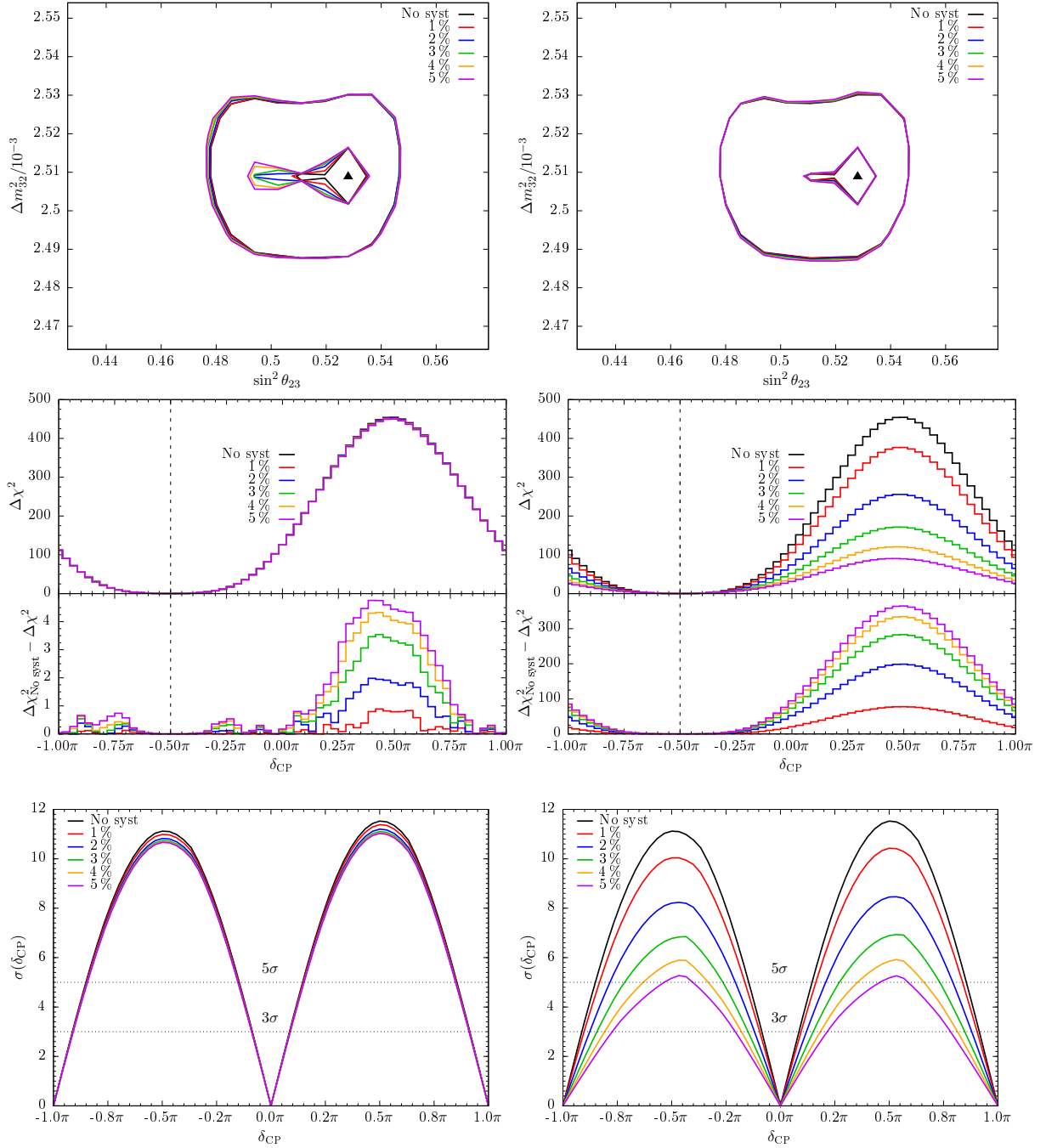


Figure 3.7: For correlated (left) and anticorrelated (right) systematics, the top panel show the contour lines for Δm_{32}^2 versus $\sin^2 \theta_{23}$. The “pointy” shape of the contours comes from the low resolution of the oscillation parameter space, which accounts for 19 points in the $\sin^2 \theta_{23}$ direction and 13 points in the Δm_{32}^2 one. On the middle plot, the χ^2 profile for δ_{CP} shows a dramatic difference between correlated (left) and anticorrelated systematics (right). The bottom panels show the difference between the profiles at different error magnitudes and the curve computed without systematic uncertainties (black). The effect on δ_{CP} is reflected on the expected significance to exclude CP conservation (bottom). The anticorrelation between the ν_e and $\bar{\nu}_e$ CC cross-section systematic errors masks the resolution power to distinguishing neutrino from antineutrino events. The result is a CP-violating effect. The dashed lines and the black triangles show the position of the best fit value, which is always at the nominal Asimov A value.

the relative error. The χ^2 profiles with respect to Δm_{32}^2 , $\sin^2 2\theta_{13}$, and $\sin^2 \theta_{23}$ are shown in Fig. 3.6 for correlated and anticorrelated errors, and a contour plot between Δm_{32}^2 and $\sin^2 \theta_{23}$ is reported in Fig. 3.7. These parameters are not significantly sensitive to the correlation between the two systematic uncertainties. The contour levels of the χ^2 versus Δm_{32}^2 and $\sin^2 \theta_{23}$ show that at the 1σ level of confidence the determination of the θ_{23} octant is slowly lost as the uncertainty increases. On the other hand, the CP phase is the parameter which shows more difference between correlation and anticorrelation, as it can be seen from the remaining panels of Fig. 3.7. When the two CC cross-sections are anticorrelated, the increment of one error brings about the decrement of the other. This results in an effective fluctuation of the number of events, exhibiting a CP violation-like phenomenon. The importance of this study set can also be appreciated from the exclusion of CP conservation, from Fig. 3.7. A large systematic uncertainty of anticorrelated cross-section parameters can therefore only aggravate the overall sensitivity to δ_{CP} . On the other hand, different values of correlated systematics do not degrade the exclusion power to CP conservation.

3.4 Systematic studies

It is expected that larger systematic uncertainties will result in a worse sensitivity, but certain errors affect the measurement of the oscillation parameters more than others. For example, these can be the uncertainties on ν_e and $\bar{\nu}_e$ charged-current cross-sections, the transverse flux model, the pion absorption probability, the energy scale of the far detector, or the flux alignment. The impact of some selected systematics is studied by modifying the nominal systematic model and analysing the overall predicted sensitivity of the experiment in these different scenarios. Doing so, it is possible to determine which systematics have the most important repercussion on the sensitivity, since it is fundamental to understand their effect at all phases of the experiment.

3.4.1 Systematic model

There are 67 systematics for the atmospheric sample, adopted from SK atmospheric studies [122]. These are listed in Appendix A where they are grouped among flux, cross-section, and event separation systematics. In this study, the atmospheric uncertainties are assumed to be uncorrelated between each other and uncorrelated with the beam systematics. A more accurate systematic study for the atmospheric analysis of HK is expected in the future. The main focus of this work is the beam sample and its systematic errors.

The T2K 2018 error model is employed [116] for the beam part. There are 74 uncertainties for flux and cross-section parameters from near detector constraints, known as the BANFF fit, acronym for Beam And ND280 Flux extrapolation task Force. These are grouped in 50 systematics—25 for the ν mode and 25 for the $\bar{\nu}$ mode—for the main four flux components (ν_e , ν_μ , $\bar{\nu}_e$, and $\bar{\nu}_\mu$), and 24 systematics for cross-section parameters. In the T2K experiment the neutrino flux and cross-section parameters are fitted from the unoscillated spectra of CC candidate events in ND280. The uncertainty from hadron-production data is the dominant source of systematic error of the flux model. It is found that some of the beamline conditions slightly change in time, and so the on-axis INGRID detector constantly monitors the stability of the flux. Even though the flux uncertainty is approximately 9% at the peak energy, its impact on oscillation parameter uncertainties is significantly smaller, given that the near and far detector measurements sample nearly the same flux.

The dominant CCQE interaction (see Section 1.4.3) is modelled with a relativistic Fermi gas nuclear model including long-range correlations using the random phase approximation (RPA) [123]. The 2p-2h model implemented is developed by Nieves and collaborators [63, 124],

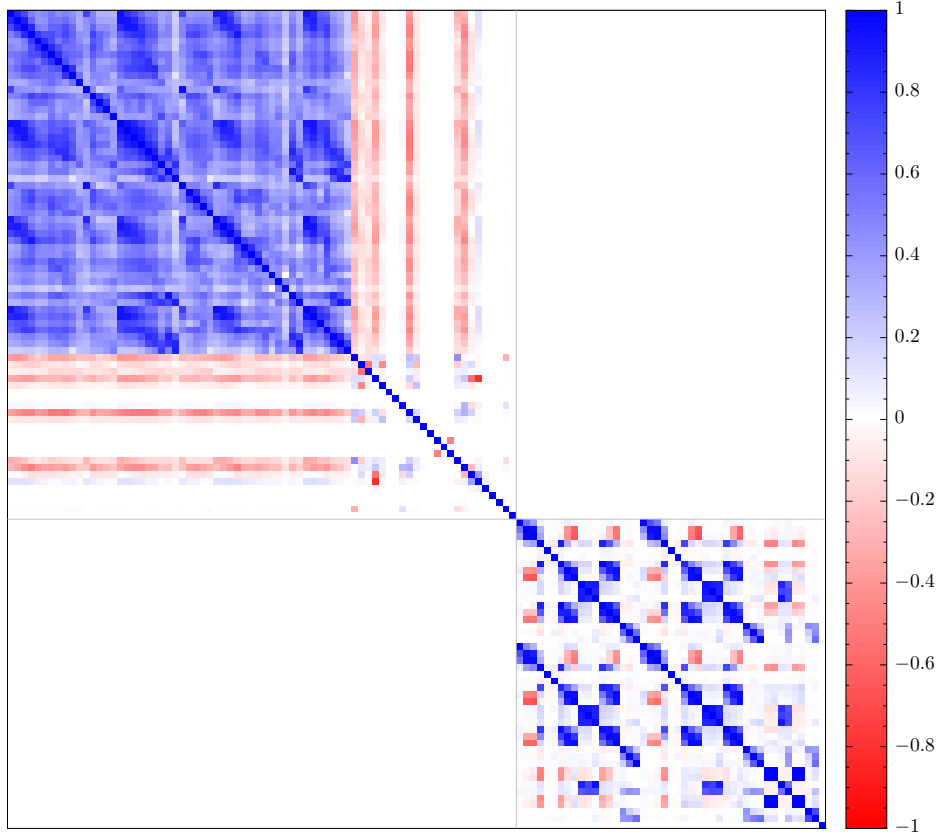


Figure 3.8: Correlation matrix of the beam systematic model. The two main blocks correspond to respectively the BANFF errors and the far detector Final State interaction errors.

which predicts multinucleon emission considering contributions from Δ -like meson exchange currents and from interactions with correlated nucleon–nucleon pairs. These different modes give rise to specific biases in the reconstructed neutrino energy when calculated with the quasi-elastic formula of Section 1.149. This effect is adjusted by introducing systematic parameters for the components of the model related to ^{12}C and ^{16}O and interactions, being these two the principal target nucleons in ND280. There is an additional uncertainty on the relative normalisation between such parameters. The q^2 dependence of the RPA correction is allowed to vary as well, parameterising it over four additional variables. Processes producing a single pion and one or more nucleons in the final state are instead described by a tuned Rein-Sehgal model [61]. The differences between radiative corrections to electron- or muon-neutrino interactions are large at low energies [125]. This is due to the different final-state lepton mass and the issue is addressed by adding uncorrelated and anticorrelated uncertainties to ν_e and $\bar{\nu}_e$ CC cross-sections in relation to the muon neutrino ones. Other important parameters are the axial-mass m_A , the Fermi momentum p_F , and the nucleon binding energy E_b , which are uncorrelated to the ^{12}C and ^{16}O systematics and are left unconstrained given the poor agreement from other neutrino experiments [126].

There are also 45 uncertainties for SK detector efficiencies and Final State Interactions (FSI), which parameterise the uncertainties on the four final-state event selections at the far detector. Among these, one uncorrelated systematic describes the energy scale uncertainty. The reconstruction of the momenta in a neutrino event is mainly based on the charge collected by the PMTs; for this reason, the resolution is mostly limited by water quality and PMT gain.

A precise momentum determination of the incoming neutrino is a necessary requirement for oscillation analysis. The calibration of the energy scale is therefore a crucial step and in SK it is performed using four well-understood independent control samples [122]. Since the energy loss dE/dx is approximately constant, the ratio between reconstructed momentum and track length of high energy stopping muon is used to regulate the energy scale for energies in the range $1 \sim 10$ GeV. The track is estimated from the entering position of the muon and the vertex of the detected Michel electron, both of which are assumed to be independent on the reconstruction method. The momentum of low-energy stopping muons with energies from 200 MeV to 500 MeV are estimated by determining the Cherenkov angle using Eqs. (2.3) and (2.4); only events with a clear Cherenkov ring and optimal reconstruction are selected, and the purity of the sample is improved by requiring the detection of the decay electron in the fiducial volume. The single neutral pions produced in NC interactions of atmospheric neutrinos are reconstructed by looking at the invariant mass of the final-state photons

$$m_{\pi^0}^2 = 2 p_{\gamma_1} p_{\gamma_2} (1 - \cos \theta) , \quad (3.32)$$

with θ being the opening angle between γ_1 and γ_2 . The error on the energy scale at around 130 MeV comes from comparing the peak positions of the data and Monte Carlo distributions of m_{π^0} . Finally, the distribution of decay electron events from stopping cosmic muons is used at energies around 40 MeV. This sample is used to test whether the detector response is uniform, since vertices and the direction of the electrons distribute homogeneously and isotropically in the fiducial volume. The stability in time of the energy scale is instead validated by the high energy stopping muons. The energy scale systematic of SK is assumed to be valid for HK.

The full list of systematics is reported in Appendix A. The correlation matrix between the beam systematics is shown as a 2D colour map on Fig. 3.8, from which the three main typologies of uncertainties — flux, cross-section, and far detector — are easily recognised. The SK and FSI systematics are visibly uncorrelated with the BANFF ones.

3.4.2 Sensitivity with the nominal systematic model

Using the predictions from Section 3.3.4 and fixing the *true* oscillation parameter combination at the Asimov A point (see Table 3.2), the χ^2 profile is now calculated with the minimisation method in previous Section 3.3.3. A combined fit of the ν_e and ν_μ samples allows to estimate the sensitivity of HK to the oscillation parameters. The χ^2 profiles against the variation of the oscillation parameters Δm_{32}^2 , $\sin^2 2\theta_{13}$, $\sin^2 \theta_{23}$, and δ_{CP} are shown in Fig. 3.9. The contour plots of the χ^2 with Δm_{32}^2 versus $\sin^2 \theta_{23}$ and δ_{CP} and $\sin^2 2\theta_{13}$ are also shown. The lines show also the effect of the Gaussian penalty term on the angle θ_{13} from reactor constraints. Unsurprisingly, this term mostly affects the χ^2 profile for $\sin^2 2\theta_{13}$ and slightly δ_{CP} as they are correlated.

The full sensitivity to exclude CP conservation computed with the nominal systematic model is shown in Fig. 3.10. The effect of the Gaussian penalty term does not impact the sensitivity of HK to CP violation, hence this term is always included in the following results. In Fig. 3.10, the sensitivity is shown at different stages of the experiment. The effect is simulated by rescaling event samples. With only a quarter of the data collected, a maximally violating CP phase could be found with a significance of 3σ , but with half of the statistics 5σ are easily reached. Increasing the collected samples, the sensitivity quickly saturates to the best exclusion of $\sim 6.5\sigma$.

The usefulness of performing a combined fit between beam and atmospheric data can be best understood from Fig. 3.11. When the expected (E_n) and observed (O_n) event distributions are built for the χ^2 calculation, a neutrino mass hierarchy must be assumed. In reality, the true mass ordering is unknown and unless this freedom is parameterised in some way, it can

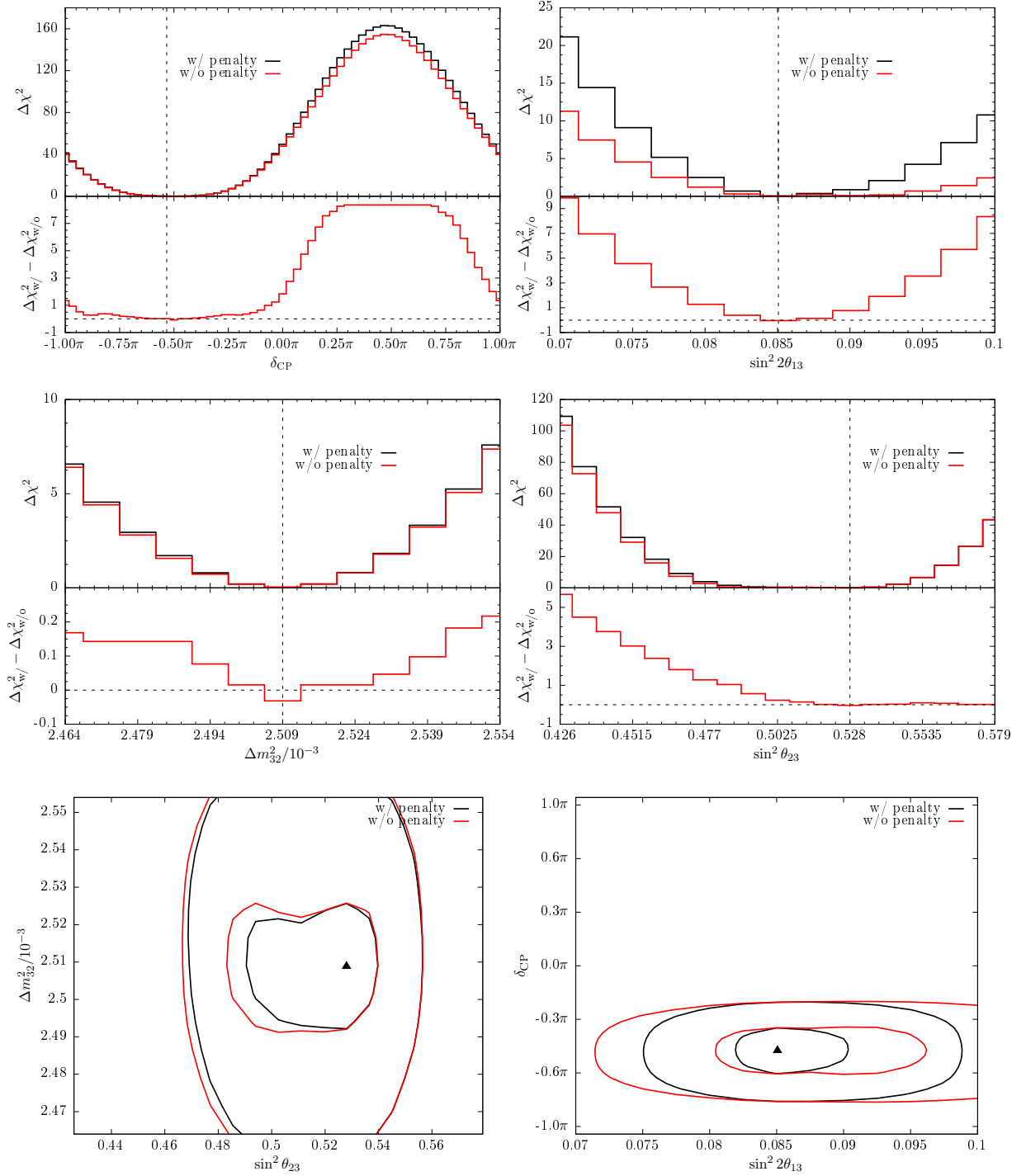


Figure 3.9: χ^2 profile for δ_{CP} (top left), $\sin^2 2\theta_{13}$ (top right), Δm^2_{32} (middle left), and $\sin^2 \theta_{23}$ (middle right), together with the contour levels for δ_{CP} versus $\sin^2 2\theta_{13}$ (bottom left) and Δm^2_{32} versus $\sin^2 \theta_{23}$ (bottom right). The bottom panels in the top four figures show the difference between the χ^2 profiles computed with the penalty term and the χ^2 profiles computed without. The dashed lines and the black triangles show the position of the best fit value, which is always at the nominal Asimov A value.

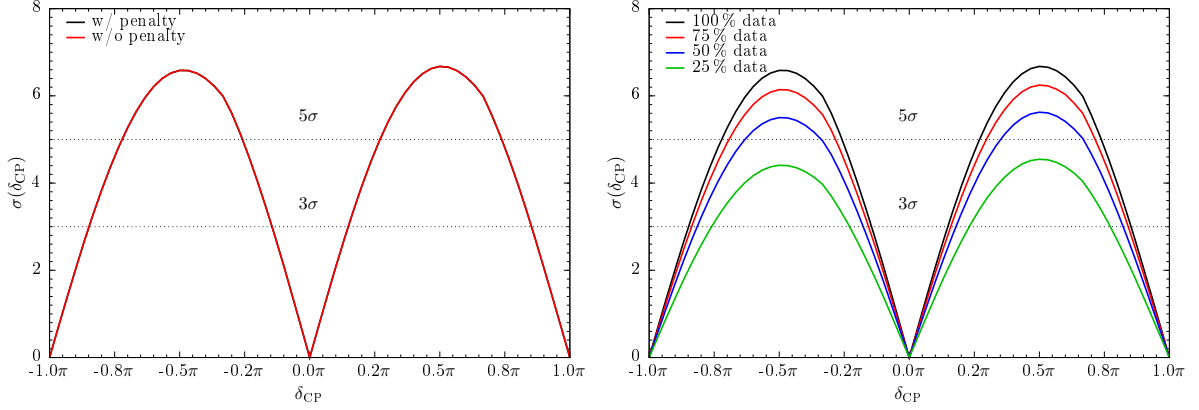


Figure 3.10: Expected significance to exclude CP conservation with the nominal model (left), revealing that the sensitivity it is not affected by the penalty term of θ_{13} from reactor constraints. On the right, the sensitivity to CP violation with full statistics (black) is compared to different amounts of collected data: with 25 % (green), 50 % (blue), and 75 % (red) of the total statistics.

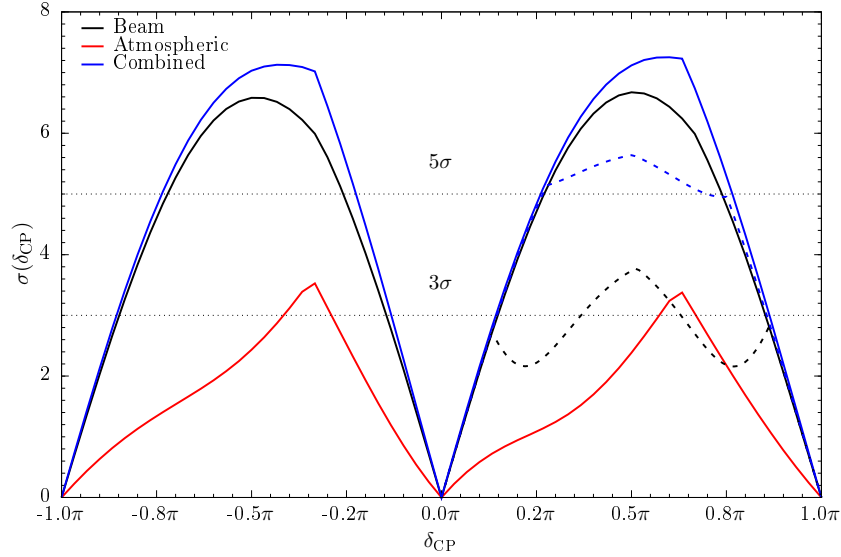


Figure 3.11: Expected significance to exclude CP conservation with the nominal model and for the beam sample (black), the atmospheric sample (red) and the combination of the two (blue). The solid lines correspond to sensitivity where the mass hierarchy is known to be normal. If the mass hierarchy is not known the sensitivity is weakened. When the true mass ordering of the beam sample is normal and inverse hierarchy is fitted, exclusion power is lost for $\delta_{CP} > 0$ (black dashed). Including the atmospheric sample in the fit restores partially the sensitivity (blue dashed).

Table 3.3: Variations of the nominal systematic model, labelled **0**. The second column specify the modification applied to the reference model: the sets in the first block have one or more parameters added, whereas one or more parameters are removed in the variations of the second block. The systematic models in the last group have the same number of parameters of the nominal model, with the modifications specified.

0	Nominal T2K model		
1a	=	0	+ ν_e CC cross-sections for $0.1 \text{ GeV} < E_{\text{true}} < 0.6 \text{ GeV}$
1b	=	0	+ ν_e CC cross-sections for $0.6 \text{ GeV} < E_{\text{true}} < 1.0 \text{ GeV}$
2a	=	0	+ $\bar{\nu}_e$ CC cross-sections for $0.1 \text{ GeV} < E_{\text{true}} < 0.6 \text{ GeV}$
2b	=	0	+ $\bar{\nu}_e$ CC cross-sections for $0.6 \text{ GeV} < E_{\text{true}} < 1.0 \text{ GeV}$
9	=	0	+ CC1 π^\pm and CC-coh cross-sections for ν_e and $\bar{\nu}_e$.
10	=	0	+ CC1 π^\pm and CC-coh cross-sections for ν_μ and $\bar{\nu}_\mu$ for $2 \text{ GeV} < E_{\text{true}} < 10 \text{ GeV}$
6a	=	0	– ν 2p-2h normalisation
7a	=	0	– $\bar{\nu}$ 2p-2h normalisation
67	=	0	– ν and $\bar{\nu}$ 2p-2h normalisation
8	=	0	× increased ν_e flux uncertainty in ν -mode beam (2%)
11a	=	0	× increased energy scale (2.4% \rightarrow 2.9%)
11b	=	0	× decreased energy scale (2.4% \rightarrow 1.9%)
flux	=	0	× flux model additions from INGRID studies

happen that the wrong mass hierarchy is used in defining the expected events. In this case, the sensitivity to certain values of δ_{CP} can deteriorate. For example, if the true mass ordering is normal hierarchy and inverted hierarchy is assumed in the fit, the sensitivity for $\delta_{\text{CP}} < 0$ remains unaffected, whereas the one for $\delta_{\text{CP}} > 0$ worsens. The opposite occurs in the reverse situation. Adding the atmospheric sample to the likelihood calculation allows to partially recover the exclusion power to CP conservation. The very long baseline of atmospheric neutrinos amplifies matter effects, thanks to which the sensitivity of the experiment to mass ordering is restored. The differences between expected and observed events thus intensify, leading to larger values of the likelihood.

3.4.3 Variations of the nominal model

Previous studies [116] found that some systematic uncertainties were not easily implemented by varying model parameters. These were then the subjects of fake data studies, where a variant systematic model was analysed under the assumptions of the default model. A series of modifications of the nominal systematic model are considered also in this study. New systematic sets are created and by performing sensitivity studies with these variations of the nominal model it is possible to determine whether certain systematic errors need more control than other. All of the produced sets are listed in Table 3.3, even though only some of them have been analysed for this thesis and they are: increment of the ν_e flux uncertainty in the ν -mode beam by 2% (labelled **8**); increment of the energy scale uncertainty, from 2.4% to 2.9% (labelled **11a**); decrement of the energy scale uncertainty, from 2.4% to 1.9% (labelled **11b**). The choice of these sets is motivated by the fact that the number of systematic errors is the same with respect to the nominal model and the modified uncertainties are well understood by the various analysis groups. The remaining variations will be analysed in future studies. The new three profiles are shown collectively with the nominal model (labelled **0**) in Fig. 3.12. The χ^2 as a function of δ_{CP} and $\sin^2 2\theta_{13}$ changes slightly with a different flux uncertainty, but it is not

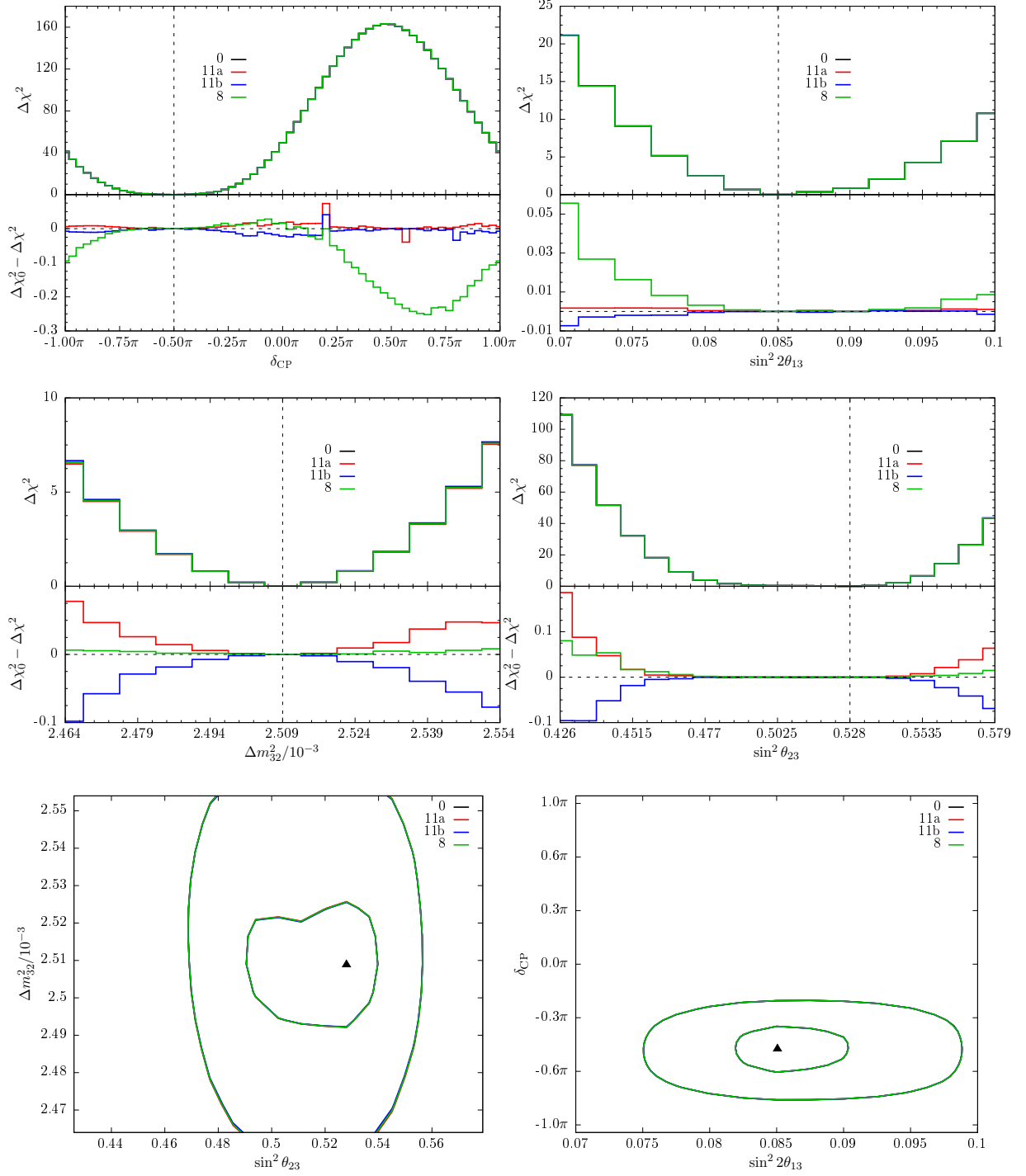


Figure 3.12: χ^2 profile for δ_{CP} (top left), $\sin^2 2\theta_{13}$ (top right), Δm_{32}^2 (middle left), and $\sin^2 \theta_{23}$ (middle right), together with the contour levels for δ_{CP} versus $\sin^2 2\theta_{13}$ (bottom left) and Δm_{32}^2 versus $\sin^2 \theta_{23}$ (bottom right). The bottom panels in the top four figures show the difference between the χ^2 profiles computed with the nominal model (0) and the variations of the nominal model itself (8, 11a, and 11b). The dashed lines and the black triangles show the position of the best fit value, which is always at the nominal Asimov A value.

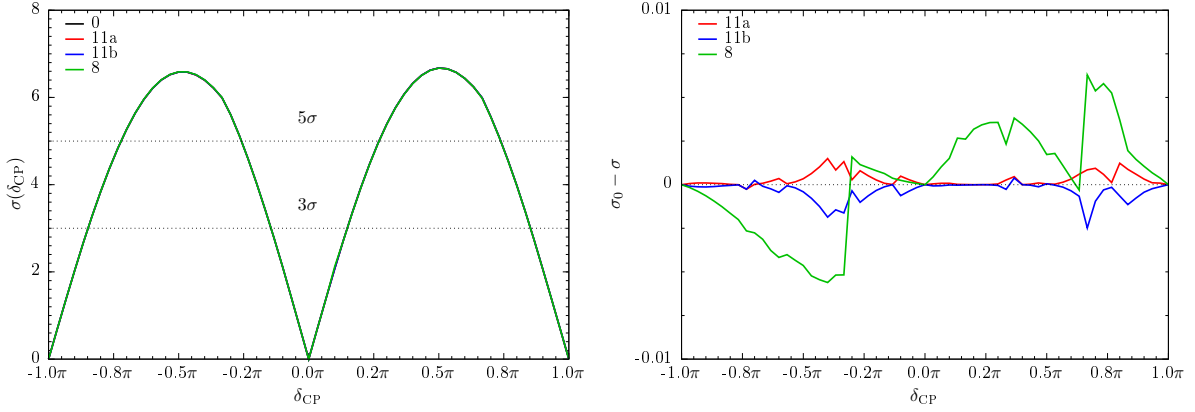


Figure 3.13: Expected significance (right) to exclude CP conservation with the nominal model (0) and its variations (8, 11a, and 11b). On the left, the difference of each curve with the nominal model show that the sensitivity does not change significantly with the modifications of the systematic model in place.

very much affected by a variation of the energy scale error. The opposite is true for χ^2 versus Δm_{32}^2 or $\sin^2 \theta_{23}$, in which varying the energy scale error is reflected in larger deviations from the nominal model away from the best fit value. The contour plots in Fig. 3.12 confirm that no appreciable deviation from the nominal model is seen for χ^2 levels corresponding to 1σ and 3σ . In terms of sensitivity, the variation induced by the modified systematic model is less than 0.1 % at values of maximal violation of CP, as it can be appreciated in Fig. 3.13. The treatment of the energy scale uncertainty with the methodology described in this chapter might be too simplistic. The linear behaviour of the systematic errors (see Eq. (3.30)) should be applied with mindfulness: it follows that the systematic parameters in the χ^2 could commute with each other. The energy scale error, however, does not since it effectively shifts the bin contents of the event distributions. It is also believed that this parameter is simultaneously constrained by the e -like samples the μ -like samples, thus exhibiting no appreciable effect on the sensitivity prediction. The calibration of the energy scale is, as a matter of fact, performed separately on stopping muon and decay electron events, as explained in Section 3.4.1. There is probably need to improve the systematic model by not only splitting the energy scale systematic between the two data samples, but also by changing the χ^2 definition and the way this parameter is treated.

Keeping in mind the above caveats, the sensitivity to δ_{CP} from Fig. 3.13 is above 6σ at full statistics. It is expected that the systematics variations of Table 3.3 should not degrade the significance of CP conservation exclusion below this value. Further studies are in place before the definitive quantitative results, since a more accurate treatment of the energy scale parameter is needed. Once the beam sample is extensively analysed, the atmospheric sample can be added to the χ^2 calculation and a more comprehensive systematic model can be adopted.

Summary

In this chapter, the sensitivity of the HK experiment to oscillation parameters has been estimated, with special emphasis on the CP-violating phase δ_{CP} . The HK experiment will collect a large amount of data thanks to both an exceptional fiducial volume and upgraded instrumentation which will allow a detailed study of the oscillation parameters. A fitting framework which combines atmospheric and beam data samples is employed for the study. The technique involves the minimisation of a Poissonian likelihood function which includes effects from systematic uncertainties and is computed at different combinations of the oscillation parameters.

The error model for the atmospheric data sample consists of 67 systematics, whereas the beam data sample is described by the T2K systematic model, made of 119 parameters. Considering the beam sample alone, it is found that Hyper-Kamiokande can exclude maximal violation of CP at full statistics with more than 6σ of significance. Some variations of the beam systematic model are also being investigated in order to understand how the experimental sensitivity is affected by certain model parameters. One of these, the energy scale error, might be treated too naively in the fitting framework and so slight modifications to both the error model and the likelihood should be considered. It is expected that the systematics variations of Table 3.3 should not degrade the significance of CP conservation exclusion below this value. Finally, performing a combined fit between beam and atmospheric data is helpful not only because more data is collected, which increments the overall sensitivity in absolute terms, but also because different neutrino energies and baselines are studied. This makes the analysis more robust, in particular regarding the uncertainty on the mass ordering: the very long baseline of atmospheric neutrinos amplifies matter effects and therefore the atmospheric sample partially recovers exclusion power to CP conservation when the neutrino hierarchy is unknown.

Chapter 4

Phenomenology of heavy neutral leptons

The evidence of three neutrino flavour oscillation is well established [17, 30, 45] and necessarily implies that the neutrino mass splittings are nonzero, as seen in Section 1.2.2. Neutrinos are therefore massive and they mix, forcing to consider extensions of the Standard Model (SM) to explain their origin. A simple means of doing so is to introduce the right-handed counterpart of SM neutrinos (see Section 1.2.1) which are singlet with respect to all SM gauge symmetries. The new Lagrangian includes a Yukawa coupling between these sterile states, the Higgs boson and the leptonic doublet, which generates Dirac mass-terms below the scale of electro-weak symmetry breaking (EWSB). Since any renormalisable term should be included in the Lagrangian, Majorana mass terms for the new singlet states are allowed. On diagonalisation of the resulting neutrino mass matrix, the heavy neutrino states, commonly known as nearly-sterile neutrinos or Heavy Neutral Leptons (HNLs) in experimental contexts, remain mainly in the sterile neutrino direction and have subweak interactions suppressed by elements of the extended mixing matrix.

These states have been connected to a vast range of phenomenological behaviours and even to cosmological implications (for a review on sterile neutrinos see Ref. [127]). For instance, nearly-sterile neutrinos in the keV region are viable warm dark matter candidates [128], whereas heavier HNLs could play a role in leptogenesis [99, 129, 130]. So far, some possible hints in favour of sterile neutrinos have emerged in neutrino appearance oscillation experiments, specifically LSND [131] and MiniBooNE [132–134] but are disfavoured by disappearance experiments [135–137], unless non-standard effects are present [138–141]. Further hints in the same mass range have been reported for mixing with electron neutrinos in the so-called reactor anomaly [142–146] and in the less statistically significant gallium one [29, 147, 148]. Explanations of the MiniBooNE low energy excess invoking GeV-scale HNLs with nonstandard interactions [149–153] have also been put forward. In these models, heavy neutral fermions are produced by neutrino up-scattering in the detector and subsequently decay into photons or electrons, which mimic an electron neutrino interaction. The interpretation of the current experimental results is still largely debated in the scientific community. Searches both for electron-like signatures in MicroBooNE, the SBN programme at Fermilab [154], and in short baseline reactor neutrino experiments, such as DANNS [146], NEOS [145], PROSPECT [155], STEREO [156], and NEUTRINO-4 [157], will shed further light on these possibilities, whereas the KATRIN experiments [158] will be able to exclude the gallium anomalies.

Apart from these controversial hints, no positive evidence of heavy neutrinos has been found to date in laboratory searches. Bounds critically depend on the HNL masses and the flavour with which they mix. Searches for kinks in Curie plots of β -decay spectra [159–163] have

placed bounds on the electronic mixing for HNL masses between the keV and MeV scales. For masses from a few MeV to a few hundreds MeV, searches for monochromatic peaks in the lepton spectrum of decaying pions and kaons place important bounds on the muonic and electronic mixing angles [164–168]. Neutrinoless double beta decay indirectly constrains Majorana HNLs from the eV to the TeV scale and lepton number violating meson and tau decays can be used to set limits on the mixing angle in narrow ranges of HNLs masses [169]. The tightest constraints come from searches for the direct production and subsequent decays of heavy neutrinos in *beam dump* experiments (see Chapter 5) and at colliders. These types of studies are almost model independent and thus can provide competitive bounds. The strongest limits to date were set by the PS191 experiment [170, 171], even though a similar search in the near detector of T2K has reached very similar constraints [172]. Other bounds of this type can be found at LEP experiments [173, 174], CHARM II [175], NuTeV [176], and similar ones [177–179], as well as collider analyses, from LHCb [180], ATLAS [181], CMS [182, 183], BELLE [184] (see also Ref. [185]). Thorough reviews of the current experimental constraints can be found in Refs. [169, 186], and in Ref. [187] for some revised bounds.

In this chapter, low-scale seesaw models are discussed linking the origin of light neutrinos to a new phenomenologically viable physics scale in Section 4.1. This elegant solution is possible thanks to a minimal extension of the SM symmetry, in which heavy neutral leptons are predicted at an energy range accessible by future neutrino experiments (see Chapter 5). Formulae to compute polarised differential rates were computed for the first time in literature in Ref. [1] and are reported in Section 4.2 and Section 4.3. The precise formulation of decay and production rates is necessary to develop a reliable study of searches of HNL decays at neutrino beam facilities. The range of interest for this study goes therefore from a few MeV up to a couple of GeV, as motivated in Section 4.3.

4.1 Heavy neutrinos in seesaw models

Given n new SM singlets, N_i , the extended Lagrangian becomes

$$\mathcal{L}_{\text{SM}+\mathcal{N}} = \mathcal{L}_{\text{SM}} + i \bar{N}_i \not{\partial} N_i + Y_{\alpha i} \bar{L}_\alpha \tilde{H} N_i + \frac{1}{2} (M_R)_{ij} \bar{N}^C_i N_j + \text{h.c.} , \quad (4.1)$$

with \mathcal{L}_{SM} denoting the SM Lagrangian and the other symbols taking their conventional meaning. Below EWSB, mass terms for neutrino states become explicitly available

$$-\mathcal{L}_{\text{mass}} = \frac{1}{2} \bar{\nu} \mathcal{M} \nu^C + \text{h.c.} , \quad (4.2)$$

where ν is such that

$$P_L \nu \equiv (\nu_e, \nu_\mu, \nu_\tau, N_1, \dots, N_n) , \quad (4.3)$$

and C denotes charge-conjugation (see Section 3.1). If no additional field content is added and only renormalisable operators are included, the low-scale mass terms will have the structure

$$\mathcal{M} = \begin{pmatrix} 0 & m_D^T \\ m_D & M_R \end{pmatrix} , \quad (4.4)$$

where m_D and M_R are complex matrices of dimensions $n \times 3$ and $n \times n$, respectively. Under the assumption that M_R is full rank, this model defines the Type I seesaw [188–191]. The light neutrino mass matrix is then retrieved by the following expansion [192]:

$$m_\nu = m_D^T M_R^{-1} m_D + \mathcal{O}([M_R^{-1} m_D]^2) . \quad (4.5)$$

The top-left zero in Eq. (4.4) arises as a consequence of $SU(2)_L$ symmetry, and similar theoretical considerations often impose further textures and hierarchies on m_D and M_R , which in turn lead to specific correlations in the physical spectrum of states. The heavy neutrino masses are approximately given by the diagonal entries of M_R and its corresponding eigenstates, the heavy nearly-sterile neutrinos N_i , have suppressed mixing with active neutrinos and are mainly composed by sterile fields. Neglecting the matrix nature of these expressions for now, if m_D takes values around the electroweak scale, acceptable neutrino masses are produced when M_R has values around the GUT scale, suggestively connecting it to a high-scale breaking of $U(1)_{B-L}$ [188]. Low-scale solutions are also possible by taking the Yukawa couplings to be similar or smaller than the other SM lepton Yukawa couplings. For example if m_D takes values in the keV range, new nearly-sterile states would exist with masses around a GeV. The resulting mixing $U_{\alpha N}$ is constrained by the contribution given to light neutrino masses and naively one can expect to have

$$|U_{\alpha N}|^2 \lesssim \frac{m_\nu}{m_N} \lesssim 10^{-10} \frac{1 \text{ GeV}}{m_N}, \quad (4.6)$$

by taking $m_\nu \lesssim 0.1 \text{ eV}$ as limit for light neutrino masses and with m_N the mass of a heavy neutrino. Specific models in which low energy neutrino masses and mixing angles are derived from the seesaw parameters allow for a broader range of values, invoking specific structures for the Yukawa couplings.

Another way to avoid the bound of Eq. (4.6) is by the cancellation between contributions to neutrino masses from larger families of sterile neutrinos. This is achieved in a class of models with approximate lepton number (LN), which can lead to phenomenologically acceptable neutrino masses. Assuming that all of the N_i states have lepton numbers of $|Q_L| = 1$, the right-handed fields $S_j = N_j^C$ are defined for any state with $Q_L = -1$. The set of flavour states can then be ordered by lepton number

$$P_L \boldsymbol{\nu} \equiv (\nu_e, \nu_\mu, \nu_\tau, N_1, \dots, N_a, S_1^C, \dots, S_b^C), \quad (4.7)$$

with $a + b = n$. These charge assignments forbid certain terms in the mass matrix, when LN is conserved. Following Eq. (4.1) and Eq. (4.4), the most general mass matrix is given when

$$m_D = (m, 0) \quad \text{and} \quad M_R = \begin{pmatrix} 0 & M^T \\ M & 0 \end{pmatrix}, \quad (4.8)$$

producing in the lepton number conserving (LNC) limit

$$\mathcal{M} = \begin{pmatrix} 0 & m^T & 0 \\ m & 0 & M \\ 0 & M^T & 0 \end{pmatrix}, \quad (4.9)$$

where m and M are complex matrices with respectively dimensions $a \times 3$ and $a \times b$. This matrix preserves LN and all its flavour states have nonzero LN. It is found that the mass spectrum, i.e. the entries of the diagonalised matrix, consists of [193]

$$\min\{3 + b, a\} \text{ Dirac pairs} \quad \text{and} \quad |3 + b - a| \text{ massless Majorana states}, \quad (4.10)$$

in which the Dirac pair masses are given by the nonzero singular values of the rectangular $a \times (3 + b)$ matrix (m^T, M^T) . Although such a mass matrix can explain the neutrino data via three Dirac pairs with $a = 3$ and $b = 0$, this solution has no natural explanation of the observed smallness of the light neutrinos. The scale of neutrino masses can be recovered by a perturbation of the above mass matrix by means of a small lepton number violating (LNV)

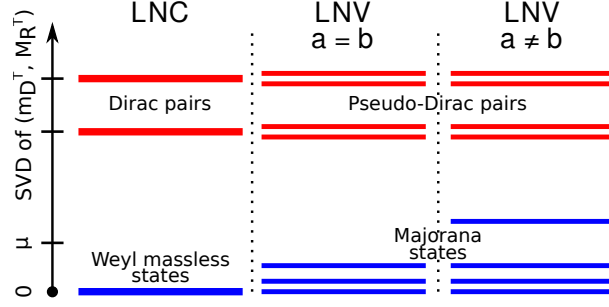


Figure 4.1: This schematic shows the different structure of the neutrino mass spectrum when LNV terms are included or not in the mass matrix. As an example, ISS(2,2) and ISS(2,3) models are shown. In the LNC limit, the high scale masses are degenerate and the states form Dirac pairs, whereas the light neutrinos are all massless Weyl states. When the LNV perturbation μ is added, the degeneracy is resolved and the Dirac pairs become pseudo-Dirac states, with a mass splitting proportional to μ . At the low scale, the neutrinos also acquire masses. When $a \neq b$ extra Majorana states appear in addition to the three light neutrinos.

parameter. In this case, the specific texture of M_R and m_D guarantees a quasi-preserved LN if the LNV parameters are natural in the 't Hooft sense [194]. This can lift eigenstates which are massless in the LNC limit to states with small masses, the magnitude of which is dictated by the LNV perturbation. Under assumptions of renormalisability, the most general LNV Lagrangian must include the following terms,

$$\mathcal{L}_{\text{LNV}} = -Y'_{\alpha i} \overline{L}_\alpha H S_i - \frac{1}{2} \mu'_{ij} \overline{N}_i^C N_j - \frac{1}{2} \mu_{ij} \overline{S}_i^C S_j . \quad (4.11)$$

Each of the terms in this Lagrangian has historically been associated with a simple independent implementation of the paradigm: the Inverse Seesaw (ISS) [195, 196], the linear seesaw [193, 197, 198], and the extended seesaw [199, 200]. The focus of this thesis is on the ISS model.

In the ISS, the texture of the perturbation assumes the values $Y' = 0$ and $\mu' = 0$, while μ controls the size of LNV effects. The mass matrix is therefore

$$\mathcal{M} = \begin{pmatrix} 0 & m_D^T & 0 \\ m_D & 0 & M_R^T \\ 0 & M_R & \mu \end{pmatrix} . \quad (4.12)$$

On diagonalisation, the light neutrino masses are found to be suppressed by the size of μ . Assuming $\mu \ll m, M$ and $a = b$, the light mass matrix takes the following form [196]:

$$m_\nu = m M^{-1} \mu (M^{-1})^T m^T + \mathcal{O}(\mu^2) . \quad (4.13)$$

It results that light neutrino masses are explained by Yukawa couplings of order one and a new physics scale a little above the electroweak scale [195, 196]. For $a \neq b$, extra massless sterile states degenerate with the light neutrinos are present in addition to the set of Dirac pairs of arbitrary masses. In the LNC limit, there is no mixing defined that involves these degenerate states, as any unitary map in the degenerate subspace is permitted. On the contrary, the introduction of the small LNV parameter μ perturbs the LNC spectrum as well as the mixing for both light and heavy neutrinos. In general, there are only two possible origins for a low-scale heavy neutrino. One scenario is when one of the massive Dirac pair is already at a low energy scale in the LNC limit and it becomes a pseudo-Dirac pair after the perturbation. The degeneracy is resolved by the μ parameter, which regulates the mass splitting of the pair. Both

in the LNC limit and in the LNV case, the mixing angles between Dirac pair and light neutrinos can be arbitrarily large. The other possibility can only occur when $a \neq b$ and it involves one of the massless Majorana fermion, initially degenerate with the light neutrinos. In the presence of LNV terms, this state is given a nonzero mass proportional to the perturbation. As the mixing between massless states is not defined in the LNC limit, the perturbation controls the induced mixing between the nearly-sterile state and the active ones. The cartoon of Fig. 4.1 illustrates how the mass spectrum changes with LNV terms, highlighting how the mass degeneracy in the LNC limit is resolved when LNV contributions are added. The notation “ISS (a, b)” will be used to denote a realisation of the model with a and b new gauge singlets of, respectively, lepton number $+1$ and -1 , and $a, b \neq 0$.

The discussion above suggests that both Majorana states and (pseudo-)Dirac states should be considered when dealing with possible phenomenological aspects of an ISS framework. In computing decay and production rates for both Majorana states and Dirac states, lepton number violating effects will be disregarded and therefore the distinction between pseudo-Dirac and Dirac states will not be relevant. The region of interest for the masses of heavy states is in the MeV–GeV range. This is motivated by the kinematic limits on production from meson decays discussed in more detail in Section 4.3. Feynman rules for Majorana states derived from Eq. (4.1) can be found in [169], or constructed using the techniques of Ref. [201]. For an explicit comparison between Dirac versus Majorana Feynman rules for heavy neutrinos, see Ref. [202].

4.2 Heavy neutrino decay

The heavy neutrino decay rates and polarised distributions necessary for studies in experimental searches are presented in this section. The calculations can be simplified by noting the following equivalences. A Majorana neutrino N decaying via a charged current process has the same differential decay rate as the Dirac neutrino N_D with the appropriate lepton number,

$$d\Gamma(N \rightarrow \ell_\alpha^- X^+) = d\Gamma(N_D \rightarrow \ell_\alpha^- X^+) , \quad (4.14)$$

$$d\Gamma(N \rightarrow \ell_\alpha^+ X^-) = d\Gamma(\bar{N}_D \rightarrow \ell_\alpha^+ X^-) , \quad (4.15)$$

where identical mass and mixing angles for both Dirac and Majorana neutrinos are taken. This equivalence can be seen directly from the Feynman rules for Dirac and Majorana fermions [201, 202], but also explicitly in the formulae below. In a neutral current (NC) decay, however, the two contractions of the NC operator lead to another contribution, and so

$$d\Gamma(N \rightarrow \nu X') = d\Gamma(N_D \rightarrow \nu X') + d\Gamma(\bar{N}_D \rightarrow \bar{\nu} X') . \quad (4.16)$$

These relations hold at the differential level if the kinematic variables are reinterpreted in the obvious way. In this sense, the Majorana process can be seen as the sum of Dirac particle and antiparticle decays. It is important to observe that in a general amplitude with Majorana states, there would also be an interference contribution between these two subprocesses. However, in all cases of interest, interference diagrams are proportional to the final-state light neutrino mass, which for the sake of simplicity is zero. Considering the total decay rates only, the Majorana decay is larger by a factor of 2 compared to the Dirac case,

$$\Gamma(N \rightarrow \nu X') = 2\Gamma(N_D \rightarrow \nu X') . \quad (4.17)$$

This is, however, only true for the total decay rates with massless final-state neutrinos.

It is instructive to reconsider this result in the light of the *practical Dirac–Majorana confusion theorem* [203, 204]. In Ref. [203], the decomposition into particle and antiparticle processes

Table 4.1: All the available channels for a HNL with a mass below the D_s^\pm mass are listed above, sorted by threshold mass. The active neutrinos are considered massless, when compared to the masses of the other particles.

Channel	Threshold	Channel	Threshold	Channel	Threshold
$\nu\nu\nu$	0 MeV	$e^\mp K^\pm$	494 MeV	$\nu\eta'$	958 MeV
$\nu e^+ e^-$	1.02 MeV	$\nu\eta$	548 MeV	$\mu^\mp K^{*\pm}$	997 MeV
$\nu e^\pm \mu^\mp$	105 MeV	$\mu^\mp K^\pm$	559 MeV	$\nu\phi$	1019 MeV
$\nu\pi^0$	135 MeV	$\nu\rho^0$	776 MeV	$\nu e^\pm \tau^\mp$	1776 MeV
$e^\mp \pi^\pm$	140 MeV	$e^\mp \rho^\pm$	776 MeV	$e^\mp D^\pm$	1870 MeV
$\nu\mu^+ \mu^-$	210 MeV	$\nu\omega$	783 MeV	$\nu\mu^\pm \tau^\mp$	1880 MeV
$\mu^\mp \pi^\pm$	245 MeV	$\mu^\mp \rho^\pm$	882 MeV	$\tau^\mp \pi^\pm$	1870 MeV
		$e^\mp K^{*\pm}$	892 MeV		

was performed for the Majorana neutrino–electron scattering via neutral current, which led to a factor of two enhancement in the total rate. However, this enhancement was shown to be absent in practice due to the polarisation of the incoming neutrino which suppresses the $\Delta L = 2$ contributions by factors of the neutrino mass. In the present case of nearly-sterile decay, where mass effects are large and essential to the calculation, there is no analogous effect: Dirac and Majorana neutrinos will have distinct total decay rates regardless of their polarisation. Hence, the total decay rates of heavy neutrinos into observable final states could in principle allow to determine the Majorana/Dirac nature of the initial state. This is not a trivial effect; for example, a pure Majorana state decays with equal probability into $e^-\pi^+$ as $e^+\pi^-$, one of its dominant and most experimentally distinctive decay modes, while a Dirac heavy neutrino will only decay into $e^-\pi^+$. Assuming charge-identification is possible in the detector, distinguishing between the two total decay rates should be possible with modest statistics. In a charge-blind search or for an NC channel, the total decay rate of Majorana neutrinos would appear to be twice as large as that of Dirac neutrinos. However, since the mixing is usually an unknown quantity, the difference between Majorana and Dirac nature in this scenario cannot be deduced as easily. There is also a more subtle impact of the nature of the decaying neutrino. Even though the total decay rate is not affected by the helicity of the initial neutrino, the helicity plays an important role on the distributions of final-state particles, which will in turn influence the observability of the signatures of neutrino decay. Although spin-averaged Majorana neutrino decay rates are well known in the literature [169, 205–207], it is important that these polarisation effects are correctly implemented when studying the distributions of final-state observables and subsequently when developing an analysis to tackle backgrounds.

In calculating the decay rates, summing over any possible outgoing states as

$$\Gamma(N \rightarrow \nu X') \equiv \sum_{i=1}^3 \Gamma(N \rightarrow \nu_i X') \quad (4.18)$$

defines a semi-inclusive decay rate into the visible particle(s) X' , such that discussions about the nature and flavours of final-state neutrinos can be avoided. Many other authors treat light neutrinos as Dirac particles, and construct the full decay width using arguments of CP invariance, in practice amounting to adding some judicious factors of two [169, 207]. Following this approach, the summed decay rate for $N \rightarrow \nu X'$ can be seen as

$$\Gamma(N \rightarrow \nu X') \equiv \sum_{\alpha=e}^{\tau} [\Gamma(N \rightarrow \nu_\alpha X') + \Gamma(N \rightarrow \bar{\nu}_\alpha X')] . \quad (4.19)$$

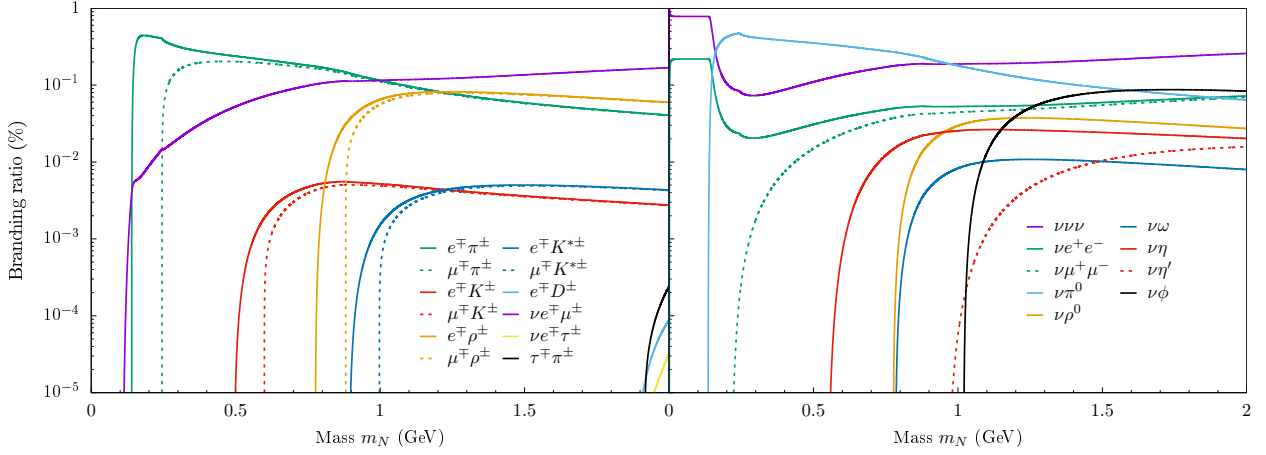


Figure 4.2: The branching ratios for HNL decays are shown above as functions of the neutrino mass, computed using the formulae presented in Section 4.2.1 and integrated over the angular variables. They are grouped in CC-mediated decays (left) and NC-mediated decays (right), in the range from 0.01 MeV up to the maximum mass limit for neutrino production, near 2 GeV. A scenario in which $|U_{eN}|^2 = |U_{\mu N}|^2 = |U_{\tau N}|^2$ is chosen here for illustrative purposes. The branching ratios of Majorana neutrinos and Dirac neutrinos are mathematically identical and therefore no distinction is stressed. The decay into three light neutrinos is fundamental for a correct computation of the branching ratios, even though fully invisible from an experimental point of view.

The two approaches are identical mathematical procedures and can both be used to compute the differential decay rates; however, the light neutrinos in most seesaw models are Majorana fermions and making a distinction between ν_α and $\bar{\nu}_\alpha$ is physically misleading. The approach could be seen as a short-hand for decay rates into polarised massless neutrinos, but this only adds a further complication when dealing with polarisation effects in the beam. The distribution of events, the role of helicity and the heavy neutrino nature are found to be obscured by this approach. In contrast, by summing over all outgoing states, the following formulae are insensitive to the Majorana/Dirac nature of the light neutrinos, and so are the physically relevant rates necessary for comparison with experimental searches since outgoing neutrinos are not reconstructed.

In the remainder of this section, the polarised heavy neutrino decay rates and distributions for Majorana and (pseudo-)Dirac neutrinos are presented. All the decay modes considered are listed in Table 4.1 and their respective branching ratios are shown in Fig. 4.2 as functions of the neutrino mass. The differential widths have been computed using the massive spinor-helicity formalism [208, 209] and checked numerically using FeynCalc [210, 211].

4.2.1 Majorana neutrinos

Pseudoscalar mesons

The semileptonic meson decays are some of the most important channels identified in previous studies [169, 212, 213] thanks to their large branching ratios and distinctive signature of two charged particles with a common vertex. Both charged and neutral pseudoscalar mesons are viable final-state particles, namely P^\pm and P^0 , and the decay widths are given in the centre

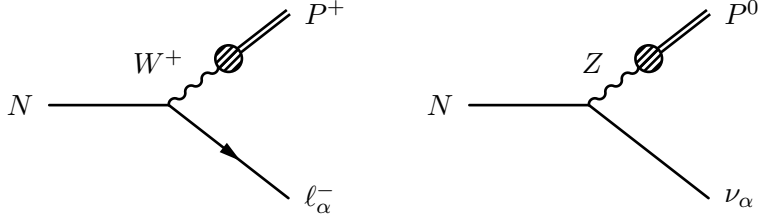


Figure 4.3: Feynman diagrams for the CC (left) and NC (right) semileptonic two-body decays into pseudoscalar meson, via the $|U_{\alpha N}|^2$ mixing. The diagrams for the analogous decays into vector mesons have the same structure. The charge-conjugated diagrams are easily retrieved. No fermionic current is specified for the HNL leg since the decaying neutrino can be both Majorana or (pseudo-)Dirac in nature. The light neutrino are Majorana fermions in the ISS realisations considered in this work.

of mass (CM) frame by

$$\frac{d\Gamma_{\pm}}{d\Omega_{\ell_{\alpha}}}(N \rightarrow \ell_{\alpha}^{-} P^{+}) = |U_{\alpha N}|^2 |V_{q\bar{q}}|^2 \frac{G_F^2 f_P^2 m_N^3}{16\pi} I_1^{\pm}(\xi_{\alpha}^2, \xi_P^2; \theta_{\alpha}) , \quad (4.20)$$

$$\frac{d\Gamma_{\pm}}{d\Omega_{\ell_{\alpha}}}(N \rightarrow \ell_{\alpha}^{+} P^{-}) = |U_{\alpha N}|^2 |V_{q\bar{q}}|^2 \frac{G_F^2 f_P^2 m_N^3}{16\pi} I_1^{\mp}(\xi_{\alpha}^2, \xi_P^2; \theta_{\alpha}) , \quad (4.21)$$

$$\frac{d\Gamma_{\pm}}{d\Omega_P}(N \rightarrow \nu P^0) = \left(\sum_{\alpha=e}^{\tau} |U_{\alpha N}|^2 \right) \frac{G_F^2 f_{P^0}^2 m_N^3}{16\pi} \frac{I_1(0, \xi_P^2)}{4\pi} , \quad (4.22)$$

where Γ_h is the decay rate for neutrinos of helicity h , $V_{q\bar{q}}$ is the appropriate CKM matrix element for the considered meson, f_P is its decay constant, and $\xi_i = m_i/m_N$ denotes the mass of the final-state particle i as a fraction of the initial-state mass. The solid angle elements $\Omega_{\ell_{\alpha}}$ and Ω_P refer respectively to the charged lepton and pseudoscalar meson angles with respect to the neutrino direction. The kinematic function

$$I_1^{\pm}(x, y; \theta) = \frac{1}{4\pi} \lambda^{\frac{1}{2}}(1, x, y) \left[(1-x)^2 - y(1+x) \pm (x-1) \lambda^{\frac{1}{2}}(1, x, y) \cos \theta \right] \quad (4.23)$$

is a generalisation of the function

$$I_1(x, y) = \lambda^{\frac{1}{2}}(1, x, y) \left[(1-x)^2 - y(1+x) \right] , \quad (4.24)$$

introduced in Ref. [169], where x and y are squared mass ratios. After integrating over the angular variables, it is found that both the pseudoscalar meson decay rates do not depend on the helicity, as expected:

$$\Gamma_{\pm}(N \rightarrow \ell_{\alpha}^{-} P^{+}) = \Gamma_{\pm}(N \rightarrow \ell_{\alpha}^{+} P^{-}) = |V_{q\bar{q}}|^2 |U_{\alpha N}|^2 \frac{G_F^2 f_P^2 m_N^3}{16\pi} I_1(\xi_{\alpha}^2, \xi_P^2) , \quad (4.25)$$

$$\Gamma_{\pm}(N \rightarrow \nu P^0) = \left(\sum_{\alpha=e}^{\tau} |U_{\alpha N}|^2 \right) \frac{G_F^2 f_{P^0}^2 m_N^3}{16\pi} I_1(0, \xi_P^2) . \quad (4.26)$$

These rates agree with those presented in Refs. [205, 207], correcting a factor of two discrepancy in the νP^0 rate of Refs. [169, 206]. The Feynman diagram for the charged and neutral pseudoscalar meson channels are shown in 4.3.

The decay into a neutral meson is isotropic in the rest frame as seen in Eq. (4.22), while the charged-pion modes in Eqs. (4.20) and (4.21) inherit their angular dependence from $I^{\pm}(x, y; \theta_{\alpha})$, where θ_{α} is the lepton angle to the beam line in the heavy neutrino rest frame. The isotropy of the neutral current decay $N \rightarrow \nu P^0$ is a manifestation of the Majorana nature of the particle,

in agreement with the discussion of Ref. [214]. It is worth noting that if final states are not charge-identified, a similar isotropy is obtained for the total rate of charged semileptonic decays,

$$\begin{aligned} \frac{d\Gamma_{\pm}}{d\Omega_{\ell_{\alpha}}}(N \rightarrow \ell_{\alpha} P) &\equiv \frac{d\Gamma_{\pm}}{d\Omega_{\ell_{\alpha}}}(N \rightarrow \ell_{\alpha}^{+} P^{-}) + \frac{d\Gamma_{\pm}}{d\Omega_{\ell_{\alpha}}}(N \rightarrow \ell_{\alpha}^{-} P^{+}) \\ &= |U_{\alpha N}|^2 |V_{q\bar{q}}|^2 \frac{G_F^2 f_P^2 m_N^3}{16\pi} \frac{I_1(\xi_{\alpha}^2, \xi_P^2)}{2\pi}. \end{aligned} \quad (4.27)$$

The formulae above apply for all pseudoscalar mesons which are kinematically allowed. For instance, below the K^0 mass, the heavy neutrino can decay only into pions, but above this limit η and η' are also allowed in the final state.

Vector mesons

Although only for higher masses, HNL can also decay into vector mesons V , both via charged current, $N \rightarrow \ell^{\mp} V^{\pm}$, and neutral current, $N \rightarrow \nu V^0$. The polarised differential distributions in the heavy neutrino rest frame are

$$\frac{d\Gamma_{\pm}}{d\Omega_{\ell_{\alpha}}}(N \rightarrow \ell_{\alpha}^{-} V^{+}) = |U_{\alpha N}|^2 |V_{q\bar{q}}|^2 \frac{G_F^2 f_V^2 m_N^3}{16\pi} I_2^{\pm}(\xi_{\alpha}^2, \xi_V^2; \theta_{\alpha}), \quad (4.28)$$

$$\frac{d\Gamma_{\pm}}{d\Omega_{\ell_{\alpha}}}(N \rightarrow \ell_{\alpha}^{+} V^{-}) = |U_{\alpha N}|^2 |V_{q\bar{q}}|^2 \frac{G_F^2 f_V^2 m_N^3}{16\pi} I_2^{\mp}(\xi_{\alpha}^2, \xi_V^2; \theta_{\alpha}), \quad (4.29)$$

$$\frac{d\Gamma_{\pm}}{d\Omega_V}(N \rightarrow \nu V^0) = \left(\sum_{\alpha=e}^{\tau} |U_{\alpha N}|^2 \right) \frac{G_F^2 f_V^2 \kappa_V^2 m_N^3}{16\pi} \frac{I_2(0, \xi_V^2)}{4\pi}, \quad (4.30)$$

where

$$\begin{aligned} I_2^{\pm}(x, y; \theta) &= \frac{1}{4\pi} \lambda^{\frac{1}{2}}(1, x, y) \left[(1+x-y)(1+x+2y) - 4x \right. \\ &\quad \left. \pm (x+2y-1)\lambda^{\frac{1}{2}}(1, x, y) \cos \theta \right] \end{aligned} \quad (4.31)$$

and

$$I_2(x, y) = \lambda^{\frac{1}{2}}(1, x, y) [(1+x-y)(1+x+2y) - 4x], \quad (4.32)$$

also presented in Ref. [169]. The total decay widths are given by

$$\Gamma(N \rightarrow \ell_{\alpha}^{-} V^{+}) = \Gamma(N \rightarrow \ell_{\alpha}^{+} V^{-}) = |U_{\alpha N}|^2 |V_{q\bar{q}}|^2 \frac{G_F^2 f_V^2 m_N^3}{16\pi} I_2(\xi_{\alpha}^2, \xi_V^2), \quad (4.33)$$

$$\Gamma(N \rightarrow \nu V^0) = \left(\sum_{\alpha=e}^{\tau} |U_{\alpha N}|^2 \right) \frac{G_F^2 f_V^2 \kappa_V^2 m_N^3}{16\pi} I_2(0, \xi_V^2), \quad (4.34)$$

where the constants κ_V are the following combinations of the Weinberg angle, which depend on the flavour structure of V^0 :

$$\kappa_{\rho} = 1 - \sin^2 \theta_W, \quad \kappa_{\omega} = \frac{4}{3} \sin^2 \theta_W, \quad \kappa_{\phi} = \frac{4}{3} \sin^2 \theta_W - 1. \quad (4.35)$$

The charged pseudovector decay rates agree with Refs. [169, 205–207] while the neutral pseudoscalar calculation agrees with the corrected version presented in Ref. [207]. The Feynman diagram for these two processes are equivalent to the pseudoscalar meson ones, shown in 4.3.

As with the pseudoscalar meson decay rates, the Majorana nature leads to an isotropic decay into a neutral vector meson. An analogous effect holds for the charged vector meson decay if

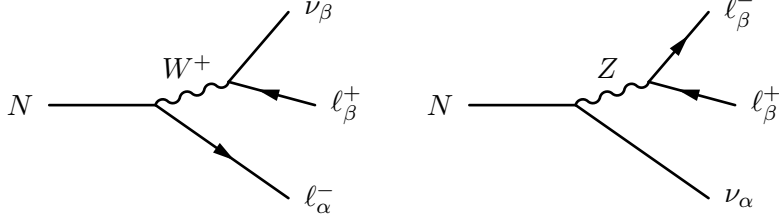


Figure 4.4: Feynman diagrams for the CC (left) and NC (right) leptonic three-body decays, via the $|U_{\alpha N}|^2$ mixing. The charge-conjugated diagram for the CC process is easily retrieved. No fermionic current is specified for the HNL leg since the decaying neutrino can be both Majorana or (pseudo-)Dirac in nature. The light neutrinos are Majorana fermions in the ISS realisations considered in this work.

the charges of final-state particles are not distinguished. In this case, the physically relevant decay distribution in the particle rest frame is given by

$$\begin{aligned} \frac{d\Gamma_{\pm}}{d\Omega_{\ell_{\alpha}}}(N \rightarrow \ell_{\alpha} V) &\equiv \frac{d\Gamma_{\pm}}{d\Omega_{\ell_{\alpha}}}(N \rightarrow \ell_{\alpha}^{-} V^{+}) + \frac{d\Gamma_{\pm}}{d\Omega_{\ell_{\alpha}}}(N \rightarrow \ell_{\alpha}^{+} V^{-}) , \\ &= |U_{\alpha N}|^2 \frac{G_F^2 f_V^2}{16\pi} |V_{q\bar{q}}|^2 m_N^3 \frac{I_2(\xi_{\alpha}^2, \xi_V^2)}{2\pi} . \end{aligned} \quad (4.36)$$

There are no vector mesons lighter than the K^0 , and these decays become relevant only for higher masses for which decays into ρ^{\pm} and $K^{*\pm}$, and for the neutral mode into ρ^0 , ω , and ϕ would be relevant.

Charged lepton pairs

Let us assign the momenta to the particles in the three-body decay as follows

$$N(k_1) \rightarrow \nu(k_2) \ell_{\alpha}^{-}(k_3) \ell_{\beta}^{+}(k_4) , \quad (4.37)$$

and denote $k_i^2 = m_i^2$. The five-dimensional phase space of the final-state particles can be parameterised using the two scaled invariant masses

$$s_1 = \frac{(k_2 + k_3)^2}{m_N^2} \quad \text{and} \quad s_2 = \frac{(k_2 + k_4)^2}{m_N^2} , \quad (4.38)$$

as well as the three lab-frame angular variables, (θ_3, φ_3) giving the direction of ℓ_{α}^{-} and φ_{43} denoting the relative azimuthal angle between ℓ_{α}^{-} and ℓ_{β}^{+} . Although $\cos \theta_4$ is not an independent element of this parametrisation, it is a physically relevant quantity which is used to simplify the presentation of the distributions below. It can be easily related to the fundamental variables $s_1, s_2, \theta_3, \varphi_3, \varphi_{43}$ as

$$\cos \theta_4 = \cos \theta_3 \cos \theta_{43} - \sin \theta_3 \sin \theta_{43} \cos \varphi_{43} , \quad (4.39)$$

with

$$\cos \theta_{43} = \frac{s_1 + s_2 - m_N^2 + 2 E_3 E_4}{|p_3| |p_4|} . \quad (4.40)$$

The differential decay rate is expressed as

$$d\Gamma_{\pm} = \frac{G_F^2 m_N^5}{16\pi^3} (|A_0|^2 \pm |A_1|^2) ds_1 ds_2 \frac{d\Omega_3}{4\pi} \frac{d\varphi_{43}}{2\pi} , \quad (4.41)$$

where Ω_3 assumes the conventional meaning and

$$|A_0|^2 \equiv C_1(s_2 - \xi_3^2)(1 + \xi_4^2 - s_2) + C_2(s_1 - \xi_4^2)(1 + \xi_3^2 - s_1) + 2C_3\xi_3\xi_4(s_1 + s_2 - \xi_3^2 - \xi_4^2) , \quad (4.42)$$

$$|A_1|^2 \equiv [C_4(s_2 - \xi_3^2) - 2C_6\xi_3\xi_4]\lambda^{\frac{1}{2}}(1, s_2, \xi_4^2)\cos\theta_4 + [C_5(s_1 - \xi_4^2) - 2C_6\xi_3\xi_4]\lambda^{\frac{1}{2}}(1, s_1, \xi_3^2)\cos\theta_3 . \quad (4.43)$$

The coefficients C_i are polynomials in chiral couplings and extended PMNS matrix elements, and they read

$$\begin{aligned} C_1 &= \sum_{\gamma=e}^{\tau} |U_{\gamma i}|^2 [(g_L^2 + g_R^2)\delta_{\alpha\beta} + \delta_{\gamma\alpha}(1 + \delta_{\alpha\beta}g_L)] , \\ C_2 &= \sum_{\gamma=e}^{\tau} |U_{\gamma i}|^2 [(g_L^2 + g_R^2)\delta_{\alpha\beta} + \delta_{\gamma\beta}(1 + \delta_{\alpha\beta}g_L)] , \\ C_3 &= 2\delta_{\alpha\beta}g_R \sum_{\gamma=e}^{\tau} |U_{\gamma i}|^2 (\delta_{\alpha\gamma} + g_L) , \\ C_4 &= \sum_{\gamma=e}^{\tau} |U_{\gamma i}|^2 [\delta_{\alpha\beta}(g_L^2 - g_R^2) + \delta_{\gamma\alpha}(1 + \delta_{\alpha\beta}g_L)] , \\ C_5 &= - \sum_{\gamma=e}^{\tau} |U_{\gamma i}|^2 [\delta_{\alpha\beta}(g_L^2 - g_R^2) + \delta_{\gamma\beta}(1 + \delta_{\alpha\beta}g_L)] , \\ C_6 &= 0 . \end{aligned} \quad (4.44)$$

On integration over the angular coordinates, however, only the $|A_0|^2$ term survives and the standard expression for the total decay rates is recovered through the following identities

$$\int ds_1 \int ds_2 (s_2 - \xi_3^2)(1 + \xi_4^2 - s_2) = \frac{I_1(0, \xi_3^2, \xi_4^2)}{12} , \quad (4.45)$$

$$\int ds_1 \int ds_2 (s_1 - \xi_4^2)(1 + \xi_3^2 - s_1) = \frac{I_1(0, \xi_4^2, \xi_3^2)}{12} , \quad (4.46)$$

$$\int ds_1 \int ds_2 2\xi_3\xi_4(s_1 + s_2 - \xi_3^2 - \xi_4^2) = \frac{I_2(0, \xi_3^2, \xi_4^2)}{12} . \quad (4.47)$$

The functions $I_1(x, y, z)$ and $I_2(x, y, z)$ are kinematic functions derived by integrating over the phase space

$$I_1(x, y, z) = 12 \int_{(\sqrt{x}+\sqrt{y})^2}^{(1-\sqrt{z})^2} \frac{ds}{s} (s - x - y) (1 + z - s) \lambda^{\frac{1}{2}}(1, x, y) \lambda^{\frac{1}{2}}(1, s, z) , \quad (4.48)$$

$$I_2(x, y, z) = 24\sqrt{yz} \int_{(\sqrt{y}+\sqrt{z})^2}^{(1-\sqrt{x})^2} \frac{ds}{s} (1 + x - s) \lambda^{\frac{1}{2}}(s, y, z) \lambda^{\frac{1}{2}}(1, s, x) . \quad (4.49)$$

Thus, the general expression for the total decay rate is again helicity independent and can be written as

$$\Gamma_{\pm}(N \rightarrow \nu \ell_{\alpha}^{-} \ell_{\beta}^{+}) = \frac{G_F^2 m_N^5}{192\pi^3} \left[C_1 I_1(0, \xi_3^2, \xi_4^2) + C_2 I_1(0, \xi_4^2, \xi_3^2) + C_3 I_2(0, \xi_3^2, \xi_4^2) \right]. \quad (4.50)$$

Using the expressions for C_i of Eq. (4.44) the total decay rates are given to first order in the heavy-active mixing parameters $U_{\alpha N}$ by

$$\Gamma_{\pm}(N \rightarrow \nu \ell_{\alpha}^{-} \ell_{\beta}^{+}) = \frac{G_F^2 m_N^5}{192\pi^3} \left[|U_{\alpha N}|^2 I_1(0, \xi_{\alpha}^2, \xi_{\beta}^2) + |U_{\beta N}|^2 I_1(0, \xi_{\beta}^2, \xi_{\alpha}^2) \right], \quad (4.51)$$

$$\Gamma_{\pm}(N \rightarrow \nu \ell_{\alpha}^{-} \ell_{\alpha}^{+}) = \frac{G_F^2 m_N^5}{96\pi^3} \sum_{\gamma=e}^{\tau} |U_{\gamma N}|^2 \left\{ (g_L g_R + \delta_{\gamma\alpha} g_R) I_2(0, \xi_{\alpha}^2, \xi_{\alpha}^2) + [g_L^2 + g_R^2 + \delta_{\gamma\alpha}(1 + 2g_L)] I_1(0, \xi_{\alpha}^2, \xi_{\alpha}^2) \right\}. \quad (4.52)$$

where $\alpha \neq \beta$, $g_L = -1/2 + \sin^2 \theta_W$ and $g_R = \sin^2 \theta_W$. The total decay rates agree with those in Refs. [169, 205–207] and correct a typographical mistake in the rates presented in Ref. [212]. The CC and NC diagrams for these three-body leptonic decays are shown in 4.4, bearing in mind that $\alpha = \beta$ is allowed and the inevitable interference terms must be considered.

All possible combinations of charged leptons except $\nu \tau^{-} \tau^{+}$ are allowed for masses below m_{D_s} . However, the decays into $\nu \tau^{\mp} e^{\pm}$ and $\nu \tau^{\mp} \mu^{\pm}$ can be neglected due to the limited phase space. The number of events from these modes is negligible with respect to other channels.

Other decays

There are some other decay rates relevant to this study but not as viable observable channels. First, the total decay width of the process $N \rightarrow \nu \bar{\nu} \nu$, mediated by the Z boson, reads

$$\Gamma(N \rightarrow \nu \bar{\nu} \nu) = \left(\sum_{\gamma=e}^{\tau} |U_{\gamma 4}|^2 \right) \frac{G_F^2 m_N^5}{96\pi^3}. \quad (4.53)$$

Although this decay mode is experimentally invisible, it is the dominant channel up to the pion mass, when two-body semileptonic decays open up, and plays a significant role in defining the branching ratios of the observable channels. The expression agrees with Refs. [169, 205–207] once the correct adjustments for Majorana and Dirac light neutrinos are applied. Secondly, there are other decay modes with small branching ratios and/or complicated final states which are not studied here. These include the one-loop decay into a photon which has received some interest as an observable signature in nonminimal models [149, 150, 215] where it may be enhanced. In the mass models considered in this work, it has a branching ratio of below 10^{-3} and will not be considered. Other interesting but neglected channels are the multi-pion decay modes discussed in Ref. [207], which are estimated to have at most a percent level branching ratio and a challenging hadronic final state for reconstruction.

4.2.2 Pseudo-Dirac neutrinos

Pseudo-Dirac particles or antiparticles are coherent superpositions of paired Majorana mass eigenstates,

$$N_P = U_{si} \nu_i + i U_{sj} \nu_j \quad \text{and} \quad \bar{N}_P = U_{si}^* \nu_i + i U_{sj}^* \nu_j, \quad (4.54)$$

where U_{sk} is the mixing between mass states and sterile flavour states. Thanks to this decomposition, the decay rate calculation can be recovered from the treatment of a pure Majorana state by summing coherently over the constituent Majorana contributions. In a true Dirac pair, the two components have identical masses and PMNS matrix elements which obey $U_{\alpha i} = \pm i U_{\alpha j}$. On coherent summation, this leads to perfect cancellation in any LNV process. For pseudo-Dirac particles, the constituent states have both a mass difference and mixing angles usually proportional to the LNV parameters introduced in Eq. (4.11), therefore of slightly different magnitudes. This leads to an imperfect cancellation in LNV modes. In spite of this, LNV decays are still allowed for pseudo-Dirac particles, but subdominant compared to pure Majorana states. The contributions to these negligible rates are suppressed by either the mass splitting or the difference in mixing angles, both of which are governed by the small LNV parameter in low-scale seesaw models. Although present, it seems unlikely that such channels would be of experimental relevance in the near future as they are always accompanied by dominant decay modes with oppositely-charged final states. The signatures of these particles is actually regulated by the leading order LNC effects and as such a strict Dirac limit is taken into the calculations of the decay rates for (pseudo-)Dirac pairs. However, if evidence for a sterile neutrino is found and significant statistics are collected, the search for LNV channels could in principle provide evidence of the Majorana or pseudo-Dirac nature of the HNL. Moreover, it would allow the measurement of the LNV parameter behind the model, which should correlate with the scale of light-neutrino masses and so provide an important test of the relationship between the novel particle and neutrino mass generation models.

The decay rates for a Dirac heavy (anti)neutrino are similar in form to those presented for the Majorana neutrino. The key differences are lepton number conservation, which acts to forbid certain channels, and differences in the angular distributions of the neutral current decays. For charged current-mediated processes, the distributions for Dirac neutrinos and antineutrinos are mathematically identical to the distributions for Majorana neutrinos. The two-body semileptonic decays are the same of Eqs. (4.20) and (4.28),

$$\frac{d\Gamma_{\pm}}{d\Omega_{\ell_{\alpha}}}(N_D \rightarrow \ell_{\alpha}^{-} P^{+}) = \frac{d\Gamma_{\mp}}{d\Omega_{\ell_{\alpha}}}(\bar{N}_D \rightarrow \ell_{\alpha}^{+} P^{-}) = \frac{d\Gamma_{\pm}}{d\Omega_{\ell_{\alpha}}}(N \rightarrow \ell_{\alpha}^{-} P^{+}) , \quad (4.55)$$

$$\frac{d\Gamma_{\pm}}{d\Omega_{\ell_{\alpha}}}(N_D \rightarrow \ell_{\alpha}^{-} V^{+}) = \frac{d\Gamma_{\mp}}{d\Omega_{\ell_{\alpha}}}(\bar{N}_D \rightarrow \ell_{\alpha}^{+} V^{-}) = \frac{d\Gamma_{\pm}}{d\Omega_{\ell_{\alpha}}}(N \rightarrow \ell_{\alpha}^{-} V^{+}) . \quad (4.56)$$

The situation for NC processes is different with respect to Majorana neutrinos. The distribution of the final-state particles is not isotropic anymore and it depends on the helicity state of the initial neutrino, in the way shown by the following differential rates

$$\begin{aligned} \frac{d\Gamma_{\pm}}{d\Omega_P}(N_D \rightarrow \nu P^0) &= \frac{d\Gamma_{\mp}}{d\Omega_P}(\bar{N}_D \rightarrow \bar{\nu} P^0) \\ &= \left(\sum_{\alpha=e}^{\tau} |U_{\alpha N}|^2 \right) \frac{G_F^2 f_{P^0}^2 m_N^3}{32\pi} I_1^{\pm}(0, \xi_P^2; \theta_P) , \end{aligned} \quad (4.57)$$

$$\begin{aligned} \frac{d\Gamma_{\pm}}{d\Omega_V}(N_D \rightarrow \nu V^0) &= \frac{d\Gamma_{\mp}}{d\Omega_V}(\bar{N}_D \rightarrow \bar{\nu} V^0) \\ &= \left(\sum_{\alpha=e}^{\tau} |U_{\alpha N}|^2 \right) \frac{G_F^2 f_V^2 \kappa_V^2 m_N^3}{32\pi} I_2^{\mp}(0, \xi_V^2; \theta_V) . \end{aligned} \quad (4.58)$$

The Feynman diagrams for these decay modes are the same of 4.3.

For three-body leptonic decays, the distribution is expressed in Eq. (4.41) with the relevant

coefficients for a Dirac neutrino

$$C_1^\nu = C_4^\nu = \sum_{\gamma=e}^{\tau} |U_{\gamma i}|^2 [\delta_{\alpha\beta} g_L^2 + \delta_{\gamma\alpha} (1 + \delta_{\alpha\beta} g_L)] , \quad (4.59)$$

$$C_2^\nu = C_5^\nu = \delta_{\alpha\beta} g_R^2 \sum_{\gamma=e}^{\tau} |U_{\gamma i}|^2 , \quad (4.60)$$

$$C_3^\nu = C_6^\nu = \delta_{\alpha\beta} g_R \sum_{\gamma=e}^{\tau} |U_{\gamma i}|^2 (\delta_{\gamma\beta} + g_L) , \quad (4.61)$$

and for a Dirac antineutrino

$$C_1^{\bar{\nu}} = -C_4^{\bar{\nu}} = \delta_{\alpha\beta} g_R^2 \sum_{\gamma=e}^{\tau} |U_{\gamma i}|^2 , \quad (4.62)$$

$$C_2^{\bar{\nu}} = -C_5^{\bar{\nu}} = \sum_{\gamma=e}^{\tau} |U_{\gamma i}|^2 [\delta_{\alpha\beta} g_L^2 + \delta_{\gamma\beta} (1 + \delta_{\alpha\beta} g_L)] , \quad (4.63)$$

$$C_3^{\bar{\nu}} = -C_6^{\bar{\nu}} = \delta_{\alpha\beta} g_R \sum_{\gamma=e}^{\tau} |U_{\gamma i}|^2 (\delta_{\alpha\gamma} + g_L) . \quad (4.64)$$

It is not surprising in view of Eq. (4.16) to observe that these coefficients are related to the ones for the Majorana case as

$$C_i = C_i^\nu + C_i^{\bar{\nu}} . \quad (4.65)$$

The total decay rates are found to be

$$\Gamma_{\pm}(N_D \rightarrow \nu \ell_{\alpha}^{-} \ell_{\beta}^{+}) = |U_{\alpha N}|^2 \frac{G_F^2 m_N^5}{192\pi^3} I_1(0, \xi_{\alpha}^2, \xi_{\beta}^2) , \quad (4.66)$$

$$\Gamma_{\pm}(\bar{N}_D \rightarrow \bar{\nu} \ell_{\alpha}^{-} \ell_{\beta}^{+}) = |U_{\beta N}|^2 \frac{G_F^2 m_N^5}{192\pi^3} I_1(0, \xi_{\beta}^2, \xi_{\alpha}^2) , \quad (4.67)$$

$$\begin{aligned} \Gamma_{\pm}(N_D \rightarrow \nu \ell_{\alpha}^{-} \ell_{\alpha}^{+}) &= \frac{G_F^2 m_N^5}{192\pi^3} \sum_{\gamma=e}^{\tau} |U_{\gamma N}|^2 \left\{ (g_L g_R + \delta_{\gamma\alpha} g_R) I_2(0, \xi_{\alpha}^2, \xi_{\alpha}^2) \right. \\ &\quad \left. + [g_L^2 + g_R^2 + \delta_{\gamma\alpha} (1 + 2g_L)] I_1(0, \xi_{\alpha}^2, \xi_{\alpha}^2) \right\} , \end{aligned} \quad (4.68)$$

$$\Gamma_{\pm}(\bar{N}_D \rightarrow \bar{\nu} \ell_{\alpha}^{-} \ell_{\alpha}^{+}) = \Gamma_{\mp}(N_D \rightarrow \nu \ell_{\alpha}^{-} \ell_{\alpha}^{+}) , \quad (4.69)$$

where $\alpha \neq \beta$. The resulting rates agree with those in Refs. [169, 205–207].

All decay rates not listed above are forbidden for a Dirac (anti)particle as the combination of production and decay would amount to a LNV process. For the available modes, all NC modes are smaller by a factor of two for a Dirac (anti)neutrino compared to the equivalent Majorana process; however, the major difference between the Dirac (anti)neutrino and Majorana distributions is that these NC channels are dependent on the angular variables. The differences in the distributions of the final-state particles could be exploited to identify the fermionic nature of the decaying HNL [214].

4.3 Heavy neutrino production

Heavy neutrinos can be produced in a beam dump experiment via the same processes that generate light neutrinos (see Section 1.3.3). If kinematically allowed, heavy neutrino states can

Table 4.2: Production channels at beam dump facilities yielding neutrinos, with the respective branching ratios (taken from Ref. [15]), considered for this work. The last column shows the maximum neutrino mass allowed if a massive state is produced. On the left, all the decays yielding ν_e , ν_μ , and $\bar{\nu}_\mu$ up to the K^0 mass are shown. On the right, the neutrino sources which depends on the D_s^+ decay chain are shown; the four τ decays listed here are the ones with the highest branching ratio.

	Channel	BR (%)	m_N (MeV)
$\pi^+ \rightarrow$	$\mu^+ \nu_\mu$	99.98	33.91
	$e^+ \nu_e$	0.01	139.06
$K^+ \rightarrow$	$\mu^+ \nu_\mu$	63.56	387.81
	$\pi^0 e^+ \nu_e$	5.07	358.19
	$\pi^0 \mu^+ \nu_\mu$	3.35	253.04
	$e^+ \nu_e$	0.16	493.17
	$\pi^\pm e^\mp \nu_e$	40.55	357.12
$K_L^0 \rightarrow$	$\pi^\pm \mu^\mp \nu_\mu$	27.04	252.38
	$\bar{\nu}_\mu e^+ \nu_e$	100.00	105.14

	Channel	BR (%)	m_N /MeV
$D_s^+ \rightarrow$	$\tau^+ \nu_\tau$	5.48	191.42
	$\mu^+ \nu_\mu$	0.55	1862.63
	$e^+ \nu_e$	0.008	1967.78
$\tau^+ \rightarrow$	$\pi^+ \pi^0 \bar{\nu}_\tau$	25.49	1502.31
	$\bar{\nu}_\tau e^+ \nu_e$	17.82	1776.35
	$\bar{\nu}_\tau \mu^+ \nu_\mu$	17.39	1671.20
	$\pi^+ \bar{\nu}_\tau$	10.82	1637.29

be sourced from two- and three-body decays of mesons and charged leptons. All the neutrino production channels considered in this analysis are listed in Table 4.2, where the heaviest neutrino mass m_N that is accessible by kinematics is also reported. The possible parent particles producing neutrinos are, up to 2 GeV in mass, pions, muons, charged and neutral kaons, strange charmed mesons D_s , and τ leptons. As explained in Section 1.3.3, the production of mesons above the kaon mass requires very energetic proton beams which the majority of neutrino accelerator experiments do not possess. For this reason, the HNL mass range considered goes from a few MeV up to almost 2 GeV.

The flux of heavy neutrinos produced is estimated starting from the flux of light neutrinos and scaling it by an energy-independent kinematic factor. Given a certain SM neutrino production process, $Q \rightarrow \nu_\alpha Q'$, a scale factor is naively defined by the ratio between the decay width of the same process producing massive neutrinos, $Q \rightarrow N Q'$, and the rate of the SM decay with light neutrinos. The full flux of nearly-sterile neutrinos with a given helicity is therefore a linear combination of the different neutrino flux components, $\phi_{Q \rightarrow \nu_\alpha}$, summing over all existing parents and all allowed flavours:

$$\frac{d\phi_N^\pm}{dE}(E_N) \approx \sum_{Q,\alpha} \mathcal{K}_\pm^{Q,\alpha}(m_N) \frac{d\phi_{Q \rightarrow \nu_\alpha}}{dE}(E_N - m_N), \quad (4.70)$$

where

$$\mathcal{K}_\pm^{Q,\alpha}(m_N) \equiv \frac{\Gamma_\pm(Q \rightarrow N Q')}{\Gamma(Q \rightarrow \nu_\alpha Q')}. \quad (4.71)$$

The ratio \mathcal{K} is proportional to the mixing parameter $|U_{\alpha N}|^2$ and contains only kinematic functions of the involved masses. These are responsible for correcting phase space and helicity terms.

The helicity state plays a fundamental role in the production rate, in contrast with the case of neutrino decays, since there is no arbitrariness in the polarisation direction this time; this is defined by the neutrino momentum in the rest frame of the parent particle. The massive spinor-helicity formalism is employed to compute the production decay rates for both Majorana and Dirac neutrinos, and these are used to build the scale factors for each neutrino helicity. Even though lepton number is preserved differently in the two cases and different Feynman rules hold, all the production channels of interest in this work are mediated by charge current interactions and therefore the rates are mathematically identical for Majorana and Dirac neutrinos. If the

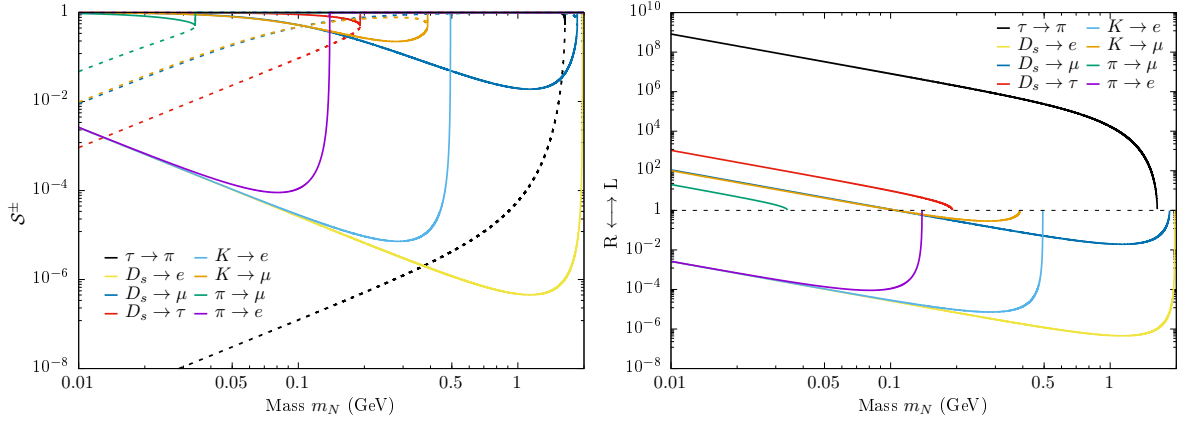


Figure 4.5: On the left, the factors \mathcal{S}^- (solid) and \mathcal{S}^+ (dashed) from Eq. (4.75) are shown. When the mass approaches to zero, the percentage of neutrinos produced with negative helicity tends to 100 %. On the right, the ratio between scale factors \mathcal{K}^+ and \mathcal{K}^- from Eq. (4.72) shows the relative amount of neutrinos with given mass produced with helicity $h = -1$ (L) and $h = +1$ (R) produced.

neutrino is Dirac, the production decay width for an antineutrino with given helicity is the same as the one of the neutrino, but with opposite helicity. The phenomenology of the scale factors is different for two- and three-body decays and so they are discussed, respectively, in Section 4.3.1 and Section 4.3.2. Only the four most probable decay modes of the τ lepton are considered in this analysis, as they provide a sufficient description of their contribution to the overall flux. The decay $\tau^+ \rightarrow \bar{\nu}_\tau \pi^+ \pi^0$ is studied only at the level of phase space sampling in this work.

4.3.1 Two-body decays

A massless neutrino (antineutrino) has its chiral and helicity states degenerate, and so it is always produced with a negative (positive) helicity. It follows that the component of the light neutrino beam produced in two-body decays of pseudoscalar mesons is polarised. The initial spin, which is zero, must be preserved in the decay, and since the helicity of the neutrino in the rest frame is fixed, the accompanying lepton is produced with a “wrong” helicity. This is permitted by the nonzero mass of the charged lepton and therefore final states with light flavour leptons undergo helicity suppression. As soon as the neutrino mass deviates from zero, the correspondence between chirality and helicity is lost and the neutrino can be produced with both polarisations. The main consequence is that the production of heavy neutrinos from light flavour mixings (electron) appears to be enhanced with respect to heavy flavours (muon and tau). The effect is particularly dramatic when the mass difference between parent meson and charged lepton widens, as it happens with the electron decay of D_s , the enhancement of which is around 10^6 for neutrino masses near 1 GeV.

The scale factor \mathcal{K}_h for leptonic decays of a pseudoscalar meson P into neutrinos with helicity h , is given by the analytic expression

$$\mathcal{K}_\pm^{P,\alpha}(m_N) = |U_{\alpha N}|^2 \frac{\lambda^{\frac{1}{2}}(1, \xi_N^2, \xi_{\ell_\alpha}^2)}{2\xi_{\ell_\alpha}^2(1 - \xi_{\ell_\alpha}^2)^2} \times \left[\xi_{\ell_\alpha}^2 + \xi_N^2 - (\xi_N^2 - \xi_{\ell_\alpha}^2)^2 \pm (\xi_N^2 - \xi_{\ell_\alpha}^2)\lambda^{\frac{1}{2}}(1, \xi_N^2, \xi_{\ell_\alpha}^2) \right], \quad (4.72)$$

where λ is the Källén function

$$\lambda(a, b, c) = (a - b - c)^2 - 4bc, \quad (4.73)$$

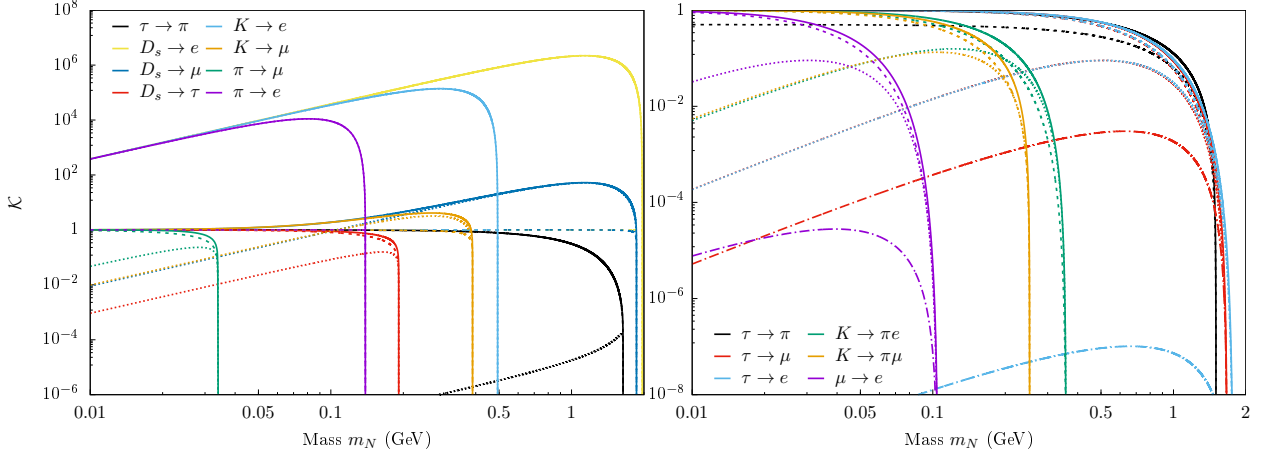


Figure 4.6: The scale factors separated by helicity components are shown. In two-body decays (left), the $h = -1$ components (dashed) for all channels do not depend on the mass. The enhancement is driven by the $h = +1$ components (dotted), which are the dominant contribution of the unpolarised factors (solid). In three-body decays (right), there are two different scale factors for purely leptonic decays, noted as $\ell_\alpha \rightarrow \ell_\beta$: if the decay is mediated by $|U_{\beta N}|^2$, for which the $h = -1$ (dashed) and the $h = +1$ (dotted) components are comparable, and if the decay is mediated by $|U_{\alpha N}|^2$, for which $h = -1$ dominates over the $h = +1$ (dotdashed). In both cases, the two parts sum up to the same quantity (solid). The kaon decays are also divided in $h = -1$ (dashed) and $h = +1$ (dotted) components; $\tau^+ \rightarrow \nu \pi^+ \pi^0$ is studied only at the phase space level.

and $\xi_i = m_i/m_X$ is the mass ratio of the final-state particle i over the parent particle mass. When summing over the helicity states, the resulting factor coincides with the one computed in Ref. [216],

$$\mathcal{K}^{P,\alpha}(m_N) = \sum_{h=\pm 1} \mathcal{K}_h^{P,\alpha}(m_N) = |U_{\alpha N}|^2 \frac{\lambda^{\frac{1}{2}}(1, \xi_N^2, \xi_{\ell_\alpha}^2)}{\xi_\alpha^2(1 - \xi_{\ell_\alpha}^2)^2} [\xi_{\ell_\alpha}^2 + \xi_N^2 - (\xi_N^2 - \xi_{\ell_\alpha}^2)^2]. \quad (4.74)$$

In order to understand the effect of Eq. (4.72), it is convenient to define the fraction of neutrinos produced with a certain helicity as

$$\mathcal{S}^\pm = \frac{\mathcal{K}_\pm^{P,\alpha}}{\mathcal{K}_{+1}^{P,\alpha} + \mathcal{K}_{-1}^{P,\alpha}} = \frac{1}{2} \left[1 \pm \frac{(\xi_N^2 - \xi_{\ell_\alpha}^2) \lambda^{\frac{1}{2}}(1, \xi_N^2, \xi_{\ell_\alpha}^2)}{\xi_{\ell_\alpha}^2 + \xi_N^2 - (\xi_N^2 - \xi_{\ell_\alpha}^2)^2} \right]. \quad (4.75)$$

In the limit of a massless neutrino, i.e. $\xi_N \rightarrow 0$, the fractions are $\mathcal{S}_+ \rightarrow 0$ and $\mathcal{S}_- \rightarrow 1$, as expected: all neutrinos are produced with a negative helicity. The opposite is true when the charged lepton is in the massless limit and the neutrinos are produced with a positive helicity. The behaviour of the ratio \mathcal{S}^\pm is shown in Fig. 4.5.

The only two-body decay of a lepton considered in this work is $\tau \rightarrow \nu_\tau \pi$, whose scale factor reads

$$\begin{aligned} \mathcal{K}_\pm^{\tau,\pi}(m_N) &= |U_{\tau N}|^2 \frac{\lambda^{\frac{1}{2}}(1, \xi_N^2, \xi_\pi^2)}{2(1 - \xi_\pi^2)^2} \\ &\times \left[(1 - \xi_N^2)^2 + \xi_\pi^2(1 + \xi_N^2) \mp (1 - \xi_N^2) \lambda^{\frac{1}{2}}(1, \xi_N^2, \xi_\pi^2) \right]. \end{aligned} \quad (4.76)$$

The structure is similar to the scale factor for pseudoscalar meson two-body decays, given in Eq. (4.72), and analogous considerations as above can be deduced. This is explained by crossing symmetries, as the matrix element of the process is the same. In this case, however, the positive helicity component does not lead to any enhancement before the phase space cut-off.

The effect of the scale factors as a function of the neutrino mass can be appreciated on the left panel of Fig. 4.6, where the enhancement of negative helicity terms is apparent. The phase space is also correctly described and the \mathcal{K} drops to zero as the neutrino mass approaches its parent mass.

4.3.2 Three-body decays

Scale factors for three-body decays are defined in the same way as two-body decay ones. Because of the different number of degrees of freedom, the helicity of the outgoing neutrinos is not fixed by the spin of the parent particles. Hence, these factors are not responsible for any enhancement in the decay rate, but they only quench the process as the neutrino mass upper limit is approached (see Table 4.2). The scale factors have nonetheless distinct behaviours depending on the helicity state involved. They are plotted as a function of the heavy neutrino mass on the right panel of Fig. 4.6.

The decay of a charged lepton (antilepton) of flavour α to a charged lepton (antilepton) of flavour β can be proportional to either $|U_{\alpha N}|^2$ or $|U_{\beta N}|^2$, producing a heavy Dirac neutrino (antineutrino) in the first case or an antineutrino (neutrino) in the second case. If the neutrino is Majorana, the decay can occur via both mixing matrix elements because the lepton number can be violated. Decays of muons and taus yield massive neutrinos with the following decay rate

$$\Gamma_{\pm}(\ell_{\alpha}^{\pm} \rightarrow \ell_{\beta}^{\pm} \nu N) = \frac{G_F^2 m_{\alpha}^5}{192\pi^3} \left[|U_{\alpha N}|^2 I_{\ell}^{\pm}(\xi_N^2, \xi_{\ell\beta}^2, 0) + |U_{\beta N}|^2 I_{\bar{\ell}}^{\pm}(0, \xi_{\ell\beta}^2, \xi_N^2) \right], \quad (4.77)$$

where the integrals $I_{\ell, \bar{\ell}}(x, y, z)$ are given by

$$I_{\ell}^{\pm}(x, y, z) = 12 \int_{(\sqrt{x}+\sqrt{y})^2}^{(1-\sqrt{z})^2} \frac{ds}{s} (1+z-s) \left[s-x-y \mp \lambda^{\frac{1}{2}}(s, x, y) \right] \lambda^{\frac{1}{2}}(s, x, y) \lambda^{\frac{1}{2}}(1, s, z), \quad (4.78)$$

$$I_{\bar{\ell}}^{\pm}(x, y, z) = 12 \int_{(\sqrt{x}+\sqrt{y})^2}^{(1-\sqrt{z})^2} \frac{ds}{s} \left[1+z-s \mp \lambda^{\frac{1}{2}}(1, s, z) \right] (s-x-y) \lambda^{\frac{1}{2}}(s, y, z) \lambda^{\frac{1}{2}}(1, s, z). \quad (4.79)$$

The helicity decompositions in I_{ℓ} and $I_{\bar{\ell}}$ are different, but the spin-averaged decay width is the same.

Neutral and charged kaons produce neutrinos in three-body semileptonic decays. Both of them can decay into either a muon or an electron and a charged pion if the decaying kaon is neutral or a neutral pion if the kaon is charged. The decay width of a pseudoscalar meson h_1 to a lighter meson h_2 is given by

$$\Gamma_{\pm}(h_1^{+,0} \rightarrow h_2^{0,+} \ell_{\alpha}^{\pm} N) = \frac{G_F^2 m_{h_1}^5}{128\pi^3} |U_{\alpha N}|^2 |V_{q\bar{q}}|^2 I_{h_1}^{\pm}(\xi_{h_2}^2, \xi_{\ell\alpha}^2, \xi_N^2). \quad (4.80)$$

The integral $I_h(x, y, z)$ is

$$I_h^{\pm}(x, y, z) = \int_{(\sqrt{x}+\sqrt{y})^2}^{(1-\sqrt{z})^2} ds \int_{t_-}^{t_+} dt \left[F^2 A^{\pm}(s, t) + G^2 B^{\pm}(s, t) - \text{Re}(F^* G) C^{\pm}(s, t) \right],$$

$$\text{with } t_{\pm} = x + z + \frac{(1-s-z)(s-y+x) \pm \lambda^{\frac{1}{2}}(s, y, z) \lambda^{\frac{1}{2}}(1, s, z)}{2s}, \quad (4.81)$$

where F and G are convenient combinations of hadronic form factors $f^{(h,h')}$. From lattice QCD considerations, form factors should carry the correct Clebsch-Gordan, but here it is safe to drop them as they are irrelevant when studying scale factors. The combinations F and G are

$$F = 2 f_+^{(h,h')}(u) = f_+^{(h,h')}(0) \left(1 + \lambda_+^{(h,h')} \frac{u}{x} \right), \quad (4.82)$$

$$\begin{aligned} G &= f_+^{(h,h')}(u) - f_-^{(h,h')}(u) \\ &= f_+^{(h,h')}(0) \left[1 + \lambda_+^{(h,h')} \frac{u}{x} - \left(\lambda_+^{(h,h')} - \lambda_0^{(h,h')} \right) \left(1 + \frac{1}{x} \right) \right], \end{aligned} \quad (4.83)$$

with λ parameterising the linear dependence [15] of the form factors with respect to the momentum transfer between the two mesons, u , directly connected to the other Mandelstam variables, s and t :

$$u = 1 + x + y + z - s - t. \quad (4.84)$$

The values of $\lambda_{+,0}$ are determined experimentally [15]. The functions A , B , and C are

$$A^\pm(s, t) = \frac{1}{2}(1 + y - t) \left[1 + z - s \mp \lambda^{\frac{1}{2}}(1, z, s) \right] - \frac{1}{2} \left[u - y - z \mp \lambda^{\frac{1}{2}}(u, y, z) \right], \quad (4.85)$$

$$B^\pm(s, t) = \frac{1}{2}(y + z)(u - y - z) + 2yz \mp (y - z) \frac{\lambda^{\frac{1}{2}}(u, y, z)}{2}, \quad (4.86)$$

$$C^\pm(s, t) = z(1 + y - t) + \left[y \pm \frac{\lambda^{\frac{1}{2}}(u, y, z)}{2} \right] (1 + z - s). \quad (4.87)$$

When summing over helicity states, the kinematic functions simplify to

$$A(s, t) = (1 + y - t)(1 + z - s) - (u - y - z), \quad (4.88)$$

$$B(s, t) = (y + z)(u - y - z) + 4yz, \quad (4.89)$$

$$C(s, t) = 2z(1 + y - t) + 2y(1 + z - s). \quad (4.90)$$

The scale factor was checked numerically against the result of Ref. [217].

The final three-body decay studied in this work is $\tau^+ \rightarrow \bar{\nu}_\tau \pi^+ \pi^0$, even though this channel is introduced only at the phase space level. The scale factors for the two helicity components are therefore assumed to be identical, $\mathcal{K}_\pm = 1/2$, such that the neutrino flux subcomponent coming from this decay consists of equal number of heavy neutrinos with helicity $h = +1$ and $h = -1$.

Summary

The origin of the light neutrino masses are elegantly described by low-scale seesaw models which can additionally predict new phenomenologically viable physics scales, accessible by next generation experiments. In this chapter, the inverse seesaw manifestation of the neutrino mass matrix has been investigated in an extended SM scenario. Depending on the precise realisation, Majorana or (pseudo-)Dirac heavy neutral leptons are allowed to decay into SM visible particles. Such heavy neutrinos can be produced in the beam with light neutrinos at neutrino beam facilities and for this reason the region of interest spans from tens of MeV up to a few GeV. Formulae to compute production and decay rates have been computed using spinor-helicity formalism so as to pay particular attention to the HNL helicity. It is found that not only Dirac and Majorana neutrinos have different total decay rates in neutral current processes, but

also that their decay distributions have a different dependency on the helicity. An effective evaluation of the heavy neutrino flux, in which the HNL mass plays an important role, has also been carried out. Certain production modes are not helicity-suppressed anymore and so they appear enhanced with respect to the same production channels for light neutrinos. The two helicity components of the neutrino flux therefore behave differently and their correct descriptions are necessary for a precise prediction of HNL decay events.

Chapter 5

HNL discovery with the DUNE experiment

In a *beam dump* experiment, an energetic beam of protons is directed into a fixed dense block of material, such as concrete or graphite in order to absorb the hadronic cascade and stop secondary charged particles. This facilitates the study of stable and long-lived particles. The approach resembles accelerator neutrino experiments, in which the production of pions, kaon, and muons is maximised to generate an intense and focused neutrino beam. A crucial difference between oscillation detectors and dedicated beam dump searches of the past is that the former are devised to enhance the SM neutrino scattering rate, while the latter try to suppress it in order to reduce backgrounds and favour the search for exotic and rare long-lived particles. It is exciting to note, however, that neutrino oscillation detectors are able to perform beam-dump-like measurements [172, 213, 218]. This is most favourable for searches of heavy neutral leptons (HNL), since they could be produced at accelerator facilities in the beam with light neutrinos (see Section 4.3). The HNL can subsequently decay in one of the ways described in Section 4.2 inside a detector in proximity of the beam target, leaving a detectable signature. The event rate is directly linked to the sterile–active neutrino mixings of the extended PMNS matrix. The strongest limits on mixing angles with heavy states were set by the PS191 experiment [170, 171], a beam dump experiment which ran at CERN in 1984. Its most stringent upper bounds on the novel mixing angles are $|U_{eN}|^2 \leq 10^{-8}$ and $|U_{\mu N}|^2 \leq 10^{-9}$ for neutrino masses between the pion and the kaon mass. Powerful proton beams and strong particle reconstruction capabilities of current and upcoming neutrino detectors will allow competitive searches for heavy and long-lived neutrinos and possible improvement of present limits. Among the running experiments, T2K has recently reached similar constraints to PS191 [172]. As an example of planned experiments, it has been shown that the *Short Baseline Neutrino program* (SBN) [154] can reach interesting bounds on HNL searches [212], despite having a naively large background which can be controlled thanks to the distinctive kinematics of neutrino decays and the high performance of Liquid Argon (LAr) technologies. Future long baseline oscillation experiments, such as the Deep Underground Neutrino Experiment (DUNE) [219], will see a greatly diluted flux of nearly-sterile neutrinos at their far detectors and consequently poor sensitivity. However, the near detector of DUNE (DUNE ND), placed 574 m from the target, has a great potential for searches of new physics [220]. Close proximity to a very intense neutrino beam and cutting-edge event reconstruction capabilities will allow the DUNE ND to undertake valuable searches for BSM physics in an entirely complementary way to the central oscillation physics programme.

In this chapter, a detailed analysis of the sensitivity of the DUNE ND to HNL in beam-dump-

style searches is presented. The following analysis is based on the theoretically consistent models from Chapter 4, in which sterile neutrinos are associated with a low-scale seesaw mechanism to address neutrino mass generation. In particular, the production modes of Table 4.2 and most of the decay channels of Table 4.1 are considered. The analysis presented here is refined and extended in comparison with previous works [220, 221], thanks to the polarised rates computed in Chapter 4 and the latest configuration of the DUNE ND [222]. The ND and the neutrino beam are described in Section 5.1; a first estimate of the ν_τ flux component is also presented. The simulation used to compute the number of HNL decays at the ND site is explained in Section 5.2, and possible backgrounds for the most relevant discovery channels are discussed there. Results of the sensitivity to HNL discovery are reported in Section 5.3. Finally, discussions of the possibility of resolving mass models and the fermionic nature of HNLs is carried out respectively in Section 5.4 and Section 5.5.

5.1 The near detector of DUNE

DUNE [219] is a long-baseline oscillation experiment that will study neutrino physics in great detail, focusing mainly on the determination of the CP violating phase, δ_{CP} , and the mass ordering, i.e. the sign of Δm_{32}^2 , and on the precision measurement of other oscillation parameters, in particular θ_{23} . These goals can be achieved thanks to both an intense neutrino beam and a high-resolution Far Detector (FD), consisting of a 40 kt Liquid Argon Time Projection Chamber (LArTPC), situated 1300 km from the beam target. The drift velocity of ionised electrons in LAr, typically of the order of cm/ μs , can be controlled with sufficient precision, by tuning the electric field to result in high spatial resolution for event reconstruction [223]. The LAr is advantageous compared to the gaseous counterpart because it is around one thousand times denser, increasing the interaction probability which is a valuable feature for neutrino physics. Employing very pure argon, the recombination of released electrons can be reduced and so the LArTPC design can be scaled to large volumes, as it will be done for DUNE. To overcome high-purity challenges, the TPC can be operated in dual phase mode, in which a portion of the chamber is filled with argon vapour. Once the drifting electrons are extracted from the liquid phase to the gaseous one, avalanche multiplication of the electrons amplifies the signal. LAr also scintillates with a high light yield, around 40 photons/keV, and differently from other liquefied noble gases LAr is transparent to its scintillation wavelength, which peaks at 126.8 nm. A photodetection system can collect the scintillation light giving an additional handle on event reconstruction. All these exceptional properties make LArTPC a powerful tool for precision neutrino physics.

A very sensitive FD alone, however, is not enough due to numerous uncertainties on the neutrino flux and cross-section parameters. A smaller and closer detector, called near detector (ND), is therefore adopted to normalise the flux of neutrinos reaching the FD and to help cancel out many of the neutrino–nucleon cross-section systematics. The DUNE ND will be placed 574 m from the target. Its design is a hybrid concept consisting of a small LArTPC placed in front of a magnetised high-pressure gaseous TPC [222]. The latter is a module complementary to the LArTPC, controlling escaping or below-threshold particles from the LArTPC, but is also capable of performing standalone measurement. For its versatile nature, it is called Multi-Purpose Detector (MPD). The subsystem LArTPC/MPD is movable inside the ND hall—following the DUNE-PRISM concept [222]—for better profiling the neutrino flux at different angles. There will be a on-axis module, called 3D Scintillation Tracker (3DST), to monitor the stability of the beam flux and neutron contamination. The configuration of the ND system in the hall is shown in Fig. 5.1. Currently, the proposed fiducial volume for the LArTPC module

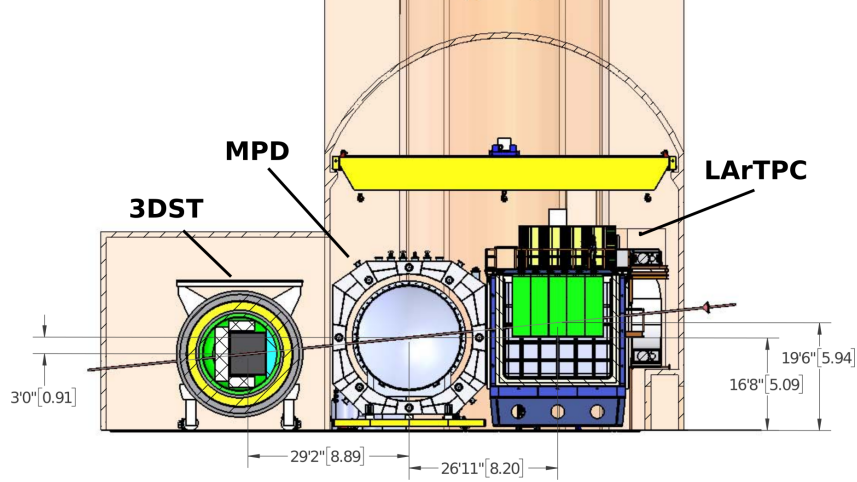


Figure 5.1: Lateral view of the near detector complex of DUNE.

is 36 m^3 and 50 t of LAr, employing the ArgonCube technology [224], whereas the design for the MPD is based on the TPC of ALICE [225]. It consists of a cylinder of 102 m^3 with gas at a pressure of 10 atm and a fiducial mass of 1 t ; the gas assumed for the study is a an $80\text{--}20$ mixture of Ar-CH_4 . The 3DST is designed to have a fiducial mass of around 8.7 t of plastic scintillating material and wavelength shifting plates. For this analysis, only the two core subdetectors, the LArTPC and the MPD, are taken into account. The main difference between these two ND modules is that the gaseous TPC has a larger volume than the LArTPC. This feature is favourable when studying rare events, like heavy neutrino decays, because more neutrinos enter the fiducial volume. Furthermore, the lower density of the MPD helps reduce the number of neutrino scattering events which are background to rare signatures. Apart from volume and density differences and relative positions in the detector hall, the two ND units are assumed to have a similar detection performance and to be on-axis; the magnetisation of the gaseous TPC is not considered for HNL discovery. These approximations simplify the study which is purely phenomenological in style. A more accurate and detailed study will be carried out by the experimental collaboration.

Thanks to its proximity to the accelerator, the ND will be exposed to an extremely intense neutrino beam, with a flux peak around five million times greater than at the FD. The Long Baseline Neutrino Facility (LBNF) at Fermilab will deploy a very energetic beam of protons, extracted from the Fermilab main injector and delivered to a graphite target. The collision produces secondary particles which are collimated by a focusing horn system and then decay forming a neutrino beam (see Section 1.3.3). Assuming an 80 GeV proton beam at 1.2 MW for the first six years and at 2.4 MW for a second set of six years [219], the ND will collect a total of 2.65×10^{22} protons on target (POT) over the lifespan of the experiment, running for the same amount of time in neutrino and antineutrino mode. The ND will be placed on-axis for half of the total runtime, whereas it will be positioned at different angles off-axis for the remaining acquisition period, enacting the DUNE-PRISM concept. The search for HNL decays can benefit to some extent with the detector positioned at off-axis angles, as the SM neutrino background is particularly reduced despite a lower signal rate. However, the modelling of the neutrino beam profile at different angles using only information from the on-axis spectrum is not trivial. Half of the total statistics will be collected with a reversed horn current configuration, but the parentage composition of the neutrino beam in $\bar{\nu}$ -mode was not provided, as well as the off-axis beam flux. In this work, just the on-axis configuration of the ND with a forward

Table 5.1: Comparison between experiments mentioned in this work. Using PS191 as a reference unit, the exposure is defined as $\text{POT} \times \text{Energy} \times \text{Volume} \times \text{Baseline}^{-2}$, where “Energy” is the proton beam energy. The NA62 and SHiP experiments are not directly comparable with SBND and DUNE ND, in that different technologies are involved; the RICH detectors are adopted as fiducial volume for NA62, whereas the volume of SHiP is estimated as the cone contained in the “hidden sector” vacuum vessel. The volume is a driving feature in the definition of the total exposure and it is of utter importance for searches of decay-in-flight events.

	PS191	DUNE ND	SBND	NA62	SHiP
Baseline	128 m	574 m	110 m	220 m	60 m
Volume	216 m ³	150 m ³	80 m ³	750 m ³	590 m ³
Energy	19.2 GeV	80 GeV	8 GeV	400 GeV	400 GeV
POT	0.86×10^{19}	1.32×10^{22}	6.6×10^{20}	3×10^{18}	2×10^{20}
Exposure	1.0	220.9	16.4	8.5	5820

horn current configuration is considered, which would correspond to a quarter of the runtime, or 0.66×10^{22} POT. The same analysis of this study can nonetheless be applied equally to the beam in antineutrino mode and it should result in a sensitivity similar to the neutrino mode configuration, being wary of the different composition of the neutrino spectrum. Even though a complete estimate of the DUNE ND sensitivity cannot be achieved, with the above caveats the total sensitivity to HNL—including off-axis angles and antineutrino mode beam—can be naively equivalent to six years of data taking, i.e. 1.32×10^{22} POT, with the beam in neutrino mode and the ND on-axis.

5.1.1 Exposure

A summary of the detector features relevant for this analysis is reported in Table 5.1, where the DUNE ND is compared to other beam dump experiments: PS191 [170, 171], SBND which is the detector of the *SBN program* with the best sensitivity to HNL [212], NA62 [226], and SHiP [227]. The total exposure of the experiment is defined as the proton accelerator beam power integrated over the total run time and scaled by the volume of the detector over the baseline squared. The beam power times the run time corresponds to the number of POT times the proton energy. With this definition, an exposure twelve times bigger is expected for the DUNE ND system with respect to SBND, and around two hundred times bigger than PS191. Although NA62 and SHiP can be considered beam dump experiments, these experiments have a different design and use technologies not directly comparable to TPC and tracker experiments; they are reported here for thoroughness since they give competitive sensitivities to HNL searches. The estimated exposure of NA62 is limited by its number of POT and by just one year of data taking; in spite of this, the experiment is optimised to study kaon decays and has good sensitivity to HNL [228]. The SHiP experiment presents an exposure thirty times bigger than the DUNE ND, but the detector is specifically designed to search for BSM physics, including heavy neutrinos [229, 230]. The decay-in-flight search hugely benefits from its 50 m long decay vessel and short baseline. The DUNE experiment, however, is planned to start before than the SHiP experiment and this new physics search is totally complementary to the main physics goal of oscillation physics; no modification of the detector design and no special data acquisition mode are required for DUNE. On the collider physics frontier, the MATHUSLA [231] and the FASER [232] experiments will perform a dedicated search for extremely weakly-interacting and long lived particles, like HNLs, for which they present interesting sensitivities [231, 233]. MATHUSLA will be a $800 \times 10^3 \text{ m}^3$ hodoscope placed on the surface above the ATLAS or

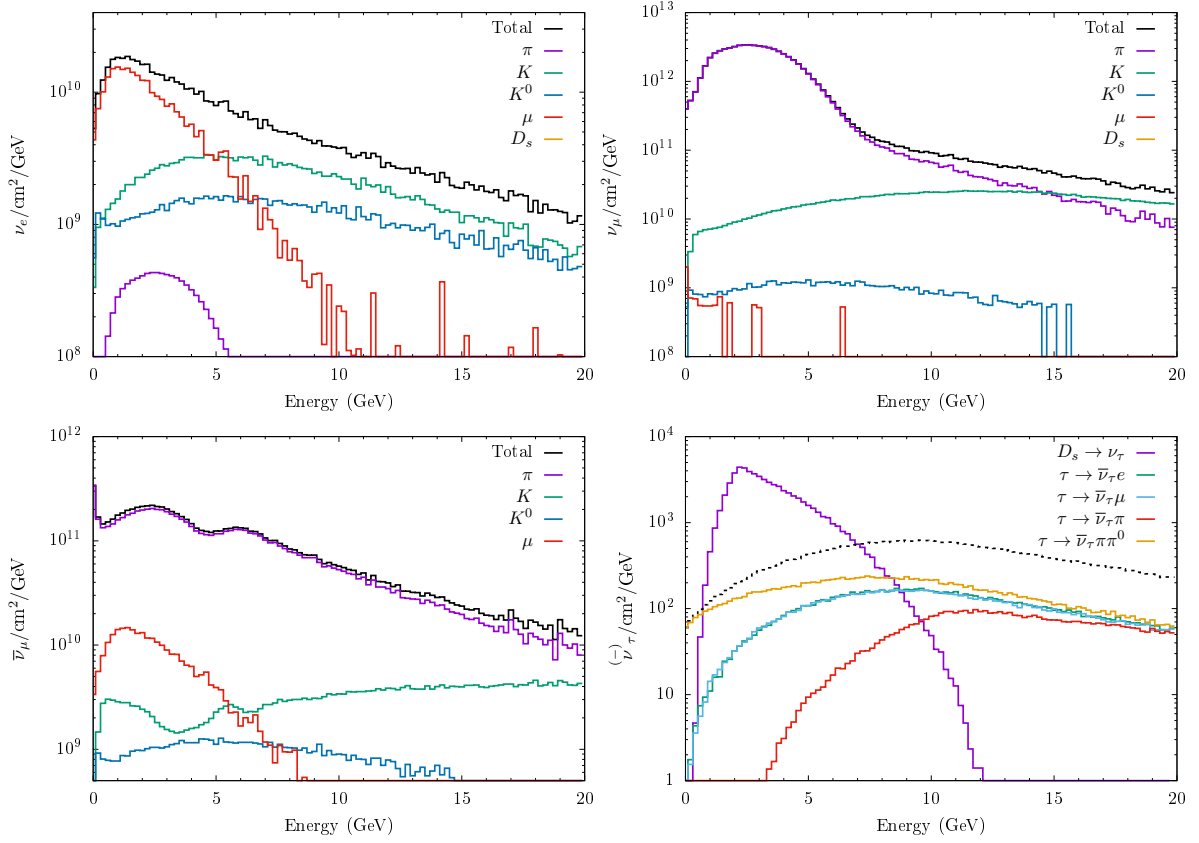


Figure 5.2: The prediction of neutrino fluxes, in neutrino mode, divided by parentage at the ND are shown above, normalised to 10^{20} POT. The ν_e component (top left) predominately originates from μ^+ decays; kaon decays are responsible for the high energy part of the spectrum. The ν_μ component (top right) obtains its main contribution from π^+ decays at low energies, whereas the K^+ decays are accountable for the long tail of the spectrum. Contributions from D_s^+ decay are out of scale for both ν_e and ν_μ . The distribution of the $\bar{\nu}_\mu$ component (bottom left) is due to negative charged secondary particles which are not successfully deflected by the horn system; the muon contribution is much more relevant than for the ν_μ component. The ν_τ component (bottom right) is only sourced from D_s decays and presents a prominent peak at low energies, whereas the $\bar{\nu}_\tau$ are produced in τ^+ lepton decays. The dotted black line is the total $\bar{\nu}_\tau$ component of the flux.

the CMS detectors. FASER will consist of a 10 m cylindrical decay volume located 480 m downstream of the ATLAS interaction point.

5.1.2 Flux prediction

The study of HNL requires the various components of the flux to be known separately by parentage, as explained in Section 4.3. Only the beam operating with a forward horn current is considered in this study. Positively charged secondary particles are therefore selected at the target and this results in a beam dominantly made of neutrinos with a smaller component of antineutrinos. The flux predictions for ν_e , ν_μ , and $\bar{\nu}_\mu$ at DUNE, provided by Ref. [234] for the reference beam, are shown in Fig. 5.2 subdivided in their parent components. The $\bar{\nu}_e$ component was not provided. The ν_μ flux is the dominant component and is principally originated by pion decays, whilst its long tail comes from kaon decays. Unsuccessfully deflected negative particles, like π^- or K^- , and antimuons are the main contributors to the $\bar{\nu}_\mu$ components, while ν_e comes predominately from muon decays and both K^+ and K^0 decays. The energy range considered is

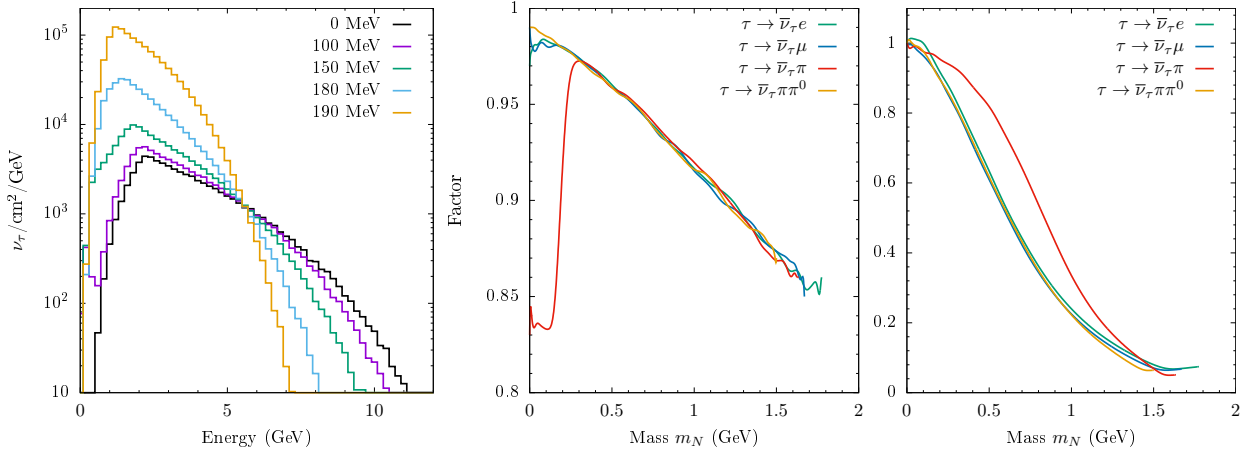


Figure 5.3: The fluxes of heavy neutrinos from $D_s^+ \rightarrow \tau^+ N$ (left) are presented for different neutrino masses and normalised to 10^{20} POT at the ND. Only phase space effects are considered here. For each different value of the neutrino mass, information on the start and end point of the spectrum and the peak of the flux are extracted and used to reshape the ν_τ spectrum. The distortion factors used to build the heavy neutrino flux from mixing with $\bar{\nu}_\tau$ are also shown: the energy range normalised to 20 GeV (middle) and the inverse of the rescaled distribution peak (right).

limited to $E < 20$ GeV, because it is the most intense region of the flux and the most relevant for this study, as it will be explained in Section 5.2.2.

An albeit-small flux of HNLs with masses above the kaon one is nonetheless expected. It could be inferred from the ν_τ flux, but this component is not available in the literature. The lightest meson with a relevant decay width to tau neutrinos is the charmed-strange meson D_s^+ which has a mass $m_{D_s} = 1968.34 \pm 0.07$ MeV [15]. It decays mostly into $\tau^+ \nu_\tau$ with a branching ratio of $(5.48 \pm 0.23)\%$. HNL with masses above the K^0 can be produced via the tau mixing, but more importantly via the muonic and electronic ones which are enhanced, as explained in Section 4.3. The meson D^+ also decays into $\tau^+ \nu_\tau$, but being lighter than the D_s^+ the decay is disfavoured by the smaller phase space with a branching ratio 50 times smaller. This meson presents three-body decay channels into ν_e and ν_μ with much higher branching ratio, but there is no enhancement for such channels into HNL, as explained in Section 4.3, and so these subdominant components are not taken into account in the present study. The proton beam has a relatively low energy for producing charm quarks with a high cross-section, so the prediction of ν_τ has not been carried out by the collaboration. For the reasons stated above, a prediction for the D_s^+ production is carried out assuming an 80 GeV proton beam hitting a fixed graphite target. The distribution at the target site is used to estimate the ν_τ flux at the ND system. In the literature, the following parametrisation has been successfully used to describe charm meson production in proton-proton collision in the centre of mass frame [235]

$$\frac{d^2\sigma}{dx_F dp_T^2} \sim (1 - |x_F|)^n e^{-bp_T^2}, \quad (5.1)$$

where $x_F = 2p_z/\sqrt{s}$, with p_z the longitudinal momentum in the CM frame. The parameters n and b were fitted from the E769 experiment and found to be $n = 6.1 \pm 0.7$ and $b = 1.08 \pm 0.09$ [236]. It is reasonable to assume that the D_s^+ meson production at the target follows the same distribution. With the help of a purpose-built Monte Carlo simulation, the D_s^+ four-momenta are generated starting from Eq. (5.1) and simulate the meson decay and the subsequent tau decays. A key simplification here is that thanks to the short lifetime of the D_s^+ and τ^+ , of the order of 10^{-13} s, the meson path is not affected by the horn system

Table 5.2: The expected rates for CC and NC interaction in the near detector are presented here, normalised to 10^{20} POT. The values were computed starting from Eq. (5.2), convolving the fluxes of Fig. 5.2 with the CC and NC cross-section predictions from GENIE [64]. Detector efficiencies are not applied. The first columns show the total number of events per tonne of argon, the second ones the proportion of CC or NC events with respect to the totality, and the last columns the event frequencies assuming 1×10^{14} POT/s.

	CC events			NC events		
	Per tonne	Ratio	Rate (Hz)	Per tonne	Ratio	Rate (Hz)
ν_e	3.0×10^3	75.6 %	152×10^{-3}	1.0×10^3	24.4 %	48.9×10^{-3}
ν_μ	236×10^3	75.2 %	12.0	77.8×10^3	24.8 %	3.95
$\bar{\nu}_\mu$	17.7×10^3	70.9 %	898×10^{-3}	7.2×10^3	29.1 %	368×10^{-3}
ν_τ	1.6×10^{-5}	17.1 %	8.3×10^{-10}	7.9×10^{-5}	82.9 %	4.0×10^{-10}
$\bar{\nu}_\tau$	5.2×10^{-5}	45.3 %	2.6×10^{-3}	6.1×10^{-5}	54.7 %	3.0×10^{-9}

nor by interactions with other accelerator components. This results in no focusing of these secondary particles and so only neutrinos emitted within the geometric acceptance of the ND form the ν_τ and $\bar{\nu}_\tau$ spectrum. The overall normalisation comes from an open charm calculation (see Appendix B for details): the number of D_s^+ per POT is found to be $(2.8 \pm 0.2) \times 10^{-6}$. The result of the simulation is reported in Fig. 5.2, where the different contributions to the ν_τ spectrum are shown. Thanks to the large number of POTs in DUNE, the total number of D_s^+ mesons produced is comparable to other dedicated experiments [237]; however, the beamline design is not optimised for heavy mesons production and the ν_τ flux seen at the ND is strongly attenuated.

Having knowledge of the parent meson distribution, the production of nearly-sterile neutrinos are directly simulated from D_s decays. The spectrum of heavy neutrinos is distorted when their mass approaches the various phase space thresholds, which appears as a further enhancement of the flux. This is due to the fact that heavier neutrinos are more easily boosted inside the geometric acceptance of the detector. Besides the peak height, the start and the end point of the energy flux are also affected, as illustrated in Fig. 5.3 in which the enhancement discussed in Section 4.3 is not included. The distribution of heavy neutrinos from τ decays also changes with the neutrino mass. These effects are taken into account by modifying the scaled neutrino flux using information retrieved by the ν_τ and $\bar{\nu}_\tau$ simulation.

5.2 Simulation of events at the DUNE ND

The number of SM neutrino–nucleon interactions expected at the DUNE ND, without considering detector effects, is calculated by integrating the charged current (CC) and neutral current (NC) total cross-sections multiplied by the light neutrino spectrum $d\phi_\nu/dE$:

$$\mathcal{N}_{\text{tot}} = \mathcal{N}_{\text{CC}} + \mathcal{N}_{\text{NC}} = N_{\text{target}} \int dE [\sigma_{\text{CC}}(E) + \sigma_{\text{NC}}(E)] \frac{d\phi_\nu}{dE}, \quad (5.2)$$

where $\sigma_{\text{CC}}(E)$ and $\sigma_{\text{NC}}(E)$ are the cross-section predictions in argon calculated by GENIE [64] and N_{target} is the total number of Ar targets. The event rates are shown in Table 5.2. It turns out that less than one ν_τ event is expected in the total run of the experiment. As a comparison, the number of ν_μ events will be 10^{10} times higher. This confirms the expectations that the ν_τ component of the flux is negligible for standard oscillation physics in the DUNE ND; on the other hand ν_τ appearance is expected at the FD. SM neutrino scatterings occurring within

Table 5.3: The table lists detection thresholds and energy/momentum and angular resolutions used in the fast MC, where “EM” delineates electro-magnetic showers and “Hadron” any other charged particle which is neither a lepton nor a pion. The momenta of pions and muons are smeared according to the containment of their tracks. If the particles enter the MPD in which they cover a length longer than the detector’s diameter or if 80 % of the tracks are contained inside the LArTPC then the relative resolution on the momentum is 5 %, otherwise a resolution of 30 % is applied. Neutrons are treated with “Hadron” resolutions, but with a 90 % detection efficiency.

Particle	Threshold	σ_{rel}	σ_{θ}
EM	30 MeV	$5\%/\sqrt{E} \oplus 1\%$	1°
Hadron	50 MeV	$30\%/\sqrt{E} \oplus 5\%$	5°
Muon	30 MeV	1% or 30% of $ \mathbf{p} $	0.3°
Pion	100 MeV	1% or 30% of $ \mathbf{p} $	0.3°

the fiducial volume of the detector could mimic the rare signal of HNL in-flight decays, as some final-state particles are common to both processes. A good estimate of the number of possible background events for each discovery channel is very important, since it dictates the true sensitivity of the experiment. A conservative background analysis is performed only to decay modes available for neutrino masses below m_{K^0} . They are $N \rightarrow \nu e^+ e^-$, $\nu e^\pm \mu^\mp$, $\nu \mu^+ \mu^-$, $\nu \pi^0$, $e^\mp \pi^\pm$, and $\mu^\mp \pi^\pm$. These channels have, as a matter of fact, the best discovery potential thanks to high branching ratios and easy-to-reconstruct final-state particles.

Particles are typically tagged by studying the topology of the tracks and the energy loss dE/dx in the active medium. However, instead of dealing with a full detector simulation, a fast Monte Carlo (MC) analysis was preferred, using as input neutrino–nucleon scattering events in argon generated by the neutrino event generator GENIE [64]. The tracks are randomly placed inside the ND system and then smeared according to a normal distribution centred on the simulated value of energy/momentum; particles with a kinetic energy above the detection threshold are then assumed to be reconstructed. The relative position between the two detectors is taken into account, in that particle tracks exiting the LArTPC end entering the MPD are reconstructed as a single track. Escaping or partially reconstructed tracks are not discarded, but treated with a different energy/momentum resolution. The initial particle energy can in fact be estimated, with some limitations, thanks to the energy dependence of the mean energy loss during the particle propagation. Possible sources of background mis-identification specific to each channel are then implemented. Detector resolutions and thresholds, summarised in Table 5.3, are taken from Ref. [238] and used for both modules of the ND.

5.2.1 Background evaluation

A strong discriminant for background events is the presence of protons, neutrons, and other hadrons in the final states, from nucleus recoils of neutrino–nucleon interactions or multinucleon resonance processes. If hadronic activity is reconstructed at the interaction vertex, then the event is clearly originated by SM neutrino–nucleon scattering and tagged as background. In the case this does not happen, for instance when the hadrons are below threshold, the multiplicity of final-state particles becomes fundamental to distinguish signal events from intrinsic background.

Mis-identification of certain tracks can worsen the channel-specific background. The main background to the pseudoscalar meson channels, $N \rightarrow \ell^\mp \pi^\pm$, are resonance ν_e or ν_μ CC interaction with single pion production or charged current incoherent and deep inelastic scatterings in which only a pair $\ell \pi$ is detected. Three-body lepton decays suffers from mis-identification of additional pions and photons emitted in CC neutrino scatterings which are mistaken for charged

Table 5.4: The decay channels with the best discovery prospect are listed here, together with their signatures and most likely background events. For any HNL decay mode, no hadronic activity such as nucleus recoil is present at the decay vertex.

Channel	Signal	Background
$N \rightarrow \nu e^+ e^-$	Two e -like tracks	ν_e CC event with γ emission or mis-reconstructed π^0 decay
$N \rightarrow \nu e^\pm \mu^\mp$	A μ - and a e -like track	ν_μ CC event with mis-reconstructed γ or ν_e CC event with one mis-reconstructed π
$N \rightarrow \nu \mu^+ \mu^-$	Two μ -like tracks	ν_μ CC event with mis-reconstructed π
$N \rightarrow \nu \pi^0$	Two γ with invariant mass m_{π^0}	Any NC interaction with only one π^0 above detection threshold
$N \rightarrow e^\mp \pi^\pm$	An e - and a π -like track	ν_e CC resonance or DIS with single π emission or only one π above threshold
$N \rightarrow \mu^\mp \pi^\pm$	A μ - and a π -like track	ν_μ CC resonance or DIS with single π emission or only one π above threshold

leptons. Despite having a similar mass, pion and muon tracks differ on average in length, as the meson track often culminates in a hadronic shower. In implementing detector effects, if no hadronic shower is detected and the track length is longer than two metres, the pion is identified as a muon. Electromagnetic shower induced by photons are identified by looking at the vertex displacement and at the dE/dx , which is twice as large being it the energy loss of a e^\pm pair. If a photon converts within two centimetres from the interaction point and either the electron or the positron of the pair is below threshold, the photon is reconstructed as a single electron. A pair of electrons with a small separation angle, less than 3° , is tagged as an electron–positron pair and the parent photon is reconstructed. The main source of photons comes from the decay of the neutral pion, which is abundantly produced in NC neutrino–nucleon interactions. Certain hadronic transitions from secondary particles of deep inelastic scatterings also emit photons. If a pair of photons shows an invariant mass comparable with the π^0 mass, the parent pion is identified. Interactions in which multiple neutral pions are produced, but only a pair of photons is detected and reconstructed, are background to the $N \rightarrow \nu \pi^0$ channel. The table of Table 5.4 summarises the main background events of the channels considered. It is found that between 2.5 % down to 0.0025 % of the neutrino–nucleon scattering events survive the particle identification process, becoming background events.

The channels which open up for masses above the kaon mass are more challenging to deal with, from an experimental point of view. The final-state particles of these modes are mostly neutral pseudoscalar mesons which decay electromagnetically or vector mesons which usually decay into a multiple lighter mesons, depending on the initial flavour content, and sometimes accompanied by photon emission. The correct identification of these short-lived states is non-trivial. For very high masses τ leptons are also produced, but their precise reconstruction requires *ad hoc* techniques. These tasks are beyond the scope of the analysis presented here and are best left to the collaboration’s superior simulation tools. Cosmogenic background is also not considered here, even though a rate of 2.7 Hz/m^2 cosmic rays is expected at the ND hall [222] due to the very little over burden. Given an area of a few square meters, the number

of cosmic rays per drift window can be nonnegligible [219], but rejection techniques are being developed with good signal efficiencies [239].

5.2.2 HNL decay events and signal efficiency

Except for N decaying into three neutrinos, all the other decay channels listed in Section 4.2 are in principle detectable. Some decay modes contribute more significantly to the physics reach thanks to larger branching ratios and lower backgrounds. Along with the number of background events, a correct estimation of the number of decays in visible channels is necessary in order to evaluate the sensitivity of the DUNE ND to the discovery of HNL. For a given visible decay mode d , the number of signal events is

$$\mathcal{N}_d = \int dE \Pi_d(E) W_d(E) \frac{d\phi_N}{dE}, \quad (5.3)$$

where $d\phi_N/dE$ is the number of heavy neutrinos expected at the ND, computed in the way described in Section 4.3. The function $\Pi_d(E)$ accounts for the probability of a heavy neutrino of energy E to decay inside the ND after covering the baseline distance L . It is expressed in the following form:

$$\Pi_d(E) = e^{-\frac{\Gamma_{\text{tot}} L}{\beta\gamma}} \left(1 - e^{-\frac{\Gamma_d L}{\beta\gamma}} \right) \frac{\Gamma_d}{\Gamma_{\text{tot}}}, \quad (5.4)$$

where λ is the length of the ND, Γ_d the decay rate for the channel d and Γ_{tot} the total decay rate. The total effect of Π_d is to favour low-energy bins of the neutrino spectrum for which the relativistic factor $\beta\gamma$ is small. The term $W_d(E)$ is a signal efficiency factor, estimated as the binned ratio of the true N energy spectrum after and before a background rejection procedure. This process aims at further reducing the number of background events still present after particle identification. It consists of simple data selection cuts optimised to reject the background while keeping an acceptable signal efficiency ($\geq 30\%$), exploiting differences in the energy and angular distributions between signal and background events. The HNL decays inside the detector are simulated by a custom MC code and the tracks are processed in the same way as it is done for background events (see Section 5.2.1). The resulting signal efficiency therefore embeds also detector effects. If no background is expected for the channel d , there is no need for applying any rejection procedure and so the signal efficiency is maximal, i.e. $W_d(E) = 1$ at all energies. The final number of background events \mathcal{B}_d and the number of signal events \mathcal{N}_d are eventually used to build the Confidence Level (C.L.) regions of sensitivity (see Section 5.3).

5.2.3 Selection example

In this section, the event rates from the background reduction and signal selection process are presented for all decay channels of both Majorana and Dirac neutrinos of a given mass. It turns out that the selection cuts are slightly different for Dirac or Majorana HNL decays. This is a consequence of certain combinations of production and decay modes which are forbidden for Dirac neutrinos, as they would lead to LNV and so the energy and angular distributions are not identical. NC-mediated decay modes also present distinct decay widths for Majorana and Dirac neutrinos in the rest frame and the difference angular dependency can be reflected in the laboratory frame.

The background evaluation is only performed for the decay channels with an important discovery potential, and these are $N \rightarrow \nu e^+ e^-$, $\nu e^\pm \mu^\mp$, $\nu \mu^+ \mu^-$, $\nu \pi^0$, $e^\mp \pi^\pm$, and $\mu^\mp \pi^\pm$. In order to reject background events, conservative event selection cuts are outlined using the differences between kinematic properties of the final-state particles from neutrino–nucleon interactions and from the rare HNL in-flight decays. Simulations of signal events with a given mass inside either

Table 5.6: The number of background events are reported before and after the event selection process is applied for two-body decay channels of HNLs. See text for details. The last row is the integrated signal efficiency.

	$N \rightarrow e^\mp \pi^\pm$				$N \rightarrow \mu^\mp \pi^\pm$			
	Majorana		Dirac		Majorana		Dirac	
ν_e	19.090	\rightarrow	0.015	0.015	0.007	\rightarrow	0.000	0.000
ν_μ	0.027	\rightarrow	0.000	0.000	25.030	\rightarrow	0.011	0.012
$\bar{\nu}_\mu$	0.025	\rightarrow	0.000	0.000	29.822	\rightarrow	0.046	0.053
$\langle \nu \rangle$	0.239	\rightarrow	0.000	0.000	24.302	\rightarrow	0.013	0.014
$\widehat{W}_{\ell\pi}$	36.4 %		35.2 %		43.3 %		40.2 %	

the LArTPC or the MPD are input to a channel-specific algorithm that discards low energy events and defines limits on angular and transverse momentum distributions. The algorithm aims at keeping an integrated signal efficiency \widehat{W}_d greater than 30 %, where

$$\widehat{W}_d = \int dE W_d(E) \quad (5.5)$$

and the signal efficiency $W_d(E)$ is introduced in Section 5.2.2.

As an example of the selection process, the results of the background analysis for an HNL with mass $m_N = 450 \text{ MeV}$ is reported here. In Tables 5.6, 5.7, and 5.8 the number of background events is reported in the form “ $\mathcal{X} \rightarrow \mathcal{Y} \mathcal{Z}$ ”, where \mathcal{X} is the per mille (10^{-3}) fraction of background events from mis-identification and \mathcal{Y} and \mathcal{Z} are fractions of irreducible background after the application of selection cuts to respectively Majorana and Dirac neutrino simulations. When the value 0.000 is shown, less than one background event per million is expected. The average number of backgrounds, $\langle \nu \rangle$, is computed by weighting the flux component contributions to the background using the respective interaction rates as weights, reported in Tab. 5.2. To obtain the number of background events, each fraction must be multiplied by the number of SM neutrino–nucleon interactions expected in the ND during the experiment lifetime. It is assumed that the ν_τ and $\bar{\nu}_\tau$ components are not responsible for background events, therefore only the ν_e , ν_μ , and $\bar{\nu}_\mu$ components are studied. The last row of each table shows the integrated efficiency of the selection cuts, introduced in Eq. (5.5).

The studied channels are grouped in three categories, which have similar kinematic features: two-body decay, which are semileptonic, three-body decay channels, which are purely leptonic instead, and decays which can be only detected via photon reconstruction.

Two-body decays

The two-body decays $N \rightarrow e^\pm \pi^\mp$ and $N \rightarrow \mu^\pm \pi^\mp$ are the most promising channels for the detection of a heavy neutrino, being the decay modes with the highest branching ratios. Since all final-state particles are charged, direct information on the parent particle is easily reconstructed, as for instance the mass of the decaying neutrino, which is the invariant mass of the process

$$m_N^2 = s = m_\ell^2 + m_\pi^2 + 2E_\ell E_\pi - 2|\mathbf{p}_\ell||\mathbf{p}_\pi| \cos \theta, \quad (5.6)$$

where θ is the opening angle between the lepton and the pion. In a two-body decay, the particles are emitted back-to-back in the neutrino reference frame, so in the laboratory frame the relative position on the perpendicular plane is mostly preserved and $(\phi_\ell - \phi_\pi)$ is expected to be close to

Table 5.7: The number of background events are reported before and after the event selection process is applied for three-body decay channels of HNLs. See text for details. The last row is the integrated signal efficiency.

	$N \rightarrow \nu e^- e^+$			$N \rightarrow \nu e^\mp \mu^\pm$			$N \rightarrow \nu \mu^- \mu^+$					
	Majorana		Dirac	Majorana		Dirac	Majorana		Dirac			
ν_e	0.190	\rightarrow	0.003	0.002	0.078	\rightarrow	0.002	0.002	0.000	\rightarrow	0.000	0.000
ν_μ	0.193	\rightarrow	0.001	0.000	0.092	\rightarrow	0.000	0.000	0.081	\rightarrow	0.001	0.001
$\bar{\nu}_\mu$	0.224	\rightarrow	0.003	0.002	0.160	\rightarrow	0.000	0.000	0.090	\rightarrow	0.008	0.006
$\langle \nu \rangle$	0.168	\rightarrow	0.001	0.000	0.090	\rightarrow	0.000	0.000	0.022	\rightarrow	0.000	0.000
$\widehat{W}_{\nu\ell\ell}$	63.4 %		55.4 %	68.6 %		71.2 %	74.0 %		68.4 %			

$\pm\pi$. Despite these distinctive signatures, these two channels are the ones with most background events, coming from charged-current interactions of ν_e , ν_μ , and $\bar{\nu}_\mu$ in which additional pions can be easily emitted in coherent or deep inelastic scatterings. Background events typically peak at low energies and present more isotropic angular distributions. Therefore, a tight energy threshold on the energies of the charge particles is imposed to accept 70 % of the signal events and a threshold on the energy of the reconstructed neutrino is defined by 90 % of the retained events. A cut is also placed on the reconstructed m_N to retain 80 % of signal events, as well as an upper limit on the transverse momenta and angles to the beamline and a lower and an upper limit on the separation angle between the charged particles. After the cuts are applied, the background events are reduced up to a factor of 2500, and the signal efficiency are ~ 35 % for the electronic channel and ~ 40 % for the muonic channel, with little difference (respectively 1 % and 3 %) between Dirac or Majorana selection windows. The background rejection and signal efficiency are shown in Table 5.6.

Three-body decays

The three-body decays studied are $N \rightarrow \nu e^- e^+$, $N \rightarrow \nu e^\mp \mu^\pm$, and $N \rightarrow \nu \mu^- \mu^+$. The event selection in this case is more challenging compared to the two-body case, due to the loss of the light neutrino which precludes the reconstruction of the decaying HNL; selection cuts cannot be defined as rigorously. However, since two charged leptons are needed to identify these channels, the resulting background rate from mis-identified photons and long-track pions is low. Even in this case, only high energy events are considered, but with a lower threshold on the charged lepton energies. The invariant mass of the two leptons has as upper limit m_N and this constrain helps to reduce the background. Lower and upper limits are also defined for the transverse momenta, as well as for the separation angles from the beamline.

The background events are reduced from a factor of 40 up to a factor of 200, with the selection requirements for Dirac neutrinos being more effective. The signal efficiency results to be better by 6 \sim 8 % points for Majorana neutrinos in the $N \rightarrow \nu e^- e^+$ and $\mu^- \mu^+$ channels, whereas the Dirac neutrino have give a better efficiency in the $N \rightarrow e^\mp \mu^\pm$ channel. High efficiency and low background make these three channels competitive for HNL discovery, despite lower branching ratios. The background rejection and signal efficiency are shown in Table 5.7.

EM-detected decays

The semileptonic decay $N \rightarrow \nu \pi^0$ may only be identified by a correct photon reconstruction, since the neutral pion decays almost 100 % of the time in two photons. This particle is produced

Table 5.8: The number of background events are reported before and after the event selection process is applied for the neutral pseudoscalar meson decay. See text for details. The last row is the integrated signal efficiency.

$N \rightarrow \nu \pi^0$				
			Majorana	Dirac
ν_e	4.135	\rightarrow	0.058	0.048
ν_μ	5.862	\rightarrow	0.053	0.039
$\bar{\nu}_\mu$	7.428	\rightarrow	0.179	0.138
$\langle \nu \rangle$	5.797	\rightarrow	0.061	0.045
$\widehat{W}_{\nu \pi^0}$			46.3 %	42.3 %

in any NC interaction with a π^0 emission. Background events occur if only two final-state photons from the neutral pion decay are above detection threshold and properly reconstructed with an invariant mass equal to m_{π^0} . The energy of the reconstructed pion is the best discriminant against background events which have typically higher energies. Lower and upper limits can be placed on the π^0 transverse momentum and angle with the beamline, but also a threshold on the energy of the photons as well as an upper limit on their angular distributions help to define the kinematics of the event. The residual background for this channel is the highest among the ones studied. Only reduction factors up to 130 can be achieved, with a notable difference between selection cuts for Majorana and Dirac HNL decays—the latter ones being more strict. The signal efficiency is $\sim 46\%$ for Majorana and $\sim 42\%$ for Dirac. It is, however, one of the decay modes with the highest branching ratio, and with advanced and dedicated techniques [240, 241] the background rejection can be improved. The background rejection and signal efficiency are shown in Table 5.8.

5.3 Sensitivities of the DUNE ND

The sensitivity regions for the discovery of heavy neutrino decays are presented in this section, for a total amount of 1.32×10^{22} POT collected with the beam in neutrino mode. All the regions are estimated at the 90 % C.L. in rejecting the null hypothesis, H_0 , by which no HNL decays are seen ($\sigma = 0$), but only background events b are expected. For a specific decay channel d , the probability of observing n events with a signal mean $\sigma = \mathcal{N}_d$ and background $b = \mathcal{B}_d$ (see Section 5.2.2) follows a Poisson distribution

$$P(n|\sigma, b) = (\sigma + b)^n \frac{e^{-(\sigma+b)}}{n!} . \quad (5.7)$$

The number of events needed in order to reject H_0 at the desired C.L. is estimated with the Feldman-Cousins method [242]. For example, if no background is expected ($W_d = 1$), an average of $n = 2.44$ events must be detected to reject H_0 with 90 % C.L. This criterion is used to define the sensitivity regions shown in this section, for both Majorana and Dirac neutrinos. The lines of the figures in this section and in Section 5.4 encompass regions of the parameter space which if true could allow to exclude the null hypothesis within the confidence level assumed. It is expected that the MPD alone has a better sensitivity than the LArTPC, thanks not only to a larger volume, but also to a less dense medium which gives lower backgrounds. As the two modules are assumed to have the same detection performance, just a combined sensitivity

Table 5.9: This table summarises the sensitivity result of Fig. 5.4. The minimum value of the mixing to Majorana HNLs to which the DUNE ND is sensitive to is reported; the value in bracket is with the background analysis included. The respective mass value at that point is also reported. The particle ℓ^\mp denotes the charged lepton with corresponding flavour given by the mixing element.

Channel	m_N/GeV , $ U_{eN} ^2/10^{-9}$	m_N/GeV , $ U_{\mu N} ^2/10^{-7}$	m_N/GeV , $ U_{\tau N} ^2/10^{-6}$
$N \rightarrow \nu e^+ e^-$	0.40 , 2.9 (24.2)	0.36 , 9.9 (73.1)	1.05 , 1.3 (17.6)
$N \rightarrow \nu e^\pm \mu^\mp$	0.41 , 2.8 (5.1)	0.36 , 4.8 (6.4)	—
$N \rightarrow \nu \mu^+ \mu^-$	0.42 , 12.0 (46.5)	0.37 , 9.2 (19.6)	1.06 , 1.5 (40.0)
$N \rightarrow \nu \pi^0$	0.39 , 1.1 (15.6)	0.35 , 1.6 (13.6)	0.88 , 0.46 (17.3)
$N \rightarrow \ell^\mp \pi^\pm$	0.39 , 0.7 (4.2)	0.36 , 1.3 (19.9)	—

of the two detectors is reported, with particle propagation between them taken into account when necessary. Charge identification capabilities of the ND are neglected and therefore this information is washed out in presenting the sensitivity plots in this and next sections. Given the charge-blind analysis, the number of events expected for Majorana neutrinos is twice as large as the number in the case of Dirac neutrinos, and so the sensitivity to Dirac neutrino decays is a factor of $\sqrt{2}$ worse than the Majorana case. The factor is justified noting that for high numbers the sensitivity is roughly quantified by $\mathcal{N}_d/\sqrt{\mathcal{N}_d + \mathcal{B}_d}$ which simplifies to $\sqrt{\mathcal{N}_d}$ for zero background. The limits reported here below refer to Majorana heavy neutrinos; the corresponding limit for which N is a Dirac fermion is easily retrieved by multiplying the upper limit by $\sqrt{2}$.

Section 5.3.1 shows the constraint that the DUNE ND can place on a simplified scenario in which a single mixing matrix element between HNL and active neutrinos dominates. The scenario in which two mixings are dominant with respect to the third one is also considered, the results of which are reported in Section 5.3.2.

5.3.1 Single dominant mixing

The sensitivity regions for the three mixings $|U_{eN}|^2$, $|U_{\mu N}|^2$, and $|U_{\tau N}|^2$ are presented here with the assumption that just one mixing element dominates over the other two. The sensitivities for the decay channels $N \rightarrow \nu e^+ e^-$, $\nu e^\pm \mu^\mp$, $\nu \mu^+ \mu^-$, $\nu \pi^0$, $e^\mp \pi^\pm$ ($|U_{eN}|^2$ only), and $\mu^\mp \pi^\pm$ ($|U_{\mu N}|^2$ only) are reported in Fig. 5.4. The solid lines corresponds to a scenario in which zero background is assumed at the ND. A background evaluation was carried out for these channels (see Section 5.2.1), in order to define a more realistic sensitivity; the resulting regions are shown as dashed lines in Fig. 5.4. The final sensitivity will lie somewhere between the lines with and without backgrounds. It is expected that further improvements to background reduction can be achieved with a dedicated analysis by the experimental collaboration, although systematic uncertainties could also degrade the sensitivity.

For both the electronic and the muonic mixings, the two-body semileptonic decay modes are the ones providing the best sensitivity for sufficiently heavy masses. With the channel $N \rightarrow e^\mp \pi^\pm$, the mixing can be constrained in the range $0.15 \text{ GeV} \lesssim m_N \lesssim 0.49 \text{ GeV}$ to be $|U_{eN}|^2 < 3 \times 10^{-9}$, with a minimum point $|U_{eN}|^2 < 7 \times 10^{-11}$ at $m_N \simeq 0.39 \text{ GeV}$. Including the background rejection, the limits are loosened by a factor of ~ 6.1 . The channel $N \rightarrow \mu^\mp \pi^\pm$ can constrain the mixing $|U_{\mu N}|^2 < 5.6 \times 10^{-10}$ in the mass range $0.25 \text{ GeV} \lesssim m_N \lesssim 0.39 \text{ GeV}$, with the best limit $|U_{\mu N}|^2 < 1.3 \times 10^{-10}$ at $m_N \simeq 0.35 \text{ GeV}$. In this case, the higher background reduce the bounds up to a factor of ~ 15.1 . The NC decay $N \rightarrow \nu \pi^0$ is the channel most affected by background and with the worst signal efficiency: the limits are higher at most by a factor of ~ 27.1 for the electronic, ~ 24.6 for the muonic, and ~ 52.6 for the tau mixing. Assuming

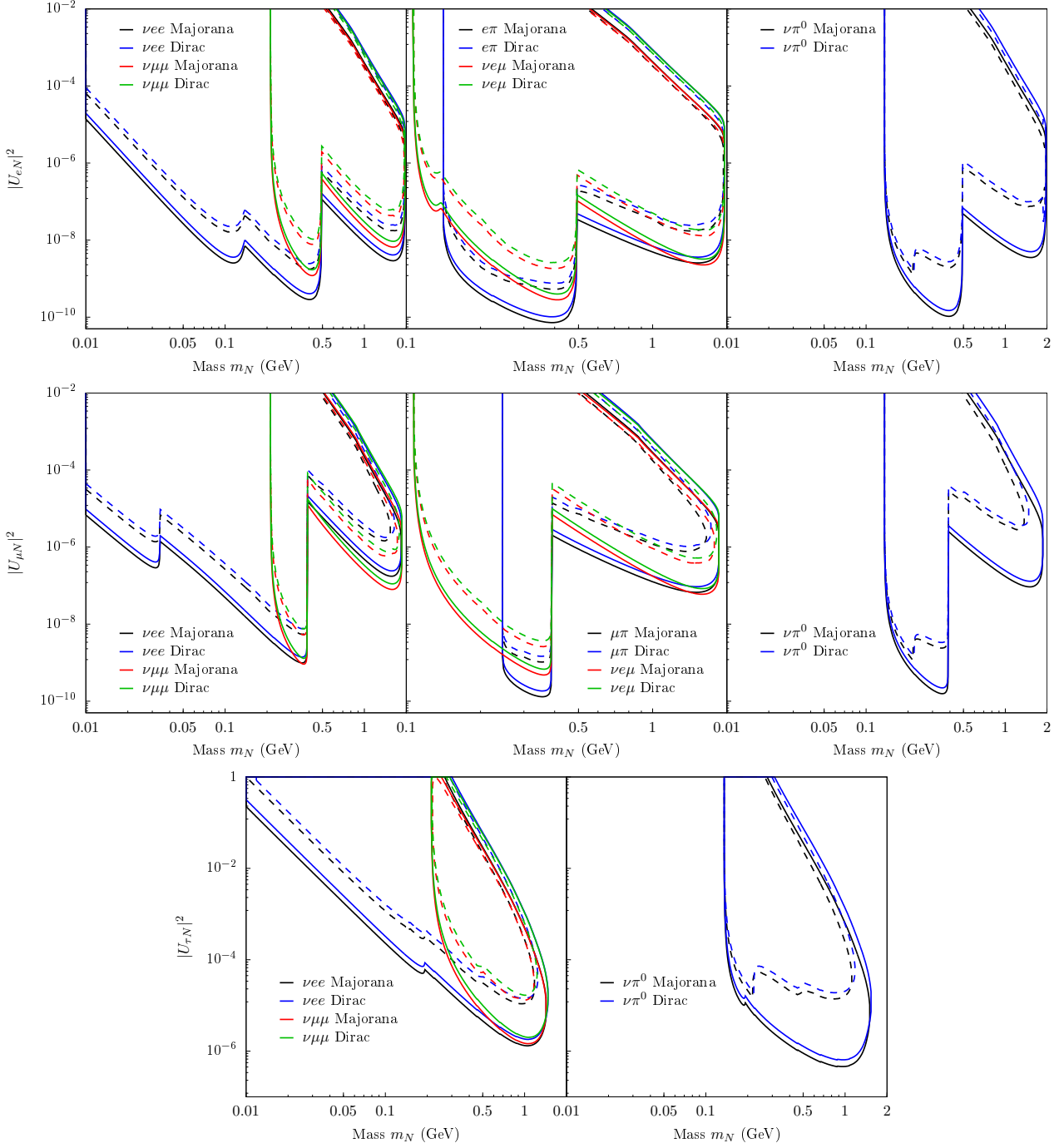


Figure 5.4: The 90 % C.L. sensitivity regions to individual channels for dominant mixings $|U_{eN}|^2$ (top), $|U_{\mu N}|^2$ (middle), and $|U_{\tau N}|^2$ (bottom) are shown. The solid lines correspond to the analysis before the background analysis, which is equivalent to a weighting factor $W_d = 1$ (see Eq. (5.3)). The dashed lines are drawn after the background analysis. The distinction between the fermionic natures are explained in the colour key.

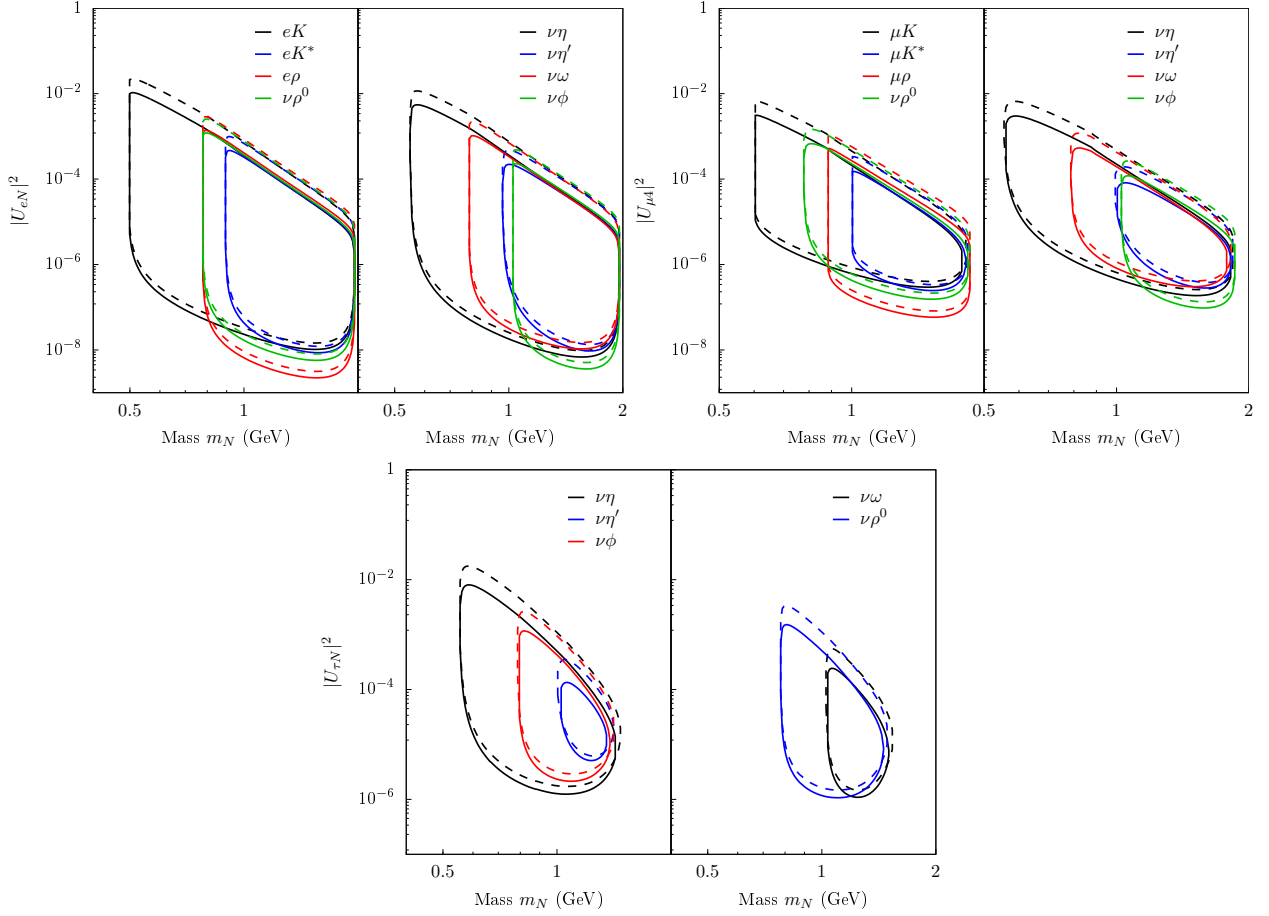


Figure 5.5: The 90 % C.L. sensitivity regions to individual channels for dominant mixings $|U_{eN}|^2$ (top left), $|U_{\mu N}|^2$ (top right), and $|U_{\tau N}|^2$ (bottom) are presented for Majorana (solid lines) and Dirac (dashed lines) neutrinos. No background analysis was performed for the channels shown here (see text). These channels become available only for masses above 0.5 GeV.

no background, instead, the constraints placed by this decay mode can be competitive, as the mixings are limited to be $|U_{eN}|^2 < 1.1 \times 10^{-10}$ at $m_N \simeq 0.39$ GeV, $|U_{\mu N}|^2 < 1.5 \times 10^{-10}$ at $m_N \simeq 0.35$ GeV, and $|U_{\tau N}|^2 < 4.6 \times 10^{-7}$ at $m_N \simeq 0.95$ GeV. There is no sensitivity to the channel $N \rightarrow \tau^\mp \pi^\pm$ because of the subdominant branching ratio and flux content.

The three-body lepton decays have a lower reach, but are more sensitive to masses above the kaon mass limit than the two-body semileptonic modes. The channel $N \rightarrow \nu e^- e^+$ is the only one that covers the whole mass range of interest and the bounds are weakened by background reduction by a factor less than 8 for mixings with electron and muon flavours. It can limit the electronic mixing down to $|U_{eN}|^2 < 2.5 \times 10^{-9}$ at $m_N \simeq 0.11$ GeV, $|U_{eN}|^2 < 2.9 \times 10^{-10}$ at $m_N \simeq 0.39$ GeV, and $|U_{eN}|^2 < 3.0 \times 10^{-9}$ at $m_N \simeq 1.6$ GeV. The channels $N \rightarrow \nu \mu^- \mu^+$ and $\nu e^\pm \mu^\mp$ perform better with the muon mixing for which the residual background is very little, as one muon and one electron or two muons are required in the final state. The bounds are weakened at most by a factor of ~ 1.8 for the muon mixing. These two channels respectively give the limits $|U_{\mu N}|^2 < 9.9 \times 10^{-10}$ at $m_N \simeq 0.37$ GeV and $|U_{\mu N}|^2 < 8.0 \times 10^{-8}$ at $m_N \simeq 1.6$ GeV, and $|U_{\mu N}|^2 < 4.8 \times 10^{-10}$ at $m_N \simeq 0.36$ GeV and $|U_{\mu N}|^2 < 5.6 \times 10^{-8}$ at $m_N \simeq 1.6$ GeV. The τ sector can only be constrained by the two NC-mediated channels, which give very similar constraints near $m_N \simeq 1.0$ GeV, these being $|U_{\tau N}|^2 < 1.3 \times 10^{-6}$ for the $\nu e^- e^+$ channel and $|U_{\tau N}|^2 < 1.5 \times 10^{-6}$ for the $\nu \mu^- \mu^+$ channel. All the results are summarised in Table 5.9.

Table 5.10: This table summarises the sensitivity result of Fig. 5.5. The minimum value of the mixing to Majorana HNLs to which the DUNE ND is sensitive to is reported, together with the respective mass value, m_N . No background analysis was carried out for the channels listed here. The particle ℓ^\mp denotes the charged lepton with corresponding flavour given by the mixing element.

Channel	$m_N/\text{GeV} , U_{eN} ^2/10^{-9}$	$m_N/\text{GeV} , U_{\mu N} ^2/10^{-7}$	$m_N/\text{GeV} , U_{\tau N} ^2/10^{-6}$
$N \rightarrow \nu \rho^0$	1.55 , 5.7	1.52 , 1.54	1.10 , 1.07
$N \rightarrow \nu \eta$	1.57 , 6.8	1.52 , 1.87	1.06 , 1.24
$N \rightarrow \nu \eta'$	1.64 , 9.5	1.58 , 2.82	1.23 , 5.09
$N \rightarrow \nu \omega$	1.55 , 7.5	1.50 , 3.03	1.09 , 2.14
$N \rightarrow \nu \phi$	1.60 , 3.6	1.58 , 0.96	1.24 , 1.09
$N \rightarrow \ell^\mp K^\pm$	1.55 , 10.3	1.49 , 2.9	—
$N \rightarrow \ell^\mp K^*^\pm$	1.57 , 8.6	1.53 , 2.5	—
$N \rightarrow \ell^\mp \rho^\pm$	1.55 , 2.2	1.53 , 58.4	—

A background study was not performed for all the other decay channels, which open up for masses above the K^0 mass, due to the fact that the final-state particles need a more complex analysis. The sensitivities to these modes are shown in Fig. 5.5, and they can place some constraints to the mixing. All the channels peak in their sensitivity for masses between 1.3 and 1.8 GeV. The best limits obtained for CC decays are $|U_{eN}|^2 < 2.3 \times 10^{-9}$ from $N \rightarrow e^\mp \rho^\pm$ and $|U_{\mu N}|^2 < 6.0 \times 10^{-8}$ from $N \rightarrow \mu^\mp \rho^\pm$; among the NC decays $|U_{eN}|^2 < 3.7 \times 10^{-9}$ and $|U_{\mu N}|^2 < 1.0 \times 10^{-7}$ both from $N \rightarrow \nu \phi$. Even for these channels, there is no sensitivity to CC processes to the tau mixing, but interesting limits are set from $N \rightarrow \nu \eta$, $N \rightarrow \nu \omega$, and $\nu \rho^0$ to be respectively $|U_{\tau N}|^2 < 1.86 \times 10^{-6}$, 3.24×10^{-6} , and 1.60×10^{-6} . The sensitivity results are summarised in Table 5.10.

5.3.2 Two dominant mixings

The bounds in a scenario in which two mixing elements are comparable and dominant over the third one are presented in this section. This case complements the previous analysis in Section 5.3.1 as, by searching for HNL decays, the experiment can constrain certain combinations of the mixing elements. This can happen when the neutrino is produced via one mixing and decays via another one, or when both mixing elements play a role in production and decay. For instance, the decay $K^+ \rightarrow \mu^+ N$ yields heavy neutrinos with a flux proportional to $|U_{\mu N}|^2$, but they can afterwards decay into the channel $\nu e^+ e^-$ also via the electronic or the tau mixing. It is important to highlight that in the case in which one mixing is responsible for the production and a different mixing for the decay then number of events is proportional to the product of the mixings $|U_{\alpha N}| |U_{\beta N}|$ if the studied channel is CC-mediated. However, if the decay channel is also sensitive to a NC exchange, the number of events is instead proportional to $|U_{\alpha N}| \sqrt{|U_{\alpha N}|^2 + |U_{\beta N}|^2}$. In the remainder of this section, the combination of two mixings will be denoted by $|U_{\alpha N}^* U_{\beta N}|$ for comparing bounds and sensitivity plots.

The combinations of mixing terms is relevant to charged Lepton Flavour Violating (cLFV) decays or flavour changing neutral current processes which can be enhanced in presence of nearly-sterile neutrinos. For example, the well-known decay $\mu^+ \rightarrow e^+ \gamma$ has a branching ratio which is sensitive to extra neutrino states. This reads

$$\text{Br}(\mu^+ \rightarrow e^+ \gamma) = \frac{3\alpha}{32\pi} \left| \sum_i \hat{U}_{\mu i}^* \hat{U}_{ei} G\left(\frac{m_i^2}{M_W^2}\right) \right|, \quad (5.8)$$

where $G(x)$ is the loop function of the process [243]. The current upper limit is set by the MEG

Table 5.11: This table summarises the sensitivity result of Fig. 5.6. The minimum value of the mixing to Majorana HNLs to which the DUNE ND is sensitive to is reported; the respective mass value at that point is also reported.

Channel	$m_N/\text{GeV} , U_{eN}^* U_{\mu N} $	$m_N/\text{GeV} , U_{\mu N}^* U_{\tau N} $	$m_N/\text{GeV} , U_{\tau N}^* U_{eN} $
$N \rightarrow \nu e^+ e^-$	0.37 , 2.35×10^{-10}	0.36 , 6.99×10^{-10}	0.40 , 2.61×10^{-10}
$N \rightarrow \nu e^\pm \mu^\mp$	0.37 , 1.87×10^{-10}	0.36 , 4.80×10^{-10}	0.41 , 2.82×10^{-10}
$N \rightarrow \nu \mu^+ \mu^-$	0.42 , 4.46×10^{-10}	0.37 , 8.56×10^{-10}	0.42 , 8.51×10^{-10}
$N \rightarrow \nu \pi^0$	0.37 , 6.42×10^{-11}	0.35 , 1.11×10^{-10}	0.39 , 7.45×10^{-11}
$N \rightarrow \nu \rho^0$	1.55 , 4.04×10^{-9}	1.52 , 1.09×10^{-7}	1.55 , 4.04×10^{-9}
$N \rightarrow \nu \eta$	1.57 , 4.84×10^{-9}	1.52 , 1.32×10^{-7}	1.57 , 4.83×10^{-9}
$N \rightarrow \nu \eta'$	1.64 , 6.73×10^{-9}	1.58 , 2.00×10^{-7}	1.64 , 6.72×10^{-9}
$N \rightarrow \nu \omega$	1.55 , 7.51×10^{-9}	1.49 , 2.14×10^{-7}	1.55 , 7.50×10^{-9}
$N \rightarrow \nu \phi$	1.60 , 2.54×10^{-9}	1.58 , 6.78×10^{-8}	1.60 , 2.54×10^{-9}
$N \rightarrow e^\mp \pi^\pm$	0.37 , 6.19×10^{-11}	—	0.39 , 7.24×10^{-11}
$N \rightarrow \mu^\mp \pi^\pm$	0.37 , 7.42×10^{-11}	0.36 , 1.31×10^{-10}	—
$N \rightarrow e^\mp K^\pm$	1.53 , 1.03×10^{-8}	—	1.53 , 1.03×10^{-8}
$N \rightarrow \mu^\mp K^\pm$	1.55 , 1.04×10^{-8}	1.64 , 3.09×10^{-7}	—
$N \rightarrow e^\mp K^{*\pm}$	1.57 , 8.65×10^{-9}	—	1.57 , 8.63×10^{-9}
$N \rightarrow \mu^\mp K^{*\pm}$	1.57 , 8.74×10^{-9}	1.50 , 2.58×10^{-7}	—
$N \rightarrow e^\mp \rho^\pm$	1.55 , 2.23×10^{-9}	—	1.55 , 2.23×10^{-9}
$N \rightarrow \mu^\mp \rho^\pm$	1.55 , 2.25×10^{-9}	1.53 , 5.90×10^{-8}	—

experiment to be $\text{Br}(\mu^+ \rightarrow e^+ \gamma) < 4.2 \times 10^{-13}$ [244]. Despite being one of the best constrained cLFV process, the bounds on $|U_{eN}^* U_{\mu N}|$ are not as good as the ones imposed by other processes, like $\mu \rightarrow eee$ or $\mu - e$ conversion on nuclei [245]. For instance, the constraint from conversion on gold nuclei is $|U_{eN}^* U_{\mu N}| < 1.6 \times 10^{-5}$ for HNL masses larger than 0.1 GeV [246]. The branching ratio of other cLFV channels, like $\tau^\pm \rightarrow e^\pm \gamma$ or $\tau^\pm \rightarrow \mu^\pm \gamma$ cannot be as simply determined and so the bounds achieved on the combination of heavy neutrino mixings are expected to be less stringent [247, 248]. Stronger bounds come from the study of three-body decays of charm and bottom mesons to charged leptons with different flavour and tau decays to pseudoscalar mesons and a charged lepton. From the search for the decay $K \rightarrow e \mu \pi$ the bound $|U_{eN}^* U_{\mu N}| < 10^{-9}$ is reached for masses $0.15 \text{ GeV} \lesssim m_N \lesssim 0.50 \text{ GeV}$; the decays $\tau \rightarrow e \pi \pi$ and $\tau \rightarrow \mu \pi \pi$ set the limits $|U_{eN}^* U_{\tau N}|, |U_{\mu N}^* U_{\tau N}| < 5 \times 10^{-6}$ for the respective mass ranges $0.14 \text{ GeV} \lesssim m_N \lesssim 1.7 \text{ GeV}$ and $0.24 \text{ GeV} \lesssim m_N \lesssim 1.7 \text{ GeV}$ [206].

Instead of dealing with a three-dimensional parameter scan of the neutrino mass and two mixing angles, the study is simplified by assigning the same value to the two mixing parameters under consideration, for which the number of HNL decays is maximal. The number of events is then reported as a function of the neutrino mass and the combination $|U_{\alpha N}^* U_{\beta N}|$. The results for all channels considered in this work are shown in Fig. 5.6. The best constraints come again from two-body semileptonic decays for all mixing combinations, the lowest upper limits being $|U_{eN}^* U_{\mu N}| < 6 \times 10^{-11}$ at $m_N \simeq 0.36 \text{ GeV}$, $|U_{\mu N}^* U_{\tau N}| < 1.3 \times 10^{-10}$ at $m_N \simeq 0.35 \text{ GeV}$, and $|U_{\tau N}^* U_{eN}| < 7 \times 10^{-11}$ at $m_N \simeq 0.39 \text{ GeV}$. Amongst the three-body leptonic decay channels, $N \rightarrow \nu ee$ has the best sensitivity for masses $m_N < m_{K^0}$, but the mode $N \rightarrow \nu e^\mp \mu^\pm$ can be actually more constraining at higher masses. Regarding the channels available only above the kaon mass threshold, decays to pseudoscalar mesons are the most sensitive between CC processes, whereas the decay $N \rightarrow \nu \phi$ gives the best constraint of the NC-mediated channels. In Table 5.11, the sensitivity results for two dominant mixings are reported.

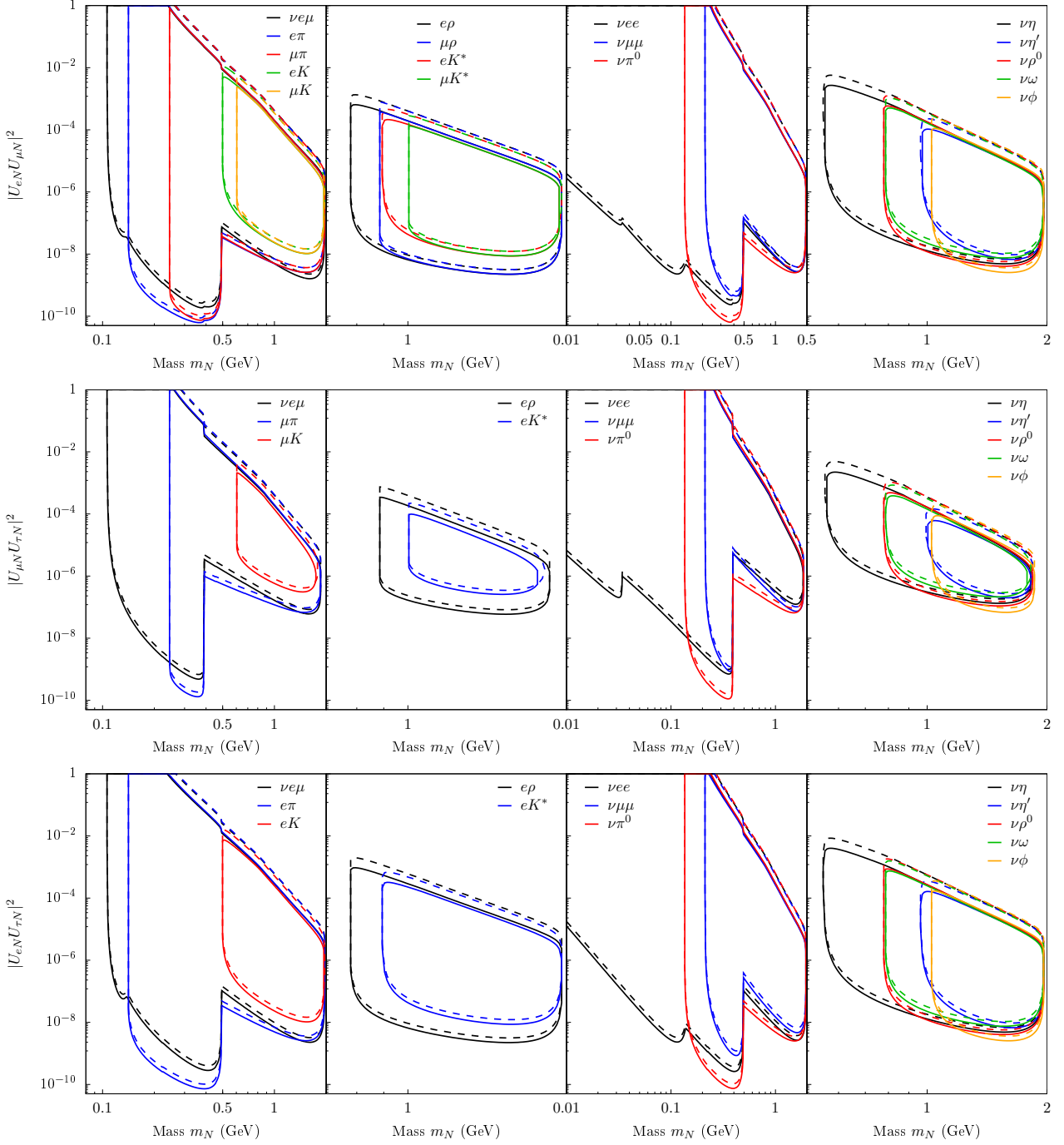


Figure 5.6: The 90 % C.L. sensitivity regions to individual channels for two dominant mixings $|U_{eN}^* U_{\mu N}|$ (top), $|U_{\mu N}^* U_{\tau N}|$ (middle), and $|U_{eN}^* U_{\tau N}|$ (bottom) are presented. All the modes considered in this work are shown here, but no background analysis is reported. As before, the solid lines correspond to the analysis with Majorana neutrinos, the dashed lines with Dirac neutrino.

5.4 Mass model constraints from the DUNE ND

From the results presented in the previous section, the DUNE ND will be sensitive to very low couplings for experimentally accessible mass values. These points of the parameter space correspond to regions viable in some realisations of low scale neutrino mass models. In view of the discussion regarding seesaw models in Section 4.1, a random scan of mass matrices is performed to define such regions of the parameter space. Three minimal ISS scenarios are chosen requiring they predict a HNL with a mass accessible by the experiment and that satisfy the experimental evidence of neutrino oscillation [249]. Following the notation introduced in Chapter 4, in the first two cases the heavy neutrino under study belongs to the lightest pseudo-Dirac pair of an ISS (2,2) and an ISS (2,3) realisation; the third scenario is an ISS (2,3) case in which the fourth massless state becomes a Majorana neutrino in the MeV–GeV region thanks to a high LNV parameter. The details of this analysis are reported in this section, together with the overall sensitivities of the DUNE ND to heavy neutrino discovery and low scale mass models. A comparison with future experiments is also included.

5.4.1 Mass model scan

Neutrino mass matrices with the same structure of Eq. (4.12) are randomly generated and numerically diagonalised. The number of physical parameters of a ISS (a, b) mass matrix is found to be $n_p = 7a + b + 2ab$ [249]. A basis in which m_D has complex entries but three of which are real and M_R is diagonal and real can be chosen without loss of generality. If the matrix entries respect the hierarchy $\mu \ll m_D \ll M_R$, the mass spectrum in the LNC limit is principally given by the diagonal values of M_R . The matrix is then perturbed to achieve the three minimal ISS scenarios introduced above; the randomly generated mass matrix \mathcal{M} is diagonalised using the Jacobi Singular Value Decomposition (SVD) as implemented in the Eigen library [250]. The Takagi decomposition,

$$\hat{U}^T \mathcal{M} \hat{U} = \text{diag}(m_1, m_2, m_3, \dots) , \quad (5.9)$$

is finally retrieved starting from the SVD decomposition $\mathcal{M} = V \Sigma U^\dagger$, from which the singular values Σ are the nonnegative square roots of the eigenvalues of $\mathcal{M}^\dagger \mathcal{M}$ and the unitary matrix is $\hat{U} = U \rho^\dagger$, where $\rho = (U^T V)^{\frac{1}{2}}$ is a unitary phase matrix.

Only matrices satisfying the current constraints on heavy neutral fermions are taken into account. The first requirement is that the eigenvalues must give the correct mass squared splittings compatible within 3σ with the measured values [17]. The condition of matching also the measured mixing angles is relaxed because the entries of the PMNS matrix are the result of the random structure of m_D and μ . Constraints on the unitarity of the mixing matrix are applied instead. The deviation from unitarity are quantified by the following Hermitian matrix:

$$\varepsilon_{\alpha\beta} \equiv |\delta_{\alpha\beta} - (\mathcal{U} \mathcal{U}^\dagger)_{\alpha\beta}| = \left| \sum_{i=4}^n \hat{U}_{\alpha i} \hat{U}_{\beta i}^* \right|. \quad (5.10)$$

The nonunitarity of the PMNS matrix has been assessed in various experiments, and the constraints depend upon the mass scale of averaged out neutrinos. For neutrino masses below the GeV scale, but heavy enough to decouple from flavour oscillations, nonunitarity effects are tested in neutrino oscillation experiment as an overall normalisation. If the neutrino mass is above the GeV scale, electroweak precision experiments provide strong constraints on nonunitarity. The

limits are summarised below (from Ref. [251–253])

$$\varepsilon_{\alpha\beta} < \begin{pmatrix} 2.4 \times 10^{-2} & 1.3 \times 10^{-2} & 3.5 \times 10^{-2} \\ \cdot & 2.2 \times 10^{-2} & 6.0 \times 10^{-3} \\ \cdot & \cdot & 1.0 \times 10^{-1} \end{pmatrix} \quad \text{if } 10 \text{ eV} \lesssim m_N \lesssim 1 \text{ GeV} , \quad (5.11)$$

$$\varepsilon_{\alpha\beta} < \begin{pmatrix} 1.3 \times 10^{-3} & 1.2 \times 10^{-5} & 1.4 \times 10^{-3} \\ \cdot & 2.2 \times 10^{-4} & 6.0 \times 10^{-4} \\ \cdot & \cdot & 2.8 \times 10^{-3} \end{pmatrix} \quad \text{if } m_N \gtrsim 1 \text{ GeV} . \quad (5.12)$$

The μ entries of the ISS matrices naturally lead to lepton flavour and lepton number violating processes. The most studied LFV process is the decay rate of $\mu^+ \rightarrow e^+ \gamma$, the branching ratio of which is given in Eq. (5.8). The current upper limit on the branching ratio is 4.2×10^{-13} , but a future upgrade of the experiment foresees to reach a limit lower than 5×10^{-14} .

Heavy neutrinos in a ISS model also contribute to the neutrinoless double beta decay. The effective neutrino mass $m_{\beta\beta}$ receives further corrections with respect to the standard expression as

$$m_{\beta\beta} \simeq \left| \sum_i \hat{U}_{ei}^2 \frac{p^2 m_i}{p^2 - m_i^2} \right| \quad (5.13)$$

where $p^2 \simeq -0.015 \text{ GeV}^2$ is the typical virtual momentum of the exchanged neutrino. The contribution from masses above the 0.1 GeV scale drops as $1/m_i^2$ while it is constant for masses below [254]. It is interesting to note that the contributions given by pseudo-Dirac pairs are subject to partial cancellation, regulated by the LNV parameters. In the LNC limit, the cancellation is maximal and the paired states do not take part in the $0\nu\beta\beta$ process. The latest result from the KamLAND-Zen experiment is interpreted as $m_{\beta\beta} < 61 \text{ meV}$ [255].

For the first two ISS scenarios, the allowed ranges span the space given by $m_D \sim 10^{[3,6]} \text{ eV}$, $M_R \sim 10^{[6,15]} \text{ eV}$, $\mu \sim 10^{[-4,1]} \text{ eV}$. Each matrix generated is verified to respect the *naturalness condition* in the 't Hooft sense [194] and that the mass spectrum presents a mass state accessible by the DUNE experiment. For the third ISS case, large entries of the submatrix μ are necessary to give the Majorana state a mass that can be probed by the experiment. The ranges of $m_D \sim 10^{[3,10]} \text{ eV}$, $M_R \sim 10^{[7,15]} \text{ eV}$, $\mu \sim 10^{[4,9]} \text{ eV}$ respects the constraints. The hierarchy and naturalness conditions are relaxed in this case. The resulting points in the space $(m_N, |U_{\alpha N}|^2)$ are clustered together and the regions defined are overlaid in Fig. 5.7. Any combination of mass and mixing element inside these areas can be justified by a valid neutrino mass matrix which can explain the light neutrino masses and survive the experimental constraints. The pseudo-Dirac pairs from the ISS (2,2) and ISS (2,3) scenarios give very similar regions, but Majorana states from the ISS (2,3) realisation can only be generated with very small couplings. A type I seesaw band, corresponding to light neutrino mass between 20 meV and 200 meV, is highlighted in the figure for comparison.

5.4.2 Overall sensitivity

The overall sensitivity of the DUNE ND to the discovery of HNL is defined here as the combination of the sensitivities to some selected channels and presented in Fig. 5.7. These channels are $N \rightarrow \nu e^+ e^-$, $\nu e^\pm \mu^\mp$, $\nu \mu^+ \mu^-$, $\nu \pi^0$, $e^\mp \pi^\pm$, and $\mu^\mp \pi^\pm$, and are preferred because of their good discovery prospect, for which a background study has also been carried out. They all give strong sensitivities, especially for masses below 0.5 GeV as it can be seen in Section 5.3. Their competitive reach is due to high branching ratios and the HNL flux being more intense at such masses. Furthermore, the final-state particles are all well-studied particles most of which leave tracks in the detector that are easy to reconstruct, thus allowing the background to be

controlled with sufficient precision. The neutrino spectrum component coming from the D_s meson allows for a weaker sensitivity to masses above the neutral kaon mass. The sensitivity study is conducted for the two scenarios in which either a Majorana or a Dirac neutrino is the decaying particle.

A comparison with previous experiments allows to appreciate the ND performance to searches of HNLs. The results of PS191 [170, 171], peak searches [164–166], CHARM [175], NuTeV [176], DELPHI [173], and T2K [172] are shown in Fig. 5.7. It is found that the DUNE ND can increase the bound on the electronic and muonic mixing elements for masses $m_N < m_{K^0}$ with respect to past experiments. The constraint on the tauonic mixing is at least comparable with previous measurements. For masses above, for which neutrino production relies on charm meson decays, the existing bounds are improved for the electronic mixing and the tauonic mixing, while just a conservative result can be achieved in the muonic case. The prospects for the SBN programme [212], NA62 [228], and the proposed SHiP [237], MATHUSLA [231], and FASER [233] with 1 m radius are also overlaid. The DUNE ND will give the best sensitivity for masses below the 0.5 GeV in all channels, but the tauonic one. However, anywhere the D_s meson production is involved, the experiment cannot outperform the predicted sensitivity of the SHiP experiment which will deploy a 400 GeV proton beam on a titanium-zinc-molybdenum alloy target, enhancing the production of charm and bottom mesons. MATHUSLA will have a similar sensitivity, collecting particles from the High Luminosity LHC phase. NA62 gives better results for the $|U_{\mu N}|^2$ mixing, but DUNE has a better sensitivity to the electron and tau channels. FASER is comparable to NA62 in sensitivity, but it can reach regions of the parameter space beyond the 2 GeV limit to which DUNE is not sensitive. Compared to a previous similar study [221], the sensitivities estimated in this analysis give stronger or at least comparable bounds. More specifically, the limits on $|U_{eN}|^2$ are stronger even considering the background events. This is true also for the limits on $|U_{\mu N}|^2$, but only for masses below 500 MeV: in Ref. [221] the sensitivity to masses above this threshold is enhanced by the contribution from B meson which is not estimated in this study. For the same reason, the limits on $|U_{\tau N}|^2$ prove to be comparable to the result of this work, despite accounting only for the D_s meson component. Moreover, a different ND configuration was assumed and no background study was performed in Ref. [221].

Finally, in Fig. 5.7 the overall sensitivity is compared with respect to regions allowed by neutrino mass models. In the electronic and muonic channels, the DUNE ND will be sensitive to a large part of the pseudo-Dirac regions, corresponding to ISS (2,2) and ISS (2,3) models, part of which have been already excluded by past experiments. The ND will also close the gap and put to test type I seesaw parameters, especially for HNL masses between 0.2 and 0.5 GeV, starting to reach the region of ISS (2,3) with large lepton number violation. For the tauonic channel, the experiment will probe only a small portion of pseudo-Dirac pairs from ISS (2,2) and ISS (2,3) models. The sensitivity is not high enough to reach type I and Majorana state regions, which not even the dedicated experiment SHiP can.

The ISS (2,3) scenario in which the pseudo-Dirac pair is accessible by the experiment also predicts a light Majorana state, the mass of which is controlled by the small LNV perturbations. This entails the presence of a third mass splitting Δm_{41}^2 , which could give an active–sterile oscillation signature in short baseline experiments, very much debated in literature (see Ref. [257] for a recent review). In figure Fig. 5.8, the new mass splitting is plotted against the mixings $|U_{e4}|^2$, $|U_{\mu 4}|^2$, and the combination usually referred to as $\sin^2 2\theta_{\mu e} \equiv 4|U_{e4}|^2|U_{\mu 4}|^2$. The mass splittings generated in the matrix scan span from $\Delta m_{31}^2 \simeq 0.0025 \text{ eV}^2$ up to 10^4 eV^2 , and the squared mixings cover a large region, down to 10^{-14} for all the flavours. The reactor anomalies could be soon excluded at the 90 % C.L. by the DANSS experiment [146] and the allowed regions from LSND [131] and MiniBooNE [132–134] require values of $\sin^2 2\theta_{\mu e} \gtrsim 10^{-3}$. The regions already excluded by these experiments are also reported in Fig. 5.8. Given the results of the

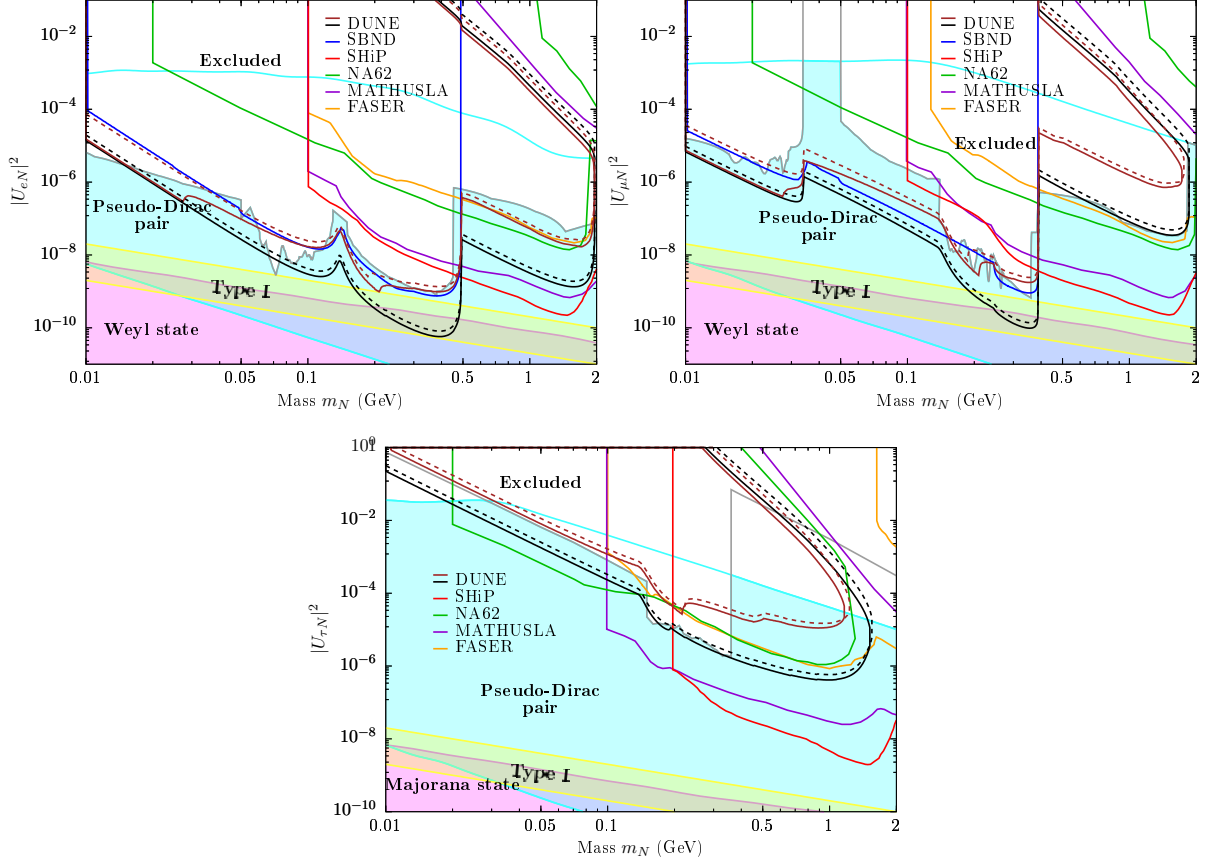


Figure 5.7: The 90 % C.L. sensitivity regions for dominant mixings $|U_{eN}|^2$ (top left), $|U_{\mu N}|^2$ (top right), and $|U_{\tau N}|^2$ (bottom) are presented combining results for channels with good discovery prospects (see text). The study is performed for Majorana neutrinos (solid) and Dirac neutrinos (dashed), in the case of no background (black) and after the background analysis (brown). The region excluded by experimental constraints (grey) is obtained by combining the results from PS191 [170, 171], peak searches [164–168], CHARM [175], NuTeV [176], DELPHI [173], and T2K [172], with the lines reinterpreted for Majorana neutrinos (see Ref. [187]). The sensitivity for the DUNE ND (black) is compared to the predictions of future experiments, SBN [212] (blue), SHiP [237] (red), NA62 [228] (green), MATHUSLA [231] (purple), and FASER [233] with 1 m radius (orange). The shaded areas corresponds to possible neutrino mass models considered in this work: the simulations of the ISS (2,2) and ISS (2,3) models where the lightest pseudo-Dirac pair is the neutrino decaying in the ND (cyan); the ISS (2,3) scenario when the single Majorana state is responsible for a signal (magenta); the type I seesaw scenario with a neutrino mass starting from 20 meV to 0.2 eV (yellow).

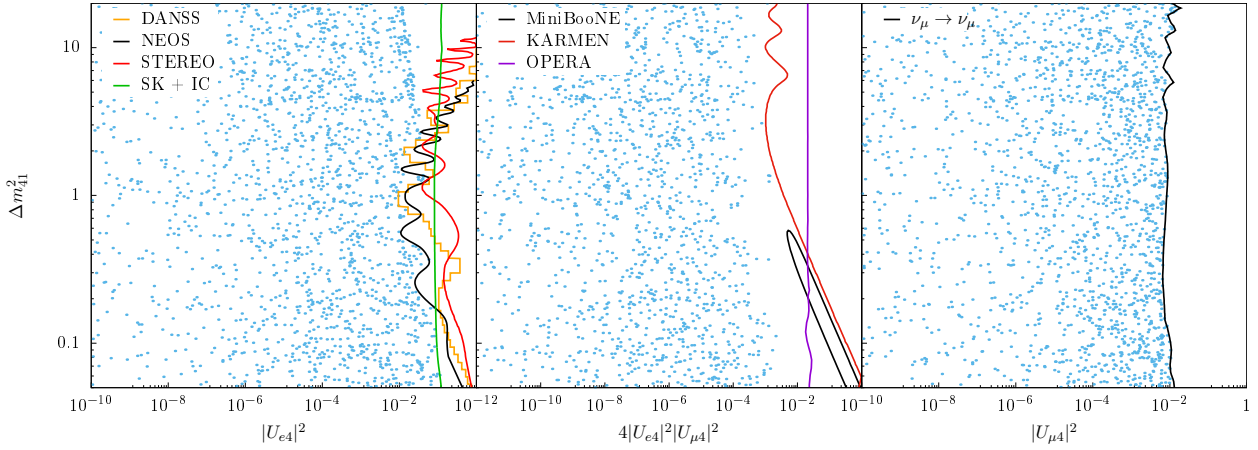


Figure 5.8: One of the two ISS (2,3) realisations considered presents a Majorana state at masses comparable with short baseline experiments. The results of the ISS (2,3) simulation (blue dots) for Δm_{41}^2 against combination of mixing angles and the experimental result at 90 % C.L. are shown. $|U_{e4}|^2$ (left) compared to DANSS [146], NEOS [145], STEREO [256], and Super-Kamiokande and IceCube combined [257]; $\sin^2 2\theta_{\mu e} = 4|U_{e4}|^2|U_{\mu 4}|^2$ (middle) compared to KARMEN2, OPERA and MiniBooNE [134], and $|U_{\mu 4}|^2$ (right) compared to a combined ν_μ disappearance analysis [257]. Only the points generated by matrices which pass the experimental constraints are shown here.

matrix scan, it is unlikely that one of the ISS (2,3) realisations considered in this work could explain simultaneously a short baseline anomaly and predict a heavy neutrino-like signal in the DUNE ND, unless for sparse and very fine-tuned points.

5.5 Determining the nature of HNLs

If such heavy neutrino states are discovered, it would be possible to distinguish the fermionic nature of the decaying HNL by studying the charge of the decay products. Thanks to the different angular dependencies of polarised decay rates for Majorana and Dirac, analysing the angular distributions of HNL decays could be in principle used to distinguish between the two scenarios [214]. As studied in Section 4.2, the two-body decay distributions for a Majorana neutrino with given helicity into a neutral final state is isotropic in the heavy neutrino rest frame. This is also true of the total decay distribution of charged final states in the absence of charge-ID in the detector. For two-body semileptonic decays, the polarised decay rate has a linear or antilinear dependency on $\cos \theta$ in the rest frame, according to the polarisation and lepton number of the neutrino, where θ is the polar angle of the charged lepton to the beamline. However, for practical applications, studying angular distributions requires modest statistics and such distributions might not be obvious anymore once they are convolved with the neutrino spectrum.

It is worth noting that aside from the neutral current distributional differences the direct distinction between charged-conjugate final states is an equally competitive means of determining the nature of the initial state. The discussion of this section focuses on the channels $N \rightarrow \ell^\mp P^\pm$, as these present the best discovery prospect. The decays into charged pseudoscalar mesons P^\pm are the channel with the highest branching ratio (see Section 4.2) and the ones with the cleanest experimental signature, despite the nonnegligible background. Moreover, the charge of the final-state lepton is directly determined by the fermionic type of the decaying neutrino. Assuming a beam purely composed of neutrinos, a Dirac HNL produced in the beam could only decay into $\ell^- P^+$, as lepton number is preserved. On the other hand, if the heavy

neutrino is Majorana, the LNV channel $\ell^+ P^-$ would be also expected with the same rate as the LNC mode. With perfect detector efficiency and performance, only one LNV event is necessary to reject LNC. In addition to the different event rate, the angular and energy distribution of the decays will vary depending on the fermionic nature of the neutrino, because of different helicity contributions. However, a beam of only neutrino is not achievable with the conventional techniques used to produce accelerator neutrinos. Unsuccessful focusing and deflection by the horn system for short-lived secondary particles is the cause of an irremovable component of antineutrinos in the neutrino mode beam. This results in an intrinsic background of LNV events which are not expected in the case of a Dirac neutrino. The same discussion applies equally to the beam in antineutrino mode.

Neglecting background from SM events, the number of HNL decay events inside the detector is computed using Eq. (5.3). For given HNL mass and mixings, let us define as σ and ρ respectively the number of signal events for the channel $\ell^- \pi^+$ and for the channel $\ell^+ \pi^-$. The probability of detecting s events for the first channel and r events for the second one follows a bi-Poisson distribution with rate parameters respectively σ and ρ :

$$P(s, r) = e^{-\sigma} \frac{\sigma^s}{s!} e^{-\rho} \frac{\rho^r}{r!} . \quad (5.14)$$

With this probability definition, a frequentist confidence regions is defined for each given point of the parameter space, i.e. a combination of σ and ρ , sorting by the ratio of probabilities [242]

$$\frac{P(s, r)}{P(\hat{s}, \hat{r})} , \quad (5.15)$$

where the best fit points are $\hat{s} = \sigma$ and $\hat{r} = \rho$ if the HNL is Dirac or $\hat{s} = \hat{r} = (\sigma + \rho)/2$ if Majorana. The Poissonian probabilities are then summed until reaching 99 % C.L., delineating in this way a region in the (σ, ρ) space. If the two regions for the case of Dirac or Majorana HNL do not overlap, then it is possible to distinguish the two scenarios with 99 % C.L. SM background can be accounted for by replacing $\sigma \rightarrow \sigma + b_\sigma$ and $\rho \rightarrow \rho + b_\rho$.

Correct charge identification is therefore a necessary requirement to distinguish between lepton number conserving and lepton number violating processes. Being magnetised, the MPD is capable of charge identification of tracks. An analysis on the determination of the HNL nature by the MPD was carried out in Ref. [258]. Although charge identification is a difficult task with liquid argon technology, some events originating inside the LArTPC module can propagate to the MPD and the charge of escaping particles could be identified in this way. This would allow the expansion of the fiducial volume of the ND sensitive to charges which strongly depends on the momentum of the final-state particles. Using the same fast MC simulation of the DUNE ND explained in Section 5.2, the charge is retrieved if the sagitta of curved tracks inside the MPD are greater than 1 cm, hundred times the spatial resolution. Assuming a high momentum and neglecting energy loss in the MPD, the condition required is

$$s \simeq \frac{L^2}{R} \simeq \frac{0.3 B}{p} L^2 (\cos^2 \theta + \sin^2 \theta \sin^2 \phi)^2 > 0.1 \text{ cm} , \quad (5.16)$$

where $B = 0.5 \text{ T}$ is the magnetic field of the MPD, p the charged particle momentum, L the length of the track, and θ and ϕ the polar and azimuth angles. The 90 % C.L. regions in which statistics is sufficient for distinguishing between Majorana and Dirac neutrinos are shown in Fig. 5.9. As specified above, the two-body pseudoscalar meson channels are used in conjunction with an expanded fiducial volume compared to Ref. [258]. A background evaluation for this specific analysis is under study. Charge identification can further reduce background from SM

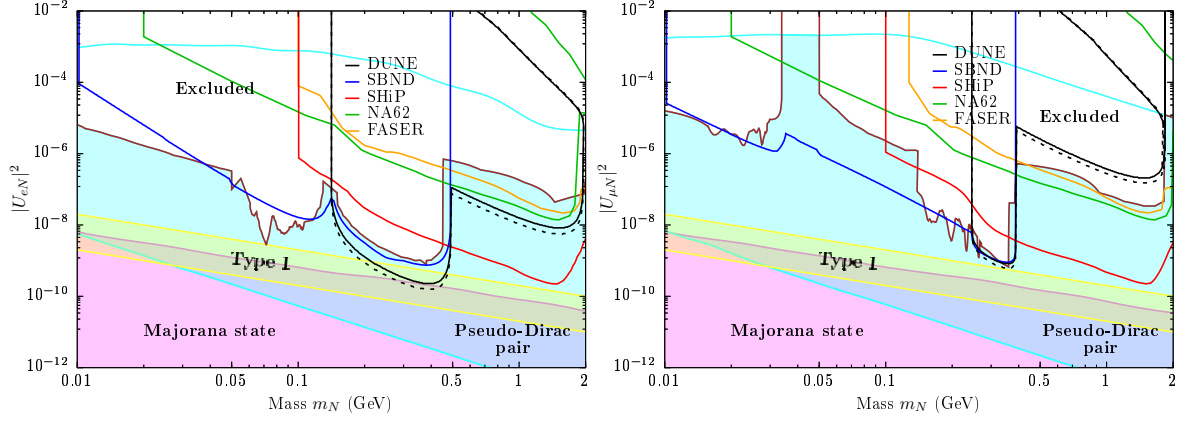


Figure 5.9: The regions in which distinction between Majorana and Dirac HNL is possible with 90 % C.L. are shown for dominant $|U_{eN}|^2$ (left) and $|U_{\mu N}|^2$ (right). The channels $N \rightarrow e^\mp \pi^\pm$ and $\mu^\mp \pi^\pm$ are used, respectively. The dashed line black line assumes 100 % charge identification, whereas the solid ones correspond to a realistic charge detection efficiency evaluated with a MC simulation. The regions are compared to the exclusion limits to HNL discovery of future experiments: SBN [212] (blue), SHiP [237] (red), NA62 [228] (green), MATHUSLA [231] (purple), and FASER [233] with 1 m radius (orange). The region excluded by experimental constraints (brown) is obtained by combining the results from PS191 [170, 171], peak searches [164–168], CHARM [175], NuTeV [176], DELPHI [173], and T2K [172]. The shaded areas corresponds to possible neutrino mass models considered in this work: the simulations of the ISS (2,2) and ISS (2,3) models where the lightest pseudo-Dirac pair is the neutrino decaying in the ND (cyan); the ISS (2,3) scenario when the single Majorana state is responsible for a signal (magenta); the type I seesaw scenario with a neutrino mass starting from 20 meV to 0.2 eV (yellow).

neutrino interactions, especially if with production of extra pions and other hadrons. HNL decays have always particles of opposite charge in the final state and this requirement can help reject more background events in the selection process.

Summary

In this chapter, the sensitivity of the DUNE ND to heavy neutral leptons in beam-dump-style searches has been estimated. The analysis is based on the calculations presented in Chapter 4, as HNLs can be produced with light neutrinos by the powerful LBNF neutrino beam and subsequently decay inside the Near Detector system. The number of heavy neutrinos is calculated by a convolution between the HNL flux, the decay probability, and detector’s efficiency and geometry. A first estimate of the ν_τ component of the beam from D_s mesons has also been carried out. The efficiency of the detector is evaluated with the help of a custom fast MC simulation and the background sources from SM neutrino–nucleon interactions are generated with GENIE. A detailed background study was also performed on decay channels with good detection prospects, defined by high branching ratios and clean detector signatures. Thanks to the vicinity to the beam target and the state-of-the-art reconstruction capabilities, the DUNE ND can place very competitive bounds to the HNL mixings with active neutrinos; the 90 % C.L. sensitivity regions have been estimated for both single and dominant mixings. For masses between 0.3 and 0.5 GeV, the ND can probe mixing elements below 10^{-9} in most cases, reaching 10^{-10} especially with two-body semi-leptonic channels via $|U_{eN}|^2$ and $|U_{\mu N}|^2$. Thanks to the D_s meson production, neutrino masses above 0.5 and up to 2 GeV are also accessible, as well as the sensitivity to the tau mixing. A random matrix scan of possible inverse seesaw realisations shows that the DUNE ND can extend current limits on mixing parameters reaching regions of

interest for neutrino mass models. If a discovery is made, some considerations can be drawn upon the nature of the new fermionic states, particularly if the charges of the final state particles can be reconstructed.

Chapter 6

Conclusions

One of the most compelling discoveries of the past few years is evidence of neutrino oscillation. The main consequence is that at least two neutrino states have a non-zero mass below the eV scale, although Dirac mass terms for neutrinos are not permitted or difficult to justify in the Standard Model. Addressing this insufficiency together with others, for example matter-antimatter asymmetry or dark matter, requires an extension of the current theory. The hope is that from accurate and precise measurements new hints of physics beyond the Standard Model (BSM) will appear and bring about a better comprehension of theoretical models. This thesis has explored just a fraction of the vast realm of topics in neutrino physics, focusing mainly on next-generation neutrino experiments. Some of the existing experiments will renovate and broaden their capabilities by adopting new detection methods, such as Super-Kamiokande and gadolinium capture. At the same time new experiments, such as Hyper-Kamiokande, will push familiar techniques to the limit to increase the precision of oscillation physics. Other upcoming experiments, such as DUNE, will implement state-of-the-art technologies on a large scale not only to study Standard Model physics, but also to perform complementary searches of BSM physics.

The benefits of gadolinium for water Cherenkov detectors have been explained in Chapter 2. Super-Kamiokande (SK) is about to start a new phase in which a hundred tons of gadolinium sulphate will be dissolved in the water tank. This will allow the detector to improve neutron tagging efficiency up to 90% — with a Gd concentration of 0.2% — transforming the experiment into a supernova observatory and improving all the ongoing analyses. There are many technical challenges when dealing with a Gd-loaded Cherenkov detector, one of which being the monitoring of gadolinium concentration in water. A new method involving UV absorption spectroscopy is being developed with promising results, as shown in Chapter 2. Gadolinium presents strong absorption lines in the region between 270 nm and 275 nm and their intensity is directly proportional to the amount of gadolinium. This technique allows for an almost continuous monitoring of the concentration, compared to the current spectroscopy technique in place which is executed with a monthly frequency. The precision reached with the UV absorption spectroscopy is around $\sim 0.3\%$ on the full load concentration of 0.2%, using a 100 cm water sample. The same device was able to reach competitive sensitivity also on the initial loading concentration of 0.02%. Regardless of gadolinium-doping, an improved method for neutron calibration of the detector was also investigated. A californium-252 source has some advantages compared to the currently employed Americium-Beryllium (Am-Be), among which the possibility of estimating the source activity indirectly. Using a GEANT4 simulation, it was found that the same calibration device used by SK has already the optimal shape to be used with ^{252}Cf instead. The Am-Be neutron source could then be replaced without further modifications of

the device, and a more accurate neutron calibration can be achieved thanks to the features of spontaneous fission events in californium-252.

The next-generation water Cherenkov detector, Hyper-Kamiokande (HK), has been introduced in Chapter 3. Thanks to unprecedented statistics and upgraded instrumentation, Hyper-Kamiokande has the potential to study a plethora of topics related to neutrino physics, with particular emphasis on neutrino oscillation and CP violation in the lepton sector. In this thesis, the sensitivity to oscillation parameters has been assessed employing a framework capable of beam and atmospheric combined fits. The atmospheric events for HK are simulated by scaling SK Monte Carlo atmospheric data and they are classified as fully-contained, partially contained, or upward-going muons events, for a total of 2224 bins. The beam-related events are classified as electron- or muon-like one ring events, for the beam in neutrino mode or antineutrino mode and they are arranged in four distributions with 87 energy bins each. These spectra are predicted from a neutrino beam flux simulation tuned with near detector constraints. Once a *true* combination of oscillation parameters is chosen, the χ^2 between observed (true) and expected events is calculated in the way explained in Chapter 3. The likelihood includes effects from systematic uncertainties and although the atmospheric model is still preliminary, the state-of-the-art T2K systematic model is adopted for the beam component instead. It consists of 119 systematics encompassing beam, cross-section, and far detector parameters. Just considering the beam sample, it is found that Hyper-Kamiokande can exclude maximal violation of CP at full statistics with more than 6σ of significance. Some variations of the beam systematic model are also being investigated in order to understand how the experimental sensitivity is affected by certain model parameters. One of these, the energy scale error, might be treated too naively in the fitting framework and so slight modifications to both the error model and the likelihood should be considered. This study, however, is preliminary and still ongoing.

In Chapter 4, the origin and lightness of the neutrino mass has been addressed in the framework of low-scale seesaw mechanisms. The addition of an arbitrary number of heavy neutral leptons is the simplest extension of the Standard Model and it is accompanied with a diverse and rich phenomenology. Some textures of the mass matrix, such as the one of the inverse seesaw, predict Majorana or pseudo-Dirac heavy neutrinos with experimentally accessible masses. These new particles could be searched for by direct production in beam dump experiments, in which the expected signature would be an in-flight decay into Standard Model particles. In this thesis, the phenomenological consequences of Majorana and Dirac states have been thoroughly investigated in light of searches of neutrino decays. The differential decay rates and production scale factors have been computed using the spinor-helicity formalism and are provided decomposed by helicity states. It was shown that Dirac and Majorana neutrinos have different total decay width in neutral current processes and measuring the rate could be an actual way of determining the nature of the initial state. Interesting differences appear between Majorana and Dirac neutrinos once the role of helicity is considered, and this could be also exploited to determine the nature of the heavy singlet fermion. The effect of helicity emerges in the differential decay rate leading to different distributions of final state particles. For example, if the HNL are Majorana, two-body decays present an isotropic distribution for both helicity states, or if Dirac, the angular distribution has a dependency proportional to $A \pm B \cos \theta$ with the sign depending on the helicity state. An effective evaluation of the heavy neutrino flux was also carried out which is not polarised to a single helicity state differently from a light neutrino flux. The production modes of nearly-sterile neutrinos are sensitive to their helicity state, thanks to mass effects which lead to the enhancement of certain channels with respect to light neutrinos. The two components of the neutrino flux behave therefore differently thanks to the dependency of decay distribution on the helicity. These results, first published in Ref. [1], set the groundwork for novel phenomenological analyses of future experiments.

For instance, the near detector complex of DUNE is capable of performing BSM searches, as described in Chapter 5. Although the main goal of the experiment is precision oscillation physics, the near detector proves to be an ideal candidate to search for heavy neutrino decays, given the intense neutrino beam and exceptional reconstruction capabilities. If at least one extra neutral state exists with a mass from few MeV to the GeV, the new singlet would be produced in the beam thanks to suppressed mixings by meson and lepton decays. The high energy of the proton beam allows neutrino masses up to 2 GeV which have also been tested by simulating D_s meson production at the target. A background study was performed on decay channels with good detection prospects, defined by high branching ratios and clean detector signatures. Due to the ND vicinity to the beam target, it is fundamental to suppress the overwhelming number of SM neutrino–nucleon interactions, which constitute the background for the rare signal of HNL decays. Most of the time, both the reconstruction of hadronic activity at the vertex and the multiplicity of final state particles are enough to distinguish between signal and background, reducing the latter down to $\lesssim 5\%$. To further reduce unwanted events, simple kinematic cuts are applied thanks to the very forward distribution of decay in-flight events, additionally suppressing the background events to less than 5×10^{-5} of the original number. The rejection prescriptions are tuned to maintain an acceptable signal efficiency, which is between $\sim 40\%$ down to $\sim 20\%$. For all the other channels, no background study was performed, mainly because the final state particles are vector mesons which present experimentally challenging and specific signatures, the study of which was out of the scope of this work. Combining the scaled flux components with the decay probabilities and signal efficiencies, the 90 % C.L. sensitivity of the near detector has been estimated to all accessible channels, for both single and dominant mixings. For masses between 0.3 and 0.5 GeV, the ND can probe mixing elements below 10^{-9} in most cases, reaching 10^{-10} , especially with two-body semi-leptonic channels for both $|U_{eN}|^2$ and $|U_{\mu N}|^2$. Thanks to the D_s meson production, neutrino masses above 0.5 and up to 2 GeV become accessible, as well as production and decay modes purely sensitive to the tau mixing. In this case, the sensitivity does not exceed 10^{-8} for the electronic and muonic channels and 5×10^{-6} for the tauonic channel. Finally, a random matrix scan of different inverse seesaw realisations was performed to define regions of allowed parameter space. It is found that the near detector can extend current limits on mixing parameters, reaching regions of interest for neutrino mass models. If a discovery is made, some considerations can be drawn upon the nature of the new fermionic states. The charges of the final state particles can help determine whether the lepton number is conserved in the event: any event clearly violating lepton number would be a manifestation of the Majorana nature of the decaying HNL.

In conclusion, neutrino physics has made giant leaps thanks to both impressive experimental efforts and remarkable theoretical progress. Neutrino oscillation has an impact on numerous fields beyond elementary particle physics, such as nuclear physics, astrophysics, and cosmology, just to name a few. The broader implications that this phenomenon brings need to be taken into account in order to study it in depth and either prove or disprove the Standard Model. The work presented in this thesis has been fundamental to progress on both the experimental and theoretical side. Next-generation neutrino experiments will produce new results that will be crucial for grasping the underlying principles of particle physics.

Acknowledgements

I would like to express my gratitude to my advisors Silvia Pascoli and Francesca Di Lodovico for their support and the opportunities given, and to my mentors Peter Ballett and Ben Richards from whom I have learned a lot and who have helped me stay afloat amongst disparate projects. I am deeply grateful for the quality and variety of discussions shared among all of us during these three and a half years.

One of the great aspects of being a joint student between two institutes is the sheer number of people met during this formidable path. I would like to acknowledge all the physicists and friends I have encountered in Durham, in London, and in Japan, who are a part of this thesis and some unforgettable memories. I hope our paths will cross again.

I would like to thank my parents, Donata Murari and Marco Boschi, and my sister, Sofia, who should, by now, know what neutrinos are. They have always stood by each and every decision I have ever made.

Finally, I would like to thank Arianna Renzini, my life partner and the best companion I could have possibly wished for in this amazing journey and so many others to come.

Appendix A

List of systematics

The meaning and the value of the systematic uncertainties of the model adopted for the oscillation analysis of Chapter 3 is reported here. The beam systematics are a combination of systematics from near detector fits (BANFF) and SK and Final State Interactions (FSI) studies. The two groups of systematics are uncorrelated.

A.1 BANFF systematics

ν -mode flux		$\bar{\nu}$ -mode flux		Cross-section	
Parameter	σ (%)	Parameter	σ (%)	Parameter	σ (%)
ν_μ (0)	0.057	ν_μ (0)	0.041	2p-2h normalisation for ^{16}O	0.673
ν_μ (1)	0.073	ν_μ (1)	0.036	C_5^A nucleon to Δ axial form factor	0.027
ν_μ (2)	0.049	ν_μ (2)	0.047	Isospin 1/2 nonresonant background scale	0.212
ν_μ (3)	0.006	ν_μ (3)	0.100	CCQE axial-mass scaling factor	0.006
ν_μ (4)	0.969	ν_μ (4)	0.087	Resonance-production axial-mass scaling	0.893
ν_μ (5)	0.987	$\bar{\nu}_\mu$ (0)	0.051	Second-class current axial	1.000
ν_μ (6)	0.056	$\bar{\nu}_\mu$ (1)	0.055	Second-class current vector	1.000
ν_μ (7)	0.071	$\bar{\nu}_\mu$ (2)	0.028	Fermi momentum for ^{16}O	0.978
ν_μ (8)	0.055	$\bar{\nu}_\mu$ (3)	0.004	CC-other shape	0.550
ν_μ (9)	0.011	$\bar{\nu}_\mu$ (4)	0.022	CC-coherent for ^{16}O normalisation	0.148
ν_μ (10)	0.001	$\bar{\nu}_\mu$ (5)	0.029	NC-coherent normalisation	0.235
$\bar{\nu}_\mu$ (0)	0.045	$\bar{\nu}_\mu$ (6)	0.068	NC-other normalisation	0.300
$\bar{\nu}_\mu$ (1)	0.011	$\bar{\nu}_\mu$ (7)	0.104	CC- ν_e normalisation	0.028
$\bar{\nu}_\mu$ (2)	0.035	$\bar{\nu}_\mu$ (8)	0.122	NC-1 γ normalisation	1.000
$\bar{\nu}_\mu$ (3)	0.097	$\bar{\nu}_\mu$ (9)	0.089	CC- ν_e normalisation	0.028
$\bar{\nu}_\mu$ (4)	0.165	$\bar{\nu}_\mu$ (10)	0.079	$\bar{\nu}$ 2p2h for ^{16}O	0.096
ν_e (0)	0.051	ν_e (0)	0.086	BeRPA coefficient A	0.741
ν_e (1)	0.048	ν_e (1)	0.100	BeRPA coefficient B	0.717
ν_e (2)	0.045	$\bar{\nu}_e$ (0)	0.045	BeRPA coefficient D	0.096
ν_e (3)	0.035	$\bar{\nu}_e$ (1)	0.036	BeRPA coefficient E	0.228
ν_e (4)	0.053	$\bar{\nu}_e$ (2)	0.041	BeRPA coefficient U	0.300
ν_e (5)	0.054	$\bar{\nu}_e$ (3)	0.037	2p-2h shape for ^{16}O	0.487
ν_e (6)	0.084	$\bar{\nu}_e$ (4)	0.080	2p-2h ^{12}C to ^{16}O normalisation	0.130
$\bar{\nu}_e$ (0)	0.093	$\bar{\nu}_e$ (5)	0.097	Binding energy on Oxygen	1.000
$\bar{\nu}_e$ (1)	0.204	$\bar{\nu}_e$ (6)	0.215		

A.2 SK & FSI systematics

One ring ν -mode		One ring $\bar{\nu}$ -mode		Multiring	
Systematic	σ (%)	Systematic	σ (%)	Systematic	σ (%)
μ -like (0)	0.008	μ -like (0)	0.008	e -like + one decay e (0)	0.197
μ -like (1)	0.013	μ -like (1)	0.009	e -like + one decay e (1)	0.165
μ -like (2)	0.015	μ -like (2)	0.010	e -like + one decay e (2)	0.502
μ -like (3)	0.176	μ -like (3)	0.140	e -like + one decay e (3)	0.236
μ -like (4)	1.006	μ -like (4)	1.005	e -like + one decay e (4)	0.192
μ -like (5)	0.660	μ -like (5)	0.659	e -like + one decay e (5)	0.189
e -like (0)	0.124	e -like (0)	0.076	e -like + one decay e (6)	0.983
e -like (1)	0.032	e -like (1)	0.033	e -like + one decay e (7)	0.523
e -like (2)	0.041	e -like (2)	0.055	SK energy scale	0.024
e -like (3)	0.271	e -like (3)	0.317		
e -like (4)	0.320	e -like (4)	0.337		
e -like (5)	0.393	e -like (5)	0.417		
e -like (6)	0.089	e -like (6)	0.060		
e -like (7)	0.050	e -like (7)	0.043		
e -like (8)	0.063	e -like (8)	0.065		
e -like (9)	0.307	e -like (9)	0.329		
e -like (10)	0.195	e -like (10)	0.198		
e -like (11)	0.473	e -like (11)	0.465		

A.3 Atmospheric systematics

Flux		Cross-section		Event separation	
Parameter	σ (%)	Parameter	σ (%)	Parameter	σ (%)
Flux norm. ($E < 1$ GeV)	0.250	Axial mass in NC	0.100	FC reduction	0.003
Flux norm. ($E > 1$ GeV)	0.150	CCQE cross-section ratio	0.100	PC reduction	0.010
$\nu/\bar{\nu}$ ($E < 1$ GeV)	0.020	CCQE $\bar{\nu}/\nu$ ratio	0.100	FC / PC sep.	0.0002
$\nu/\bar{\nu}$ ($1 < E < 10$ GeV)	0.030	CCQE μ/e ratio	0.100	PC stop/through sep. (0)	0.068
$\nu/\bar{\nu}$ ($E > 10$ GeV)	0.050	Single meson cross-section	0.200	PC stop/through sep. (1)	0.085
$\bar{\nu}_e/\nu_e$ ($E < 1$ GeV)	0.050	DIS cross-section	0.050	PC stop/through sep. (2)	0.403
$\bar{\nu}_e/\nu_e$ ($1 < E < 10$ GeV)	0.050	DIS model comparisons	0.100	Non- ν background e -like	0.010
$\bar{\nu}_e/\nu_e$ ($E > 10$ GeV)	0.080	DIS Q^2 distribution (0)	0.100	Non- ν background μ -like	0.010
$\bar{\nu}_\mu/\nu_\mu$ ($E < 1$ GeV)	0.020	DIS Q^2 distribution (1)	0.100	Non- ν background one ring	0.176
$\bar{\nu}_\mu/\nu_\mu$ ($1 < E < 10$ GeV)	0.060	Coherent π production	1.000	Non- ν background multiring	0.116
$\bar{\nu}_\mu/\nu_\mu$ ($E > 10$ GeV)	0.150	NC / CC	0.200	Fiducial volume	0.020
Up/down	0.010	ν_τ cross-section	0.250	Ring sep.	0.10
Horizontal/vertical	0.010	Pion production, π^0/π	0.400	Particle-ID one ring	0.01
K/π	0.100	Pion production, $\bar{\nu}/\nu$	0.100	Particle-ID multiring	0.10
ν path length	0.100	Hadron simulation	0.100	Energy calibration	0.023
Relative norm. FC	0.050			Up/down energy calibration	0.003
Relative norm. PC+UP- μ	0.050			UP- μ stop/through sep.	0.006
Solar activity	0.100			UP- μ reduction	0.010
Matter effects	0.068			Path cut for UP- μ through	0.015
Δm_{21}^2 error	0.000			Energy cut for stop UP- μ	0.017
$\sin^2 \theta_{12}$ error	0.021			UP- μ shower/nonshower sep.	0.030
$\sin^2 \theta_{13}$ error	0.008			Background UP- μ nonshower	0.170
				Background UP- μ stop	0.170
				Background UP- μ shower	0.240
				$\nu_e/\bar{\nu}_e$ sep.	0.068
				Sub-GeV two ring π^0	0.056
				Decay- e tagging	0.100
				π decay tagging error	0.100
				One ring π^0 fit	0.100
				Multiring electron/other sep.	0.100

Appendix B

Open charm production

Following the same procedure as the one described in Ref. [237], the number of strange D mesons can be estimated as

$$\mathcal{N}_{D_s} = \frac{\sigma_{c\bar{c}}}{\sigma_{pA}} f_{D_s} = (2.8 \pm 0.2) \times 10^{-6} , \quad (\text{B.1})$$

where $\sigma_{c\bar{c}} = 12 \pm 1 \mu\text{b}$ is the proton–target open charm cross section, $\sigma_{pA} = 331.4 \pm 3.4 \text{ mb}$ is the total inelastic proton–target on carbon ($A = {}^{12}\text{C}$) [259] cross section, and $f_{D_s} = 7.7\%$ is the D_s fragmentation fraction [260]. The open charm production cross section is computed at the leading order in perturbation theory, with a graphite fixed target and a 80 GeV proton p . The correct process to consider is the proton–nucleon interaction, therefore

$$\sigma_{c\bar{c}} \equiv \sigma(pA \rightarrow c\bar{c} + X) \approx A \sigma(pN \rightarrow c\bar{c} + X) , \quad (\text{B.2})$$

using the correct Parton Distribution Function (PDF) for a bound nucleon N in the nucleus A . There are four diagrams, shown in figure Fig. B.1, that contributes to the cross section, but three of them interfere with each other. These cross sections are well-known SM calculations and can be found in Ref. [15]. The integrated cross section is:

$$\begin{aligned} \sigma(pN \rightarrow c\bar{c} + X) = & \int_{\tau_0}^1 dx_1 \int_{\frac{\tau_0}{x_1}}^1 dx_2 \int d\Omega \left[\left(f_{g/p}^1 f_{g/A}^2 + f_{g/p}^2 f_{g/A}^1 \right) \frac{d\sigma_{gg \rightarrow c\bar{c}}}{d\Omega} \right. \\ & \left. + \sum_{q=u,d,s} \left(f_{q/p}^1 f_{\bar{q}/A}^2 + f_{q/p}^2 f_{\bar{q}/A}^1 + f_{\bar{q}/p}^1 f_{q/A}^2 + f_{\bar{q}/p}^2 f_{q/A}^1 \right) \frac{d\sigma_{q\bar{q} \rightarrow c\bar{c}}}{d\Omega} \right] , \quad (\text{B.3}) \end{aligned}$$

with $\tau_0 = \hat{s}_0/s$ and \hat{s}_0 being the threshold energy at the partonic level and $s = 2m_p(m_p + E_p)$ is the centre of mass energy, given that $m_p \simeq m_n$. The partonic structure of the nucleus is described by the functions $f_{\rho/\eta}^i = f_{\rho/\eta}(x_i, M_F)$, which are interpreted as the probability of finding a parton ρ in the particle η carrying a x_i fraction of the momentum of η , at the energy scale M_F . The two momentum fractions are related by $x_1 x_2 s = \hat{s}$, where the hat symbol denotes the energy of the parton-level process.

A factorisation scale of $M_F = 2.1 m_c$ for the computation of $\sigma_{c\bar{c}}$ is adopted, while the renormalisation scale of α_s is set to $\mu_R = 1.6 m_c$, and the charm mass has the value

$$m_c = (1.28 \pm 0.03) \text{ GeV} . \quad (\text{B.4})$$

The integration is regulated for $|\cos \theta| < 0.8$, with θ the angle in the centre of mass frame. The theoretical curve in Fig. 7.4(a) of Ref. [237] was used to check this calculation, and it was successfully reproduced up to NLO corrections. For the generation of PDF the LHAPDF libraries [261] and the nCTEQ15 PDF set [262] are used, resulting in $\sigma_{pA \rightarrow c\bar{c}} = (12 \pm 1) \mu\text{b}$, for an 80 GeV protons on a graphite target.

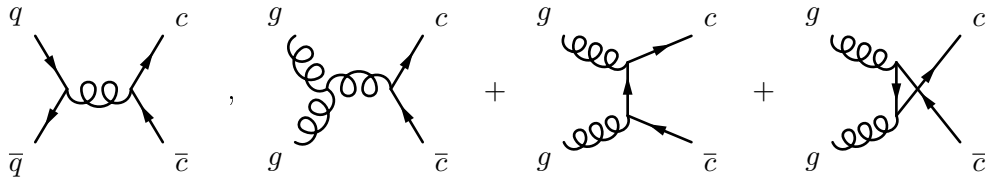


Figure B.1: These are the four diagrams contributing to the hard process in open charm production. The diagrams with gluons in the initial state interfere with each other giving rise to cross terms in the colour structure.

Bibliography

- [1] P. Ballett, T. Boschi, and S. Pascoli, [JHEP **2003** \(2020\) 111](#), [arXiv:1905.00284 \[hep-ph\]](#).
- [2] C.-N. Yang and R. L. Mills, [Phys. Rev. **96** \(1954\) 191](#).
- [3] S. L. Glashow, [Nucl. Phys. **22** \(1961\) 579](#).
- [4] S. Weinberg, [Phys. Rev. Lett. **19** \(1967\) 1264](#).
- [5] A. Salam, [Conf. Proc. C **680519** \(1968\) 367](#).
- [6] P. W. Higgs, [Phys. Rev. Lett. **13** \(1964\) 508](#).
- [7] P. W. Higgs, [Phys. Lett. **12** \(1964\) 132](#).
- [8] A. D. Sakharov, [Pisma Zh. Eksp. Teor. Fiz. **5** \(1967\) 32](#).
- [9] F. Zwicky, [Helv. Phys. Acta **6** \(1933\) 110](#).
- [10] V. C. Rubin and W. K. Ford, Jr., [Astrophys. J. **159** \(1970\) 379](#).
- [11] N. Aghanim *et al.* [Planck Collaboration], [arXiv:1807.06209 \[astro-ph.CO\]](#).
- [12] T. Nakano and K. Nishijima, [Prog. Theor. Phys. **10** \(1953\) 581](#).
- [13] M. Gell-Mann, [Nuovo Cim. **4** \(1956\) no.S2, 848](#).
- [14] M. Goldhaber, L. Grodzins, and A. W. Sunyar, [Phys. Rev. **109** \(1958\) 1015](#).
- [15] M. Tanabashi *et al.* [Particle Data Group Collaboration], [Phys. Rev. D **98** \(2018\) no.3, 030001](#).
- [16] S. L. Glashow, J. Iliopoulos, and L. Maiani, [Phys. Rev. D **2** \(1970\) 1285](#).
- [17] I. Esteban *et al.*, [JHEP **1901** \(2019\) 106](#), [arXiv:1811.05487 \[hep-ph\]](#).
- [18] L. Wolfenstein, [Phys. Rev. D **17** \(1978\) 2369](#).
- [19] S. P. Mikheyev and A. Yu. Smirnov, [Sov. J. Nucl. Phys. **42** \(1985\) 913](#).
- [20] S. P. Mikheev and A. Yu. Smirnov, [Nuovo Cim. C **9** \(1986\) 17](#).
- [21] S. J. Parke, [Phys. Rev. Lett. **57** \(1986\) 1275](#).
- [22] E. Giusarma *et al.*, [Phys. Rev. D **88** \(2013\) no.6, 063515](#), [arXiv:1306.5544 \[astro-ph.CO\]](#).
- [23] E. Majorana, [Nuovo Cim. **14** \(1937\) 171](#).

- [24] J. N. Bahcall *et al.*, [Astrophys. J. **137** \(1963\) 344](#).
- [25] J. N. Bahcall and R. K. Ulrich, [Rev. Mod. Phys. **60** \(1988\) 297](#).
- [26] K. Lande *et al.*, [AIP Conf. Proc. **243** \(1992\) 1122](#).
- [27] M. Altmann *et al.* [GNO Collaboration], [Phys. Lett. B **616** \(2005\) 174](#), [[hep-ex/0504037](#)].
- [28] J. N. Abdurashitov *et al.* [SAGE Collaboration], [J. Exp. Theor. Phys. **95** \(2002\) 181](#), [[astro-ph/0204245](#)].
- [29] J. N. Abdurashitov *et al.*, [Phys. Rev. C **73** \(2006\) 045805](#), [[nucl-ex/0512041](#)].
- [30] B. Aharmim *et al.* [SNO Collaboration], [Phys. Rev. C **72** \(2005\) 055502](#), [[nucl-ex/0502021](#)].
- [31] R. Tartaglia [BOREXINO Collaboration], [Nucl. Instrum. Meth. A **461** \(2001\) 327](#).
- [32] G. Bellini *et al.* [BOREXINO Collaboration], [Nature **512** \(2014\) no.7515, 383](#).
- [33] J. N. Bahcall and C. Pena-Garay, [New J. Phys. **6** \(2004\) 63](#), [[hep-ph/0404061](#)].
- [34] S. Chandrasekhar, [Astrophys. J. **74** \(1931\) 81](#).
- [35] T. Totani *et al.*, [Astrophys. J. **496** \(1998\) 216](#), [[astro-ph/9710203](#)].
- [36] K. Nakazato *et al.*, [Astrophys. J. Suppl. **205** \(2013\) 2](#), [arXiv:1210.6841 \[astro-ph.HE\]](#).
- [37] I. Tamborra *et al.*, [Phys. Rev. D **90** \(2014\) no.4, 045032](#), [arXiv:1406.0006 \[astro-ph.SR\]](#).
- [38] G. A. Tammann, W. Loeffler, and A. Schroder, [Astrophys. J. Suppl. **92** \(1994\) 487](#).
- [39] J. F. Beacom, [Ann. Rev. Nucl. Part. Sci. **60** \(2010\) 439](#), [arXiv:1004.3311 \[astro-ph.HE\]](#).
- [40] J. Blumer, R. Engel, and J. R. Horandel, [Prog. Part. Nucl. Phys. **63** \(2009\) 293](#), [[arXiv:0904.0725 \[astro-ph.HE\]](#)].
- [41] J. Abraham *et al.* [Pierre Auger Collaboration], [Phys. Rev. Lett. **101** \(2008\) 061101](#), [[arXiv:0806.4302 \[astro-ph\]](#)].
- [42] K. Greisen, [Phys. Rev. Lett. **16** \(1966\) 748](#).
- [43] G. T. Zatsepin and V. A. Kuzmin, [JETP Lett. **4** \(1966\) 78](#).
- [44] M. Honda *et al.*, [Phys. Rev. D **70** \(2004\) 043008](#), [[astro-ph/0404457](#)].
- [45] Y. Fukuda *et al.* [Super-Kamiokande Collaboration], [Phys. Rev. Lett. **81** \(1998\) 1562](#), [[hep-ex/9807003](#)].
- [46] M. Honda *et al.*, [Phys. Rev. D **75** \(2007\) 043006](#), [[astro-ph/0611418](#)].
- [47] A. A. Aguilar-Arevalo *et al.* [MiniBooNE Collaboration], [Phys. Rev. D **79** \(2009\) 072002](#), [[arXiv:0806.1449 \[hep-ex\]](#)].
- [48] K. Abe *et al.* [T2K Collaboration], [Phys. Rev. D **87** \(2013\) no.1, 012001](#), [[arXiv:1211.0469 \[hep-ex\]](#)].
- [49] D. S. Ayres *et al.* [NOvA Collaboration], [[hep-ex/0503053](#)].

- [50] D. Beavis *et al.* [E899 Collaboration], [BNL-52459\(1995\)](#).
- [51] D. Akimov *et al.* [COHERENT Collaboration], [Science](#) **357** (2017) no.6356, 1123, [arXiv:1708.01294 \[nucl-ex\]](#).
- [52] D. Z. Freedman, [Phys. Rev. D](#) **9** (1974) 1389.
- [53] A. Drukier and L. Stodolsky, [Phys. Rev. D](#) **30** (1984) 2295.
- [54] D. Akimov *et al.* [COHERENT Collaboration], [arXiv:1509.08702 \[physics.ins-det\]](#).
- [55] P. Coloma *et al.*, [Phys. Rev. D](#) **96** (2017) no.11, 115007, [arXiv:1708.02899 \[hep-ph\]](#).
- [56] C. Giunti, [Phys. Rev. D](#) **101** (2020) no.3, 035039, [arXiv:1909.00466 \[hep-ph\]](#).
- [57] S. Fukuda *et al.* [Super-Kamiokande Collaboration], [Phys. Lett. B](#) **539** (2002) 179, [\[hep-ex/0205075\]](#).
- [58] P. Vogel and J. F. Beacom, [Phys. Rev. D](#) **60** (1999) 053003, [\[hep-ph/9903554\]](#).
- [59] F. J. Ernst, R. G. Sachs, and K. C. Wali, [Phys. Rev.](#) **119** (1960) 1105.
- [60] J. A. Formaggio and G. P. Zeller, [Rev. Mod. Phys.](#) **84** (2012) 1307, [arXiv:1305.7513 \[hep-ex\]](#).
- [61] D. Rein and L. M. Sehgal, [Annals Phys.](#) **133** (1981) 79.
- [62] M. Martini *et al.*, [Phys. Rev. C](#) **80** (2009) 065501, [arXiv:0910.2622 \[nucl-th\]](#).
- [63] J. Nieves, I. Ruiz Simo, and M. J. Vicente Vacas, [Phys. Rev. C](#) **83** (2011) 045501, [arXiv:1102.2777 \[hep-ph\]](#).
- [64] C. Andreopoulos *et al.*, [Nucl. Instrum. Meth. A](#) **614** (2010) 87, [arXiv:0905.2517 \[hep-ph\]](#).
- [65] Y. Hayato, [Nucl. Phys. Proc. Suppl.](#) **112** (2002) 171.
- [66] H. Zhang *et al.* [Super-Kamiokande Collaboration], [Astropart. Phys.](#) **60** (2015) 41, [arXiv:1311.3738 \[hep-ex\]](#).
- [67] Y. Zhang *et al.* [Super-Kamiokande Collaboration], [Phys. Rev. D](#) **93** (2016) no.1, 012004, [arXiv:1509.08168 \[hep-ex\]](#).
- [68] L. Marti *et al.*, [Nucl. Instrum. Meth. A](#) **959** (2020) 163549, [arXiv:1908.11532 \[physics.ins-det\]](#).
- [69] A. R. Back *et al.* [ANNIE Collaboration], [arXiv:1912.03186 \[physics.ins-det\]](#).
- [70] J. K. Ahn *et al.* [RENO Collaboration], [arXiv:1003.1391 \[hep-ex\]](#).
- [71] P. A. Cerenkov, [Phys. Rev.](#) **52** (1937) 378.
- [72] I. M. Frank and I. E. Tamm, [Compt. Rend. Acad. Sci. URSS](#) **14** (1937) no.3, 109.
- [73] G. Ambrosi *et al.*, [Nuovo Cim. C](#) **40** (2017) no.1, 78, [arXiv:1612.08605 \[astro-ph.IM\]](#).
- [74] R. Abbasi *et al.* [IceCube Collaboration], [Nucl. Instrum. Meth. A](#) **601** (2009) 294, [arXiv:0810.4930 \[physics.ins-det\]](#).

- [75] J. H. Bickel (2013). *Fundamentals of Nuclear Engineering*, [Lecture series](#).
- [76] Y. Fukuda *et al.* [Super-Kamiokande Collaboration], *Nucl. Instrum. Meth. A* **501** (2003) 418.
- [77] H. Nishino *et al.*, *Nucl. Instrum. Meth. A* **610** (2009) 710, [arXiv:0911.0986 \[physics.ins-det\]](#).
- [78] M. Kaplinghat, G. Steigman, and T. Walker, *Phys. Rev. D* **62** (2000) 043001, [\[astro-ph/9912391\]](#).
- [79] S. W. Li and J. F. Beacom, *Phys. Rev. D* **91** (2015) no.10, 105005, [arXiv:1503.04823 \[hep-ph\]](#).
- [80] K. Bays *et al.* [Super-Kamiokande Collaboration], *Phys. Rev. D* **85** (2012) 052007, [arXiv:1111.5031 \[hep-ex\]](#).
- [81] M. Malek *et al.* [Super-Kamiokande Collaboration], *Phys. Rev. Lett.* **90** (2003) 061101, [\[hep-ex/0209028\]](#).
- [82] S. Horiuchi, J. F. Beacom, and E. Dwek, *Phys. Rev. D* **79** (2009) 083013, [arXiv:0812.3157 \[astro-ph\]](#).
- [83] R. Laha and J. F. Beacom, *Phys. Rev. D* **89** (2014) 063007, [arXiv:1311.6407 \[astro-ph.HE\]](#).
- [84] C. Simpson *et al.* [Super-Kamiokande Collaboration], *Astrophys. J.* **885** (2019) 133, [arXiv:1908.07551 \[astro-ph.HE\]](#).
- [85] J. F. Beacom and M. R. Vagins, *Phys. Rev. Lett.* **93** (2004) 171101, [\[hep-ph/0309300\]](#).
- [86] D. A. Brown *et al.*, *Nucl. Data Sheets* **148** (2018) 1.
- [87] V. Zerkov and B. Pritychenko, *Nuclear Instruments and Methods in Physics Research Section A: Accelerators, Spectrometers, Detectors and Associated Equipment* **888** (2018) 31 .
- [88] D. Cokinos and E. Melkonian, *Phys. Rev. C* **15** (1977) 1636.
- [89] T. J. Irvine (2014). *Development of Neutron-Tagging Techniques and Application to Atmospheric Neutrino Oscillation Analysis in Super-Kamiokande*, [Doctoral dissertation](#).
- [90] H. Watanabe *et al.* [Super-Kamiokande Collaboration], *Astropart. Phys.* **31** (2009) 320, [arXiv:0811.0735 \[hep-ex\]](#).
- [91] E. Lorch, *The International journal of applied radiation and isotopes* **24** (1973) no.10, 585—591.
- [92] A. B. Smith, P. R. Fields, and A. M. Friedman, *Phys. Rev.* **104** (1956) 699.
- [93] A. B. Smith, P. R. Fields, and J. H. Roberts, *Phys. Rev.* **108** (1957) 411.
- [94] H. Labranche (2004). *Time Series Analysis For The Californium Source In Sudbury Neutrino Observatory*, [Doctoral dissertation](#).
- [95] S. Agostinelli *et al.* [GEANT4 Collaboration], *Nucl. Instrum. Meth. A* **506** (2003) 250.

- [96] D. C. Morton, *The Astrophysical Journal Supplement Series* **130** (2000) no.2, 403.
- [97] Beer, *Annalen der Physik und Chemie* **162** (1852) no.5, 78–88.
- [98] G. R. Farrar and M. Shaposhnikov, *Phys. Rev. D* **50** (1994) 774, [[hep-ph/9305275](#)].
- [99] M. Fukugita and T. Yanagida, *Phys. Lett. B* **174** (1986) 45.
- [100] J. H. Christenson *et al.*, *Phys. Rev. Lett.* **13** (1964) 138.
- [101] B. Aubert *et al.* [BaBar Collaboration], *Phys. Rev. Lett.* **86** (2001) 2515, [[hep-ex/0102030](#)].
- [102] K. Abe *et al.* [Belle Collaboration], *Phys. Rev. Lett.* **87** (2001) 091802, [[hep-ex/0107061](#)].
- [103] R. Aaij *et al.* [LHCb Collaboration], *Phys. Rev. Lett.* **110** (2013) no.22, 221601, [[arXiv:1304.6173](#)] [[hep-ex](#)].
- [104] R. Aaij *et al.* [LHCb Collaboration], *Phys. Rev. Lett.* **122** (2019) no.21, 211803, [[arXiv:1903.08726](#)] [[hep-ex](#)].
- [105] C. Jarlskog, *Phys. Rev. Lett.* **55** (1985) 1039.
- [106] K. Abe *et al.* [T2K Collaboration], *Nature* **580** (2020) no.7803, 339, [[arXiv:1910.03887](#)] [[hep-ex](#)].
- [107] S. Pascoli, S. T. Petcov, and A. Riotto, *Nucl. Phys. B* **774** (2007) 1, [[hep-ph/0611338](#)].
- [108] K. Abe *et al.* [T2K Collaboration], *Phys. Rev. Lett.* **107** (2011) 041801, [[arXiv:1106.2822](#)] [[hep-ex](#)].
- [109] Y. Abe *et al.* [Double Chooz Collaboration], *Phys. Rev. Lett.* **108** (2012) 131801, [[arXiv:1112.6353](#)] [[hep-ex](#)].
- [110] F. P. An *et al.* [Daya Bay Collaboration], *Phys. Rev. Lett.* **108** (2012) 171803, [[arXiv:1203.1669](#)] [[hep-ex](#)].
- [111] J. K. Ahn *et al.* [RENO Collaboration], *Phys. Rev. Lett.* **108** (2012) 191802, [[arXiv:1204.0626](#)] [[hep-ex](#)].
- [112] K. Abe *et al.* [Hyper-Kamiokande Collaboration], [[arXiv:1805.04163](#)] [[physics.ins-det](#)].
- [113] K. Abe *et al.* [T2K Collaboration], *Nucl. Instrum. Meth. A* **659** (2011) 106, [[arXiv:1106.1238](#)] [[physics.ins-det](#)].
- [114] M. Jiang *et al.* [Super-Kamiokande Collaboration], *PTEP* **2019** (2019) no.5, 053F01, [[arXiv:1901.03230](#)] [[hep-ex](#)].
- [115] C. Andreopoulos *et al.* (2020) , *The VALOR neutrino fit group*.
- [116] K. Abe *et al.* [T2K Collaboration], *Phys. Rev. Lett.* **121** (2018) no.17, 171802, [[arXiv:1807.07891](#)] [[hep-ex](#)].
- [117] G. L. Fogli *et al.*, *Phys. Rev. D* **66** (2002) 053010, [[hep-ph/0206162](#)].
- [118] K. Levenberg, *Quarterly of Applied Mathematics* **2** (1944) no.2, 164–168.

- [119] D. W. Marquardt, [Journal of the Society for Industrial and Applied Mathematics](#) **11** (1963) no.2, 431.
- [120] M. Transtrum and J. Sethna, [arXiv:1201.5885 \[physics.data-an\]](#).
- [121] R. Brun *et al.*, [CERN-W5013\(1994\)](#).
- [122] K. Abe *et al.* [Super-Kamiokande Collaboration], [Phys. Rev. D](#) **97** (2018) no.7, 072001, [arXiv:1710.09126 \[hep-ex\]](#).
- [123] J. Nieves, J. E. Amaro, and M. Valverde, [Phys. Rev. C](#) **70** (2004) 055503 (Erratum: [Phys.Rev.C](#) **72**, 019902 (2005)), [\[nucl-th/0408005\]](#).
- [124] R. Gran *et al.*, [Phys. Rev. D](#) **88** (2013) no.11, 113007, [arXiv:1307.8105 \[hep-ph\]](#).
- [125] M. Day and K. S. McFarland, [Phys. Rev. D](#) **86** (2012) 053003, [arXiv:1206.6745 \[hep-ph\]](#).
- [126] M. Kabirnezhad, [Phys. Rev. D](#) **97** (2018) no.1, 013002, [arXiv:1711.02403 \[hep-ph\]](#).
- [127] K. N. Abazajian *et al.*, [arXiv:1204.5379 \[hep-ph\]](#).
- [128] T. Asaka, S. Blanchet, and M. Shaposhnikov, [Phys. Lett. B](#) **631** (2005) 151, [\[hep-ph/0503065\]](#).
- [129] L. Covi, E. Roulet, and F. Vissani, [Phys. Lett. B](#) **384** (1996) 169, [\[hep-ph/9605319\]](#).
- [130] A. Pilaftsis, [Phys. Rev. D](#) **56** (1997) 5431, [\[hep-ph/9707235\]](#).
- [131] A. Aguilar-Arevalo *et al.* [LSND Collaboration], [Phys. Rev. D](#) **64** (2001) 112007, [\[hep-ex/0104049\]](#).
- [132] A. A. Aguilar-Arevalo *et al.* [MiniBooNE Collaboration], [arXiv:1207.4809 \[hep-ex\]](#).
- [133] A. A. Aguilar-Arevalo *et al.* [MiniBooNE Collaboration], [Phys. Rev. Lett.](#) **110** (2013) 161801, [arXiv:1303.2588 \[hep-ex\]](#).
- [134] A. A. Aguilar-Arevalo *et al.* [MiniBooNE Collaboration], [Phys. Rev. Lett.](#) **121** (2018) no.22, 221801, [arXiv:1805.12028 \[hep-ex\]](#).
- [135] M. G. Aartsen *et al.* [IceCube Collaboration], [Phys. Rev. Lett.](#) **117** (2016) no.7, 071801, [arXiv:1605.01990 \[hep-ex\]](#).
- [136] P. Adamson *et al.* [MINOS+ Collaboration], [Phys. Rev. Lett.](#) **122** (2019) no.9, 091803, [arXiv:1710.06488 \[hep-ex\]](#).
- [137] M. G. Aartsen *et al.* [IceCube Collaboration], [Phys. Rev. D](#) **95** (2017) no.11, 112002, [arXiv:1702.05160 \[hep-ex\]](#).
- [138] J. Liao and D. Marfatia, [Phys. Rev. Lett.](#) **117** (2016) no.7, 071802, [arXiv:1602.08766 \[hep-ph\]](#).
- [139] J. Liao, D. Marfatia, and K. Whisnant, [Phys. Rev. D](#) **99** (2019) no.1, 015016, [arXiv:1810.01000 \[hep-ph\]](#).
- [140] A. Esmaili and H. Nunokawa, [Eur. Phys. J. C](#) **79** (2019) no.1, 70, [arXiv:1810.11940 \[hep-ph\]](#).

- [141] P. B. Denton, Y. Farzan, and I. M. Shoemaker, *Phys. Rev. D* **99** (2019) no.3, 035003, [arXiv:1811.01310 \[hep-ph\]](#).
- [142] T. A. Mueller *et al.*, *Phys. Rev. C* **83** (2011) 054615, [arXiv:1101.2663 \[hep-ex\]](#).
- [143] G. Mention *et al.*, *Phys. Rev. D* **83** (2011) 073006, [arXiv:1101.2755 \[hep-ex\]](#).
- [144] P. Huber, *Phys. Rev. C* **84** (2011) 024617 (Erratum: *Phys. Rev. C* **85**, 029901(2012)), [arXiv:1106.0687 \[hep-ph\]](#).
- [145] Y. Ko *et al.* [NEOS Collaboration], *Phys. Rev. Lett.* **118** (2017) no.12, 121802, [arXiv:1610.05134 \[hep-ex\]](#).
- [146] I. Alekseev *et al.* [DANSS Collaboration], *Phys. Lett. B* **787** (2018) 56, [arXiv:1804.04046 \[hep-ex\]](#).
- [147] M. Laveder, *Nucl. Phys. Proc. Suppl.* **168** (2007) 344.
- [148] C. Giunti and M. Laveder, *Mod. Phys. Lett. A* **22** (2007) 2499, [\[hep-ph/0610352\]](#).
- [149] S. N. Gninenko, *Phys. Rev. Lett.* **103** (2009) 241802, [arXiv:0902.3802 \[hep-ph\]](#).
- [150] S. N. Gninenko, *Phys. Rev. D* **83** (2011) 015015, [arXiv:1009.5536 \[hep-ph\]](#).
- [151] M. Masip, P. Masjuan, and D. Meloni, *JHEP* **1301** (2013) 106, [arXiv:1210.1519 \[hep-ph\]](#).
- [152] E. Bertuzzo *et al.*, *Phys. Rev. Lett.* **121** (2018) no.24, 241801, [arXiv:1807.09877 \[hep-ph\]](#).
- [153] P. Ballett, S. Pascoli, and M. Ross-Lonergan, *Phys. Rev. D* **99** (2019) 071701, [arXiv:1808.02915 \[hep-ph\]](#).
- [154] M. Antonello *et al.* [MicroBooNE, LAr1-ND, ICARUS-WA104 Collaboration], [arXiv:1503.01520 \[physics.ins-det\]](#).
- [155] J. Ashenfelter *et al.* [PROSPECT Collaboration], *Phys. Rev. Lett.* **121** (2018) no.25, 251802, [arXiv:1806.02784 \[hep-ex\]](#).
- [156] H. Almazán *et al.* [STEREO Collaboration], *Phys. Rev. Lett.* **121** (2018) no.16, 161801, [arXiv:1806.02096 \[hep-ex\]](#).
- [157] A. P. Serebrov *et al.* [NEUTRINO-4 Collaboration], *Pisma Zh. Eksp. Teor. Fiz.* **109** (2019) no.4, 209, [arXiv:1809.10561 \[hep-ex\]](#).
- [158] S. Mertens *et al.* [KATRIN Collaboration], *J. Phys. G* **46** (2019) no.6, 065203, [arXiv:1810.06711 \[physics.ins-det\]](#).
- [159] M. Galeazzi *et al.*, *Phys. Rev. Lett.* **86** (2001) 1978.
- [160] K. H. Hiddemann, H. Daniel, and O. Schwentker, *J. Phys. G* **21** (1995) 639.
- [161] E. Holzschuh *et al.*, *Phys. Lett. B* **451** (1999) 247.
- [162] E. Holzschuh *et al.*, *Phys. Lett. B* **482** (2000) 1.
- [163] J. Deutsch, M. Lebrun, and R. Prieels, *Nucl. Phys. A* **518** (1990) 149.

- [164] A. V. Artamonov *et al.* [E949 Collaboration], *Phys. Rev. D* **91** (2015) no.5, 052001 (Erratum: *Phys. Rev. D* **91**, no.5, 059903(2015)), [arXiv:1411.3963 \[hep-ex\]](#).
- [165] D. I. Britton *et al.*, *Phys. Rev. Lett.* **68** (1992) 3000.
- [166] D. I. Britton *et al.*, *Phys. Rev. D* **46** (1992) R885.
- [167] A. Aguilar-Arevalo *et al.* [PIENU Collaboration], *Phys. Rev. D* **97** (2018) no.7, 072012, [arXiv:1712.03275 \[hep-ex\]](#).
- [168] A. Aguilar-Arevalo *et al.* [PIENU Collaboration], *Phys. Lett. B* **798** (2019) 134980, [arXiv:1904.03269 \[hep-ex\]](#).
- [169] A. Atre *et al.*, *JHEP* **0905** (2009) 030, [arXiv:0901.3589 \[hep-ph\]](#).
- [170] G. Bernardi *et al.*, *Phys. Lett.* **166B** (1986) 479.
- [171] G. Bernardi *et al.*, *Phys. Lett. B* **203** (1988) 332.
- [172] K. Abe *et al.* [T2K Collaboration], *Phys. Rev. D* **100** (2019) no.5, 052006, [arXiv:1902.07598 \[hep-ex\]](#).
- [173] P. Abreu *et al.* [DELPHI Collaboration], *Z. Phys. C* **74** (1997) 57 (Erratum: *Z. Phys. C* **75**, 580(1997)).
- [174] O. Adriani *et al.* [L3 Collaboration], *Phys. Lett. B* **295** (1992) 371.
- [175] P. Vilain *et al.* [CHARM II Collaboration], *Phys. Lett. B* **343** (1995) 453.
- [176] A. Vaitaitis *et al.* [NuTeV, E815 Collaboration], *Phys. Rev. Lett.* **83** (1999) 4943, [\[hep-ex/9908011\]](#).
- [177] J. Badier *et al.* [NA3 Collaboration], *Z. Phys. C* **31** (1986) 341.
- [178] A. M. Cooper-Sarkar *et al.* [WA66 Collaboration], *Phys. Lett.* **160B** (1985) 207.
- [179] E. Gallas *et al.* [FMMF Collaboration], *Phys. Rev. D* **52** (1995) 6.
- [180] R. Aaij *et al.* [LHCb Collaboration], *Phys. Rev. Lett.* **112** (2014) no.13, 131802, [arXiv:1401.5361 \[hep-ex\]](#).
- [181] M. Aaboud *et al.* [ATLAS Collaboration], *JHEP* **1901** (2019) 016, [arXiv:1809.11105 \[hep-ex\]](#).
- [182] A. M. Sirunyan *et al.* [CMS Collaboration], *Phys. Rev. Lett.* **120** (2018) no.22, 221801, [arXiv:1802.02965 \[hep-ex\]](#).
- [183] A. M. Sirunyan *et al.* [CMS Collaboration], *JHEP* **1901** (2019) 122, [arXiv:1806.10905 \[hep-ex\]](#).
- [184] D. Liventsev *et al.* [Belle Collaboration], *Phys. Rev. D* **87** (2013) no.7, 071102 (Erratum: *Phys. Rev. D* **95**, no.9, 099903(2017)), [arXiv:1301.1105 \[hep-ex\]](#).
- [185] J. Harrison [LHCb, BaBar, Belle Collaboration], *Nucl. Part. Phys. Proc.* **260** (2015) 143.
- [186] M. Drewes and B. Garbrecht, *Nucl. Phys. B* **921** (2017) 250, [arXiv:1502.00477 \[hep-ph\]](#).

- [187] O. Ruchayskiy and A. Ivashko, *JHEP* **1206** (2012) 100, [arXiv:1112.3319 \[hep-ph\]](#).
- [188] P. Minkowski, *Phys. Lett.* **67B** (1977) 421.
- [189] R. N. Mohapatra and G. Senjanovic, *Phys. Rev. Lett.* **44** (1980) 912.
- [190] M. Gell-Mann, P. Ramond, and R. Slansky, *Conf. Proc. C* **790927** (1979) 315, [arXiv:1306.4669 \[hep-th\]](#).
- [191] T. Yanagida, *Conf. Proc. C* **7902131** (1979) 95.
- [192] W. Grimus and L. Lavoura, *JHEP* **0011** (2000) 042, [[hep-ph/0008179](#)].
- [193] D. Wyler and L. Wolfenstein, *Nucl. Phys. B* **218** (1983) 205.
- [194] G. 't Hooft *et al.*, *NATO Sci. Ser. B* **59** (1980) pp.1.
- [195] R. N. Mohapatra and J. W. F. Valle, *Phys. Rev. D* **34** (1986) 1642.
- [196] M. C. Gonzalez-Garcia and J. W. F. Valle, *Phys. Lett. B* **216** (1989) 360.
- [197] E. K. Akhmedov *et al.*, *Phys. Lett. B* **368** (1996) 270, [[hep-ph/9507275](#)].
- [198] E. K. Akhmedov *et al.*, *Phys. Rev. D* **53** (1996) 2752, [[hep-ph/9509255](#)].
- [199] S. M. Barr, *Phys. Rev. Lett.* **92** (2004) 101601, [[hep-ph/0309152](#)].
- [200] S. K. Kang and C. S. Kim, *Phys. Lett. B* **646** (2007) 248, [[hep-ph/0607072](#)].
- [201] A. Denner *et al.*, *Phys. Lett. B* **291** (1992) 278.
- [202] A. Abada *et al.*, *Phys. Rev. D* **95** (2017) no.7, 075023, [arXiv:1612.04737 \[hep-ph\]](#).
- [203] B. Kayser and R. E. Shrock, *Phys. Lett.* **112B** (1982) 137.
- [204] B. Kayser, *Phys. Rev. D* **26** (1982) 1662.
- [205] D. Gorbunov and M. Shaposhnikov, *JHEP* **0710** (2007) 015 (Erratum: *JHEP*11,101(2013)), [arXiv:0705.1729 \[hep-ph\]](#).
- [206] J. C. Helo, S. Kovalenko, and I. Schmidt, *Nucl. Phys. B* **853** (2011) 80, [arXiv:1005.1607 \[hep-ph\]](#).
- [207] K. Bondarenko *et al.*, *JHEP* **1811** (2018) 032, [arXiv:1805.08567 \[hep-ph\]](#).
- [208] S. Dittmaier, *Phys. Rev. D* **59** (1998) 016007, [[hep-ph/9805445](#)].
- [209] J. L. Diaz-Cruz, B. O. Larios, and O. Meza-Aldama, *J. Phys. Conf. Ser.* **761** (2016) no.1, 012012, [arXiv:1608.04129 \[hep-ph\]](#).
- [210] V. Shtabovenko, R. Mertig, and F. Orellana, *Comput. Phys. Commun.* **207** (2016) 432, [arXiv:1601.01167 \[hep-ph\]](#).
- [211] R. Mertig, M. Bohm, and A. Denner, *Comput. Phys. Commun.* **64** (1991) 345.
- [212] P. Ballett, S. Pascoli, and M. Ross-Lonergan, *JHEP* **1704** (2017) 102, [arXiv:1610.08512 \[hep-ph\]](#).

- [213] T. Asaka, S. Eijima, and A. Watanabe, *JHEP* **1303** (2013) 125, [arXiv:1212.1062 \[hep-ph\]](#).
- [214] A. B. Balantekin, A. de Gouvêa, and B. Kayser, *Phys. Lett. B* **789** (2019) 488, [arXiv:1808.10518 \[hep-ph\]](#).
- [215] G. Magill, R. Plestid, and Y.-D. Pospelov, Maxim and Tsai, *Phys. Rev. D* **98** (2018) no.11, 115015, [arXiv:1803.03262 \[hep-ph\]](#).
- [216] R. E. Shrock, *Phys. Rev. D* **24** (1981) 1275.
- [217] A. Abada *et al.*, *JHEP* **1402** (2014) 091, [arXiv:1311.2830 \[hep-ph\]](#).
- [218] A. Kusenko, S. Pascoli, and D. Semikoz, *JHEP* **0511** (2005) 028, [[hep-ph/0405198](#)].
- [219] B. Abi *et al.* [DUNE Collaboration], [arXiv:1807.10334 \[physics.ins-det\]](#).
- [220] C. Adams *et al.* [LBNE Collaboration], [arXiv:1307.7335 \[hep-ex\]](#).
- [221] I. Krasnov, *Phys. Rev. D* **100** (2019) no.7, 075023, [arXiv:1902.06099 \[hep-ph\]](#).
- [222] B. Abi *et al.* [DUNE Collaboration], [arXiv:2002.02967 \[physics.ins-det\]](#).
- [223] C. Rubbia, CERN-EP-INT-77-08(1977).
- [224] J. Asaadi *et al.*, *JINST* **13** (2018) no.02, C02008.
- [225] P. Glassel and P. Glaessel [ALICE TPC Collaboration], *J. Phys. G* **30** (2004) S1083.
- [226] E. Cortina Gil *et al.* [NA62 Collaboration], *JINST* **12** (2017) no.05, P05025, [arXiv:1703.08501 \[physics.ins-det\]](#).
- [227] M. Anelli *et al.* [SHiP Collaboration], [arXiv:1504.04956 \[physics.ins-det\]](#).
- [228] M. Drewes *et al.*, [arXiv:1806.00100 \[hep-ph\]](#).
- [229] C. Ahdida *et al.* [SHiP Collaboration], *JHEP* **1904** (2019) 077, [arXiv:1811.00930 \[hep-ph\]](#).
- [230] A. Caputo *et al.*, *Eur. Phys. J. C* **77** (2017) no.4, 258, [arXiv:1611.05000 \[hep-ph\]](#).
- [231] D. Curtin *et al.*, *Rept. Prog. Phys.* **82** (2019) no.11, 116201, [arXiv:1806.07396 \[hep-ph\]](#).
- [232] A. Ariga *et al.* [FASER Collaboration], *Phys. Rev. D* **99** (2019) no.9, 095011, [arXiv:1811.12522 \[hep-ph\]](#).
- [233] F. Kling and S. Trojanowski, *Phys. Rev. D* **97** (2018) no.9, 095016, [arXiv:1801.08947 \[hep-ph\]](#).
- [234] L. Fields *et al.* [DUNE Collaboration], Private communication (2017).
- [235] R. Ammar *et al.*, *Phys. Rev. Lett.* **61** (1988) 2185.
- [236] G. A. Alves *et al.* [E769 Collaboration], *Phys. Rev. Lett.* **77** (1996) 2392.
- [237] S. Alekhin *et al.*, *Rept. Prog. Phys.* **79** (2016) no.12, 124201, [arXiv:1504.04855 \[hep-ph\]](#).
- [238] T. Alion *et al.* [DUNE Collaboration], [arXiv:1606.09550 \[physics.ins-det\]](#).

- [239] C. Adams *et al.* [MicroBooNE Collaboration], *Eur. Phys. J. C* **79** (2019) no.8, 673, [arXiv:1812.05679 \[physics.ins-det\]](#).
- [240] A. Ankowski *et al.* [ICARUS Collaboration], *Acta Phys. Polon. B* **41** (2010) 103, [arXiv:0812.2373 \[hep-ex\]](#).
- [241] J. J. Back *et al.*, *Eur. Phys. J. C* **73** (2013) no.3, 2369, [arXiv:1210.2215 \[physics.ins-det\]](#).
- [242] G. J. Feldman and R. D. Cousins, *Phys. Rev. D* **57** (1998) 3873, [[physics/9711021](#)].
- [243] A. Ilakovac and A. Pilaftsis, *Nucl. Phys. B* **437** (1995) 491, [[hep-ph/9403398](#)].
- [244] A. M. Baldini *et al.* [MEG Collaboration], *Eur. Phys. J. C* **76** (2016) no.8, 434, [arXiv:1605.05081 \[hep-ex\]](#).
- [245] R. Alonso *et al.*, *JHEP* **1301** (2013) 118, [arXiv:1209.2679 \[hep-ph\]](#).
- [246] N. G. Deshpande *et al.*, *Phys. Lett. B* **703** (2011) 562, [arXiv:1106.5085 \[hep-ph\]](#).
- [247] A. J. Buras *et al.*, *JHEP* **1009** (2010) 104, [arXiv:1006.5356 \[hep-ph\]](#).
- [248] A. Abada *et al.*, *Eur. Phys. J. C* **77** (2017) no.5, 304, [arXiv:1612.05548 \[hep-ph\]](#).
- [249] A. Abada and M. Lucente, *Nucl. Phys. B* **885** (2014) 651, [arXiv:1401.1507 \[hep-ph\]](#).
- [250] G. Guennebaud, B. Jacob, *et al.* (2010). *Eigen v3*, C++ library.
- [251] S. Antusch, J. P. Baumann, and E. Fernandez-Martinez, *Nucl. Phys. B* **810** (2009) 369, [arXiv:0807.1003 \[hep-ph\]](#).
- [252] E. Fernandez-Martinez, J. Hernandez-Garcia, and J. Lopez-Pavon, *JHEP* **1608** (2016) 033, [arXiv:1605.08774 \[hep-ph\]](#).
- [253] M. Blennow *et al.*, *JHEP* **1704** (2017) 153, [arXiv:1609.08637 \[hep-ph\]](#).
- [254] M. Blennow *et al.*, *JHEP* **1007** (2010) 096, [arXiv:1005.3240 \[hep-ph\]](#).
- [255] A. Gando *et al.* [KamLAND-Zen Collaboration], *Phys. Rev. Lett.* **117** (2016) no.8, 082503, [arXiv:1605.02889 \[hep-ex\]](#).
- [256] H. Almazán Molina *et al.* [STEREO Collaboration], [arXiv:1912.06582 \[hep-ex\]](#).
- [257] M. Dentler *et al.*, *JHEP* **1808** (2018) 010, [arXiv:1803.10661 \[hep-ph\]](#).
- [258] J. M. Berryman *et al.*, *JHEP* **2002** (2020) 174, [arXiv:1912.07622 \[hep-ph\]](#).
- [259] P. V. Ramana Murthy *et al.*, *Nucl. Phys. B* **92** (1975) 269.
- [260] H. Abramowicz *et al.* [ZEUS Collaboration], *JHEP* **1309** (2013) 058, [arXiv:1306.4862 \[hep-ex\]](#).
- [261] A. Buckley *et al.*, *Eur. Phys. J. C* **75** (2015) 132, [arXiv:1412.7420 \[hep-ph\]](#).
- [262] K. Kovarik *et al.*, *Phys. Rev. D* **93** (2016) no.8, 085037, [arXiv:1509.00792 \[hep-ph\]](#).